BEILSTEIN JOURNAL OF NANOTECHNOLOGY

Biological and bioinspired adhesion and friction

Edited by Stanislav N. Gorb and Kerstin Koch

Imprint

Beilstein Journal of Nanotechnology
www.bjnano.org
ISSN 2190-4286
Email: journals-support@beilstein-institut.de

The *Beilstein Journal of Nanotechnology* is published by the Beilstein-Institut zur Förderung der Chemischen Wissenschaften.

Beilstein-Institut zur Förderung der Chemischen Wissenschaften
Trakehner Straße 7–9
60487 Frankfurt am Main
Germany
www.beilstein-institut.de

BEILSTEIN JOURNAL OF NANOTECHNOLOGY

From sticky to slippery: Biological and biologically-inspired adhesion and friction

Stanislav N. Gorb*[1] and Kerstin Koch[2]

Editorial

Open Access

Address:
[1]Functional Morphology and Biomechanics, Zoological Institute, Kiel University, Am Botanischen Garten 1–9, Kiel 24098, Germany and [2]Rhine-Waal-University of Applied Sciences, Landwehr 4, 47533 Kleve, Germany

Email:
Stanislav N. Gorb* - sgorb@zoologie.uni-kiel.de

* Corresponding author

Beilstein J. Nanotechnol. **2014,** *5,* 1450–1451.
doi:10.3762/bjnano.5.157

Received: 20 July 2014
Accepted: 13 August 2014
Published: 03 September 2014

This article is part of the Thematic Series "Biological and bioinspired adhesion and friction".

Editor-in-Chief: T. Schimmel

Physical phenomena such as adhesion and friction are widely-spread in biological systems. They rely on a combination of various mechanisms (Figure 1). Since living creatures move on land, in air and in water, there are numerous mechanical interactions between their body surfaces and the environment. Moreover, the motion of cells and tissues inside their bodies is an important part of developmental processes, circulation, respiration, excretion, and any other kind of motility. All these processes rely on adhesion and friction and are continuously under evolutionary pressure, which has contributed to the appearance of highly-specialized surfaces adapted to the enhancement, reduction, or optimization of their frictional and adhesive behavior. The study of these adaptations may also provide inspirations for the design of biologically-inspired artificial surfaces.

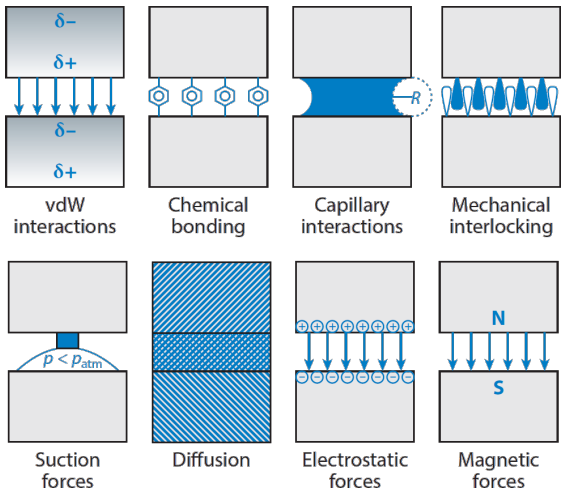

Figure 1: Different physical phenomena contribute to adhesion and friction in biological systems. From left to right: intermolecular van der Waals (vdW) interactions, chemical bonding, capillary interactions, mechanical interlocking, suction forces, diffusion of one surface material into the other contacting material, and electrostatic and magnetic forces. δ^+ and δ^- illustrate the instantaneous formation of dipoles, *R* the curvature of the meniscus, *p* the pressure, and N and S the north pole and south pole, respectively. Reproduced with permission from [1]. Copyright 2014 Annual Reviews.

The majority of books which discuss the biomechanics of contact phenomena are restricted to selected few model systems most of which deal with materials of the human body or implants. However, a human is only one among millions of living species of organisms, and interesting adhesion- and friction-related contact problems can be found everywhere in bio-

logical systems. Different types of cells, insect feet, snake skin, plant traps, and bird wings are just a few striking examples of a tremendous diversity of biological surfaces and systems with remarkable contact behavior about many of which our knowledge is limited compared to medically relevant biotribosystems.

Since the 90s a large number of studies have been published which focus on the biotribology and the bioadhesion in various biological systems. The research on frictional and adhesive properties of very diverse biological surfaces and interfaces became a broad research field at the boundary between physics and biology. Modern experimental approaches combine a variety of microscopy methods, such as light microscopy, white-light interferometry, TEM, SEM, cryo-SEM, and AFM, with force measurement techniques at the macro-, micro- and especially at the nanoscale. This Thematic Series is a collection of experimental and theoretical studies which range from insect adhesion, bacterial adhesion and skin friction to artificial biomimetic systems, e.g., snake-skin inspired polymer patterns or gecko tape. The Thematic Series does not attempt to give a comprehensive overview of the emerging field of biological contact mechanics. Rather, it is composed of a sequence of contributions devoted to recent developments within this field. The articles highlight recent achievements in the understanding of contact phenomena in biology. They also detail the process of transferring these findings into technical materials and surfaces.

Additionally, numerous experimental methods for the characterization of the tribological properties of biological surfaces at macro-, micro-, and nanoscale levels are demonstrated in this Thematic Series. This compilation of articles is an example of interdisciplinary science as it combines approaches from biology, physics, engineering, tribology and materials science. The articles of this Thematic Series are intended to be of interest to both engineers and physicists who work with biological systems as well as to biologists who study the physics of friction and adhesion.

We would like to thank all the authors for contributing their beautiful work to this Thematic Series! Moreover, we are grateful to all referees for their promptly provided reports which facilitated the high quality of the manuscripts and also allowed us to publish in a timely manner. Finally, we thank the Editorial Office at the Beilstein-Institut for their continuous great support.

Stanislav N. Gorb and Kerstin Koch

Kiel and Kleve, July 2014

Reference

1. Heepe, L.; Gorb, S. N. *Annu. Rev. Mater. Res.* **2014,** *44,* 173–203. doi:10.1146/annurev-matsci-062910-100458

License and Terms

The definitive version of this article is the electronic one which can be found at:
doi:10.3762/bjnano.5.157

Beilstein Journal of Nanotechnology

Friction behavior of a microstructured polymer surface inspired by snake skin

Martina J. Baum*, Lars Heepe and Stanislav N. Gorb

Full Research Paper

Open Access

Address:
Functional Morphology and Biomechanics, Zoological Institute, Kiel University, Am Botanischen Garten 1–9, Kiel 24098, Germany

Email:
Martina J. Baum* - mbaum@zoologie.uni-kiel.de;
Stanislav N. Gorb - sgorb@zoologie.uni-kiel.de

* Corresponding author

Keywords:
fast Fourier transformation; friction; polymer; snake inspired; stick-slip

Beilstein J. Nanotechnol. **2014,** *5,* 83–97.
doi:10.3762/bjnano.5.8

Received: 02 October 2013
Accepted: 09 January 2014
Published: 24 January 2014

This article is part of the Thematic Series "Biological and bioinspired adhesion and friction".

Associate Editor: K. Koch

Abstract

The aim of this study was to understand the influence of microstructures found on ventral scales of the biological model, *Lampropeltis getula californiae*, the California King Snake, on the friction behavior. For this purpose, we compared snake-inspired anisotropic microstructured surfaces to other microstructured surfaces with isotropic and anisotropic geometry. To exclude that the friction measurements were influenced by physico-chemical variations, all friction measurements were performed on the same epoxy polymer. For frictional measurements a microtribometer was used. Original data were processed by fast Fourier transformation (FFT) with a zero frequency related to the average friction and other peaks resulting from periodic stick-slip behavior. The data showed that the specific ventral surface ornamentation of snakes does not only reduce the frictional coefficient and generate anisotropic frictional properties, but also reduces stick-slip vibrations during sliding, which might be an adaptation to reduce wear. Based on this extensive comparative study of different microstructured polymer samples, it was experimentally demonstrated that the friction-induced stick-slip behavior does not solely depend on the frictional coefficient of the contact pair.

Introduction

The absence of extremities in snakes has strong tribological consequences for the material of their skin. The ventral body side of the snake is in continuous contact with the substrate. Therefore ventral scales must have optimized frictional properties. In order to generate propulsion during locomotion high friction and to slide along the substrate low friction must be generated [1]. Additionally, a minimum abrasion rate is necessary to enable long lasting optimal frictional properties [1]. Thus, to facilitate effective locomotion, the ventral body surface needs to possess anisotropic frictional properties, which can originate from macroscopic structures [2,3] such as the overlapping scales. The arrangement of scales provides the possibility

of interlocking between their edges and asperities of the substrate. Also microscopic structures of the skin scales, so called microornamentation [1,4-13], and specific adaptations of the material architecture of the skin, like highly ordered embedded fibers [14], which can potentially influence material properties [15,16], might contribute to the frictional anisotropy.

The role of microornamentation in frictional properties of the snake skin was extensively examined [2,3,9,11,12]. We previously showed a strong influence of the stiffness of the underlying layers of the epidermis on the anisotropic frictional properties of the skin [17]. This finding demonstrates "snake skin" as a highly complex frictional system with numerous variables influencing its frictional properties. The surface of the ventral scale of the snake *Lampropeltis getula californiae* (Figure 1a) was previously examined in detail by scanning electron microscope (SEM) (Figure 1b). Based on this morphological data [17], snake-inspired microstructured polymer surfaces (SIMPS) [18] were developed (Figure 1c). Such an implementation of the surface geometry, similar to biological microstructures of the snake, into a mechanically and chemically well-defined polymeric material, epoxy resin [19], enabled us a comparable and reproducible investigation of the influence of the surface microstructure on the frictional properties.

In order to gain insight in the influence of the snake-inspired anisotropic surface topography, additional surface topographies were investigated. The frictional coefficient of these surfaces and their stick-slip behavior were compared with those of SIMPS. The phenomenon of stick-slip is known to influence friction as well as abrasion and thus is important for technical contact surfaces. Stick-slip motion, the quasi-periodic "sticking" and "slipping" of the contacting surfaces under relative motion, can be often observed on dry, non-lubricated contacts [20-24].

The dimensions, in which this phenomenon occurs, can vary from macroscopic to atomic ones. The underlying physical effects range from the interlocking of surface asperities to van-der-Waals force [22-26]. Stick-slip is hard to describe, because it is affected by multiple geometrical and physical parameters of both frictional partners influencing the resonance frequency and its dampening. In most technical systems, the stick-slip phenomenon is unwanted, because it leads to vibrations, sometimes with acoustic emissions, to an increase in abrasion and to stronger energy dissipation, to an increase in maintenance costs of industrial facilities due to (1) the higher need of lubricants, (2) the replacement costs of machine parts, and (3) the loss of productivity due to maintenance. However, the presence of the

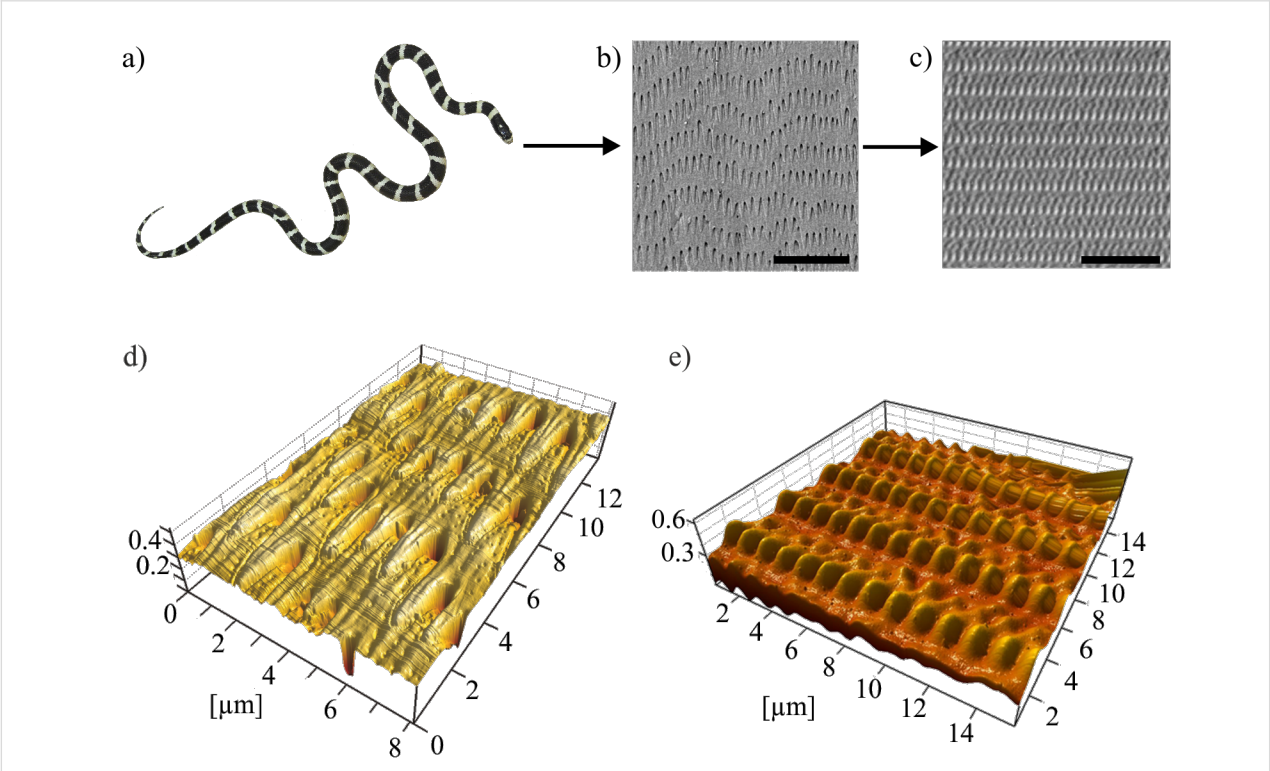

Figure 1: From snake skin to SIMPS. a) Photograph of *L. g. californiae* , the California King Snake; b) SEM micrograph of a ventral scale of *L. g. californiae*; c) SEM micrograph of the snake-inspired microstructured polymer surface – SIMPS. Scale bars: 10 µm. 3-dimensional image of d) snake skin from *L. g. californiae* and e) SIMPS based on AFM data.

stick-slip phenomenon might be also welcome in a small number of applications, like in playing the violin by moving the bow over the strings and inducing stick-slip-based vibrations of the strings [23,25,26].

In order to describe the frictional behavior in our frictional system, we have chosen an experimental setup with a limited number of variables. Using a microtribometer frictional properties were characterized by measuring tangential and normal force for the relative motion of a smooth glass ball (diameter 1 mm) brought into contact with nominal flat surfaces. The frictional counterpart (substrate) was kept constant, enabling us to investigate the influence of different surface topographies of polymer samples on the stick-slip phenomenon and on the frictional behavior in general. The different types of samples bear microstructures in comparable dimensions to those of the snake skin. Each selected type of microstructure is used to investigate the influence of certain features of snake scales responsible for specific frictional behavior.

Results

In order to characterize the influence of surface topography on frictional properties frictional measurements on differently microstructured polymer surfaces were performed. In this study we used randomly rough surfaces (RRS) with isotropic roughness. By contrast, periodical groove-like polymer surface (PGMS) consisted of equal lines and spaces with well-defined pitch lengths. The geometry of the microstructures on polymer molds of *L. g. californiae* (PMLG) from ventral scales of the snake are regular tooth-like shaped and caudally oriented (parallel to the snake's body axis). The microstructure of the snake-inspired microstructured polymer surface (SIMPS) can be abstracted as a geometrical combination of parallel lines (the denticulations), which are periodically interrupted by the elevated tips. This microstructure possesses similar shapes and dimensions of those of the biological model, the microornamentation of the ventral scales of *L. g. californiae*. Detailed information on the investigated surfaces is listed in Table 1.

Stick-slip behavior of periodical groove-like polymer surface (PGMS)

The results obtained of the FFT offer the possibility to determine the mean frictional coefficient based on the signal's bias, which is determined as the amplitude of the zero-frequency. For the PGMS, these results are listed in Table 2.

Frictional measurements performed perpendicular to the orientation of the microstructures of the PGMSs showed a wide variety of frictional responses (Figure 2). The surface with a pitch dimension of 5 µm shows a dominant frequency at 12.2 Hz, which, at the used speed of 50 µm/s, corresponds to a wavelength of 4.1 µm (Figure 2b). A comparable correlation

Table 1: Surface roughness (Ra) of all investigated polymer surfaces. "On line" roughness was measured on top of the line, along the microstructure. λ: pitch dimension. SD: standard deviation.

Sample			R_a [µm]	SD
	Periodic groove-like microstructure	PGMS - λ: 5 µm	0.18	0.02
	Periodic groove-like microstructure	PGMS - λ: 25 µm	4.95	0.37
	Periodic groove-like microstructure	PGMS - λ: 50 µm	21.75	0.26
	Periodic groove-like microstructure	PGMS - λ: 100 µm	42.50	1.47
	Periodic groove-like microstructure	PGMS - on line	0.03	0.01
	Randomly rough surface	RRS - 0.3 µm	0.23	0.00
	Randomly rough surface	RRS - 1 µm	0.41	0.01
	Randomly rough surface	RRS - 3 µm	1.11	0.11
	Randomly rough surface	RRS - 9 µm	2.39	0.07
	Randomly rough surface	RRS - 12 µm	7.64	0.13
	Polymeric mold of *L. g. californiae*	PMLG	0.09	0.04
	Snake-inspired microstructured surface	SIMPS	0.10	0.13
	Smooth surface	Smooth surface	0.02	0.01

Table 2: Mean frictional coefficients (μ) of periodical groove-like polymer surface – PGMS determined by the zero-frequency of the FFTs and standard deviation (SD). λ: pitch dimension.

Sample	Frictional coefficient in direction of measurement relative to orientation of microstructure:			
	 perpendicular		 parallel	
	μ	SD	μ	SD
PGMS - λ: 5 μm	0.30	0.01	0.23	0.02
PGMS - λ: 25 μm	0.16	0.01	0.21	0.01
PGMS - λ: 50 μm	0.18	0.01	0.22	0.02
PGMS - λ: 100 μm	0.24	0.01	0.19	0.02

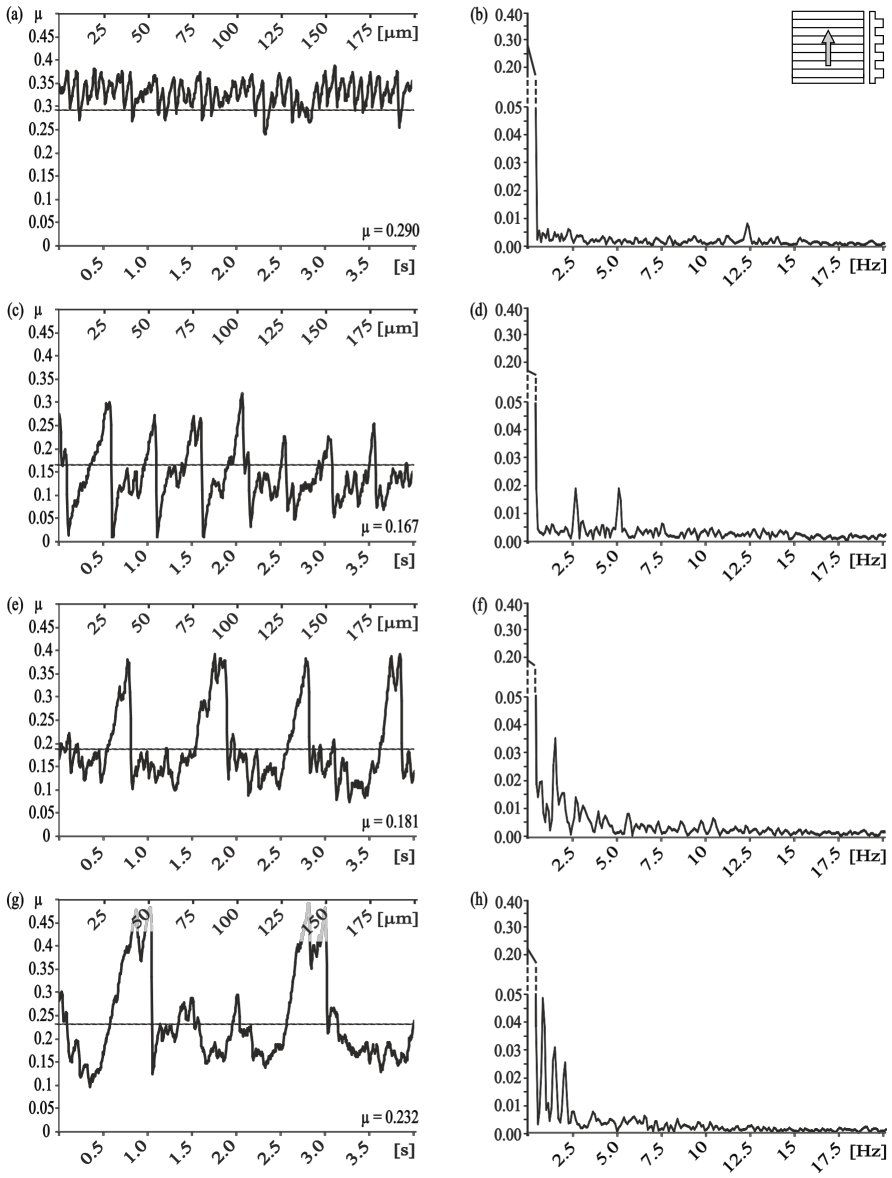

Figure 2: Results of frictional measurements on periodical groove-like polymer surface – PGMS perpendicular to the orientation of the microstructure. Left column, frictional signal in the spatial/time domain. Right column, frictional signal in the frequency domain after FFT; the ordinate shows the single-sided amplitude spectrum – SSAS. PGMS pitch dimension: a,b) 5 μm, c,d) 25 μm, e,f) 50 μm and g,h) 100 μm.

between the microstructure's pitch dimension and the dominating frequency can also be found for all other PGMS (Figure 2d,f,h). Superimposed harmonic oscillations can be found for pitch dimensions of 25 µm and 100 µm (Figure 2d,h). With the measurement direction rotated by 90°, we found completely different results for the frequency analysis (Figure 3). For the smallest and the second smallest pitch dimensions (5 µm and 25 µm, respectively) no dominant

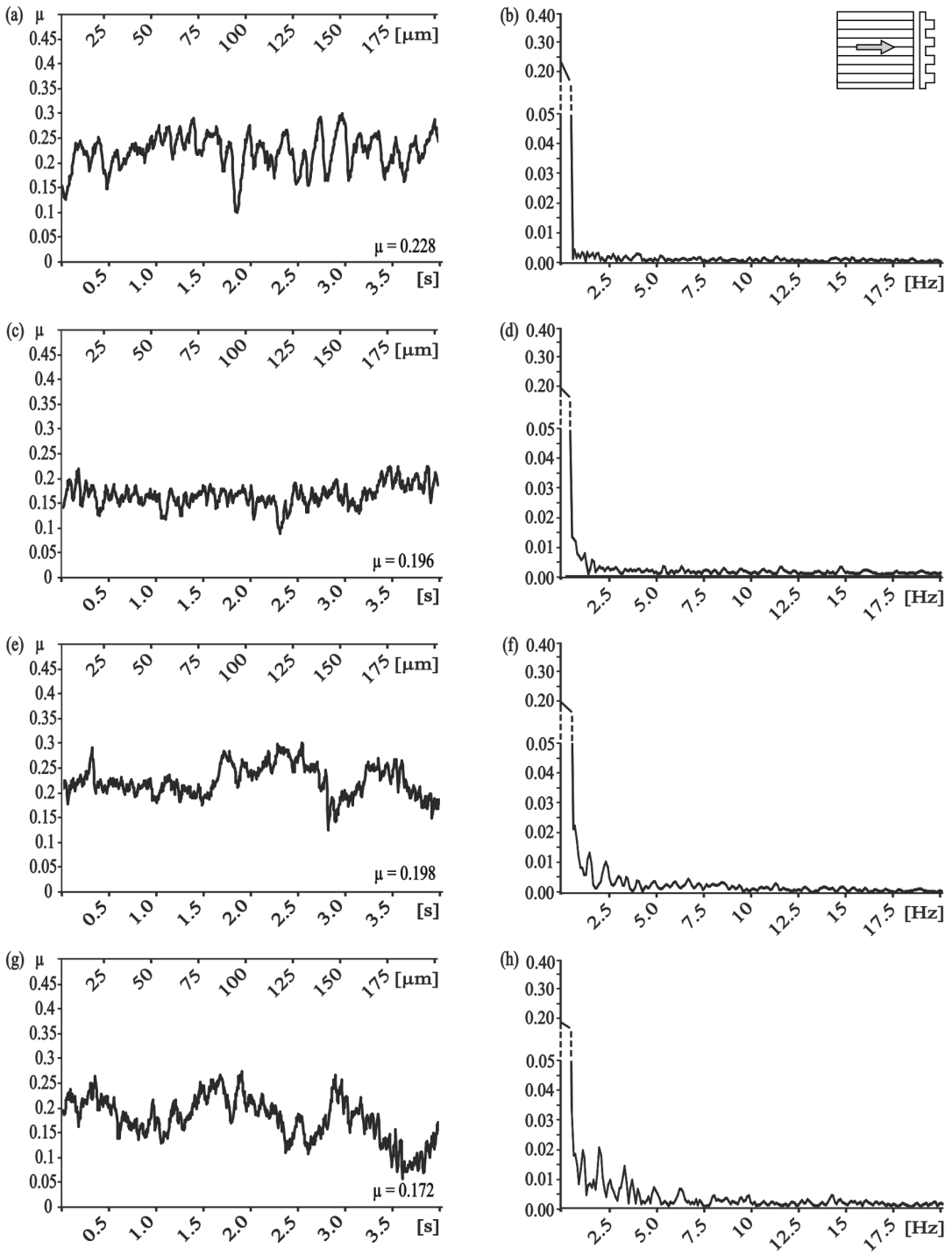

Figure 3: Results of frictional measurements on periodical groove-like polymer surface – PGMS parallel to the orientation of the microstructure. Left column, frictional signal in the spatial/time domain. Right column, frictional signal in the frequency domain after FFT; the ordinate shows the single-sided amplitude spectrum – SSAS. PGMS pitch dimension: a,b) 5 µm, c,d) 25 µm, e,f) 50 µm, g,h) 100 µm.

frequency was found (Figure 3b,d). A correlation to the pitch dimension was found for the PGMS with a structural wavelength of 50 µm, nevertheless the amplitude of the frequency spectrum was quite low (Figure 3f). Similar low amplitudes were found for the PGMS 100 µm, but the observed frequencies do not directly correlate with the microstructure dimension (Figure 3h).

Comparison of the frictional behavior in different sliding directions within each dimension of pitches, showed a strong frictional anisotropy and strong variation in the occurrence of stick-slip induced vibrations, especially at pitch dimensions of 5 µm and 25 µm. For the smallest dimension of PGMS, less vibrations and a lower frictional coefficient occurred at parallel direction of measurement, if compared to the perpendicular direction (Table 2; Figure 2b; 3b). For the PGMS with a structural wavelength of 25 µm, the vibration frequency in the parallel direction was also reduced, but the frictional coefficient in this direction was higher, than in the perpendicular direction (Table 2; Figure 2d; 3d). The results obtained on the other PGMS dimensions (50 µm and 100 µm) do not allow a clear statement on the stick-slip behavior, but a variation in the frictional coefficient between the directions of measurement were found as well (Table 2; Figure 2f,h; Figure 3f,h).

Stick-slip behavior of randomly-rough surfaces (RRS) with different grain size

The frictional measurements on RRS showed a strong influence of the surface roughness on the frictional coefficient. A minimum in friction was measured on a surface with grain size of 9 µm (Table 3). In the frequency domain, the amplitude of dominant frequencies are medium (maximal amplitude: 0.015–0.025) (Figure 4b,d) for the smaller grain size, and strong (Figure 4f,h) to very strong (Figure 4j) (maximal amplitude: >0.025) for the bigger grain sizes.

Stick-slip behavior of epoxy molds of ventral snake scales (PMLG)

The frictional measurements on polymer molds from ventral scales of *L. g. californiae* (PMLG) showed anisotropic frictional properties. The measurement along the microstructure, corresponding to the forward motion of a snake, resulted in a frictional coefficient of 0.31 ± 0.02. In opposite direction, this coefficient was significantly higher (0.32 ± 0.01). Comparison of results obtained in these sliding directions to those obtained in the lateral direction demonstrated the pronounced frictional anisotropy (µ lateral: 0.36 ± 0.02). The occurrence of stick-slip behavior was minimal (maximal amplitude: <0.01) for the forward (Figure 5b) and backward (Figure 5d) directions, whereas it was slightly stronger (maximal amplitude: 0.015–0.025) (Figure 5f) for the lateral direction. For all measured directions on this type of microstructured surface, no dominant frequency was detected.

Stick-slip behavior of snake-inspired microstructured polymer surface (SIMPS)

The frictional measurements on SIMPS show a low frictional coefficient of 0.17 ± 0.00 along the microstructure and a higher one of 0.25 ± 0.01 in the opposite and in the lateral direction of 0.25 ± 0.01. The detected dominant frequency after performed FFT (Figure 6b) corresponds to a wavelength of 2.9 µm which correlates with the distance between two rows of snake-inspired finger-shaped microstructures (Figure 1c,e).

The frictional measurements on the mold of a smooth surface showed an erratic frictional behavior with a medium frictional coefficient of 0.32 ± 0.01 (Figure 6g,h).

Discussion

We used FFT to analyze signals obtained from frictional measurements. It allowed us to gain the average frictional coefficient and information on both the dominating frequencies and amplitudes of the frictional signal. Therefore, we were able to investigate in great detail the variations in the frictional behavior depending on the surface topography.

Our data did not confirm the previous statement (e.g., [27,28]) that a low frictional coefficient correlates with no or a minimal occurrence of stick-slip behavior. The contact pairs with the lowest frictional coefficients showed in the frequency spectrum

Table 3: Mean frictional coefficients of randomly-rough surfaces – RRS determined by zero-frequency of the FFTs curve.

Sample	Frictional coefficient	
	µ	SD
RRS - 0.3 µm	0.27	0.01
RRS - 1 µm	0.26	0.00
RRS - 3 µm	0.20	0.01
RRS - 9 µm	0.19	0.00
RRS - 12 µm	0.24	0.01

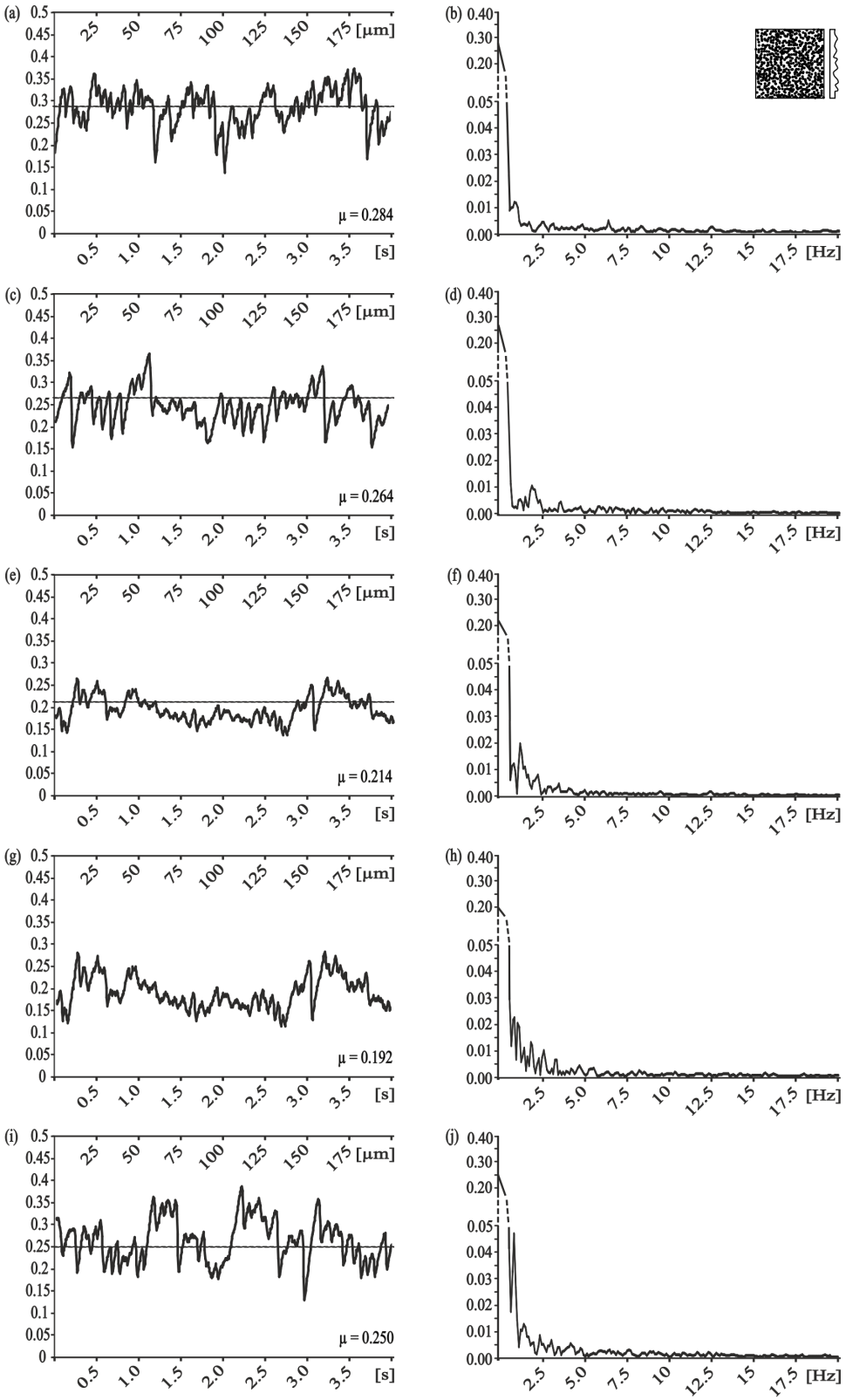

Figure 4: Results of frictional measurements on randomly-rough surfaces – RRS. Left column, frictional signal in the spatial/time domain. Right column, frictional signal in the frequency domain after FFT; the ordinate shows the single-sided amplitude spectrum - SSAS. Grain size of RRS: a,b) 0.3 µm, c,d) 1 µm, e,f) 3 µm, g,h) 9 µm, i,j) 12 µm.

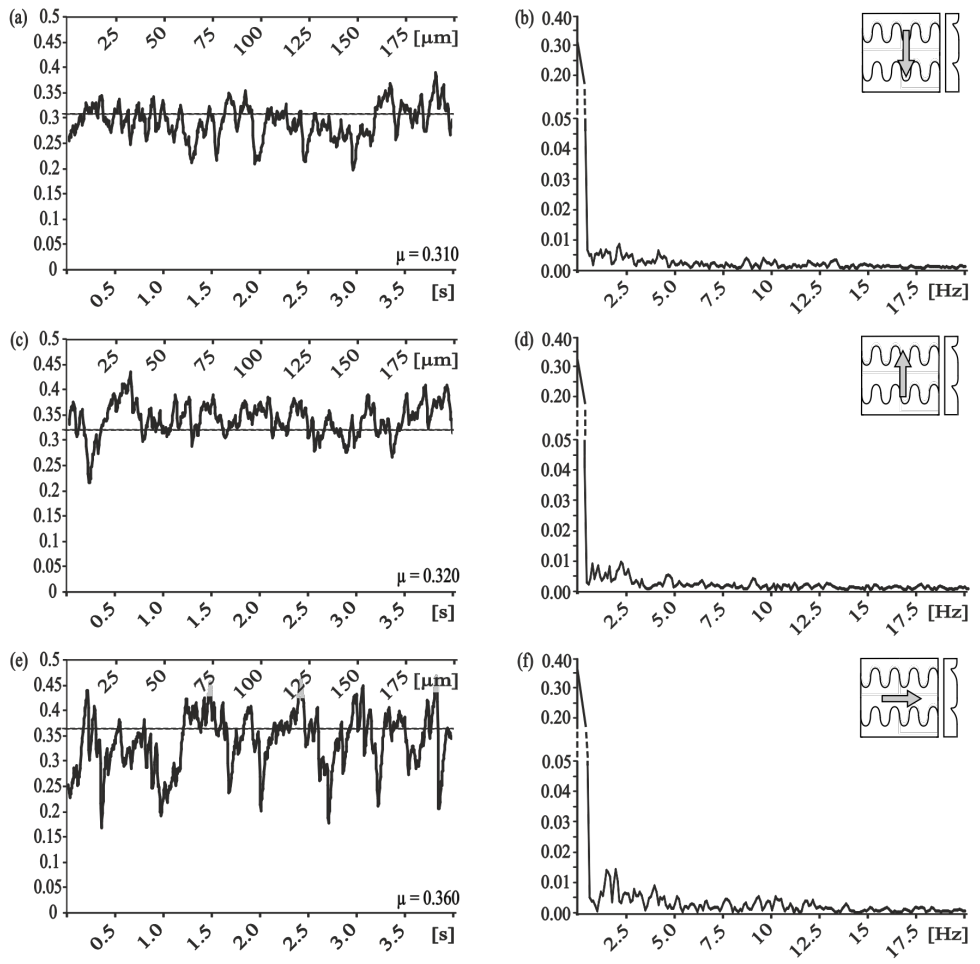

Figure 5: Frequency analysis of frictional coefficients measured on molds of snake skin (*L. g. californiae*) - PMLG. Left column, frictional signal in the spatial/time domain. Right column, frictional signal in the frequency domain after FFT; ordinate shows single-sided amplitude spectrum - SSAS. Measurement direction: a,b) along the microstructure, c,d) against the microstructure and e,f) lateral to the microstructure.

maximal amplitudes between 0.010–0.025, not minimal stick-slip amplitudes (maximal amplitude: <0.010), as expected. Substrates that showed almost no stick-slip behavior had medium to high frictional coefficients.

The stick-slip phenomenon is very important for technical surfaces under tribological stress, but only little understood and hard to quantify and control. There are many approaches to optimize frictional properties of surfaces and to affect the occurrence of stick-slip, e.g., (1) wet or solid lubrication, (2) additional application of dampening polymers, (3) use of specific microstructures or (4) application of vibrations (e.g., [23,29]).

The application of small amplitude vibrations perpendicular to the sliding direction is a remarkable approach to eliminate stick-slip. This mechanical control of the frictional system is aimed at reducing the frictional coefficient and to reduce or to eliminate stick-slip motion by stabilization of the relative motion of the sliding partners [23,28-30]. Applying vibrations normal to sliding directions can modulate the real contact area between sliding partners like microstructured surfaces, meaning external vibrations lead to a "virtual" surface roughness and are thereby able to influence frictional properties in a comparable way.

Reducing friction-induced instabilities by active dampening is advantageous due to simple controllability and adaptability to changing system properties, e.g., changing temperature. The resulting reduction in stick-slip motion can be caused by the interference of the induced vibrations with the stick-slip motion of the sliding surfaces and the externally applied vibrations normal to the sliding direction.

A similar effect can be reached by the application of microstructures to the sliding surfaces. The microstructure results in a continuous and defined periodical forming and

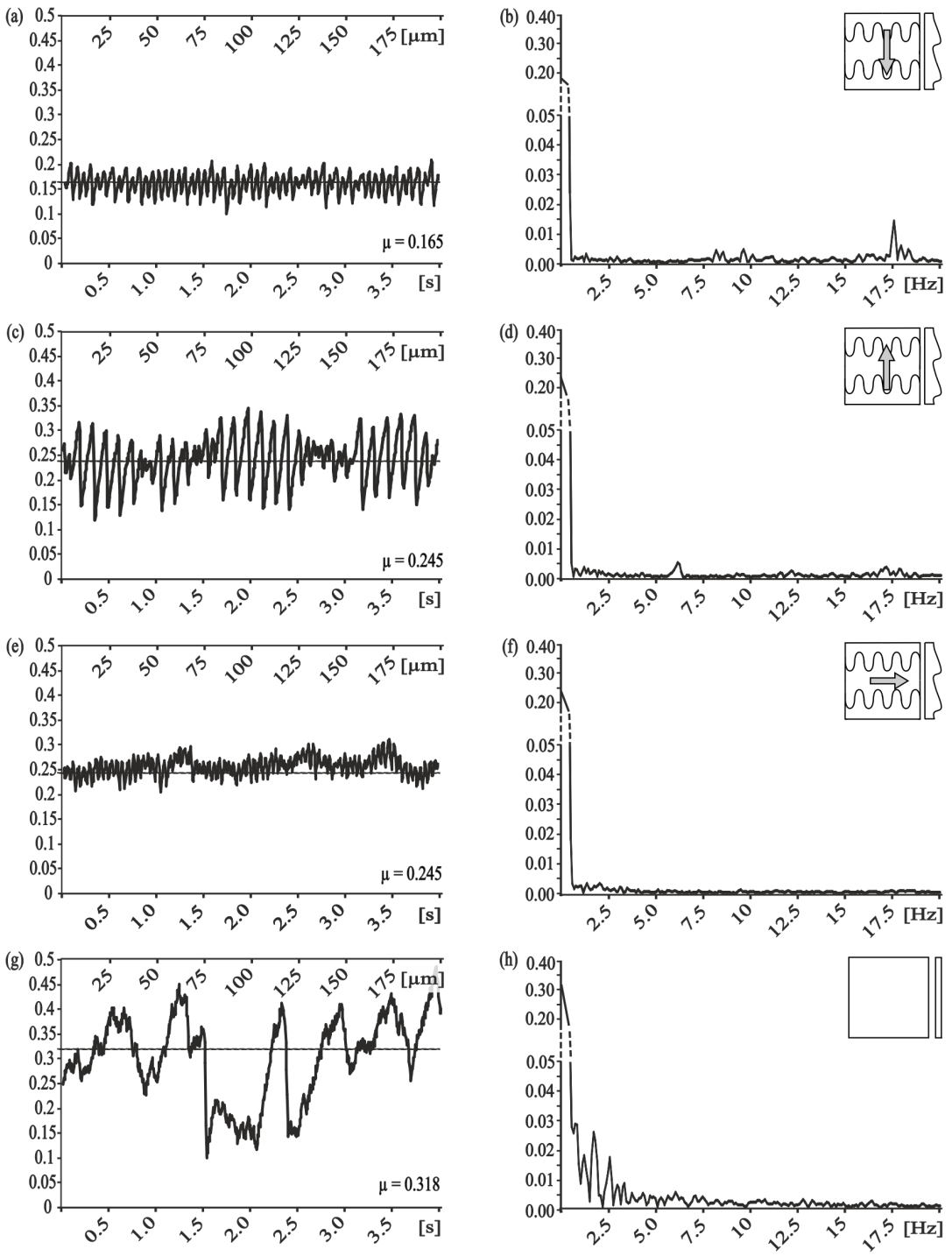

Figure 6: Frequency analysis of the frictional coefficient measured on snake-inspired microstructured polymer surface - SIMPS (a–f) and smooth surface (h,i). Left column, frictional signal in the spatial/time domain. Right column, frictional signal in the frequency domain after FFT; the ordinate shows the single-sided amplitude spectrum - SSAS. Measurement direction: a,b) along the microstructure, c,d) against the microstructure and e,f) lateral to the microstructure, g,h) on smooth surface.

breaking of contact, which can be a source for discrete occurring oscillations and thereby specific frequencies within a frictional signal. By optimizing the dimensions of the microstructure and specific vibrations induced in this way, this could be a method to reduce stick-slip motion without the need of an external oscillator [23,27,31-33]. Due to the fact that frictional properties in general and stick-slip behavior in particular also strongly depend on material properties of the sliding partners,

the optimal stick-slip reducing dimension of microstructures must be engineered for every single technical application. Nevertheless, it could be a very effective way to reduce frictional energy loss and friction-induced wear.

In the present paper, systematic investigation of the influence of different types of geometry and dimensions of the microstructure on frictional coefficients and the stick-slip behavior, we made following observations. Sliding perpendicular to the PGMS is a proper way to induce vibrations with discrete frequencies (Figure 2). Based on the fact that every dry frictional system is confronted by the stick-slip motion of sliding, flat, solid surfaces [23,25], the use of microstructures like PGMS oriented perpendicular to the sliding may be a promising way to reduce stick-slip and tune the frequency of stick-slip motion by varying the microstructure dimensions.

In order to interpret the results obtained on PGMS it is necessary to take a closer look at relative dimensions between the pitch size of the microstructure and the glass ball as the counterpart. Calculated penetration depths of the glass ball into the microstructures, based on geometry only are listed in Table 4.

It is necessary to notice that the spatial resolution of the microtribometer for cantilever deflection in normal direction is too low to detect the deflection on microstructures with pitch dimensions of 5 µm and 25 µm (penetration depth: 0.002 µm and 0.039 µm, respectively, for details see Table 4). One explanation why we were nevertheless able to observe distinct frequencies in the frictional signal within these dimensions could be the periodic variation in the real contact area during sliding perpendicular to the microstructure. These periodic changes in the real contact area cause variations in critical stiction length as reported in Yu and Wang (2012) [34]. Presuming this assumption is right, we were able to detect the stiction length measured perpendicular to the microstructure on PGMS with pitch dimensions of 5 µm and 25 µm. The observed frequencies measured perpendicular to the large-scale microstructures (PGMS pitch dimensions of 50 µm and 100 µm) can be induced by a combination of the interlocking phenomenon between the frictional partners and the variation of real contact area.

Sliding along the PGMS shows a more chaotic frictional behavior with no distinct single frequencies within the frictional signal. Statistic analysis of these data showed only a significant difference in between the biggest and the smallest pitch dimensions ($p < 0.001$, one way ANOVA followed by the Holm–Sidak method).

Dealing with the results of friction measurements perpendicular and along the microstructures, one could assume that the influence of the interlocking phenomenon on the frictional coefficient is rising with increasing pitch dimensions. However, our experimental setup showed that reduced stick-slip motion does not mandatorily correlate with a low frictional coefficient. For example, frictional measurements parallel to the small-sized microstructure showed very little stick-slip motion, but a relatively high frictional coefficient (Figure 3a–d). Bigger dimensions of the microstructure caused a decrease of the frictional coefficient, but an increase in the amplitude of the stick-slip-induced vibrations (Figure 3g,h).

Frictional measurements on RRS showed similar results regarding the non-discrete frequencies within the frictional signal. Consistent with the results for the PGMS, the lowest frictional coefficient did not correlate with a minimal stick-slip motion. Results for frictional measurements on polymeric molds from a living snake (PGLG) showed comparatively high frictional coefficients independent of measurement directions, but none the less, evident frictional anisotropy. Compared to other measured surfaces mentioned above, the stick-slip motion was reduced here, and the frictional coefficients increased. We concluded from these findings, that the anisotropic frictional properties of snake skin [17] cannot be simply be copied by producing polymeric replicas of the original snake surface. The frictional coefficient of snake skin is not only influenced by the surface microstructure but by multiple parameters [17,35]. Frictional measurements on SIMPS showed anisotropic frictional properties and quite different types of stick-slip behavior (Figure 6) in the measurements along the microstructure, showing the lowest frictional coefficient and moderate occurrence of stick-slip. The similarity in the reduction of stick-slip-motion in PMLG and SIMPS led us to conclude, that this physical phenomenon is influenced by surface microstructures. The

Table 4: Penetration depths of the glass ball into the periodical groove-like polymer surface – PGMS at different pitch dimensions based on geometry only. The calculated values, which lay beyond the system's resolution in vertical direction (cantilever deflection in vertical direction, smaller 50 nm), are shown in italics.

	PGMS - 5 µm	PGMS - 25 µm	PGMS - 50 µm	PGMS - 100 µm
Penetration depth [µm]	*0.002*	*0.039*	0.156	0.625

cause for this effect is possibly the periodicity of the microstructure, which can influence the critical stiction length during sliding, as reported by Yu and Wang (2012) [34]. Due to the fact, that snake skin has to fulfill multiple functions it can be assumed, that the tribological optimization is related to multiple physical phenomena, meaning the surface modifications bring frictional optimization [17], reduction of wear rate [35] and as shown in our study at hand reduction in stick-slip motion with it. The reduction of stick-slip behavior is directly related to the reduction of wear. Additionally, "controlled" stick-slip motion compared to "uncontrolled", randomly appearing stick-slip makes the occurring forces within a frictional system more predictable and prevents the occurrence of maximum forces, which could damage the system [31,33]. Therefore the reduction in stick-slip behavior can help to maintain optimal frictional properties of a tribological system.

To investigate the correlation between frictional coefficient and stick-slip behavior, the data were grouped into (i) low frictional coefficient and (ii) reduced stick-slip motion. The group (i) included the following samples under particular experimental conditions: PGMS, λ = 25 µm, perpendicular to the microstructure ($\mu = 0.167 \pm 0.008$); PGMS, λ = 100 µm, parallel to the microstructure ($\mu = 0.172 \pm 0.024$); RRS - 9 µm ($\mu = 0.192 \pm 0.007$); and SIMPS, along the microstructure ($\mu = 0.165 \pm 0.010$). The frequency analysis of frictional measurements on these microstructured surfaces showed frequencies of medium amplitude (maximal amplitude: 0.015–0.025).

The group (ii) of samples with reduced stick-slip motion was subdivided depending on the maximal amplitude into two groups, where stick-slip motion was (a) nearly eliminated (maximal amplitude: <0.005) and (b) strongly reduced (amplitude <0.015). Members of the first group were SIMPS measured in lateral direction and PGMS with pitch dimension of 5 µm measured parallel to the microstructure. For both samples and experimental setups, the amplitudes of the stick-slip frequencies were smaller than 0.005, and the frictional coefficients were relatively high, 0.250 ± 0.018 and 0.228 ± 0.016, respectively. The second group with reduced stick-slip motion contained the following surfaces: PGMS with pitch dimensions of 25 µm and 50 µm measured parallel to the microstructure ($\mu = 0.196 \pm 0.011$, $\mu = 0.198 \pm 0.022$, respectively); PGMS with pitch dimension of 5 µm measured perpendicular to the microstructure ($\mu = 0.290 \pm 0.006$); RRS - 0.3 µm ($\mu = 0.284 \pm 0.027$) and RRS - 1 µm ($\mu = 0.264 \pm 0.008$); molds of the snake along ($\mu = 0.31 \pm 0.018$), against ($\mu = 0.32 \pm 0.009$), and lateral ($\mu = 0.361 \pm 0.016$) to the microstructure; and SIMPS along ($\mu = 0.165 \pm 0.010$), against ($\mu = 0.245 \pm 0.019$), and lateral ($\mu = 0.250 \pm 0.018$) to the microstructure.

Following the accepted assumption of a correlation between stick-slip motion and frictional coefficient (e.g., [27,28]), one would expect to find low frictional coefficient accompanied by reduced stick-slip motion, but we were not able to confirm this expectation for frictional systems examined. One explanation of this could be the fact that most experiments on solid frictional systems were performed on metal-metal contact pair (e.g., [15,23,25]) and thereby differ in their physical properties very much from polymeric systems under consideration.

In the previous study, we focused on the effect of the effective elastic modulus on friction and thereby on the dampening within the frictional system snake-substrate [17]. We investigated the effect by measuring friction of snake skin with and without soft cushioning. It was assumed that the ability of the snakes to vary the effective elastic modulus by varying their body stiffness is useful to optimize their tribological properties in adaptation to different substrates and locomotion modes [2,36,37]. Given that the effective elastic modulus is varied in a highly optimized frictional system like snakes and taking the present data into account, the dampening has a big influence on the occurrence of stick-slip phenomenon during sliding. It is postulated that the amplitude of friction-induced vibrations is dependent on the system's dampening (e.g., [23,29]). The investigation of the effect of dampening on the frictional coefficient and stick-slip motion in biological surfaces may represent a short cut towards frictional systems with reduced stick-slip.

Material and methods

Surface fabrication and characterization

Following types of surface topography were masters: (i) a periodically groove-like microstructured polymer surface (PGMS), (ii) randomly rough surfaces (RRS) with grain sizes of 0.3, 1, 3, 9 and 12 µm (FibrMet Discs, Buehler GmbH, Düsseldorf, Germany), (iii) polymeric molds of ventral scales of *L. g. californiae* (PMLG) and (iv) a snake inspired polymer surface (SIMPS), produced in cooperation with the Leonhard Kurz Group Stiftung & Co (Fürth, Germany) and (v) a smooth glass surface as reference (Figure 7). Experiments on molds of the ventral snake surface and on SIMPS were conducted to reveal the performances of snake-inspired microstructures. The PGMS samples, characterized by a rectangular profile in cross section with four different structural wavelengths of 5, 25, 50 and 100 µm containing equal ridges and grooves (produced by the Laser Zentrum Hannover e. V., Hannover, Germany). Those were taken for the purpose of investigating the scale effects of the microstructure. Additionally, by sliding along or across the microstructure, it was possible to investigate the influence of an anisotropic geometry of microstructures on frictional properties. The RRS samples with different grain sizes were used to

investigate the influence of the surface roughness, the contact area, and the interlocking of surface asperities.

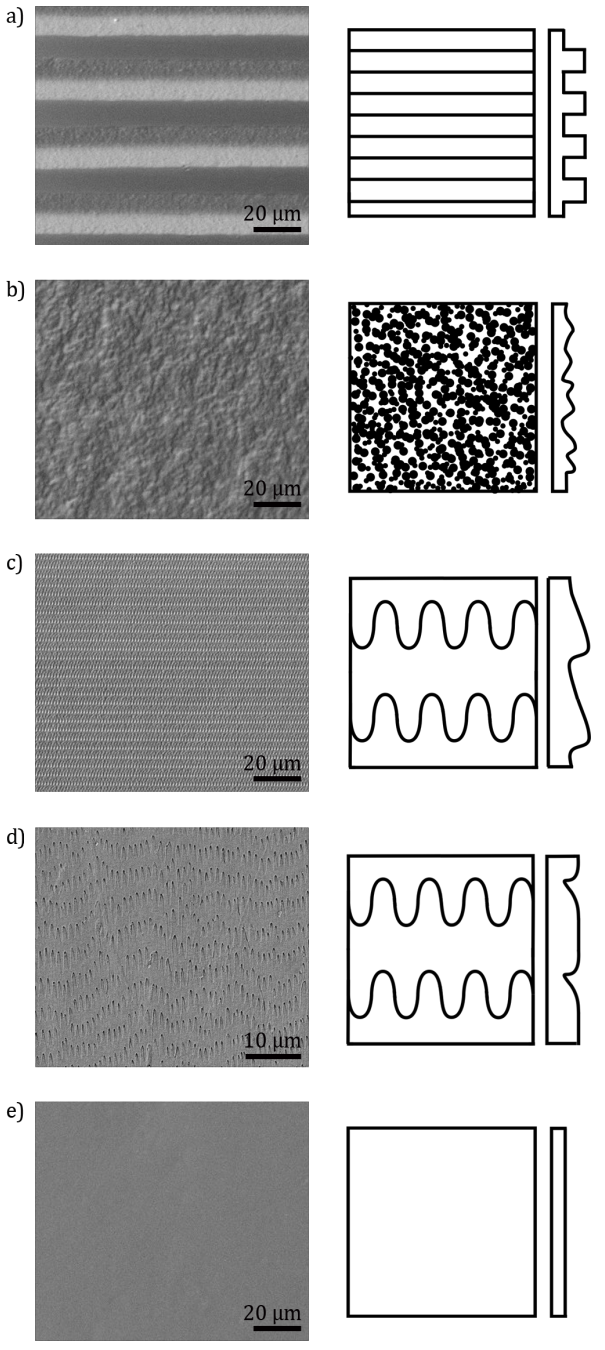

Figure 7: Exemplary overview of the topography of the examined polymer surfaces. Left column: SEM-micrographs. Right column: schematic top view and profile of the surface microstructure. a) Periodical groove-like polymer surface – PGMS (pitch: 25 µm). b) Randomly-rough surfaces – RRS (grain size: 1 µm). c) Snake-inspired microstructured polymer surface – SIMPS. d) Mold of the ventral scale of *L. g. californiae* - PMLG. e) Smooth surface.

The detailed values for surface roughness are listed in Table 1. The polymer surfaces were produced by a two-step molding technique [38]. In the first step, the master surface was covered with fluid two-component polyvinylsiloxane (PVS) (Coltène President light body, Coltène Whaledent Dentalvertriebs Ltd., Constance, Germany), which polymerizes within few minutes. In the subsequent second step, the negative cast was filled with the low-viscosity epoxy resin [19]. This polymer (Polysciences Inc., Eppelheim, Germany) consists of (1) nonenyl succinic anhydride (NSA) (61.3%), (2) 3,4-epoxycyclohexylmethyl-3,4-epoxycyclohexyl-carboxylate (ERL 4221) (23.6%), (3) diglycidyl ether of polypropyleneglycol (D.E.R. 736) (14.2%), and (4) *N*,*N*-dimethylaminoethanol (DMAE) (0.9%). The polymerization of the resin took place over night at 70 °C.

The surface roughness (R_a) of molds was measured with a white light interferometer (New View 6000, ZygoLOT, Darmstadt, Germany). For metrologic characterization of the surface microstructures, the image analysis software SigmaScanPro 5.0 (SPSS Inc., Chicago, USA) was used. Roughness (R_a) perpendicular to the lines of the PGMS samples was calculated depending on the pitch width and depth.

For surface visualization, two scanning electron microscopes (SEM) were used (Hitachi S-4800 and TM-3000, Hitachi High-Technologies Corporation, Tokyo, Japan) at an acceleration voltage of 2–3 kV and 5 kV, respectively. The polymer material was fixed by adhesive pad and sputter-coated with gold/palladium (80:20) with a layer thickness of 20 nm. For sputter-coating, the high vacuum sputter coater Leica EM SCD500 (Leica Microsystems GmbH, Wetzlar, Germany) was used.

Detailed characterization of the surface topography was performed by a NanoWizard® atomic force microscope (JPK Instruments), mounted on an inverted light microscope (Zeiss Axiovert 135, Carl Zeiss MicroImaging GmbH). The SIMPS were imaged by using the intermittent contact mode of the AFM. The error channel (also known as the amplitude channel) visualizes the change in damping of the cantilever amplitude while scanning the surface. Only images obtained with the error channel are shown, because this visualization method is helpful to gain a more vivid imaging of the surface topography. Scans were carried out at a 1 Hz scan rate and a resolution of 1024 × 1024 pixels with an intermittent contact mode cantilever (c = 50 Nm^{-1}, NST-NCHF, Nascatec GmbH, Stuttgart, Germany), at ambient conditions (room temperature 24 °C, relative humidity 41%). NanoWizard® SPM software 3.3.23 (JPK Instruments) was used to obtain AFM images and NanoWizard® image processing software 3.3.25 was applied to extract 3D surface profiles.

Frictional measurement

Frictional measurements were carried out with the microtribometer Basalt-MUST (TETRA GmbH, Ilmenau, Germany). 2-dimensional force detection was accomplished by a metal cantilever (C_{Fn}: 22.3 N/m, C_{Ft}: 23.1 N/m). The spacial resolution of the system in detection a deflection of the cantilever was 50 nm. The averaged applied normal force was 0.6 mN. The measurement was performed over a sliding distance of 500 µm at a velocity of 50 µm/s. As contact partner, a glass ball with a diameter of 1 mm was chosen and fixed to the cantilever by cyanoacrylate glue (Ergo 5925 Elastomer, Tagelswangen, Switzerland). The roughness of the glass ball determined by a white light interferometer (NewView, ZygoLOT GmbH, Darmstadt, Germany) was R_a = 0.006 µm. The polymer surfaces were fixed on metallic sample holders by cyanoacrylate glue.

To characterize frictional properties of the periodic groove-like patterned surfaces (PGMS) friction measurements in two different directions were done: parallel to the microstructure (i) and perpendicular to the microstructure (ii) (Figure 8a). For frictional characterization frictional measurements on polymeric moulds of *L. g. californiae* (PMLG) were executed in four different directions: along the microstructure (i), corresponding to the forward movement of the animal, against the microstructure (ii), corresponding to the opposite direction, and lateral direction relative to the body axis (Figure 8b). The frictional properties of the SIMPS, was measured in three different directions: along the anisotropic microstructure (i), against the anisotropic microstructure (ii), and in the lateral direction, perpendicular to both other directions (iii) (Figure 8c). For the characterization of surfaces with isotropic topography (RRS and smooth surface), frictional measurements were done in one directions.

Individual measurements were repeated 15 times on each SIMPS and on the smooth reference surface. For the molds of the snake scales three frictional measurements on three different scales of three different individuals were performed. The other surfaces were tested five times each. Each measurement was performed on a new area of the surface to minimize the influence of abrasion. Obtained data were statistically analyzed with SigmaPlot 11.0 software (SPSS Inc., Chicago, USA). Kruskal-Wallis one way ANOVAs followed by Holm–Sidak tests with a significance level of $p < 0.05$ were performed.

The contact area was calculated by the Hertz-model [39] using the data on E-moduli of the polymerized Spurr resin and the glass ball (7 GPa and 70 GPa, respectively [40]) and an assumed Poisson ratio of 0.5 for both materials. The calculation of the contact area (Hertz-model) between non-microstructured polymer surface and smooth glass ball gave an apparent area of 40 µm^2.

To characterize the frictional properties of the surfaces with microstructures with anisotropic geometry, the measurements were performed in different sliding directions: along, against, and lateral to the microstructures, as illustrated in Figure 8.

Data processing

The stick-slip behavior of microstructured polymer surfaces was characterized by the analysis of the frequency spectrum gained by fast Fourier transformation (FFT) of the frictional signal (of the spatial domain). In general, the FFT is used to transform a function of time into a function of frequency. In the frequency spectrum, the temporal domain of a sinusoidal signal can be visualized in the spatial domain. By performing an inverse FFT, the original signal can be reproduced. Until now, most investigations on the stick-slip phenomenon are based on the simple consideration of the frictional coefficient over the measured distance or time (e.g., [20,21,26-28,33,41-43]). However, this technique is not sufficient to identify dominant frequencies, when several sinusoidal oscillations are overlapping each other. In this case, only a detailed analysis of the frequency spectrum can identify all present frequencies and

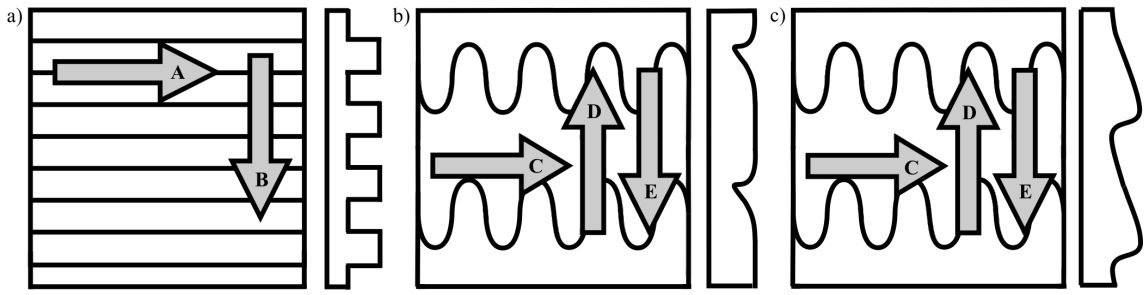

Figure 8: Scheme of surface geometry and sliding directions of friction measurement, top view (left) and side view (right). a) Periodical groove-like polymer surface - PGMS, b) Polymeric mould of *L. g. californiae* – PMLG, c) Snake-inspired microstructured polymer surface – SIMPS. Directions of measurement: A: parallel to microstructure, B: perpendicular to microstructure, C: lateral to microstructure, D: against microstructure, E: along microstructure.

their corresponding amplitudes. By using this approach for data analysis, we were able to identify friction induced vibrations caused by the stick-slip phenomenon as well as the frictional coefficient with the same mathematical tool. Within the frequency spectrum, the mean friction coefficient and frequencies of the dominant friction-induced vibrations can be identified.

In detail, the following procedure was applied to analyze friction behavior, exemplarily shown in form of a typical friction curve with the friction coefficient (defined according to Coulomb's friction law μ = Ft/Fn) over time or displacement, respectively (Figure 9). The exemplary data results from the experiment, where a glass sphere moved perpendicular to the microstructure of a PGMS with a pitch size of 5 μm. One section of the data, typically representing a distance of about 100 μm and exhibiting dynamic friction (without static friction and obvious disturbances) was chosen for further processing (Figure 9a). The data set was then Fourier transformed after zero padding to the next power of 2 and weighting by a Hamming window. Data processing was performed using the build-in *fft*-command of MATLAB Version 7.12.0.635 (R2011a) (MathWorks Inc., Ismaning, Germany). For the sake of convenience, we only show the single-sided amplitude spectrum (SSAS). Figure 9b shows the SSAS of the data section shown in Figure 9a. In general, the zero frequency peak is the off-set or bias of the friction curve and can be identified as the average friction coefficient. Furthermore, a characteristic peak at 79.3 Hz was found in all measurements and is attributed to the resonance frequency of the experimental setup (glass ball fixed on a metal cantilever in contact with the surface). Since no measurement frequencies higher than 20 Hz were obtained, except for the resonance frequency, the SSAS is cut at that frequency. Whenever a periodic friction behavior was observed, e.g., induced by the periodic microstructure, a peak at a specific frequency or wavelength was detected in the SSAS. Exemplary, in Figure 9b, a peak at about 12.2 Hz, corresponding to a wavelength of about 4.1 μm at the deployed speed of 50 μm/s, is revealed. Since this correlates well with the pitch of 5 μm of the PGMS surface, we are confident with our procedure.

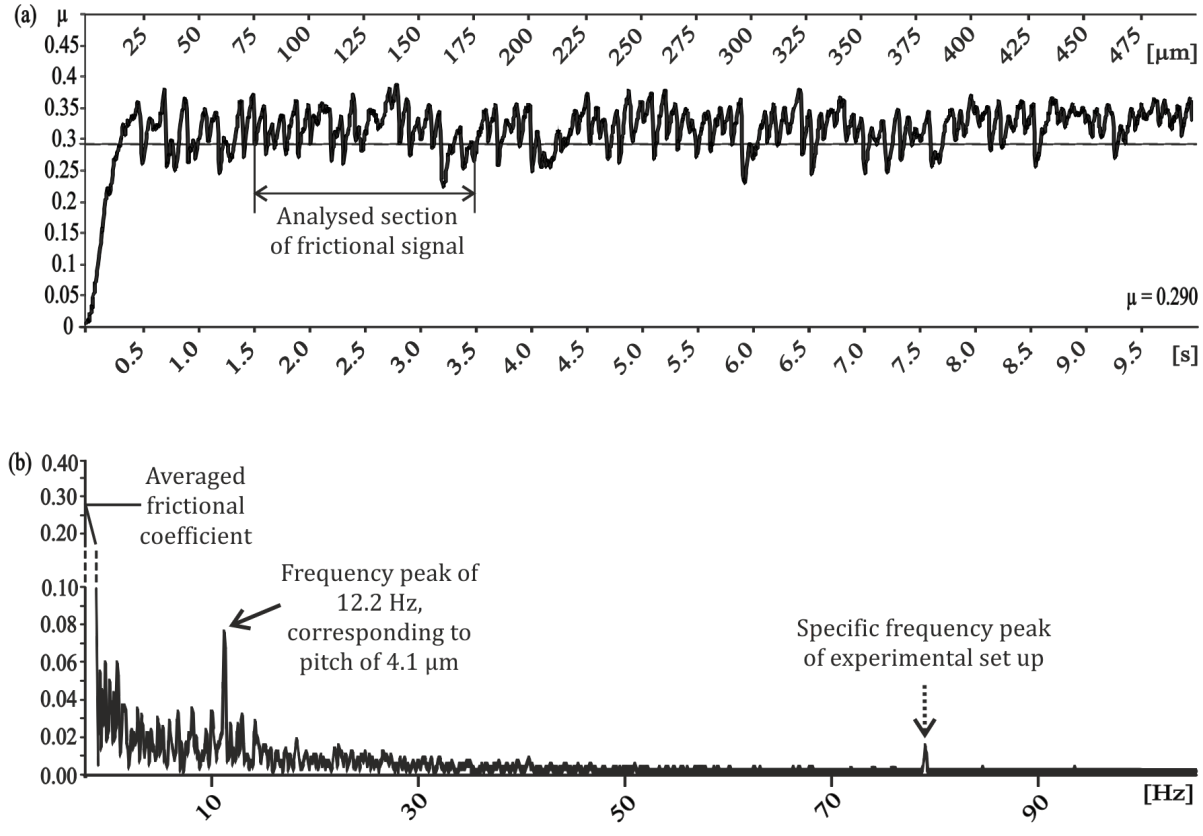

Figure 9: Example of data analysis of the frictional signal measured on the periodical groove-like polymer surface – PGMS (pitch dimension: 5 μm) perpendicular to the orientation of the microstructure, a) in spacial/time domain. Averaged frictional coefficient and exemplary selected section of frictional signal for data processing; b) in frequency domain based on FFT, ordinate shows single-sided amplitude spectrum – SSAS. Intersection of the graph on the ordinate presents the averaged frictional coefficient. At 12.2 Hz a dominating frequency according to a pitch of 4.1 μm can be identified. This correlates well to the pitch of 5 μm (lines and spaces of the substrate). Dotted arrow points out the resonance frequency peak, which is the property of the experimental setup, because it could be found in each combination of tribometer, glass ball, and epoxy mold samples.

Acknowledgements

The authors are thankful to Henrik Peisker and Kirstin Dening for technical support using the AFM. This work was funded by the Federal Ministry of Education and Research, Germany within the BIONA program (01 RB 0812A) to SNG.

References

1. Renous, S.; Gasc, J. P.; Diop, A. *Fortschr. Zool.* **1985,** *30,* 487–489.
2. Gray, J.; Lissmann, H. W. *J. Exp. Biol.* **1950,** *26,* 354–367.
3. Marvi, H.; Hu, D. L. *J. R. Soc., Interface* **2012,** *9,* 3067–3080. doi:10.1098/rsif.2012.0132
4. Leydig, F. *Archiv für mikroskopische Anatomie* **1873,** *9,* 753–794.
5. Hoge, A. R.; Santos, P. S. *Science* **1953,** *118,* 410–411. doi:10.1126/science.118.3067.410
6. Maderson, P. F. A. *Br. J. Herpetol.* **1964,** *3,* 151–154.
7. Maderson, P. F. A. *Am. Zool.* **1972,** *12,* 159–171.
8. Price, R. M. *Br. J. Herpetol.* **1982,** *16,* 294–306.
9. Hazel, J.; Stone, M.; Grace, M. S.; Tsukruk, V. V. *J. Biomech.* **1999,** *32,* 477–484. doi:10.1016/S0021-9290(99)00013-5
10. Gower, D. J. *J. Morphol.* **2003,** *258,* 249–268. doi:10.1002/jmor.10147
11. Berthé, R. A.; Westhoff, G.; Bleckmann, H.; Gorb, S. N. *J. Comp. Physiol., A* **2009,** *195,* 311–318. doi:10.1007/s00359-008-0408-1
12. Abdel-Aal, H. A.; Vargiolu, R.; Zahouani, H.; El Mansori, M. *Wear* **2012,** *290–291,* 51–60. doi:10.1016/j.wear.2012.05.015
13. Schmidt, C.; Gorb, S. N. *Zoologica* **2012,** *157,* 1–106.
14. Klein, M.-C. G.; Gorb, S. N. *Zoologica*, in press.
15. Lancaster, J. K. *Brit. J. Appl. Phys.* **1968,** *2,* 549–560.
16. Politi, Y.; Priewasser, M.; Pippel, E.; Zaslansky, P.; Hartmann, J.; Siegel, S.; Li, C.; Barth, F. G.; Fratzl, P. *Adv. Funct. Mater.* **2012,** *22,* 2519–2528. doi:10.1002/adfm.201200063
17. Benz, M. J.; Kovalev, A. E.; Gorb, S. N. *Proc. SPIE8339* **2012,** 83390X. doi:10.1117/12.916972
18. Baum, M. J.; Fadeeva, E.; Gorb, S. N. Dry friction of a microstructured polymer surface inspired by snake skin, in preparation.
19. Spurr, A. R. *J. Ultrastruct. Res.* **1969,** *26,* 31–43. doi:10.1016/S0022-5320(69)90033-1
20. Li, K.; Ni, B. Y.; Li, J. C. M. *J. Mater. Res.* **1996,** *11,* 1574–1580. doi:10.1557/JMR.1996.0197
21. Jang, H.; Ko, K.; Kim, S. J.; Basch, R. H.; Fash, J. W. *Wear* **2004,** *256,* 406–414. doi:10.1016/S0043-1648(03)00445-9
22. Nosonovsky, M.; Bhushan, B. *Mater. Sci. Eng., R* **2007,** *58,* 162–193. doi:10.1016/j.mser.2007.09.001
23. Popov, V. L. *Contact mechanics and friction – Physical principles and Applications;* Springer-Verlag: Berlin, Heidelberg, Germany, 2010.
24. Bhushan, B. *Fundamentals of Tribology and Bridging the Gap Between the Macro- and Micro/Nanoscales;* NATO Science Series II, Vol. 10; Kluwer Academic Pub.: Dordrecht, Netherlands, 2001.
25. Persson, B. N. J. *Sliding friction: physical principles and applications,* 2nd ed.; Springer-Verlag: Berlin, Heidelberg, Germany, 2000. doi:10.1007/978-3-662-04283-0
26. Scherge, M.; Gorb, S. N. *Biological micro- and nanotribology;* Springer-Verlag: Berlin, Heidelberg, Germany, 2001. doi:10.1007/978-3-662-04431-5
27. Berman, A. D.; Ducker, W. A.; Israelachvili, J. N. *Langmuir* **1996,** *12,* 4559–4563. doi:10.1021/la950896z
28. Urbakh, M.; Klafter, J.; Gourdon, D.; Israelachvilli, J. *Nature* **2004,** *430,* 525–528. doi:10.1038/nature02750
29. Kinkaid, N. M.; O'Reilly, O. M.; Papadopoulos, P. *J. Sound Vibrat.* **2003,** *267,* 105–166. doi:10.1016/S0022-460X(02)01573-0
30. Cochard, A.; Bureau, L.; Baumberger, T. *J. Appl. Mech.* **2003,** *70,* 220–226. doi:10.1115/1.1546241
31. Rabinowicz, E. *Friction and Wear of Materials;* John Wiley & Sons: New York, USA, 1965.
32. Varenberg, M.; Gorb, S. N. *Adv. Mater.* **2009,** *21,* 483–486. doi:10.1002/adma.200802734
33. Murarash, B.; Itovich, Y.; Varenberg, M. *Soft Matter* **2011,** *7,* 5553–5557. doi:10.1039/c1sm00015b
34. Yu, C.; Wang, J. Q. *Sci. Rep.* **2012,** *2,* No. 988. doi:10.1038/srep00988
35. Klein, M.-C. G.; Gorb, S. N. *J. R. Soc. Interface* **2012,** *76,* 3140–3155. doi:10.1098/rsif.2012.0479
36. Gray, J. *J. Exp. Biol.* **1946,** *23,* 249–268.
37. Westheide, W.; Rieger, R. *Spezielle Zoologie-Teil 2: Wirbel- oder Schädeltiere;* Springer-Verlag: München, Germany, 2004.
38. Gorb, S. N. *Microsc. Today* **2007,** *3,* 44–46.
39. Hertz, H. *Journal für die reine und angewandte Mathematik* **1881,** *92,* 156–171.
40. Peisker, H.; Gorb, S. N. *J. Exp. Biol.* **2010,** *213,* 3457–3462. doi:10.1242/jeb.043661
41. Byerlee, J. D. *Tectonophysics* **1970,** *9,* 475–486. doi:10.1016/0040-1951(70)90059-4
42. Heslot, F.; Baumberger, T.; Perrin, B.; Caroli, B.; Caroli, C. *Phys. Rev. E* **1994,** *49,* 4973–4988. doi:10.1103/PhysRevE.49.4973
43. Bhushan, B. *Wear* **2005,** *259,* 1507–1531. doi:10.1016/j.wear.2005.01.010

License and Terms

Beilstein Journal of Nanotechnology

Hairy suckers: the surface microstructure and its possible functional significance in the *Octopus vulgaris* sucker

Francesca Tramacere[*1], Esther Appel[2], Barbara Mazzolai[*1] and Stanislav N. Gorb[*2]

Letter

Open Access

Address:
[1]Center for Micro-BioRobotics, Istituto Italiano di Tecnologia, viale Rinaldo Piaggio 34, Pontedera 56025, Italy and [2]Functional Morphology and Biomechanics, Zoological Institute, Kiel University, Am Botanischen Garten 1–9, Kiel 24098, Germany

Email:
Francesca Tramacere[*] - francesca.tramacere@iit.it; Barbara Mazzolai[*] - barbara.mazzolai@iit.it; Stanislav N. Gorb[*] - sgorb@zoologie.uni-kiel.de

* Corresponding author

Keywords:
adhesion; attachment; Mollusca; octopus sucker; underwater sealing

Beilstein J. Nanotechnol. **2014,** *5,* 561–565.
doi:10.3762/bjnano.5.66

Received: 28 January 2014
Accepted: 08 April 2014
Published: 02 May 2014

This article is part of the Thematic Series "Biological and bioinspired adhesion and friction".

Associate Editor: K. Koch

Abstract

Octopus suckers are able to attach to any smooth surface and many rough surfaces. Here, we have discovered that the sucker surface, which has been hypothesised to be responsible for sealing the orifice during adhesion, is not smooth as previously assumed, but is completely covered by a dense network of hair-like micro-outgrowths. This finding is particularly important because it provides another demonstration of the role of hair-structures in a sealing mechanism in water, similar to that previously described for clingfish and abalones. Moreover, the discovered hairs may provide an additional adhesive mechanism that works in concert with suction. The discovered surface structures might be potentially interesting for biomimetics of novel technical suction cups with improved adhesion capabilities on non-smooth surfaces.

Introduction

An octopus sucker consists of two portions: an upper hollow cup, the acetabulum; and a lower disk-like portion, the infundibulum, located at the attachment face of the sucker (Figure 1a,b). It is known that octopus suckers adhere not only to perfectly smooth surfaces but also to surfaces with a certain roughness [1], where technical suction cups usually fail [2,3]. This ability can be explained by the exceptional materials properties, i.e., softness, of the infundibulum [4]. However, it remains unclear how the octopus is able to remain attached to a wall or object for a long period of time [1]. Recently, it has been shown that in *Octopus vulgaris*, the acetabulum does not have a spherical shape as was previously described in the literature [1]; rather, there is a well-developed protuberance on its roof sticking out towards the orifice (Figure 1b) [5].

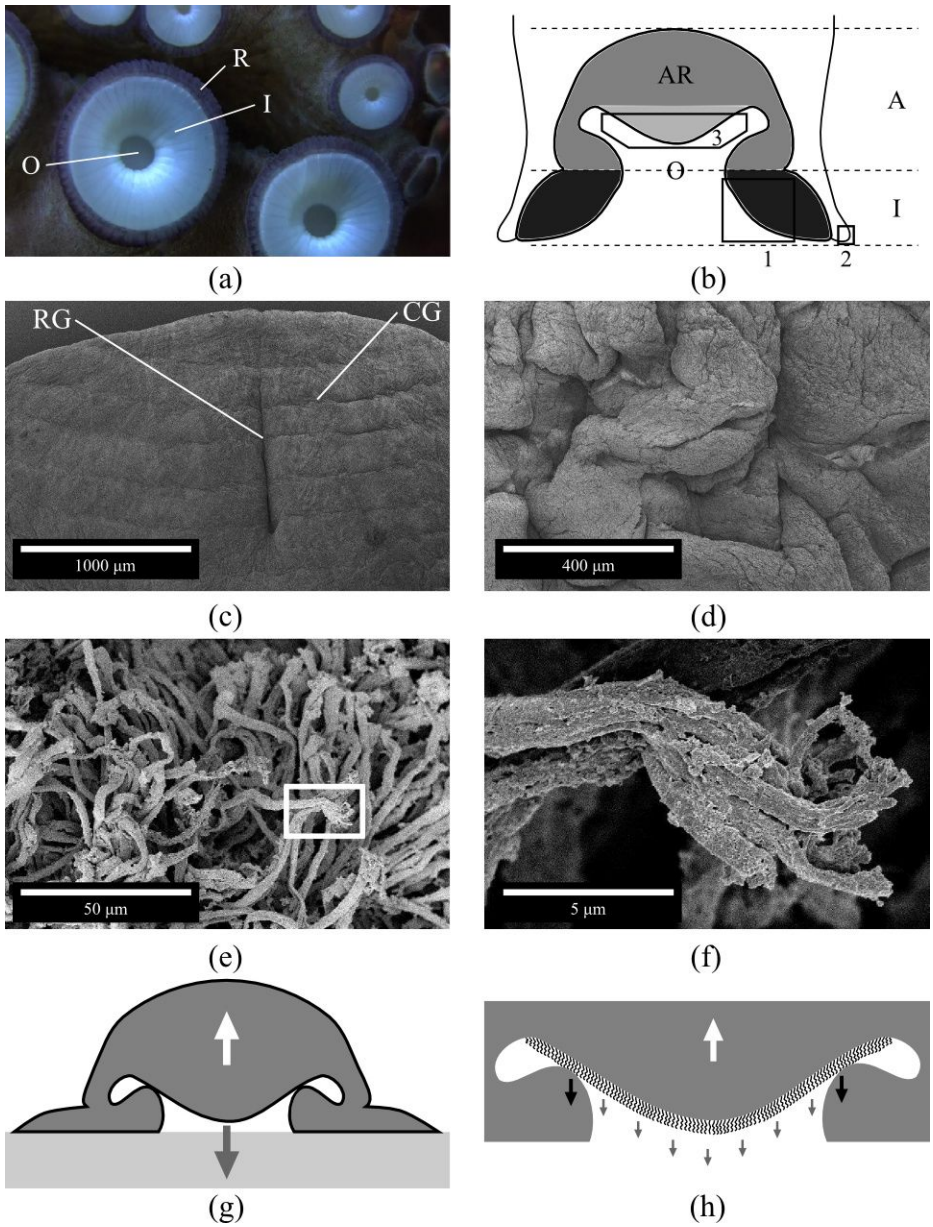

Figure 1: (a) Photograph of the frontal view of an octopus sucker. Infundibulum (I); orifice (O); and rim (R). (b) Schematic structure (transversal section) of an octopus sucker. The upper part in grey (light and dark grey) is the acetabulum (A). The lower disk-like black-coloured portion is the infundibulum (I). The light grey-coloured portion is the protuberance of the acetabular roof (AR); and O is the orifice. (c–f) Scanning electron microscopy images of an octopus sucker. (c) Infundibulum (please, refer to black box 1 in (b)). Radial (RG) and circumferential (CG) grooves. (d) Rim (please, refer to black box 2 in (b) and label R in (a)). (e) Surface of acetabular protuberance (please, refer to black box 3 in (b)). (f) Enlargement of white box in (e). (g) Sucker configuration during adhesion process [5]. The restoring elastic force (white arrow) is balanced by the cohesive forces of the water (grey arrow). (h) Enlargement of (g) considering the contribution of hairs. The restoring elastic force (white arrow) is counterbalanced by the cohesive forces of the water (grey arrows) and the adhesion force exerted by hairs (black arrows).

Additionally, it has been hypothesised that this acetabular protuberance plays a crucial role in increasing the performance of the adhesive system [5]. The pressing of the acetabular protuberance against the orifice was suggested to close the orifice when the suction is active [5]. Thus, if the suction muscles stop contracting, the maintenance of the low pressure at the interface is guaranteed by the closure of the orifice [5]. This mechanism would allow the octopus to perform an efficient attachment for a long period of time with minimal energy consumption. A specialised microstructure, as recently shown for clingfish [3] and abalone molluscs [6], might play an important watertight role in this minimal energy consumption hypothesis [5].

For studying this, we used scanning electron microscopy (SEM) at high resolution to explore the microstructure of different octopus sucker surfaces (acetabular protuberance and infundibulum). Considering the substantial interest of engineers in this biological system as a source of inspiration [7-10] for biomimetics of novel technical suction cups, our findings may provide an interesting idea for improving the adhesion capability of artificial devices on non-smooth surfaces.

Experimental

The surfaces of the acetabular protuberance and infundibulum of *Octopus vulgaris* suckers were observed by using a Hitachi S-4800 (Hitachi High-Technologies Corp., Tokyo, Japan) scanning electron microscope. Both sexes with a body mass range from 400 to 850 g were analysed. Animals were obtained from licensed fishermen, who captured these animals from the bay of Livorno (Italy) in October 2012 for human consumption. The suckers were taken from freshly killed animals. All facilities and procedures complied with European law (Directive 2010/63/EU).

For SEM, the freshly explanted suckers were fixed in 70% ethanol. Small portions of the acetabulum and infundibulum were dehydrated and then, critical point dried by using a critical point drying apparatus (E3000 Series, Quorum Technologies, UK). Dried samples were mounted on aluminium stubs and sputter coated with a 10 nm thick layer of gold–palladium (SCD 500 sputter coater equipped with QSG 100 quartz film thickness monitor, BAL-TEC, Liechtenstein).

Results

The arms of the octopus species examined (*Octopus vulgaris*) are characterised by two rows of suckers with diameters that range from a few centimetres (in the proximal region) to a few millimetres (in the distal region). All the suckers investigated presented the same gross/general morphology. The infundibulum (please refer to I in Figure 1a,b), which is the externally visible portion of the sucker, is entirely encircled by an epithelial rim (please refer to R in Figure 1a) and communicates with the internal portion of the sucker (please refer to A in Figure 1b) through an orifice (please refer to O in Figure 1(a,b). On the acetabular roof (please refer to AR in Figure 1b), there is a protuberance that sticks out toward the orifice (Figure 1b).

The infundibulum, which is the portion that comes in contact with the substrate during attachment, exhibits a dense network of radial and circumferential grooves on its surface (please refer to RG and CG in Figure 1c). The radial grooves appear deeper than the circumferential ones. In addition, the entire surface of the infundibulum is covered by randomly distributed, interconnected ridges. The rim that encircles the infundibulum appears like a deeply folded, loose epithelium, characterised by numerous grooves and ridges (Figure 1d).

The surface of the acetabular protuberance is completely covered with a dense network of brush-like hairs, which are approximately 50 µm (±18 µm, n = 25) long and have a diameter of 2 µm (±0.9 µm, n = 25) (Figure 1e,f). Each hair apically branches into very small filaments, which are approximately 5 µm (±2.8 µm, n = 18) long and have a diameter of 0.3 µm (±0.2 µm, n = 25) (Figure 1f). These hairy structures are only localised on the acetabular protuberance and are completely absent in the infundibular portion.

Discussion

The surface of the infundibulum allows strong adaptation to any type of non-smooth substrate. It was observed that an octopus is able to attach to very rough surfaces generating a pressure difference of up to 0.268 MPa [11]. To obtain such an adhesion force, a perfect seal at the interface between the sucker and the substrate is crucial. Similar to abalone, in which the external surface of its side foot is characterised by many crests and grooves, in octopus suckers the seal is guaranteed by the presence of ridges and grooves on the rim encircling the infundibulum. These structures allow the octopus suckers, as well as the abalone feet, to perfectly adapt to the contour of the objects with which they come in contact.

The most important discovery of this work is the presence of hairs on the acetabular protuberance. This is of particular interest because to the best of our knowledge, these microstructures are unknown in the literature. Moreover, the presence of such hierarchical hairs on the entire surface of the acetabular protuberance supports the adhesion mechanism recently suggested for *O. vulgaris* [5]. To obtain an efficient attachment mechanism for a long period of time, the adhesion configuration shown in Figure 1g should be maintained without any muscular effort. In detail, the restoring elastic force (please refer to white arrow in Figure 1g), responsible for the detachment of the acetabular protuberance from the upper surface of the side wall of the orifice, needs to be balanced. In [5], such a force is balanced by the cohesive forces of the water in the infundibular portion (the water under tension behaves like a solid) (please refer to grey arrow in Figure 1g). Based on our recent results, an adhesion force (please refer to black arrows in Figure 1f), exerted by the dense network of hairs, is present on the surface of the acetabular protuberance. This force might work in addition to the cohesive forces of water, assisting in keeping the orifice closed for extended periods of time and significantly increasing the resistance to the restoring force. In this new scenario, the restoring elastic force is balanced by the cohesive forces of the water in the infundibular compartment and the

adhesion force exerted by the hairs. In this way, the forces are in equilibrium and the sucker is able to maintain the adhesion configuration without any further energy consumption (muscular involvement). Moreover, the acetabular protuberance could work as a valve that enables and disables the adhesion process [5], and the hairs could ensure the watertight closure of the valve.

A similar hair structure was also found in the northern clingfish, *Gobiesox maeandricus* [3]. On its ventral side, this fish bears an adhesive disc that allows the animal to attach on smooth surfaces and on very rough surfaces and to resist strong water currents. The hairs structures observed in the fish are quite similar in size and aspect ratio to the hairs described here in the octopus sucker. In addition, the sole foot epithelium of abalone *Haliotis tuberculata* is characterised by a dense field of long hairs, here called cilia, that measure 0.2–0.3 μm in diameter [6]. In this case, small ciliary tufts occur at a very low density in the side foot; whereas, they become significantly more dense in the sole foot. Similar to octopus suckers, the cilia are covered by a layer of mucus. However, in all the three cases (octopus, abalone, and clingfish), the hairs lack the spatulate termini that are well known in the attachment pads of terrestrial animals [12,13]. In the case of the clingfish, it was hypothesised that the amazing tenacity observed for this fish could be related to the hierarchical structure of the hairs ("microvilli") [3]. Moreover, the absence of spatulate termini contact elements as well as the presence of water and mucus between hairs and respective substrates suggest that biological structures operating underwater cannot exploit filament-like structures to generate van der Waals forces [3]. We completely agree with this idea and think that under wet adhesion conditions, a system consisting of hairs, mucus, and water (just like octopus suckers) could improve attachment due to following mechanisms: (i) exploiting the presence of mucus and filaments to increase the viscosity coefficient at the interface and to resist to the shear forces; and (ii) exploiting the high bulk modulus of water between the sucker and substrate that resists tensile stress (detachment force). Moreover, some studies on artificial materials have demonstrated that fibrillar microstructures are preferred to flat surfaces in applications in which a total attachment force must be generated in a binary on/off state [14]. These studies also reveal that structured surfaces show a 25% increase in pull-off force when immersed in water, and their underwater attachment is 20 times more effective than that of flat surfaces [15].

The grooves found in the infundibulum area generating a dense network of interconnected channels are instead fundamental for increasing the adhesion area subjected to the suction. Due to the presence of a particular surface microstructure, an octopus can maintain attachment for long periods of time without muscular effort and thus without energy expenditure. This functional mechanism represents a very interesting source of inspiration for engineers and robotics specialists in the development of novel biomimetic adhesion devices.

Acknowledgements

The authors thank Joachim Oesert (Zoological Institute: Functional Morphology and Biomechanics, Kiel University) for his skilful technical assistance at the SEM facility. This work was supported by a grant from COST Action TD0906 "Biological Adhesives: from Biology to Biomimetics" (COST-STSM-TD0906-11884).

References

1. Kier, W. M.; Smith, A. M. *Integr. Comp. Biol.* **2002,** *42,* 1146–1153. doi:10.1093/icb/42.6.1146
2. Berengueres, J.; Tadakuma, K.; Kamoi, T.; Kratz, R. Compliant Distributed Magnetic Adhesion Device for Wall Climbing. In *Proceedings of the International Conference on Robotics and Automation,* April 10–14, 2007; IEEE: New York, NY, USA, 2007; pp 1256–1261.
3. Wainwright, D. K.; Kleinteich, T.; Kleinteich, A.; Gorb, S. N.; Summers, A. P. *Biol. Lett.* **2013,** *9,* 20130234. doi:10.1098/rsbl.2013.0234
4. Tramacere, F.; Kovalev, A.; Kleinteich, T.; Gorb, S. N.; Mazzolai, B. *J. R. Soc. Interface* **2014,** *11,* 20130816. doi:10.1098/rsif.2013.0816
5. Tramacere, F.; Beccai, L.; Kuba, M.; Gozzi, A.; Bifone, A.; Mazzolai, B. *PLoS One* **2013,** *8,* e65074. doi:10.1371/journal.pone.0065074
6. Bravo Portela, I.; Martinez-Zorzano, V. S.; Molist-Perez, I.; Molist García, P. *Sci. World J.* **2012,** *2012,* 960159.
7. Grasso, F. W.; Setlur, P. *Bioinspiration Biomimetics* **2007,** *2,* S170. doi:10.1088/1748-3182/2/4/S06
8. Hu, B.-s.; Wang, L.-w.; Fu, Z.; Zhao, Y.-z. *Int. J. Adv. Rob. Syst.* **2009,** *6,* 151–160. doi:10.5772/7228
9. Tramacere, F.; Beccai, L.; Sinibaldi, E.; Laschi, C.; Mazzolai, B. *Procedia Comput. Sci.* **2011,** *7,* 192–193. doi:10.1016/j.procs.2011.09.053
10. Tramacere, F.; Beccai, L.; Mattioli, F.; Sinibaldi, E.; Mazzolai, B. Artificial adhesion mechanisms inspired by octopus suckers. In *Proceedings of the International Conference on Robotics and Automation (ICRA),* St. Paul, MN, USA, May 14–18, 2012; IEEE: New York, NY, USA, 2012; pp 3846–3851.
11. Smith, A. M. *J. Exp. Biol.* **1991,** *157,* 257–271.
12. Persson, B. N. J.; Gorb, S. *J. Chem. Phys.* **2003,** *119,* 11437. doi:10.1063/1.1621854
13. Varenberg, M.; Pugno, N. M.; Gorb, S. N. *Soft Matter* **2010,** *6,* 3269–3272. doi:10.1039/c003207g
14. Varenberg, M.; Gorb, S. *J. R. Soc. Interface* **2007,** *4,* 721–725. doi:10.1098/rsif.2007.0222
15. Varenberg, M.; Gorb, S. *J. R. Soc. Interface* **2008,** *5,* 383–385. doi:10.1098/rsif.2007.1171

Beilstein Journal of Nanotechnology

The surface microstructure of cusps and leaflets in rabbit and mouse heart valves

Xia Ye[1], Bharat Bhushan[*2], Ming Zhou[3] and Weining Lei[1]

Full Research Paper

Open Access

Address:
[1]School of Mechanical Engineering, Jiangsu University of Technology, Changzhou Jiangsu 213001, China, [2]Nanoprobe Laboratory for Bio- & Nanotechnology and Biomimetics (NLB2), The Ohio State University, 201 W 19th Ave., Columbus, OH 43210, USA and [3]Center of Photonics Fabrication, Jiangsu University, Zhenjiang Jiangsu 212013, China

Email:
Bharat Bhushan[*] - bhushan.2@osu.edu

* Corresponding author

Keywords:
contact angle; geometric parameter; heart valve; hemocompatibility; microstructure

Beilstein J. Nanotechnol. **2014,** *5,* 622–629.
doi:10.3762/bjnano.5.73

Received: 15 August 2013
Accepted: 17 April 2014
Published: 13 May 2014

This article is part of the Thematic Series "Biological and bioinspired adhesion and friction".

Guest Editor: S. N. Gorb

Abstract

In this investigation, scanning electron microscopy was used to characterize the microstructure on the surfaces of animal heart valve cusps/leaflets. The results showed that though these surfaces appear smooth to the naked eye, they are actually comprised of a double hierarchical structure consisting of a cobblestone-like microstructure and nano-cilia along with mastoids with a directional arrangement. Such nanostructures could play a very important role in the hemocompatibility characteristics of heart valves. On this basis, the model of the microstructure was constructed and theoretical analysis was used to obtain optimal geometric parameters for the rough surface of artificial valve cusps/leaflets. This model may help improve reconstructive techniques and it may be beneficial in the design and fabrication of valve substitutes or partial substitutes. Namely, the model may help ameliorate heart valve replacement surgery.

Introduction

Bionics, or biomimetics, have made tremendous developments in the past decade due to advancements in nano- and biotechnologies. After millions of years of evolution and optimization, the surfaces of many organisms have formed a variety of special micro- and nanoscale hierarchical structures. These structures show many perfect characteristics such as superhydrophobicity, low adhesion, and drag reduction. Therefore, studying the surfaces of natural organisms is extremely important and significant. Moreover, results of this study could have a substantial effect on the manufacturing of artificial biological products. During the past decade, the special surface microstructures of plant leaves have been studied beginning with the lotus leaf [1-3]. Researchers then studied the microstructures of the India canna leaf, the rice leaf, and the leaf of *Colocasia esculenta* [4,5]. Subsequently, the study of surface microstructures expanded to animals. Researchers studied surface microstructures of the water skipper's leg, the moth's eye, shark skin, the darkling beetle, and the cicada's wing [6-15]. At the same

time, the relationship between superhydrophobicity and surface microstructures attracted strong interest. A large number of surfaces with all kinds of microstructures are manufactured by physical or chemical methods [16-22]. These manufactured surfaces have a wide range of applications in industry, agriculture, military and other areas [23-26].

Heart valves are located between the atria and both right and left ventricles, between the aorta and the left ventricle, and between the pulmonary artery and the right ventricle. These valves play a key role by forcing blood to flow in one direction through the heart and all blood vessels throughout the body. If valvular lesions occur a heart valve will need to be replaced. But once an artificial heart valve is implanted its surface changes by absorbing blood proteins, by platelet adhesion, and by the eventual formation of thrombi. Despite many efforts, blood clots are still an urgent and unsolved problem. In this paper, the surface microstructures of heart valve cusps/leaflets taken from animals are studied along with the effect of these microstructures on blood flow characteristics. Thus, this study will help improve the hemocompatibility of artificial heart valves.

Experimental

Sample preparation: The thoracic cavities of the rabbits and the mice were cut open by using scissors and the hearts were removed. After irrigating with phosphate buffered saline (PBS), the hearts were fixed in a solution of 2.5% glutaraldehyde (Res Group Co., Ltd. chemical reagents) for 2 h. Then the atria and ventricles were cut open, and all of the heart valves (including aortic, mitral and tricuspid) were removed. The valves were placed in a freeze-dryer (ES-2030 vacuum freeze-drying device, Hitachi Japan) to be frozen, dehydrated, and dried with *tert*-butanol for 2–3 h at a temperature of −10 °C.

Characterization of the microstructure on the surface of the heart valve: The heart valves were observed by using the scanning electron microscope (S-3000N scanning electron microscope SEM, Hitachi Japan) at a voltage of 10 kV in order to characterize the microstructures on their surfaces. To improve the conductivity of the sample, before being observed the dried heart valves were treated with spray-gold (E-1010 ion sputtering device, Hitachi Japan) having a coating thickness of approximately 5 nm.

Results and Discussion

The microstructure on the surface of the aortic valve cusps

The aortic valve controls the direction of blood flow from the left ventricle to the aorta. When the ventricle is in systole, the intraventricular pressure increases dramatically. Until it exceeds the arterial pressure, the aortic valve opens. The blood from the left ventricle flows to the aorta and passes through the aortic valve. With the ending of ventricular pumping, the ventricle begins in diastole. Meanwhile, the intraventricular pressure rapidly decreases until it is equal to the arterial pressure, the aortic valve closes and blood does not flow backwards. The scanning electron microscopy (SEM) image of the aortic valve of the mouse is shown in Figure 1.

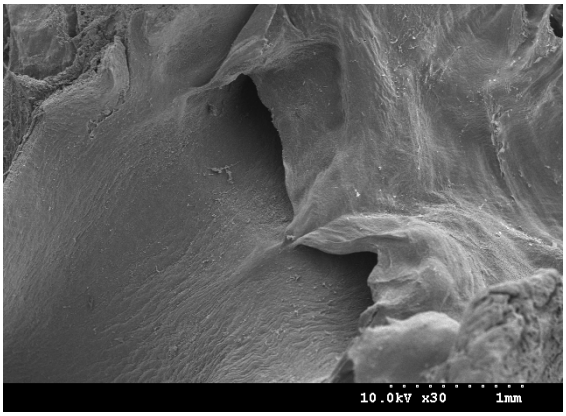

Figure 1: SEM image of the aortic valve of the mouse.

The microstructure on the surface of the aortic valve cusps is shown in Figure 2. It is evident from these images that a regular cobblestone-like structure appears on the surface of the heart valve cusps. This structure is similar to the microstructure on the surface of the lotus leaf. This cobblestone-like structure is uniformly distributed on the surface of the valve cusps and the bottom diameter of each “cobblestone” is approximately 5–9 μm. Figure 2b shows a high-resolution SEM image of the microstructure. In this image the hierarchical structure is formed of tenuous villi and “cobblestones”, and each villu has a diameter of 140–190 nm and a height of 350–500 nm. Because of the presence of a micro–nano composite hierarchical structure on the surface of the aortic valve cusps the actual contact area between blood and the surface of the valve is greatly reduced when blood flows through the valve. Thus the resistance to blood flow by the surface of the valve is reduced and the adhesion of blood platelets is also reduced. Eventually, the formation of blood clots is greatly reduced.

Even more interesting, through the scanning electron microscope we found that the arrangement of the mastoids on the surface of the aortic valve cusps is directional. Figure 3 shows the arrangement of the mastoids along the blood flow of the aortic valve. It was found that the direction of the mastoids arrangement is the same as the direction of the blood flow, that is the same as the direction of the force transmission and it

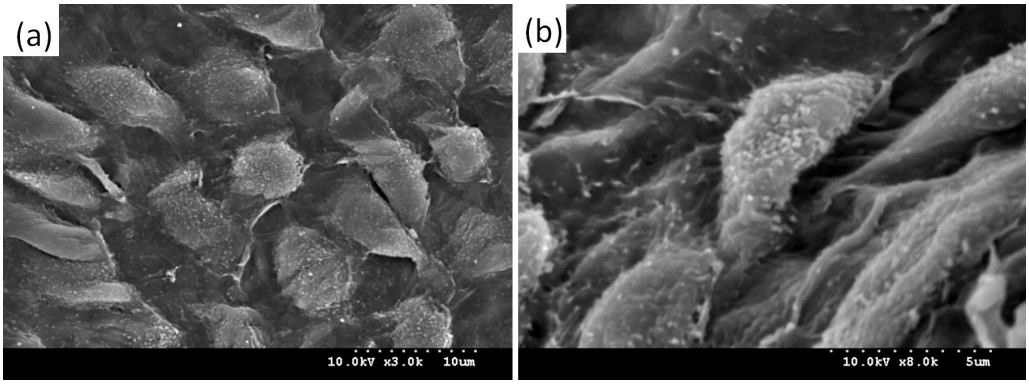

Figure 2: SEM images of the microstructure on the aortic valve cusps surface: (a) the cobblestone structure; (b) the cilia structure.

happens to be the same as the arrangement of the microstructure on the surface of the rice leaf studied by Jiang Lei [3]. Precisely because of the arrangement of this microstructure, blood flows more easily in the direction indicated by the red arrow than in the direction perpendicular to the arrow.

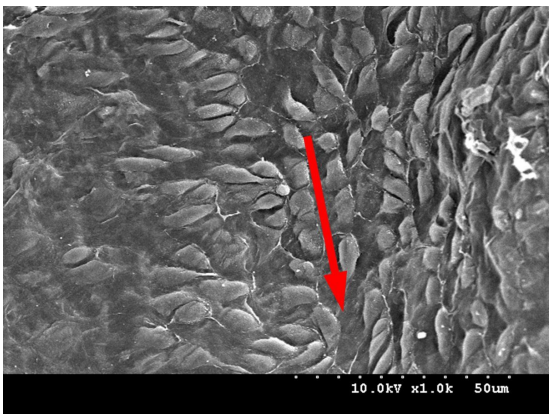

Figure 3: The direction of aligned cobblestones in the direction of blood flow.

The microstructure on the surface of the mitral valve leaflets

Mitral is derived from the word “miter”, which is a bishop’s hat with two points. The mitral valve is used to control the unidirectional blood flow from the left atrium to the left ventricle. It is composed of two valve leaflets connected via the chordae tendineae to the papillary muscles, which are located in the myocardium (shown in Figure 4). When the atrium is in systole, the volume of the atrium decreases and then the atrial pressure increases, so the leaflets of the mitral valve open allowing blood to pass through the valve without difficulty to flow from the left atrium to the left ventricle. Subsequently, the atrium is in diastole and the ventricle is in systole. The papillary muscles located in the myocardium also contract with the contraction of the ventricle and the chordae tendineae are stretched. Then leaflets close to prevent the blood from backflowing. At this point, the leaflet is just like a sail and the chordae tendineae are just like ropes. Under normal circumstances, sails are filled by wind (that is the blood) and bellied out to their ideal bulge to control the direction of a ship (that is to ensure unidirectional blood flow). However, in the case of mitral valve disease, such as leaflets lengthy, weakness of myocardial contractility and ruptured or fused tendon causing uneven pulling force, some wind (blood) will pass through the sails (mitral valve leaflets) when the ventricle is in systole. This abnormal phenomenon may lead to the occurance of hemodynamic changes and the increase of cardiac load, causing cardiac hypertrophy, heart failure and other series of heart diseases.

Figure 4: The mitral valve of the mouse.

The microstructure on the surface of the mouse’s mitral valve leaflets is shown in Figure 5. From this image, we find that the micro–nano composite hierarchical structure is also present on the surface of the mitral valve leaflets. Namely the distribution

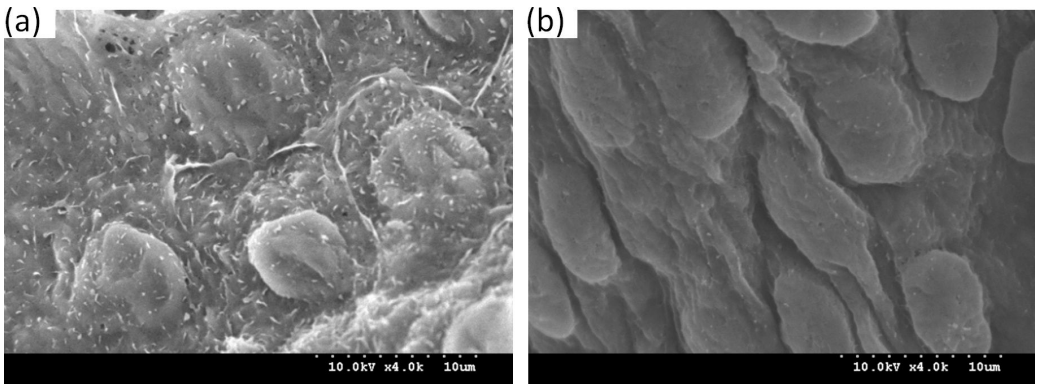

Figure 5: SEM images of the microstructure on the mitral valve leaflets surface: (a) non-heparinized; (b) heparinized.

of the nano-scale cilia structure on the micron papillae is similar to the distribution of the microstructure on the surface of the aortic valve cusps. Without treatment by heparin there is a lot of mucus attached to the mitral valve leaflets surface. Therefore the mastoid structure is not obvious (shown in Figure 5a), but the cilia structure is seen clearly. The structures shown in Figure 5b were on the surface of the mitral valve leaflets that were treated with heparin. Because of rolling caused by heparin, the cilia structure was destroyed, so it is not obvious. However, because of the elimination of mucus, the mastoid structure became very clear.

In addition, the arrangement of the microstructure on the surface of the mitral valve leaflets can be seen as directional, and its direction is consistent with the direction of blood flow, as shown in Figure 6. The arrow in Figure 6 is pointed in the direction of blood flow. Compared to the blood flow in the perpendicular direction, the blood flowing in the direction of the arrow has less resistance and less adhesion of platelets to the valve leaflets' surface will occur. It is mainly due to the proportion of the liquid–gas phase being larger during the liquid–solid–gas-phase contact between the valve's surface and blood is larger, because of the increasing of the gap between the mastoids. Eventually, in the direction of the arrow, the formation of thrombus will be reduced.

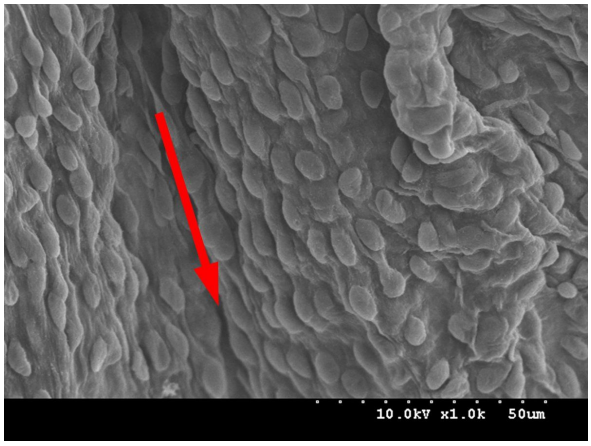

Figure 6: The direction of aligned "cobblestones" on the mitral valve leaflet's surface.

The microstructure on the surface of tricuspid valve leaflets

The tricuspid valve controls the unidirectional flow of blood from the right atrium to right ventricle. Because it is composed of three leaflets it is called a tricuspid valve. The rabbit heart is 4 to 5 times larger than the heart of the mouse, so the tricuspid valve of the rabbit is larger than that of the mouse. Figure 7 shows the SEM images of the rabbit's tricuspid valve leaflets. The structure of the tricuspid valve is similar to that of the mitral vlave. Through the chordae tendineae, the valve leaflets are also connected to the papillary muscles located in the myocardium, which is the same as the mitral valve. Additionally, both the mechanism and the time of opening and closing of these two kinds of valve are identical. When the atrium is in systole and the ventricle is in diastole, both of them open. On the contrary, when the ventricle is in systole and the atrium is in diastole, both of them close. The difference between them is that the tricuspid valve with three leaflets ensures the unidirectional flow of blood from right atrium to the right ventricle. The microstructure on the surface of the rabbit's tricuspid valve leaflets is shown in Figure 7b. As shown in the figure, there are also micro- and nano-scale cilia mastoid composite hierarchical structures exsiting on the surface of the rabbit's tricuspid valve leaflets.

Besides the aortic, mitral and tricuspid valves, there is another kind of heart valve, the pulmonary valve. The pulmonary valve controls the direction of blood flow only from the right ventricle to the pulmonary. The pulmonary valve often acts as an autolo-

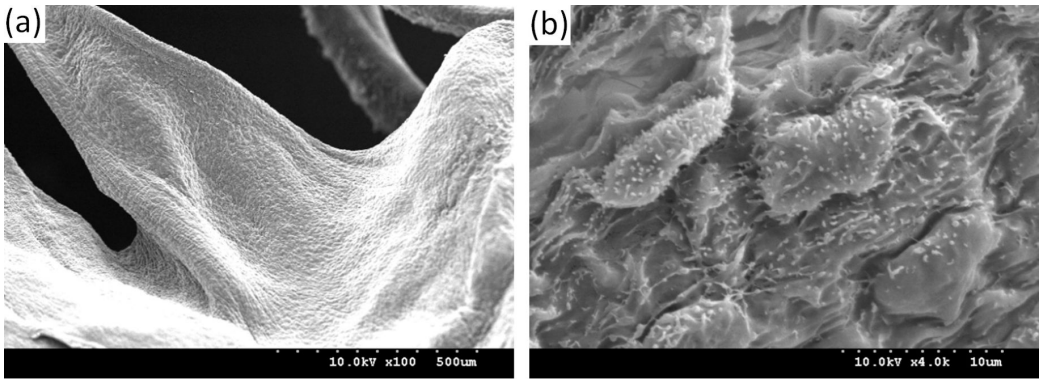

Figure 7: (a) SEM image of the tricuspid valve leaflets of the rabbit; (b) SEM image of the microstructure on the tricuspid valve leaflets surface.

gous substitute to replace the aortic valve during the Ross-operation, because they are very similar in structure and in the mechanism of openging and closing. However, the intraventricular pressure is different between the left and the right ventricle. Therefore, it is necessary to study the microstructure on the surface of the pulmonary valve cusps in order to find the differences and/or similarities of both valve cusps. Furthermore, according to the different directions of blood flow between atrial and ventricle, the orientation of the superficial structures on the surface of both sides of the mitral or tricuspid leaflets should be investigated. All of these will be our reseach interests in furture and this study will enormously help us to design and manufacture the microstructure on the surface of artificial vavle.

Design and parameter characterization of the microstructure on the surfaces

Because of the hierarchical micro–nano composite structure, the surface of a heart valve is regarded as rough. According to Adamson and Gast [27], a model of the relationship between superhydrophobicity and the hierarchical structure could be created. Since the hierarchical structure on the surface of a valve is so similar to the fractal structure described by the Koch curve [28], the fractal structure equation can be used to calculate the fractal roughness factor. By changing the roughness factor, the relationship between the contact angle of the rough surface θ_f and that of the smooth surface θ_Y can be described by Equation 1:

$$\cos\theta_f = f_1\left(\frac{L}{l}\right)^{D-2}\cos\theta_Y - f_2 \quad (1)$$

Where f_1 and f_2 are the surface area fractions of solid-liquid and gas-liquid on the rough surface respectively, $f_1 + f_2 = 1$. $(L/l)^{D-2}$ is the surface roughness fractor. L and l are the extremal dimensions of the upper and lower limits of the fractal surface respectively. D is the fractal cone. For the heart valves, L and l correspond to the diameter of the cobblestones and the dimension of the nano-cilia respectively. In the Koch curve, D is about 2.2618 in three-dimensional space and (L/l) is 3^n, where the size of n is determined by the specific fractal structure, and the surface roughness factor will increase with the increasing of n. Therefore, if the upper limit L is constant, the value of l will decrease with the increasing of the n value.

In practical research, we always hope to construct more regular microstructures on surfaces in order to make research more convenient. According to the structure of the biological prototype, the familiar mastoid microstructure arranged in a regular array could be applied to the surface of an artificial heart valve. The front view and top view of the mastoid array microstructure is shown in Figure 8. The outline of the mastoid is assumed as paraboloid. The shape of a paraboloid of revolution is described by

$$y = kx^2 \quad (2)$$

where x is the radial coordinate and y is the vertical coordinate measured downward from the apex (Figure 8). The higher the value of the constant parameter k, the steeper the shape of the paraboloid. The geometry size of a mastoid is as follow: basal radius a, spacing b and height h, as illustrated in Figure 8.

By investigating the one period lined out by the broken line frame in the top view of Figure 8, we will find that the actual area of the paraboloid is given by Equation 3. Therefore the total area of the rough surface is expressed by Equation 4.

$$S_1 = 2\int_0^h 2\pi\left(\frac{y}{k}\right)^2 dy = \frac{8\pi}{3}ah \quad (3)$$

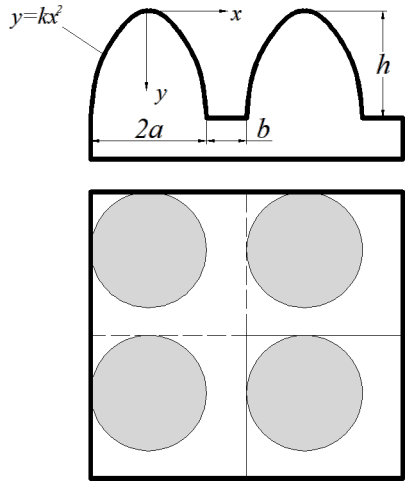

Figure 8: Sketch of the mastoid array microstructure: *a* is the basal diameter of a single mastoid, *b* is the space between two mastoids and *h* is the height of the mastoid.

$$S_a = S_1 + \left[(2a+b)^2 - \pi a^2 \right] \tag{4}$$

Its projected area is $S_p = (2a + b)^2$, then, according to the definition, the roughness coefficient r will be given by the following Equation 5:

$$r = \frac{S_a}{S_p} = \frac{\frac{8\pi}{3}B + \left[(2+A)^2 - \pi \right]}{(2+A)^2} \tag{5}$$

In this formula, two surface characteristic values, i.e., periodic space A ($A = b/a$) and aspect ratio B ($B = h/a$) are defined. When a droplet is at Cassie status, the bottom of it partially contacts with the top of the mastoid and the contact depth h′ is determined by the contact angle between the droplet and the solid (namely Young's contact angle θ_Y), which is shown in Figure 9. Since the size of the droplet is much larger than that of the microstructure, the bottom of the droplet can be approximated as a straight line and the contact area of the liquid–solid can be approximated as the small paraboloid with base radius a′, and height h'. According to Equation 3, the superficial area of the small paraboloid can be obtained as

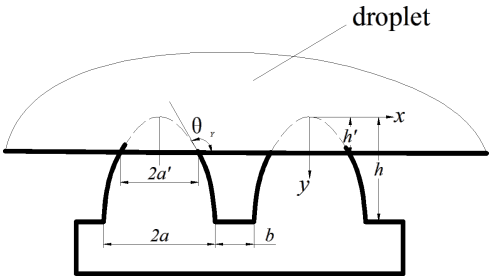

Figure 9: A droplet in Cassie state on the mastoid microstructure surface.

$$S_1' = \frac{8\pi}{3} a' h' \tag{6}$$

Since the equation of the parabola is $y = kx^2$, at the interface, there is:

$$\frac{dy}{dx} = 2ka' \tag{7}$$

At the same time,

$$\frac{dy}{dx} = \tan\left(\pi - \theta_Y\right) \tag{8}$$

From Equation 7 and Equation 8, the base radius a' can be given as

$$a' = -\frac{a^2}{2h}\tan\theta_Y \tag{9}$$

The height h' can be obtained as

$$h' = \frac{a^2}{4h}\tan^2\theta_Y \tag{10}$$

From Equation 9, Equation 10 and Equation 6 the area of the small paraboloid can be obtained as

$$S_1' = -\frac{\pi a^4}{3h^2}\tan^3\theta_Y \tag{11}$$

According to the definition, the area fraction f of the solid surface protuberance can be given as

$$f = \frac{S_1'}{(2a+b)^2 - \pi a'^2 + S_1'} \tag{12}$$

Therefore f can be obtained as

$$f = \frac{12\tan^3\theta_Y}{12k\left(2 + b/a\right)^2 - \pi\tan^2\theta_Y\left(3 + 4\tan\theta_Y\right)} \tag{13}$$

Substituting r in Wenzel's equation [20,21] we will obtain the relationship between the apparent contact angle on the wetted surface, θ_W, and Young's contact angle θ_Y (i.e., the intrinsical contact angle).

$$\cos\theta_W = \left[\frac{(8B-3)\pi}{3(2+A)^2}+1\right]\cos\theta_Y \quad (14)$$

Substituting f in Wenzel's equation [29,30] and Cassie's equation [31,32], we will also obtain the relationship between the apparent contact angle on the composite surface θ_{CB} and Young's contact angle θ_Y.

$$\cos\theta_{CB} = -1+\frac{12\tan^3\theta_Y}{12k(2+A)^2-\pi\tan^2\theta_Y(3+4\tan\theta_Y)}(1+\cos\theta_Y) \quad (15)$$

As can be seen from the above two equations, the apparent contact angle of Wenzel's droplet on the mastoid microstructure arranged in a regular array is related to the periodic space, A, and the aspect ratio, B. The apparent contact angle increases with the increasing of B and decreases with the increasing of A. While the apparent contact angle of a droplet in Cassie state decreases with the increasing of A, but also relates to the steepness, k, of the mastoid structure.

Equation 14 and Equation 15 can be used as theoretically predicted formulas of the apparent contact angles on mastoid array microstructure surfaces for the two contact states of a droplet. They are also generally applicable equations for expressing the relationship between geometric parameters of mastoid array microstructures and the apparent contact angles.

Conclusion

Learning from nature gives us the inspiration to generate topographic structures on artificial surfaces, which improves the characteristics of these surfaces. In this paper, we have studied the microstructures on the surfaces of a mouse and a rabbit's heart valve cusps/leaflets by using SEM. The hierarchical structures can be found on the surfaces of heart valve leaflets from both the mouse and the rabbit. The hierarchical structure consists of a cobblestone-like microstructure and nano-cilia. The directional arrangement of the cobblestones-like microstructure and nanoscale cilia may greatly influence the properties of blood flow and anti-clotting. According to the morphology and microstructure of the biological surface, to simplify the design and manufacturing, the mastoid microstructures arranged in a regular array have been constructed on the artifical heart valve's surface. Then theoretically predicted formulas of the apparent contact angles on such surfaces have been deduced from classical wetting theories. Next the proper geometric parameters of the microstructures that indirectly control the difference of the apparent contact angles should be decided. That will provide an intuitive guide for designing artificial heart valve surfaces. In later research, based on the above theorical study we should manufacture the mastoid microstructures on the biological materials surface. Further study of the relationship between anticoagulant properties and geometries of the microstructure through the experimental method is needed. Finding an artificial heart valve surface with better hemocompatibility holds great significance for the replacement of mechanical heart valves.

Acknowledgements

This research is supported by the Natural Science foundation of Jiangsu Province (BK2010203) and the Key Laboratory Opening foundation of Jiangsu Province (GZ201109) and Jiangsu Overseas Research & Training Program for University Prominent Young & Middle-aged Teachers and Presidents.

References

1. Neinhuis, C.; Barthlott, W. *Ann. Bot. (Oxford, U. K.)* **1997,** *79,* 667–677. doi:10.1006/anbo.1997.0400
2. Barthlott, W.; Neithhuis, C. *Planta* **1997,** *202,* 1–8. doi:10.1007/s004250050096
3. Feng, L.; Li, S.; Li, Y.; Li, H.; Zhang, L.; Zhai, J.; Song, Y.; Liu, B.; Jiang, L.; Zhu, D. *Adv. Mater.* **2002,** *14,* 1857–1860. doi:10.1002/adma.200290020
4. Bhushan, B.; Jung, Y. C. *Nanotechnology* **2006,** *17,* 2758–2772. doi:10.1088/0957-4484/17/11/008
5. Guo, Z.; Liu, W.; Su, B.-L. *J. Colloid Interface Sci.* **2011,** *353,* 335–355. doi:10.1016/j.jcis.2010.08.047
6. Parker, A. R.; Lawrence, C. R. *Nature* **2001,** *414,* 33–34. doi:10.1038/35102108
7. Cong, Q.; Chen, G. H.; Fang, Y.; Ren, L. Q. *J. Bionic Eng.* **2004,** *1,* 249–255.
8. Feng, X.-Q.; Gao, X.; Wu, Z.; Jiang, L.; Zheng, Q.-S. *Langmuir* **2007,** *23,* 4892–4896. doi:10.1021/la063039b
9. Sun, M.; Watson, G. S.; Zheng, Y.; Watson, J. A.; Liang, A. *J. Exp. Biol.* **2009,** *212,* 3148–3155. doi:10.1242/jeb.033373
10. Watson, G. S.; Cribb, B. W.; Watson, J. A. *J. Struct. Biol.* **2010,** *171,* 44–51. doi:10.1016/j.jsb.2010.03.008
11. Watson, J. A.; Cribb, B. W.; Hu, H.-M.; Watson, G. S. *Biophys. J.* **2011,** *100,* 1149–1155. doi:10.1016/j.bpj.2010.12.3736
12. Hu, H.-M.; Watson, G. S.; Cribb, B. W.; Watson, J. A. *J. Exp. Biol.* **2011,** *214,* 915–920. doi:10.1242/jeb.051128
13. Gao, X.; Jiang, L. *Nature* **2004,** *432,* 36. doi:10.1038/432036a
14. Ye, X.; Zhou, M.; Li, J.; Liu, H.-x.; Yuan, R.; Yang, H.-f.; Li, B.-j.; Cai, L. *Nanotechnol. Precis. Eng.* **2009,** *7,* 381–386.
15. Sun, T.; Feng, L.; Gao, X.; Jiang, L. *Acc. Chem. Res.* **2005,** *38,* 644–652. doi:10.1021/ar040224c
16. Qian, B.; Shen, Z. *Langmuir* **2005,** *21,* 9007–9009. doi:10.1021/la051308c
17. Onda, T.; Shibuichi, S.; Satoh, N.; Tsujii, K. *Langmuir* **1996,** *12,* 2125–2127. doi:10.1021/la950418o
18. Sun, M.; Luo, C.; Xu, L.; Ji, H.; Ouyang, Q.; Yu, D.; Chen, Y. *Langmuir* **2005,** *21,* 8978–8981. doi:10.1021/la050316q

19. Ma, M.; Hill, R. M.; Lowery, J. L.; Fridrikh, S. V.; Rutledge, G. C. *Langmuir* **2005,** *21,* 5549–5554. doi:10.1021/la047064y
20. Nakajima, A.; Abe, K.; Hashimoto, K.; Watanabe, T. *Thin Solid Films* **2000,** *376,* 140–143. doi:10.1016/S0040-6090(00)01417-6
21. Tavana, H.; Amirfazli, A.; Neumann, A. W. *Langmuir* **2006,** *22,* 5556–5559. doi:10.1021/la0607757
22. Tadanaga, K.; Kitamuro, K.; Morinaga, J.; Kotani, Y.; Matsuda, A.; Minami, T. *Chem. Lett.* **2000,** *29,* 864–865. doi:10.1246/cl.2000.864
23. Nosonovsky, M.; Bhushan, B. *Curr. Opin. Colloid Interface Sci.* **2009,** *14,* 270–280. doi:10.1016/j.cocis.2009.05.004
24. Green, D. W.; Watson, G. S.; Watson, J.; Abraham, S. J. K. *Adv. Healthcare Mater.* **2012,** *1,* 140–148. doi:10.1002/adhm.201100039
25. Bhushan, B. *Beilstein J. Nanotechnol.* **2011,** *2,* 66–84. doi:10.3762/bjnano.2.9
26. Bhushan, B.; Jung, Y. C. *Prog. Mater. Sci.* **2011,** *56,* 1–108. doi:10.1016/j.pmatsci.2010.04.003
27. Adamson, A. W.; Gast, A. P. *Physical Chemistry of Surface,* 6th ed.; John Wiley & Sons: New York, NY, USA, 1997.
28. Mandelbrot, B. B. *The Fractal Geometry of Nature;* W. H. Freeman: San Francisco, CA, USA, 1982.
29. Wenzel, R. N. *Ind. Eng. Chem.* **1936,** *28,* 988–994. doi:10.1021/ie50320a024
30. Wenzel, R. N. *J. Phys. Chem.* **1949,** *53,* 1466–1467. doi:10.1021/j150474a015
31. Cassie, A. B. D.; Baxter, S. *Trans. Faraday Soc.* **1944,** *40,* 546–551. doi:10.1039/TF9444000546
32. Cassie, A. B. D. *Discuss. Faraday Soc.* **1948,** *3,* 11–16. doi:10.1039/DF9480300011

License and Terms

Beilstein Journal of Nanotechnology

The optimal shape of elastomer mushroom-like fibers for high and robust adhesion

Burak Aksak*[1], Korhan Sahin[2] and Metin Sitti[3]

Full Research Paper

Open Access

Address:
[1]Department of Mechanical Engineering, Texas Tech University, Lubbock, TX 79409, USA, [2]Aerospace Engineering, University of Illinois at Urbana-Champaign, Urbana, IL 61801, USA and [3]Department of Mechanical Engineering, Carnegie Mellon University, Pittsburgh, PA 15213, USA

Email:
Burak Aksak* - burak.aksak@ttu.edu

* Corresponding author

Keywords:
gecko; mushroom-like fibers; adhesion

Beilstein J. Nanotechnol. **2014,** *5,* 630–638.
doi:10.3762/bjnano.5.74

Received: 18 September 2013
Accepted: 17 April 2014
Published: 14 May 2014

This article is part of the Thematic Series "Biological and bioinspired adhesion and friction".

Guest Editor: S. N. Gorb

Abstract

Over the last decade, significant effort has been put into mimicking the ability of the gecko lizard to strongly and reversibly cling to surfaces, by using synthetic structures. Among these structures, mushroom-like elastomer fiber arrays have demonstrated promising performance on smooth surfaces matching the adhesive strengths obtained with the natural gecko foot-pads. It is possible to improve the already impressive adhesive performance of mushroom-like fibers provided that the underlying adhesion mechanism is understood. Here, the adhesion mechanism of bio-inspired mushroom-like fibers is investigated by implementing the Dugdale–Barenblatt cohesive zone model into finite elements simulations. It is found that the magnitude of pull-off stress depends on the edge angle θ and the ratio of the tip radius to the stalk radius β of the mushroom-like fiber. Pull-off stress is also found to depend on a dimensionless parameter χ, the ratio of the fiber radius to a length-scale related to the dominance of adhesive stress. As an estimate, the optimal parameters are found to be $\beta = 1.1$ and $\theta = 45°$. Further, the location of crack initiation is found to depend on χ for given β and θ. An analytical model for pull-off stress, which depends on the location of crack initiation as well as on θ and β, is proposed and found to agree with the simulation results. Results obtained in this work provide a geometrical guideline for designing robust bio-inspired dry fibrillar adhesives.

Introduction

We need to look no further than nature to find inspiration for many of the technologies we work on today. One such field that observations on natural systems have impacted significantly in the recent years is adhesive technologies. While conventional adhesives rely on very soft materials or viscous liquids, nature offers a unique system composed of adhesive elements made of relatively rigid materials. These adhesive elements are comprised of millions of tiny fibers varying in size and geometrical complexity depending on the animal that bears them [1]. Some insects, spiders, and anoles have fibers with effective

diameters of the order of micrometers. Other animals such as the gecko lizard bear micro-scale stalks, which branch down to nano-scale fibers forming intricate hierarchical structures. The common aspect of fibrillar structuring is its ability to conform to the adhering surface, improve contact area and create an attractive force between individual fibers and the surface. In geckos, this attractive force is believed to arise from van der Waals interactions between the terminal end of an individual fiber and the surface [2,3]. A recent study by Hsu et al. [4] suggests that the presence of phospholipids on the tips of the fibers aid in adhesion. It has also been shown that humidity levels change the clinging ability of geckos significantly [5-8]. Regardless of the adhesion mechanism, the cumulative effect from the adhesion contribution of every fiber in contact is capable of generating adhesive strengths up to 100 kPa [9] as observed for the gecko lizard. A great deal of research has been performed to analyze the structure of natural fibrillar adhesives and measure their performance [2,3,6,8-11], to understand the main principles of enhanced adhesion [12-25], and to fabricate synthetic counterparts of biological fiber adhesives [16,21,26-36].

A common aspect of natural fibers among species, which is of interest in this work, is that the cross section of a natural fiber is rarely constant along its longitudinal axis. It increases close to its terminal end forming what is referred to in literature as *mushroom/spatulae-shaped fibers* [2,21,30,33,37]. While initial fabrication attempts for synthetic adhesives were limited to constant cross section cylindrical fibers [16,20,34,35], the realization of the actual shape of natural fibers has led to synthetic mushroom-like fibers (Figure 1). Adhesives comprised of mushroom-like fibers have shown significant improvements over cylindrical fibers. Furthermore, measured adhesive strengths have matched, and in some instances such as smooth surface applications, surpassed the adhesive strengths recorded for gecko footpads [21,30,33,37].

Work by del Campo et al. [21] reports enhancements in pull-off loads as much as 40-fold with mushroom-like fibers over cylindrical fibers of equal height and stalk radius. Interestingly, for the mushroom-shaped fibers that exhibited this enhancement, the contact area is only 1.7 times the contact area of flat tip cylindrical fibers. This fact points to the existence of an adhesion enhancement mechanism other than just the increase in contact area with mushroom-like fibers. Spuskanyuk et al. [38] used the assumption of pre-existing annular cracks and Griffith's energy criterion for crack propagation to study the enhancement mechanism for mushroom-like fibers. They concluded that for a given load and crack length, the relatively higher energy release rate for a cylindrical fiber induced pull-off at significantly lower loads than mushroom-like fibers. In

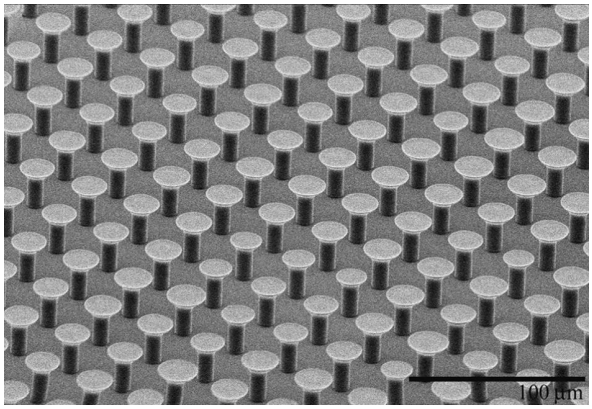

Figure 1: Scanning electron microscope image of polyurethane mushroom-like fibers with 4 µm stalk radius, 8 µm tip radius, and 20 µm height.

their analysis, the ratio of pull-off force of a mushroom-like fiber to that of a cylindrical fiber varies significantly depending on the size of the annular crack. Carbone et al. [39] also looked at the adhesion mechanism of mushroom-like fibers and concluded that these fibers are superior to cylindrical fibers in their ability to eliminate stress singularities as well as stabilize defects at the interface. They considered edge angles to be 90° and theoretically determined pull-off stress as well as propose maps for detachment behavior of these structures. Carbone and Pierro [40] performed further optimization studies to determine an optimal shape for mushroom-like fibers based on the microfiber geometry fabricated by Gorb et al. [33]. We compare their results with findings in this work in section Results in detail.

In this work we study the effect of geometry, defined by the edge angle θ and the ratio of the tip radius to the stalk radius β, on pull-off stress of mushroom-like fibers by using a cohesive zone model and finite elements (FE) simulations. Description of the cohesive zone model and numerical simulations are included in sections "Cohesive zone model" and "Numerical simulations", respectively. After that, the results of the finite element simulations are presented, and in the subsequent section the detachment behavior of individual fibers, the effect of tip apex shape and friction, a model to estimate pull-off stress for mushroom-like fibers, and a comparison between cylindrical and mushroom-like fibers in terms of pull-off stress are discussed.

Cohesive zone model

Adhesion problems can be studied by using a cohesive zone model such as the Dugdale–Barenblatt (DB) model [41,42]. It is a simple cohesive zone model in which the interface separates when the normal interfacial stress reaches the theoretical

strength of the interface σ_o. The interface continues to separate at σ_o until the separation reaches a critical distance δ_c, after which the interface can no longer support stress, resulting in a crack to initiate. The region where the separation of interface occurs is referred to as the *cohesive zone*. In this model, the work of adhesion is given by $w_{adh} = \sigma_o\delta_c$. Tang et al. [15] found the pull-off force of a soft, elastic cylindrical fiber in contact with a rigid flat surface whose height is much larger than its radius by using the DB cohesive zone model. According to their study, normalized pull-off stress $\Phi \equiv \sigma_s/\sigma_o$ depends on a single dimensionless parameter χ defined as

$$\chi \equiv \frac{\sigma_o{}^2 a(1-\nu^2)}{2\pi E w_{adh}} = \frac{\sigma_o a(1-\nu^2)}{2\pi E \delta_c}. \quad (1)$$

Here, a is the radius, E is the elastic modulus, and ν is the Poisson's ratio of the fiber. The dimensionless parameter χ is the ratio of the fiber radius to a length-scale related to the dominance of the interfacial adhesive forces. Hence, when $\chi << 1$, an attractive stress that is equal to the intrinsic adhesive stress covers the entire fiber tip and the pull-off stress approaches the theoretical limit, $\Phi = 1$ (i.e., $\sigma_s = \sigma_o$). This regime is referred to as the *flaw-insensitive regime*. On the other hand, when $\chi >> 1$, σ_o acts over a small portion of the interface, which results in the pull-off stress being much smaller than the theoretical limit, $\sigma_s << \sigma_o$. This regime is referred to as the *flaw-sensitive regime*. The non-dimensional parameter χ is also relevant to the adhesion problem of mushroom-like fibers. Thus, pull-off results will be presented as a function of χ. Later in section Discussion, a pull-off stress model based on χ will be presented.

Numerical simulations

Simulations are performed for a mushroom-like fiber illustrated in Figure 2 by using the analysis software COMSOL Multi-Physics 4.3 FE. It is assumed that the fiber is in full friction contact with a rigid smooth surface, which is in line with our observations during experiments with mushroom-like polyurethane fibers [32,37]. The DB cohesive zone model is implemented and modified slightly to avoid divergence of the numerical solution. Step function from zero stress to σ_o in the cohesive zone model is replaced with a high stiffness relation between the attractive stress and interfacial opening where the interface is required to separate by 10% of δ_c before cohesive zone forms (i.e., σ_o is reached) [24]. Unless stated otherwise, the simulation parameters are a = 1 μm, E = 3 MPa, ν = 0.5 and σ_o = 100 kPa. The tip radius a_t is varied from 1.05 μm to 2 μm while the edge angle θ is varied from 25 to 80°. It is important to note that the tip corner (wedge) is chosen so that the wedge angle is also equal to θ. The effect of the wedge angle being different from θ is briefly addressed in the section Discussion.

The height of the fiber h is fixed at 10 μm. Dimensionless parameter χ is varied by changing δ_c for fixed a_t, E, ν and σ_o. While applying a displacement Δ gradually to the base of the fiber, the pull-off load is determined from the far field tensile stress σ_{ff} the fiber bears when the maximum interfacial separation equals δ_c. We found that the tensile load reaches its maximum at the instant δ_c is reached at the interface (see Figure 3). Knowing the pull-off load p_s, the pull-off stress is calculated from $\sigma_s = p_s/(\pi a_t{}^2)$.

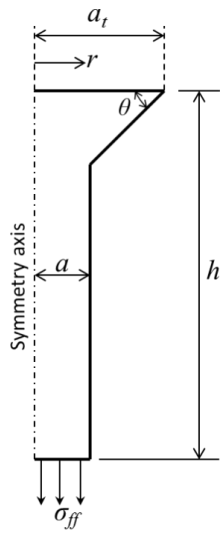

Figure 2: Two-dimensional axial symmetry model for a mushroom-like fiber. The tip (top surface) is fixed in radial direction to simulate full-friction contact. DB cohesive zone model is implemented at the tip of the fiber in FE simulations.

Results

Pull-off stress for all tip-to-base ratios $\beta \equiv a_t / a$ and edge angles θ are shown for select χ values in Figure 4. Contour plots show clear peaks at β = 1.1–1.2 and θ = 45° suggesting that these values are optimal for maximum pull-off stress. As expected, the peak pull-off stress drops with increasing χ with the highest value at Φ = 0.97 for χ = 5 and the lowest value at Φ = 0.88 for χ = 40 both obtained for β = 1.1 and θ = 45°. Figure 5a shows pull-off stress for β =1.1 for all θ as a function of χ. In line with the data presented in Figure 4, θ = 45° yields the highest pull-off stress for all χ, except when $\chi << 1$. In the regime where $\chi << 1$, pull-off is flaw-insensitive and it is expected that Φ = 1 regardless of β, θ, and χ. This confirms findings by Tang et al. [15] and Gao and Yao [12].

In Figure 5a, one observes that for θ ≤ 45°, the pull-off stress saturates towards a constant value as χ increases. In contrast for θ > 45°, the pull-off stress continuously drops with increasing χ. The dependence of pull-off stress on the edge angle at the limit $\chi \to \infty$ (i.e., $\delta \to 0$) can be explained by using the study of

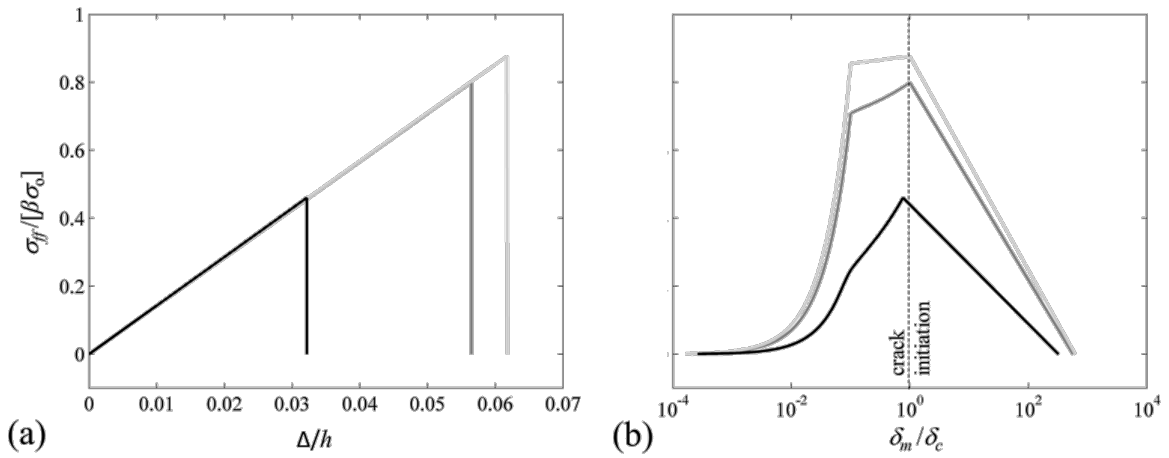

Figure 3: Average tensile stress at the tip of the fiber (a) as a function of normalized far field displacement Δ/*h*, and (b) as a function of normalized maximum interfacial separation δ_m/δ_c for β = 1.2 and θ = 25° (dark gray), θ = 45° (light gray), and θ = 75° (black). Here, δ_c = 1 nm (χ = 6). Peaks in each plot for specific θ coincide and correspond to normalized pull-off stress Φ. Tensile load drops immediately after the maximum interfacial separation reaches the critical separation indicating that the contact is unstable following crack initiation. The discontinuity at $\delta_m/\delta_c \approx 0.1$ prior to crack initiation in (b) marks the instant when a cohesive zone starts to form.

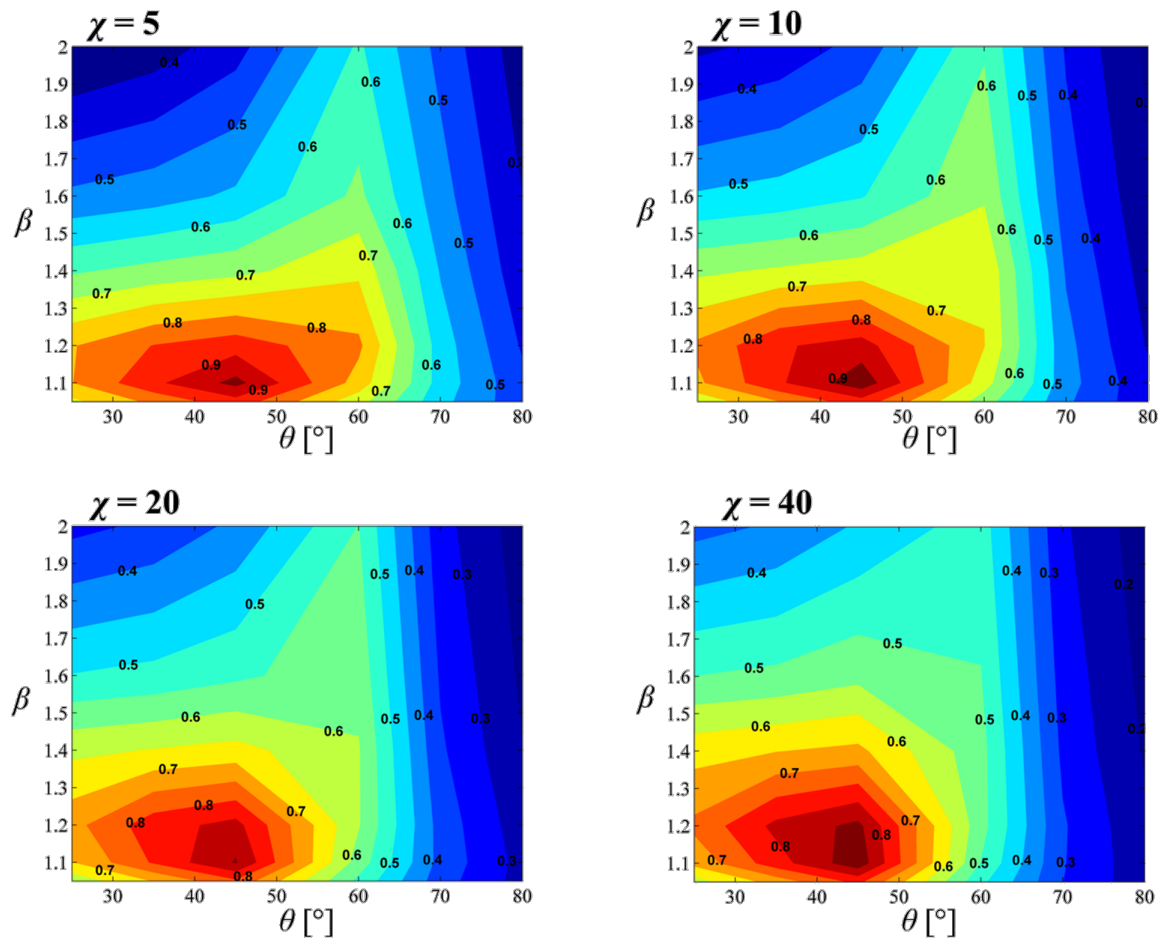

Figure 4: Normalized pull-off stress Φ contour plots for χ = 5 (top left), χ = 10 (top right), χ = 20 (bottom left), and χ = 40 (bottom right) as a function of β and θ. The peak Φ for each case lies within β = 1.1–1.2 and θ = 45°.

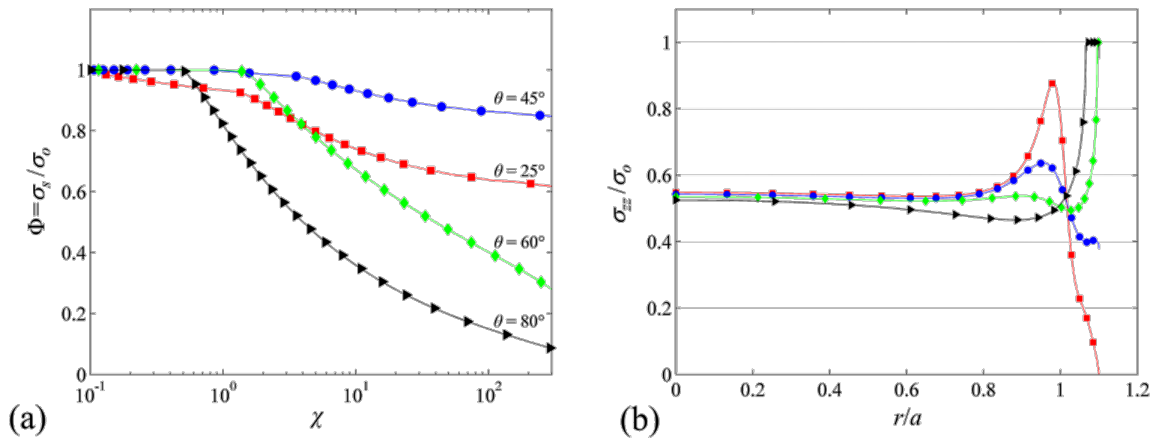

Figure 5: (a) Normalized pull-off stress as a function of χ for β = 1.1 and θ = {25°, 45°, 60°, 80°}. (b) Normalized stress at the tip for Δ/*h* = 0.0217 for the same β and θ as in (a). A cohesive zone is present at the edge both for θ = 60° and θ = 80°, while it has not formed for θ = 25° and θ = 45° yet.

Bogy [43] on stress singularities at bimaterial wedge interfaces. For a soft incompressible elastomer (i.e, Poisson's ratio ν = 0.5) in full-friction contact with a rigid substrate, stress at the edge of the fiber tip is finite for θ ≤ 45° and singular for θ > 45°, (see Supporting Information File 1 for details). Stress profiles of a mushroom-like fiber with β = 1.1 and θ = {25°,45°, 60°, 80°} are shown for a far field displacement of Δ/*h* = 0.0217 in Figure 5b. Due to the singularity, a cohesive zone is present at the edge of the fiber both for θ = 60° and θ = 80° while cohesive zone has not formed for θ = 25° and θ = 45° yet. Let us assume that $\delta_c = 0$, which implies that pull-off will occur shortly after the maximum tensile stress at the interface reaches σ_o. If there is a stress singularity at the edge of the tip, normal stress will be equal to σ_o at the edge the moment a tensile load is applied to the fiber. The interface will open starting at the edge and pull-off will depend on whether this opening is less than or equal to δ_c. On the other hand, if stress is finite everywhere at the interface, a sufficiently large tensile load has to be applied before a cohesive zone starts forming. This implies that regardless of the value of δ_c, pull-off load has a finite lower limit if θ ≤ 45°. The existence of this lower limit provides robust adhesion because regardless of the value of χ, one can expect to obtain a pull-off stress equal to this lower limit in the least. In particular for fibers with θ = 45° and β = 1.1, this lower limit for normalized pull-off stress is remarkably Φ = 0.85 which ensures high and robust adhesion.

Let us compare our results with previous findings of Carbone and Pierro [40]. Carbone and Pierro used the Griffith method to design an optimal fiber shape based on the synthetic adhesives developed by Gorb et al. [33]. They concluded that for optimal adhesion, which is essentially a measure of pull-off force for a single fiber, 2 ≤ β ≤ 3 and *s*/*a* = 0.2–0.3. Here, *s* is the thickness of the circular disk at the terminal end and *s* would be zero for our case. The discrepancy between their findings and ours can be attributed to three main factors. In their analysis, the apex angle is fixed at 90°, which leads to a singularity at the edge for fiber geometries if β < 2. As expected, the tip-size should be large to eliminate this singularity (i.e., equivalent stress intensity factor at the contact edge approaches zero), which necessitates the condition for 2 ≤ β ≤ 3. They then adjust *s* to avoid stress peaks and ensure uniform stress distribution at the tip and find that *s*/*a* =0.2–0.3 yields a peak free stress distribution. In our case, the apex angle is a variable and for θ ≤ 45°, the singularity at the edge disappears regardless of the value of β. Therefore, the condition β > 2 is not a necessary condition for the fiber geometry considered in this work, which is based on the fiber shapes included in Figure 1 and previous studies [32,37]. We find β = 1.1–1.2 to be optimal for uniform stress distribution. The second factor is the difference in what is considered optimal. In their study, Carbone and Pierro considered the far field stress, a measure for the pull-off stress of a single fiber, as the optimization function. Thus, the optimal parameters offered are to maximize single fiber pull-off load. They include a qualitative argument that increasing the tip size reduces the maximum number of fibers per unit area, and therefore β > 3 should be avoided. In our study, the optimization function is the pull-off stress per unit contact area of a single fiber, which quantitatively factors in the effect of contact area. The third factor is that they determine their equivalent stress intensity factor using both mode I and mode II stress intensity factors. Mode II (fracture mode) opening was not considered in our study and could be important especially for highly adhesive interfaces. We therefore expect discrepancies between the optimal solutions due to the differences in the model geometry, optimization function, and adhesion modeling.

Discussion

Crack initiation and pull-off model

The location of crack initiation (i.e., where the interface opening equals δ_c) depends both on tip shape parameters θ and β, and the value of χ. For $\theta \leq 45°$, since normal stress is finite everywhere at the tip, cohesive zone forms when and where the maximum normal stress reaches σ_o. This location corresponds to $r/a = 0$ (center) for $\theta = 45°$ and all β (refer to Figure 5b for normal stress profiles). Simulation results show that the location of crack initiation is independent of χ for this set of tip parameters. For $\theta > 45°$ on the other hand, the crack initiation is always at the edge for sufficiently large χ. For certain combinations of β and θ, for instance $\beta = 1.4$ and $\theta = 60°$, although the normal stress at the tip is highest at the edge, it does not increase monotonically from the center to the edge of the tip. Stress profile has a minimum at $r/a \approx 1$ (Figure 5b). For sufficiently low χ, gradually increasing far field displacement causes a cohesive zone to form at the edge first. Since δ_c is relatively large for low χ, increase in tension does not immediately result in a crack to initiate at the edge. In the meantime the stress in the center gradually increases reaching σ_o at which a second cohesive zone starts to form. The center separates faster than the edge, which results in a crack to initiate at the center. It is observed that crack initiation switches to the center of the fiber if stress at the center is able to reach σ_o prior to a crack initiating at the edge.

Similar to the pull-off stress model proposed by Tang et al. [15], derived with the assumption that the size of the cohesive zone is much smaller compared to the tip radius, pull-off stress can be estimated according to where the crack initiates as

$$\Phi = \frac{\sigma_s}{\sigma_o} = \begin{cases} B_e[\beta\chi]^{-\alpha} & \text{for edge crack,} \quad (a) \\ B_c[\beta\chi]^{-0.5} + \Gamma_c & \text{for center crack.} \quad (b) \end{cases} \quad (2)$$

Here, α can be found for a given edge angle θ using Equation S1 in Supporting Information File 1. For a crack initiating at the center, there is a square-root singularity and thus $\alpha = 0.5$ as shown in Equation 2b. The numerical constants B_e and B_c are form factors that are determined by fitting Equation 2a and Equation 2b to the simulation data for given β, θ, and χ. The constant Γ_c is approximately the value of the pull-off stress when the crack initiation switches from the edge to the center of the fiber for $\theta > 45°$. It is determined by fitting Equation 2b to simulation data. For $\theta \leq 45°$ and a crack initiating at the center for all χ, Γ_c is the lower bound for normalized pull-off stress at the limit $\chi \to \infty$. Figure 6 shows the simulation data and the model fits using Equation 2a and Equation 2b.The proposed model is in agreement with the simulation data except when $\chi \to 0$. Equation 2 is not valid in this regime as the cohesive zone occupies a relatively larger portion of the tip. Additionally, for certain combinations of β and θ, a crack initiates at $r/a \approx 1$ due to a stress peak at this location. Equation 2 is not valid in this case.

Crack initiation at the center of the fiber shown in simulations was also seen experimentally by Varenberg et al. [44], Heepe et

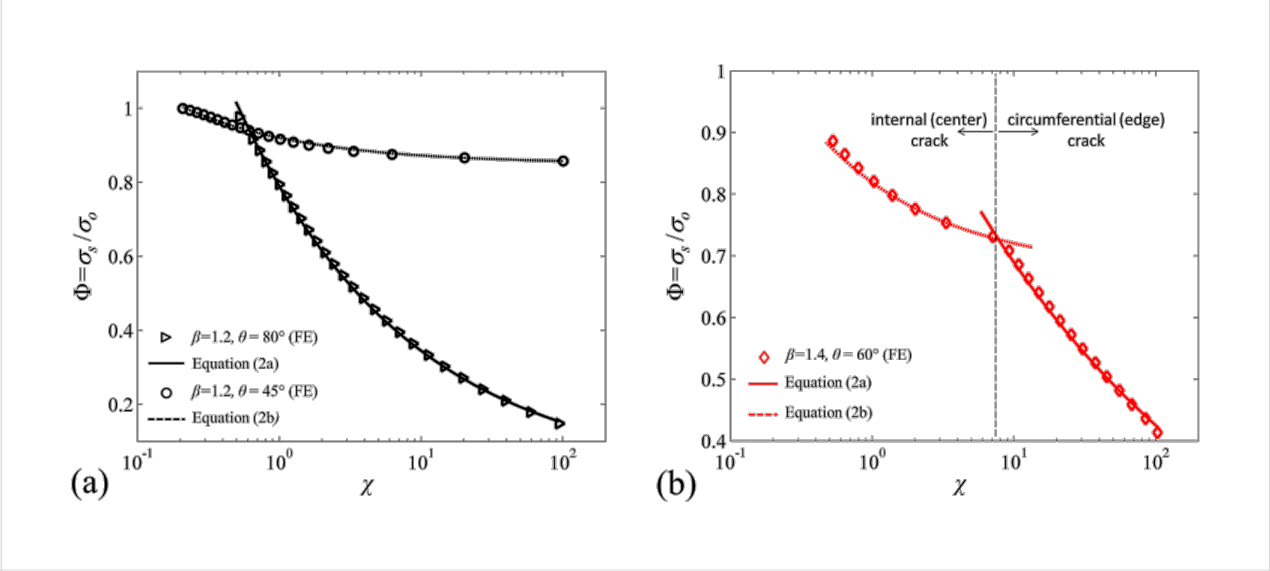

Figure 6: (a) Simulation results (triangle markers) for $\beta = 1.2$, $\theta = 80°$ for which a crack initiates at the edge for all χ. Solid line represents Equation 2a with $B_e = 0.84$ and $\alpha = 0.36$. Also included are the simulation results (circle markers) for $\beta = 1.2$ and $\theta = 45°$ for which a crack initiates at the center for all χ. Dashed line represents Equation 2b with $B_c = 0.076$ and $\Gamma_c = 0.85$. (b) Simulation results for $\beta = 1.4$, $\theta = 60°$ for which a crack initiates at the edge for $\chi > 7$ and at the center for $\chi < 7$. Solid line represents Equation 2a with $B_e = 1.2$ and $\alpha = 0.21$. Dashed line represents Equation 2b with $B_c = 0.17$ and $\Gamma_c = 0.68$.

al. [45], and Murphy et al. [32]. Both Heepe et al. and Varenberg et al. presented experimental results with mushroom-like fibers by using high speed imaging and showed that the detachment of the fiber was initiated with an internal crack. Similarly, Murphy et al. observed under tensile loading of polyurethane mushroom-like fibers that an internal crack formed and propagated in a matter of milliseconds leading to contact failure.

All the simulation results show that $\Phi = 1$ in the flaw-insensitive regime ($\chi << 1$) regardless of the value of θ and β. This is in agreement with Gao and Yao [12], and Tang et al. [15], who suggest that for fibers with small radii (i.e., small χ for a given material and adhering surface), pull-off stress is equal to the intrinsic adhesive stress and is independent of the tip shape.

The effect of interfacial friction

The choice of fiber material and the adhering surface could result in friction ranging from no friction to full friction between the fiber tip and the adhering surface. As shown in Supporting Information File 1 (Figure S1), the magnitude of singular stress at the vicinity of the tip apex is higher for full friction interfaces than frictionless interfaces. Additionally, the limit wedge angle for finite stress increases from 45 to 90°. Thus, the full friction case represents the worst case scenario in terms of the stress singularity at the apex of the mushroom-like fiber and the optimal parameters found in this study, namely $\beta = 1.2$ and $\theta = 45°$, would be the conservative choices for fibrillar adhesive design. Note that Equation 2a and Equation 2b are still applicable for frictionless contact where one can obtain α by using Equation S2 rather than Equation S1 in Supporting Information File 1.

Pull-off stress comparison between mushroom-like and cylindrical fibers

For $\chi << 1$, i.e., for very small fiber radii (typically less than 1 μm), the pull-off stress equals intrinsic adhesive stress and is insensitive to the tip shape. This is in agreement with our results. However, for large χ, the tip shape significantly affects adhesion. Del Campo et al. [21] measured pull-off loads for mushroom-like fibers and cylindrical fibers of the same height, stalk radius and packing density. While they measured approximately 0.7 mN for cylindrical fibers with a hemispherical glass indenter, the measured pull-off load was approximately 28 mN with mushroom-like fibers, a 40-fold increase. Reported values are approximate pull-off loads near saturation as interpreted from the graphical data presented in [21]. Let us define an enhancement factor e as the ratio of the pull-off load between two different fiber arrays. For an experiment that uses hemispherical glass indenter with a radius much larger than the dimensions of an individual fiber in the array, the enhancement factor of mushroom-like fibers over the cylindrical fibers with the same packing density, stalk radius, height, and material becomes

$$e = \frac{P_{s,m}}{P_{s,c}} = \beta^4 \left(\frac{\sigma_{s,m}}{\sigma_{s,c}} \right)^2 . \quad (3)$$

Here, P_m and P_c are the pull-off loads for the mushroom-like and cylindrical fiber arrays, respectively. The derivation of Equation 3 is detailed in Supporting Information File 1. Their experiments were carried out with polydimethylsiloxane (PDMS) cylindrical and mushroom-like fibers. For cylindrical fibers, $a = 10$ μm and $h = 25$ μm. The tip radius for mushroom–like fibers were $a_t = 13$ μm and they shared the same a and h with the cylindrical fibers. For both samples, the packing densities (number of fibers per unit area) were the same. According to our model, $\beta = 1.3$ and although the edge angle was not reported in their work, we will assume $\theta = 45°$ for simplicity. For $\beta = 1.3$ and $\theta = 45°$, a conservative estimate of normalized pull-off stress according to our model is $\sigma_{s,m} = \Gamma_c \sigma_o = 0.74\sigma_o$. For cylindrical fibers, $\sigma_{s,c} = 0.83\chi^{-0.4}\sigma_o$ as shown by Tang et al. [15]. For the described fiber arrays, Equation 3 becomes $e = 2.27\chi^{0.8}$. Let us assume PDMS to be incompressible ($\nu = 0.5$) with elastic modulus $E = 1.42$ MPa [16]. For glass–PDMS contact, $w_{adh} = 25$ mJ/m^2 [46]. Let us also assume an intrinsic adhesive stress of $\sigma_o = 1$ MPa, a reasonable value for PDMS [47-49]. By inserting the materials properties, interfacial properties and fiber dimensions into Equation 1, one finds $\chi = 33.6$ and in turn $e = 38$. This estimate is close to $e = 40$ that del Campo et al. [21] obtained in their measurements.

The implications tip apex shape on pull-off stress

The manufacturing technique used to fabricate mushroom-like fibers may not yield a sharp corner (i.e., wedge) for individual fibers at the edge of the tip [21,30,32,37,44]. This implies that the wedge angle will be different from the edge angle defined in this work, which may significantly affect the pull-off stress. To demonstrate this effect, we performed simulations for mushroom-like fibers with $\beta = 1.2$ and $\theta = 45°$ employing three different wedge shapes; namely 45° wedge, 90° wedge and rounded wedge. The radius of curvature was set to 10 nm for the rounded wedge. In case of the 90° wedge, a 10 nm high rectangle was added to the tip (see Figure 7). For all three cases, the size of the tip in contact was kept at 1.2 μm ensuring constant $\beta = 1.2$. As shown in Figure 7, the wedge angle has significant effect on pull-off stress for relatively high χ values where a crack initiates at the edge for both the rounded and 90° wedge. Below a critical χ, the pull-off stress for all three cases follow the same path once a crack is initiated at the center indicating little dependence on the wedge angle. Thus, a qualitative

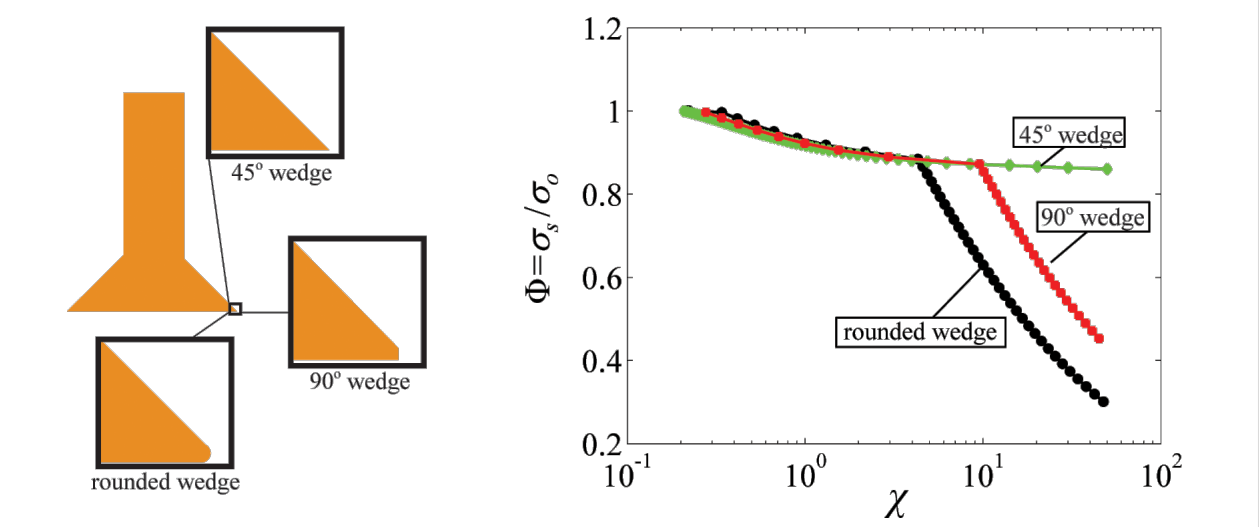

Figure 7: (left) Illustration of three different wedge angles for the mushroom-tipped fibers with β = 1.2 and θ = 45°. (right) Simulation results for 45° wedge (diamond markers), 90° wedge (square markers), and rounded wedge (circular markers).

argument suggests that while fibers with small diameters and high elastic modulus (large χ) favor wedge-angle independence, the dependence of pull-off stress to the wedge angle is significant for high strength interfaces (small χ). This is assuming that the critical separation distance is in the order of 1 nm and somewhat constant for van der Waals interactions.

Conclusion

In summary, the pull-off stress for an individual mushroom-like fiber was modelled using DB cohesive zone model and FE analyses. This study revealed critical information about the detachment mechanism of mushroom-like fibers and how this behaviour is influenced by the geometry as well as the interfacial properties. A simple geometrical guideline to ensure high and robust adhesion relative to the intrinsic adhesive stress was offered. While these results are important for designing dry fibrillar adhesives, they are only concerned with the performance when the loading is axial. The effect of shear loading should also be considered along with the results of this study in designing fibrillar adhesives.

Supporting Information

Supporting Information File 1

Details of mathematical modeling.
[http://www.beilstein-journals.org/bjnano/content/supplementary/2190-4286-5-74-S1.pdf]

Acknowledgements

Part of this work was funded by National Science Foundation (IPP-0930610).

References

1. Arzt, E.; Gorb, S.; Spolenak, R. *Proc. Natl. Acad. Sci. U. S. A.* **2003,** *100,* 10603–10606. doi:10.1073/pnas.1534701100
2. Autumn, K.; Liang, Y. A.; Hsieh, S. T.; Zesch, W.; Chan, W. P.; Kenny, T. W.; Fearing, R.; Full, R. J. *Nature* **2000,** *405,* 681–685. doi:10.1038/35015073
3. Autumn, K.; Sitti, M.; Liang, Y. A.; Peattie, A. M.; Hansen, W. R.; Sponberg, S.; Kenny, T. W.; Fearing, R.; Israelachvili, J. N.; Full, R. J. *Proc. Natl. Acad. Sci. U. S. A.* **2002,** *99,* 12252–12256. doi:10.1073/pnas.192252799
4. Hsu, P. Y.; Ge, L.; Li, X.; Stark, A. Y.; Wesdemiotis, C.; Niewiarowski, P. H.; Dhinojwala, A. *J. R. Soc., Interface* **2012,** *9,* 657–664. doi:10.1098/rsif.2011.0370
5. Buhl, S.; Greiner, C.; del Campo, A.; Arzt, E. *Int. J. Mater. Res.* **2009,** *100,* 1119–1126. doi:10.3139/146.110146
6. Huber, G.; Mantz, H.; Spolenak, R.; Mecke, K.; Jacobs, K.; Gorb, S. N.; Arzt, E. *Proc. Natl. Acad. Sci. U. S. A.* **2005,** *102,* 16293–16296. doi:10.1073/pnas.0506328102
7. Prowse, M. S.; Wilkinson, M.; Puthoff, J. B.; Mayer, G.; Autumn, K. *Acta Biomater.* **2011,** *7,* 733–738. doi:10.1016/j.actbio.2010.09.036
8. Puthoff, J. B.; Prowse, M. S.; Wilkinson, M.; Autumn, K. *J. Exp. Biol.* **2010,** *213,* 3699–3704. doi:10.1242/jeb.047654
9. Irschick, D. J.; Austin, C. C.; Petren, K.; Fisher, R. N.; Losos, J. B.; Ellers, O. *Biol. J. Linn. Soc.* **1996,** *59,* 21–35. doi:10.1111/j.1095-8312.1996.tb01451.x
10. Hansen, W. R.; Autumn, K. *Proc. Natl. Acad. Sci. U. S. A.* **2005,** *102,* 385–389. doi:10.1073/pnas.0408304102
11. Autumn, K.; Gravish, N.; Wilkinson, M.; Santos, D.; Spenko, M.; Cutsosky, M. *Integr. Comp. Biol.* **2006,** *46* (Suppl. 1), E5. doi:10.1093/icb/icl056
12. Gao, H.; Yao, H. *Proc. Natl. Acad. Sci. U. S. A.* **2004,** *101,* 7851–7856. doi:10.1073/pnas.0400757101
13. Glassmaker, N. J.; Jagota, A.; Hui, C.-Y.; Kim, J. *J. R. Soc., Interface* **2004,** *1,* 23–33. doi:10.1098/rsif.2004.0004
14. Hui, C.-Y.; Glassmaker, N. J.; Tang, T.; Jagota, A. *J. R. Soc., Interface* **2004,** *1,* 35–48. doi:10.1098/rsif.2004.0005

15. Tang, T.; Hui, C.-Y.; Glassmaker, N. J. *J. R. Soc., Interface* **2005,** *2,* 505–516. doi:10.1098/rsif.2005.0070
16. Majidi, C.; Groff, R. E.; Maeno, Y.; Schubert, B.; Baek, S.; Bush, B.; Maboudian, R.; Gravish, N.; Wilkinson, M.; Autumn, K.; Fearing, R. S. *Phys. Rev. Lett.* **2006,** *97,* 076103. doi:10.1103/PhysRevLett.97.076103
17. Schargott, M.; Popov, V. L.; Gorb, S. *J. Theor. Biol.* **2006,** *243,* 48–53. doi:10.1016/j.jtbi.2006.05.023
18. Tian, Y.; Pesika, N.; Zeng, H.; Rosenberg, K.; Zhao, B.; McGuiggan, P.; Autumn, K.; Israelachvili, J. *Proc. Natl. Acad. Sci. U. S. A.* **2006,** *103,* 19320–19325. doi:10.1073/pnas.0608841103
19. Varenberg, M.; Peressadko, A.; Gorb, S.; Arzt, E. *Appl. Phys. Lett.* **2006,** *89,* 121905. doi:10.1063/1.2356099
20. Aksak, B.; Murphy, M. P.; Sitti, M. *Langmuir* **2007,** *23,* 3322–3332. doi:10.1021/la062697t
21. del Campo, A.; Greiner, C.; Arzt, E. *Langmuir* **2007,** *23,* 10235–10243. doi:10.1021/la7010502
22. Cañas, N.; Kamperman, M.; Völker, B.; Kroner, E.; McMeeking, R. M.; Arzt, E. *Acta Biomater.* **2012,** *8,* 282–288. doi:10.1016/j.actbio.2011.08.028
23. Persson, B. N. J. *J. Chem. Phys.* **2003,** *118,* 7614–7621. doi:10.1063/1.1562192
24. Aksak, B.; Hui, C.-Y.; Sitti, M. *J. R. Soc., Interface* **2011,** *8,* 1166–1175. doi:10.1098/rsif.2010.0582
25. Chen, B.; Wu, P. D.; Gao, H. *Proc. R. Soc. London, Ser. A* **2008,** *464,* 1639–1652. doi:10.1098/rspa.2007.0350
26. Yurdumakan, B.; Raravikar, N. R.; Ajayan, P. M.; Dhinojwala, A. *Chem. Commun.* **2005,** 3799–3801. doi:10.1039/b506047h
27. Aksak, B.; Sitti, M.; Cassell, A.; Li, J.; Meyyappan, M.; Callen, P. *Appl. Phys. Lett.* **2007,** *91,* 061906. doi:10.1063/1.2767997
28. Qu, L. T.; Dai, L.; Stone, M.; Xia, Z.; Wang, Z. L. *Science* **2008,** *322,* 238–242. doi:10.1126/science.1159503
29. Noderer, W. L.; Shen, L.; Vajpayee, S.; Glassmaker, N. J.; Jagota, A.; Hui, C.-Y. *Proc. R. Soc. London, Ser. A* **2007,** *463,* 2631–2654. doi:10.1098/rspa.2007.1891
30. Kim, S.; Sitti, M. *Appl. Phys. Lett.* **2006,** *89,* 261911. doi:10.1063/1.2424442
31. Murphy, M. P.; Kim, S.; Sitti, M. *ACS Appl. Mater. Interfaces* **2009,** *1,* 849–855. doi:10.1021/am8002439
32. Murphy, M. P.; Aksak, B.; Sitti, M. *Small* **2009,** *5,* 170–175. doi:10.1002/smll.200801161
33. Gorb, S.; Varenberg, M.; Peressadko, A.; Tuma, J. *J. R. Soc., Interface* **2007,** *4,* 271–275. doi:10.1098/rsif.2006.0164
34. Geim, A. K.; Dubonos, S. V.; Grigorieva, I. V.; Novoselov, K. S.; Zhukov, A. A.; Shapoval, S. Yu. *Nat. Mater.* **2003,** *2,* 461–463. doi:10.1038/nmat917
35. Greiner, C.; del Campo, A.; Arzt, E. *Langmuir* **2007,** *23,* 3495–3502. doi:10.1021/la0633987
36. Jeong, H. E.; Lee, J.-K.; Kim, H. N.; Moon, S. H.; Suh, K. Y. *Proc. Natl. Acad. Sci. U. S. A.* **2009,** *106,* 5639–5644. doi:10.1073/pnas.0900323106
37. Murphy, M. P.; Aksak, B.; Sitti, M. *J. Adhes. Sci. Technol.* **2007,** *21,* 1281–1296. doi:10.1163/156856107782328380
38. Spuskanyuk, A. V.; McMeeking, R. M.; Deshpande, V. S.; Arzt, E. *Acta Biomater.* **2008,** *4,* 1669–1676. doi:10.1016/j.actbio.2008.05.026
39. Carbone, G.; Pierro, E.; Gorb, S. N. *Soft Matter* **2011,** *7,* 5545–5552. doi:10.1039/c0sm01482f
40. Carbone, G.; Pierro, E. *Small* **2012,** *8,* 1449–1454. doi:10.1002/smll.201102021
41. Dugdale, D. S. *J. Mech. Phys. Solids* **1960,** *8,* 100–104. doi:10.1016/0022-5096(60)90013-2
42. Barenblatt, G. I. The Mathematical Theory of Equilibrium Cracks in Brittle Fracture. In *Advances in Applied Mechanics;* Dryden, H. L.; von Kármán, T.; Kuerti, G.; van den Dungen, F. H.; Howarth, L., Eds.; Elsevier, 1962; Vol. 7, pp 55–129.
43. Bogy, D. B. *J. Appl. Mech.* **1971,** *38,* 377–386. doi:10.1115/1.3408786
44. Varenberg, M.; Gorb, S. *J. R. Soc., Interface* **2008,** *5,* 785–789. doi:10.1098/rsif.2007.1201
45. Heepe, L.; Kovalev, A. E.; Filippov, A. E.; Gorb, S. N. *Phys. Rev. Lett.* **2013,** *111,* 104301. doi:10.1103/PhysRevLett.111.104301
46. Waters, J. F.; Guduru, P. R. *Proc. R. Soc. London, Ser. A* **2010,** *466,* 1303–1325. doi:10.1098/rspa.2009.0461
47. Tang, T.; Jagota, A.; Chaudhury, M. K.; Hui, C.-Y. *J. Adhes.* **2006,** *82,* 671–696. doi:10.1080/00218460600775781
48. Maugis, D. *Contact, Adhesion and Rupture of Elastic Solids;* Springer Series in Solid-State Sciences, Vol. 130; Springer, 2000.
49. Hui, C.-Y.; Jagota, A.; Bennison, S. J.; Londono, J. D. *Proc. R. Soc. London, Ser. A* **2003,** *459,* 1489–1516. doi:10.1098/rspa.2002.1057

License and Terms

Beilstein Journal of Nanotechnology

Fibrillar adhesion with no clusterisation: Functional significance of material gradient along adhesive setae of insects

Stanislav N. Gorb*[1] and Alexander E. Filippov[2]

Full Research Paper

Open Access

Address:
[1]Department Functional Morphology and Biomechanics, Zoological Institute of the Kiel University, Am Botanischen Garten 1–9, D-24098 Kiel, Germany and [2]Donetsk Institute for Physics and Engineering, National Academy of Sciences of Ukraine, Donetsk, Ukraine

Email:
Stanislav N. Gorb* - sgorb@zoologie.uni-kiel.de

* Corresponding author

Keywords:
adhesion; attachment; biomechanics; computer modelling; cuticle; locomotion; material; surface

Beilstein J. Nanotechnol. **2014,** *5,* 837–845.
doi:10.3762/bjnano.5.95

Received: 26 January 2014
Accepted: 15 May 2014
Published: 12 June 2014

This article is part of the Thematic Series "Biological and bioinspired adhesion and friction".

Associate Editor: K. Koch

Abstract

It has been recently demonstrated that adhesive tarsal setae of beetles possess material gradients along their length. These gradients presumably represent an evolutionary optimization enhancing the adaptation to rough surfaces while simultaneously preventing clusterisation of the setae by lateral collapse. The numerical experiment of the present study has clearly demonstrated that gradient-bearing fibers with short soft tips and stiff bases have greater advantage in maximizing adhesion and minimizing clusterisation in multiple attachment–detachment cycles, if compared to the fibers with longer soft tips on the stiff bases and fibers with stiff tips on the soft bases. This study not only manifests the crucial role of gradients in material properties along the setae in beetle fibrillar adhesive system, but predicts that similar gradients must have been convergently evolved in various lineages of arthropods.

Introduction

The contact formation of insect adhesive pads on various substrates depends on the pad ability to adapt to different surface topographies. The quality of contact may be increased due to the presence of specific micro- and nanostructures [1-5]. Crack trapping mechanisms in adhesive systems with multiple contacts provide advantages in attachment on rough substrates [6]. Also hierarchical organization of insect pad structures enables formation of multiple contacts that contribute to an enhancement of overall length of the total peeling line [7].

We have recently shown that thin tape-like contact tips of hairs (setae) in combination with applied shear force lead to the formation of maximal real contact area without slippage within the contact [8]. Due to this reason, the material flexibility is important for contact formation of adhesive pads. Flexible materials may generate large contact area between the pad and substrate at minimal normal load. On the other hand, elongated structures, made of too flexible materials, have low mechanical stability [9]: insect setae made of too soft material can buckle

and collapse resulting in so called clusterisation/condensation [10,11]. Due to such clusterisation, functional advantage from multiple adhesive contacts may strongly decrease. That is why, material properties of insect adhesive setae represent an optimization problem, which is solved in the course of biological evolution by the presence of gradients of thickness and mechanical properties. Thickness gradients of insect setae are well known in various adhesive setae due to numerous scanning electron microscopy studies [1]. Recently, we presented the combined study on the material structure and local mechanical properties in tarsal setae of the beetle *Coccinella septempunctata* and demonstrated the presence of a material gradient at the level of each single seta [12].

Setal elasticity modulus, probed by atomic force microscope (AFM), ranges from 1.2 MPa at the tip [12] to 6.8 GPa at the base. At the setal tip, we revealed the rubber-like protein resilin in rather high concentrations [13,14], whereas at the base of the seta the sclerotised cuticle is dominating. Between tip and the base, there is a gradient of material composition revealed by confocal laser scanning microscopy (CLSM). This gradient is hypothesized to be an evolutionary optimization enhancing adaptation of adhesive pads to rough surfaces, while simultaneously preventing setal clusterisation. Such an optimisation presumably increases the performance of the adhesive system in general. However, this hypothesis is difficult to prove experimentally using native biological specimens. That is why we decided to test it by the numerical simulation, which is the main aim of the present study.

In this paper we ask following questions:

1. Does the presence of the material gradient along the setae contribute to the proper contact formation?
2. Which particular gradient reduces clusterisation of setae?

Results and Discussion

Structure and material properties of biological system

Previous CLSM analysis of the setal tips has clearly demonstrated the presence of the rubber-like protein resilin in rather high concentrations [12,15]. Both central and proximal parts of the setae were dominated by green, yellow and red autofluorescences due to the presence of other presumably sclerotised

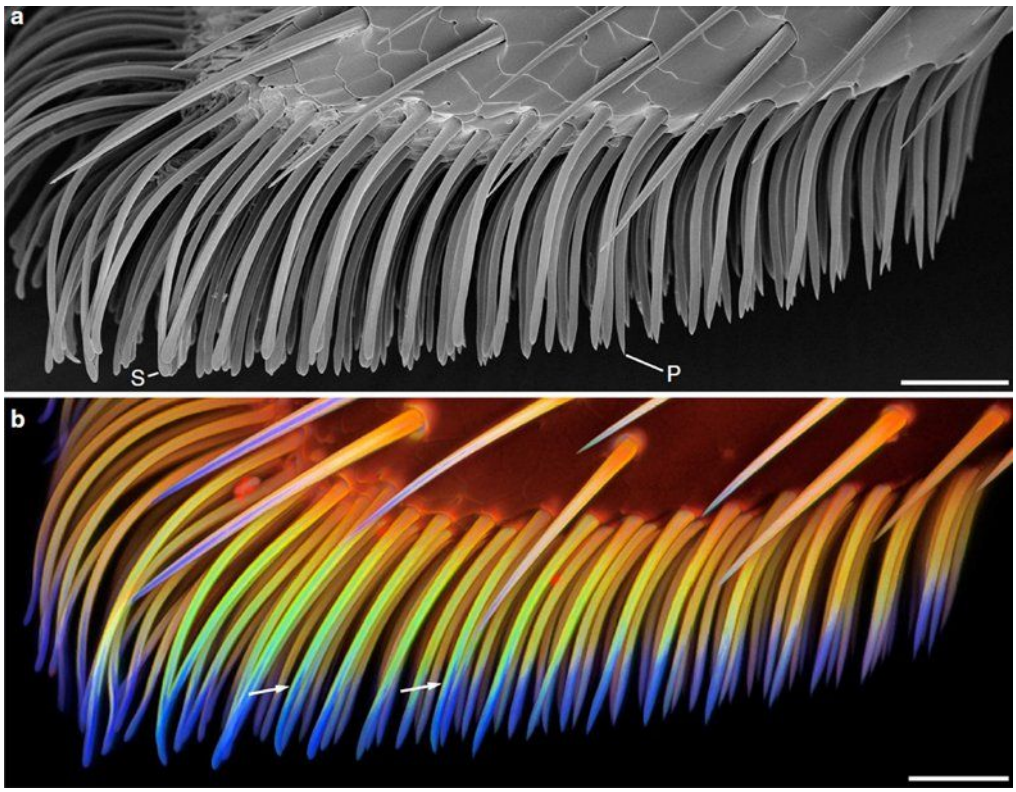

Figure 1: Morphology and material composition of adhesive tarsal setae. Ventral part of the second adhesive pad of a foreleg of a female *Coccinella septempunctata*, lateral view. (a) Scanning electron micrograph (the specimen was dried using 1-propanol). (b) CLSM maximum intensity projection showing an overlay of the four different autofluorescences mentioned in the text. The arrows indicate the dorso-ventral material gradient in exemplary setae. S, exemplary spatula-like seta; P, exemplary seta with a pointed tip. Scale bars, 25 µm. From [12] (Nature Publishing Group).

proteins and very likely chitin (Figure 1). Between the resilin-dominated distal part and more sclerotised basal part of the seta, a rather pronounced longitudinal gradient of material composition was revealed. AFM-nanoindentation experiments have revealed rather low elasticity modulus at the setal tip (1.2 ± 0.3 MPa), but the high one at the setal base (2.43 ± 1.9 GPa) [12]. This information about the gradients of material properties in real beetle setae was used in the numerical model presented below.

Numerical model

In principle, to model mechanics of the setae a classical beam theory can be applied. However, for long array of the beams it needs in extremely time consuming numerical calculation. To avoid it we apply here minimalistic, but quite realistic model, which was proposed for the same system few years ago and described in details in the paper [16]. Here we adapt the model to include gradient material properties of insect setae. The model includes following elements. An array of initially parallel fibers attached to a hard planar base. Stiffness of the fibers $F_{elastic}$ is continuously varied along their length and can be changed from very soft one to much stiffer or even almost rigid one (but still with some degree of flexibility). Longitudinal $\vec{F}^{\|}_{jk}$ and transversal $\vec{F}^{\perp}_{j}$ stiffness of the fibers are simulated by the following interaction between the segments $\vec{F}^{\|}_{jk} = K^{\|}(\vec{r}_j - \vec{r}_k)\left[1-(\vec{r}_j-\vec{r}_k)^2/dr^2\right]$, and $\vec{F}^{\perp}_{j} = K^{\perp}(2\vec{r}_j - \vec{r}_{j+1} - \vec{r}_{j-1})$.

Here we limit ourselves by two-dimensional model, where values $\vec{r}_j = \{x_j, y_j\}$ are the coordinates of the beginning of the segment j; $k = j \pm 1$. Longitudinal force, $\vec{F}^{\|}_{jk}$, is described by a two-minima potential, which tends to keep a distance between the points $\vec{r}_j$ and $\vec{r}_{j\pm1}$ close to the equilibrium length of the segment dr. Transversal force, $\vec{F}^{\perp}_{j}$ keeps $\vec{r}_j$ close to the mean value $(\vec{r}_{j+1} + \vec{r}_{j-1})/2$ between its nearest neighbors, and tends to hold the angle between the neighboring segments close to 180°.

The ends of the fibers are attracted to the surface by a sum of molecular and capillary forces. For the sake of simplicity we simulate it by the gradient of Morse potential $U_{vdW}(r) = U_0(1 - \exp(-r/r_0))^2$, where r is a distance between the end of fiber and surface, with physically reasonable amplitude U_0 = 10 nN·nm and the minimum located at the distance r_0 = 0.01 μm from the surface [17,18].

Rigid surface of the substrate, where the fibers attach to, has semi-fractal structure with given Fourier spectrum and amplitude of roughness [8]. It can be simulated similar to the approach we previously used in [8] by the self-affine fractal surface given by real part of $Y(x) = A\iint dq_x C(q)\exp(iq_x x + \zeta)$ with scaling spectral density. Here A is amplitude of surface roughness, i is imaginary unit, q_x are Fourier components along x direction, and ζ is a random phase.

Details of the generation procedure for the profile $Y(x)$ have been described in a number of previous papers [19,20]. In the current literature [21] it is accepted that majority of physical surfaces have scale-invariant spectrum $C(q) = 1/q^{\beta}$ with exponent β ≈ 0.9. The amplitude of the numerical "surface" is taken to be comparable with the radius of van der Waals interaction $A = r_0$.

Soft parts of every fiber, which normally are physically thin and flexible, interact with corresponding regions of other fibers of the array. Since for the majority of studied biological fibrillar adhesive systems, there is no evidence that seta–substrate and seta–seta interactions are different, we assumed that interaction force has the same (van der Waals) origin as their attraction to the hard wall. Assumptions similar to this have been also previously taken by other authors for their models [10,11]. Due to this, it is natural to take it in the same form $U_{interact}(r_{jk}) = U_0(1-\exp(-r_{jk}/r_0))^2$ with comparable characteristic parameters U_0, r_0. For simplicity of the model, we reduce mutual interaction of the fibers by the interaction of the nearest neighbors: $r_{nn+1} = |\vec{r}_n - \vec{r}_{n\pm1}|$.

For studied problem, one can neglect effects of inertia and treat the system as over-damped. In this approximation, differential equation of motion does not contain second time derivative and can be formally written in the form $\partial\vec{r}/\partial t = \vec{F}/\gamma$, where γ is dissipative constant and force accumulates all above interactions $\vec{F} = \vec{F}_{elastic} + \vec{F}_{vdW} + \vec{F}_{interact}$. As usually, corresponding components of the forces in the equations of motion are equal to the derivatives: $F^{z}_{vdW} = \partial U_{vdW}/\partial z; F^{x}_{vdW} = \partial U_{vdW}/\partial x$, $F^{z,ij}_{elastic} = \partial U^{ij}_{elastic}/\partial z; F^{x,ij}_{elastic} = \partial U^{ij}_{elastic}/\partial x$ and $F^{z,j}_{bending} = \partial U^{j}_{bending}/\partial z; F^{x,j}_{bending} = \partial U^{j}_{bending}/\partial x$. Below we 'a-posteriori' normalize γ^{-1} to get typical relaxation times of the system (around 10 ms).

Conceptual structure of the model is illustrated in Figure 2. Rigid surface of the substrate is shown by upper solid curves. In order to understand the potential functional role of the material gradients found in beetles [12], we study three different kinds of fiber arrays: (a) long stiff fibers with short elastic ends; (b) long elastic fibers connected to the basal plate by the short hard roots; (c) relatively stiff fibers with short soft elastic filaments connected to the base. All these variants are shown in subplots (a), (b) and (c) respectively.

In all the cases the stiffness of the fibers is continuously varied along vertical coordinate. To simulate it we apply smooth step

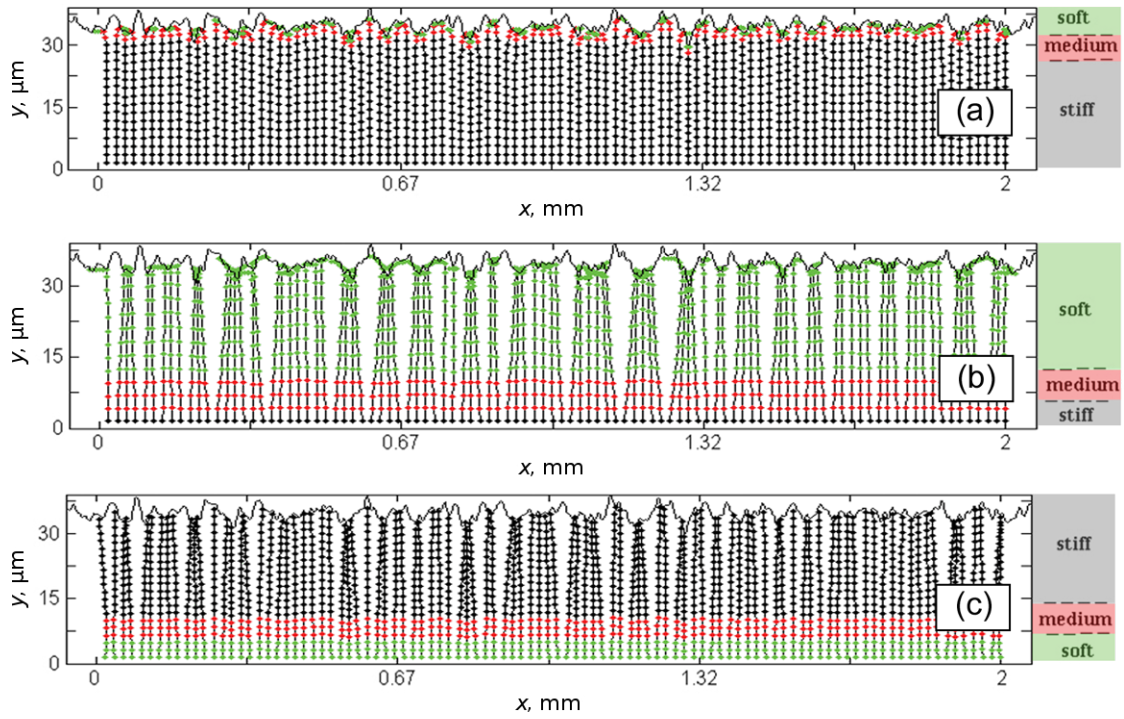

Figure 2: Typical configurations of the filamentary structure (setal array) attached to the stiff support (below) in adhesive contact with random fractal surface (above). This numerical model was used to mimic biological setal arrays shown in Figure 1. Three types of fibers, (1) stiff fibers with short elastic ends, (2) long elastic fibers connected to the base by short stiff roots, and (3) stiff fibers with soft elastic segments near the base are shown in subplots (a), (b) and (c), respectively. Different stiffness of segments is conditionally shown by circles with different colours. Stiff, medium and soft segments are marked by black, red and green circles, respectively.

function $\Theta(y) = 1/[1 + \exp(-(y - y_0)/\Delta)]$ with regulated position of bend y_0 and width Δ. This function tends to unit, when $y << y_0$, and gradually goes to zero in the opposite limit. This allows modeling all above mentioned cases in common approach. Stiffness previously experimentally estimated for insect adhesive setae are as follows: 1.31 $N \cdot m^{-1}$ (fly *Calliphora vicina* [22]), 0.192–0.693 $N \cdot m^{-1}$ (beetle *Gastrophysa viridula* [23]).

To illustrate different stiffness of fiber segments shown in the Figure 2, we formally divided the stiffness into three regions: (1) close to the maximal stiffness, (2) less than half of the maximal stiffness (a region around y_0 with the width Δ), and (3) less than 0.1 of the maximal stiffness. These parts are conditionally shown in the plots by different colours. Stiff, medium and soft segments are marked by black, red and green circles respectively. It is important to mention that our model is certainly limited. It does not account for plastic deformations, geometrical nonlinearity due to large deformations or friction effects. It is focused only on study of the effect of stiffness gradient on contact adhesion problem.

Our numerical procedure is organized as follows. We take originally unperturbed arrays of parallel fibers attached to the horizontal hard base, bring them into contact with numerically generated rigid fractal surface and solve numerically differential equations of motion by standard procedure of Matlab software. The fibers distort due to interaction between them and surface as well as due to their mutual interaction with the neighbors. Many of fibers are attracted to the same individual asperities of the surface. This attraction enhances their mutual interaction in contrast to original unperturbed state.

One can record time-depending distortions of the fibers as well as variation of the interaction forces, to control the process of contact formation and stop it, when the system reaches certain stationary configuration. After this, we can remove rigid substrate surface and allow the system to relax spontaneously to some new stationary state.

Many of the fibers, which were preliminary attracted to the same asperities of the surface, still strongly interact and remain close one to another, collecting into local clusters. Mutual attraction between the fibers competes with the elastic forces inside the fibers which try to return them to the straight position and the whole array as well to its original parallel-organized structure. Further scenario of setal arrangement develop-

ment certainly depends on the relationship between these forces and their spatial distribution. In some cases, structure can return back to the original state, but in some cases it can not. If it is so, the fibers remain collected into strongly confined bunches (so-called clustering/condensation phenomenon).

This phenomenon is very important from the practical point of view, because the clustered system is not ready to attach efficiently to every new surface during next contact events. That is why, in the present work, we mainly concentrated on the study of this effect. Qualitative results related to the clustering are summarized in Figure 3, where the same systems shown in Figure 2 are presented after their detachment from the surface and sufficiently long transient period of relaxation to the static state.

It is clearly seen that in contrast to strongly clustered systems with long flexible (Figure 3b) or long hard filaments (Figure 3c), the system with long hard filaments having short flexible ends (Figure 3a) practically returns back to its original configuration. This observation leads to a very important question. To get complete return to the original state after relaxation, it is important to have quite short flexible ends of the fibers in contrast to their complete length, but may be strong deformation of these ends in attached state is not enough to produce sufficiently strong attachment force?

To compare attraction forces in all the cases (a)–(c), we performed their accumulation over all contacting segments during entire time interval of the attachment (Figure 4). Let us remind that first stage (attachment) of our numerical experiment is organized as follows. We take originally unperturbed arrays of parallel fibers and put them on the horizontal rigid base, at fixed distance from numerically generated rigid fractal surface. The fibers adapt to the surface. During this process the force between them and surface changes and we record its time dependence while it reaches stationary asymptotic value. Because rigid horizontal base is fixed the force never falls down to zero, but tends a constant value depending on the case (a)–(b). It is seen from the Figure 4 that maximal forces in the cases (a) and (b) are comparable. Moreover, the potential barrier (the difference between maximum of force at the beginning and its minimum, which system gets after good adaptation to the rigid surface) is even higher in the case (a). Qualitatively this effect appears, because flexible filaments are too long in the case (b). Last case (c) with long hard filaments rotating around

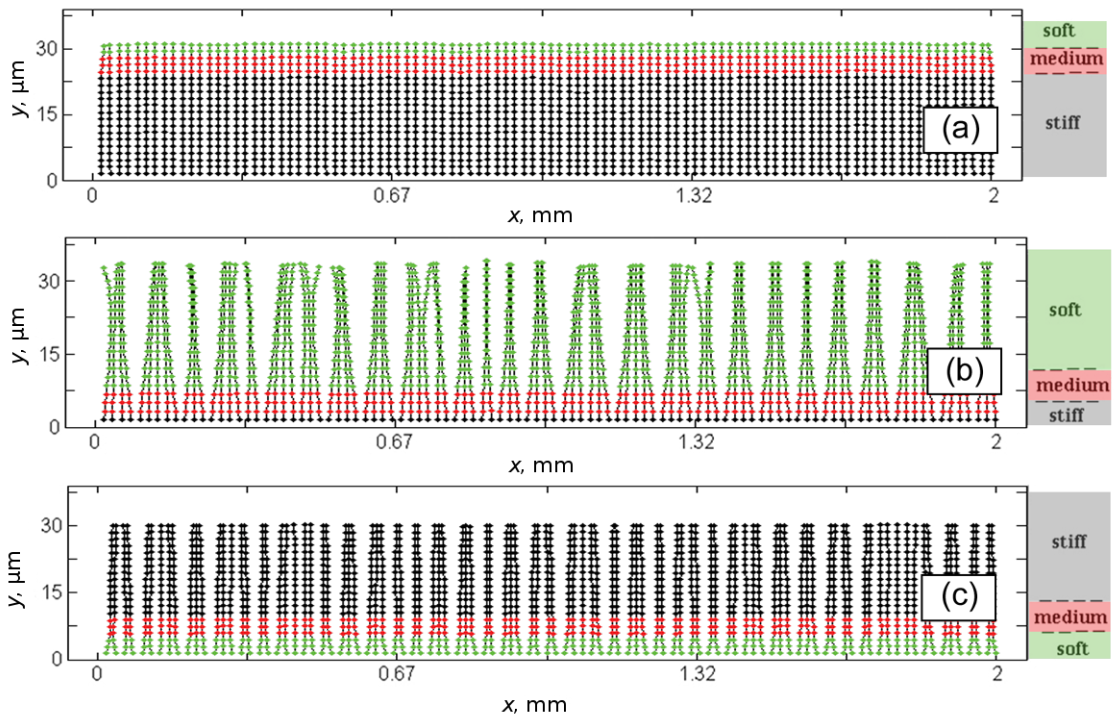

Figure 3: The same system as presented in Figure 2 shown after detachment from the fractal surface and sufficiently long relaxation to the static state. The difference between strongly clustered systems having either long elastic (b) or long stiff filaments (c) and the system with short soft ends (a), which practically returns back to its original configuration, is clearly seen. See also complementary movies 1, 2, 3 (Supporting Information File 1), which correspond to the cases (a), (b), (c), respectively.

their flexible roots, cannot perfectly adapt to the surface. As a result, maximum of the attachment force here remains much lower than in two previous cases (a) and (b).

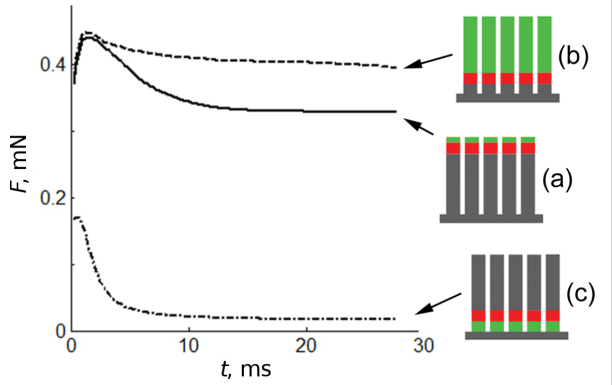

Figure 4: Time depending vertical forces developed during attachment of initially unperturbed systems to the hard surface. Solid, dashed and dash-dotted lines correspond to the cases (a), (b) and (c) of previous figures, respectively.

To accumulate time-dependent information about deformations of the fibers we calculate array $\{dx_j\}$, $j = 1,2,\ldots N_x$ of the distances between contact ends of the nearest neighbors $dx_j = x_{j+1} - x_j$. Let us note that we are using dx_j for small but finite distances (not differential). We use this notation to conserve coincidence with all our previous publications using the same or close models and hope, it will not cause any misunderstanding. Time evolution of every such array during complete attachment–detachment cycles for all (a)–(c) cases is shown in Figure 5. Each line in the plots corresponds to one particular time-depending distance between a pair of the closest neighbors $dx_j = x_{j+1} - x_j$. All these distances are normalized to the distance of original unperturbed periodic system, so $dx_j = 1$ at $t = 0$.

The history of the process is clearly seen from the plots. When some fibers are attracted to the same asperities of the surface and form the clusters, the distance between their ends goes to zero $dx_j = x_{j+1} - x_j \to 0$. At the same time, the distance between the fibers from different clusters generally grows. This distance must correlate with a characteristic distance between the asperities, but it remains random for random fractal surface. Finally, attached configuration delivers a complex compromise between: (1) stiffness of the fibers; (2) fractal structure of the surface; (3) strengths of all the interactions.

When the surface is removed, the system of fiber array relaxes to new final configuration which is driven by a compromise between stiffness and mutual interaction of the fibers only. If stiffness dominates, the system can return to the original unperturbed state. Time-depending history of this process is clearly recorded in the subplot Figure 5a. It is interesting to note that stiff fibers of case (c), having strong elastic energy cannot completely return back to initial state. They remain glued by their top ends.

To analyze the results statistically one can calculate histograms of the probability $P = P(dx)$ to find a particular value of the distance $dx_j = x_{j+1} - x_j$ between nearest fibers. It is done for a

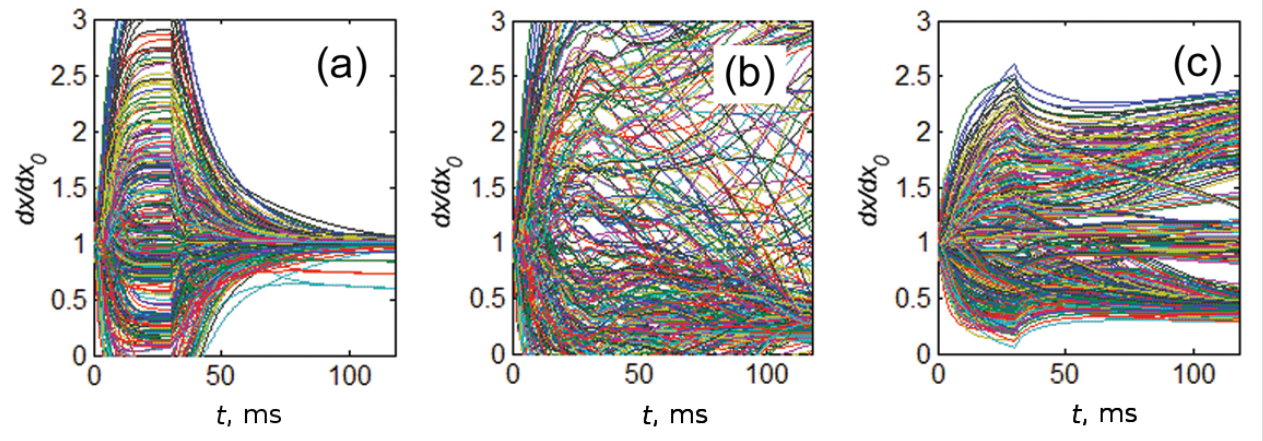

Figure 5: Time evolution of arrays $\{dx_j\}$ of distances $j = 1,2,\ldots N_x$ between ends of nearest neighbors $dx_j = x_{j+1} - x_j$ during single attachment–detachment cycle for the same cases (a)–(c) as before. All the distances are normalized to the distance of original unperturbed periodic system: $dx_j = dx_0$ at $t = 0$. Each line in the plots corresponds to a time-depending distance between one pair of the neighbors $dx_j = x_{j+1} - x_j$. In attached state, all the filaments tend to a configuration, which represents certain compromise between stiffness, adhesion to the surface and mutual interaction of the fibers. After detachment, the system relaxes to asymptotic configuration corresponding to a compromise between the stiffness and mutual interaction of the fibers only.

sequence of discrete time steps and summarized in Figure 6. The cases (a)–(c) in this figure are the same as above.

These data make information presented in Figure 5 clearer. Initial peak of the probability around $dx = 1$ corresponds to almost unperturbed configuration at small time, just the first contact with the surface. As time goes by around 25 ms all three types of systems deform their filaments into the configurations with smooth distribution $P(dx)$. It means that different distances $dx_j = x_{j+1} - x_j$ appear with comparable probabilities. With the time, in systems with soft ends ((a) and (b)), many fibers are attracted to the same asperities of the surface. As result the probabilities get well pronounced maximums near $dx \approx 0$. After detachment all the systems tend to asymptotic probability distributions which perfectly agree with the observed final configurations shown in Figure 3 and Figure 5.

Biological significance

Pure bulk materials are absent in biology: biological materials are always composites. Also material gradients are well known in biological systems, where particular change in composition of different bulk materials along a biological structure may lead to novel and often unexpected properties. This has been previously shown for insect cuticle [24,25], snake skin [26], human teeth [27,28], and other biological composites.

The gradients have been also recently reported for smooth attachment devices of insects [29]. Interestingly, the gradients in smooth pads of locusts and bushcrickets are different from gradients reported in hairy pads of ladybird beetles [12]. Smooth adhesive pads consist of a softer core covered by a stiffer layer, whereas hairy pads have opposite arrangement: stiffer bases combined with softer distal part. Both types of gradients combine conformability to the surface roughness of the substrate and resistance to the environment.

The opposite directionality of gradients can be well explained by difference in pad architecture. Smooth pads consist of branching rods or cellular foams, which in combination with fluid-filled spaces between solid structures hold the shape of the pad. This principle is combined with the presence of a relatively stiff superficial layer that terminates the fibers. The layer keeps the distance between tips of fibers at some constant value (and in species living in arid environments protects the pad from desiccation) [29,30]. In the hairy pads, adhesive setae are not terminated by continuous layer and can potentially buckle and cluster together [10,11]. As strong degree of clusterisation leads to the decrease of functional advantages from multiple contacts [7], this is reduced by the presence of gradients of thickness [1] and mechanical properties [12].

Whereas disadvantages of purely stiff and purely soft fiber arrays are intuitively clear, it is difficult to judge about the advantages of various gradients from the fiber base to the fiber tip (soft-to-stiff/downstream and stiff-to-soft/upstream). The numerical experiment of the present study has clearly demonstrated that gradient-bearing fibers with short soft tips and stiff gradients (short upstream gradient) has greater advantage in maximizing adhesion and minimizing clusterisation in multiple attachment-detachment cycles, if compared to the fibers with longer soft tips on the stiff bases (long upstream gradient) and fibers with stiff tips on the soft bases (downstream gradient). Such short upstream gradients were recently described in beetles [12], however, we can predict that similar gradients must have been convergently evolved in various lineages of arthropods.

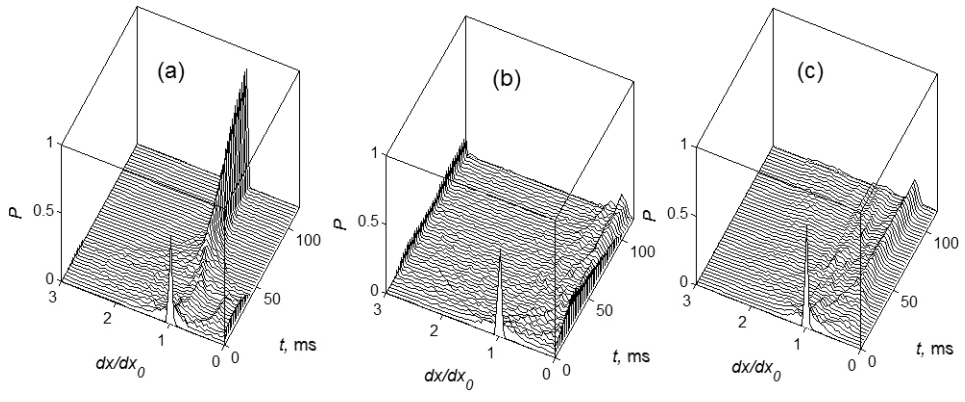

Figure 6: Statistical analysis of the plots presented in Figure 5. The sequences of the histograms show time evolution of the probability $P = P(dx)$ to find a particular value of the distance $dx_j = x_{j+1} - x_j$ between nearest fibers. The cases (a)–(c) are the same as above. Starting from unperturbed configuration (initial peak of probability around $dx_j = dx_0$) all the systems evolve to the smooth distributions $P(dx)$. In clustered attached state (see cases (a) and (b)) the probabilities have well pronounced maximums at $dx \approx 0$. After detachment from the surface all the systems tend to the distributions $P(dx)$, which perfectly agree with the observed final states shown in Figure 3 and Figure 5.

Supporting Information

Movie 1: Behaviour of the model array of setae/fibers, which have short soft ends and stiff bases during attachment-detachment cycle (a). Different stiffness of the segments of fibers is conditionally shown by different colors. Stiff, medium and soft segments are marked by black, red and green circles respectively. The subplots in the bottom (from left to right) show time dependent vertical force, evolution of the array of distances $dx_j = x_{j+1} - x_j$ between contact ends of nearest neighbors and instant histogram $P(dx)$ of the distribution of these distances. It is seen directly from the movie, how the system deforms near the surface and how it gradually returns back to the original state after detachment.

Movie 2: The same as Movie 1 for the array of long soft fibers. The colors and subplots are the same as those in the Movie 1. In contrast to the previous case, this system cannot overcome strong deformations of mutually glued filaments and does not return to the original unperturbed state.

Movie 3: The same as the previous Movies 1 and 2 for hard fibers softly connected with the bottom plate by few soft intermediate segments. Despite of stiffness of the filaments the structure is still able to adapt to the surface due to fiber rotation around their soft parts. As result, system gets quite satisfactory attachment to the rough surface, but it practically does not return back to the initial unperturbed state after detachment.

Supporting Information File 1

Movies 1–3.
[http://www.beilstein-journals.org/bjnano/content/supplementary/2190-4286-5-95-S1.zip]

Acknowledgements

We would like to acknowledge valuable discussions with J. Michels and H. Peisker (Kiel University, Germany). This work was supported by German Science Foundation (DFG, No. GO 995/10-1 and Project No. C-10 within SFB 677).

References

1. Gorb, S. N. *Attachment Devices of Insect Cuticle;* Kluwer Academic Publishers: Dordrecht, the Netherlands, 2001.
2. Gorb, S. N.; Beutel, R. G. *Naturwissenschaften* **2001,** *88,* 530–534. doi:10.1007/s00114-001-0274-y
3. Gorb, S. N.; Beutel, R. G.; Gorb, E. V.; Jiao, Y.; Kastner, V.; Niederegger, S.; Popov, V. L.; Scherge, M.; Schwarz, U.; Vötsch, W. *Integr. Comp. Biol.* **2002,** *42,* 1127–1139. doi:10.1093/icb/42.6.1127
4. Creton, C.; Gorb, S. N. *MRS Bull.* **2007,** *32,* 466–472. doi:10.1557/mrs2007.79
5. Voigt, D.; Schuppert, J. M.; Dattinger, S.; Gorb, S. N. *J. Insect Physiol.* **2008,** *54,* 765–776. doi:10.1016/j.jinsphys.2008.02.006
6. Hui, C.-Y.; Glassmaker, N. J.; Tang, T.; Jagota, A. *J. R. Soc., Interface* **2004,** *1,* 35–48. doi:10.1098/rsif.2004.0005
7. Varenberg, M.; Pugno, N. M.; Gorb, S. N. *Soft Matter* **2010,** *6,* 3269–3272. doi:10.1039/c003207g
8. Filippov, A. E.; Popov, V. L.; Gorb, S. N. *J. Theor. Biol.* **2011,** *276,* 126–131. doi:10.1016/j.jtbi.2011.01.049
9. Borodich, F. M.; Gorb, E. V.; Gorb, S. N. *Appl. Phys. A* **2010,** *100,* 63–71. doi:10.1007/s00339-010-5794-x
10. Jagota, A.; Bennison, S. J. *Integr. Comp. Biol.* **2002,** *42,* 1140–1145. doi:10.1093/icb/42.6.1140
11. Spolenak, R.; Gorb, S. N.; Arzt, E. *Acta Biomater.* **2005,** *1,* 5–13. doi:10.1016/j.actbio.2004.08.004
12. Peisker, H.; Michels, J.; Gorb, S. N. *Nat. Commun.* **2013,** *4,* No. 1661. doi:10.1038/ncomms2576
13. Weis-Fogh, T. *J. Exp. Biol.* **1960,** *37,* 889–907.
14. Weis-Fogh, T. *J. Mol. Biol.* **1961,** *3,* 648–667. doi:10.1016/S0022-2836(61)80028-4
15. Michels, J.; Gorb, S. N. J. *J. Microsc. (Oxford, U. K.)* **2012,** *245,* 1–16. doi:10.1111/j.1365-2818.2011.03523.x
16. Filippov, A. E.; Popov, V. L. *Phys. Rev. E* **2007,** *75,* 027103. doi:10.1103/PhysRevE.75.027103
17. Langer, M. G.; Ruppersberg, J. P.; Gorb, S. N. *Proc. R. Soc. London, Ser. B* **2004,** *271,* 2209–2215. doi:10.1098/rspb.2004.2850
18. Huber, G.; Gorb, S. N.; Spolenak, R.; Arzt, E. *Biol. Lett.* **2005,** *1,* 2–4. doi:10.1098/rsbl.2004.0254
19. Filippov, A. E.; Popov, V. L. *J. Phys.: Condens. Matter* **2007,** *19,* 096012. doi:10.1088/0953-8984/19/9/096012
20. Popov, V. L.; Starcevic, J.; Filippov, A. E. *Phys. Rev. E* **2007,** *75,* 066104. doi:10.1103/PhysRevE.75.066104
21. Persson, B. N. J.; Gorb, S. N. *J. Chem. Phys.* **2003,** *119,* 11437–11444. doi:10.1063/1.1621854
22. Niederegger, S.; Gorb, S.; Jiao, Y. *J. Comp. Physiol., A* **2002,** *187,* 961–970. doi:10.1007/s00359-001-0265-7
23. Bullock, J. M. R.; Federle, W. *Naturwissenschaften* **2011,** *98,* 381–387. doi:10.1007/s00114-011-0781-4
24. Vincent, J. F. V. *Composites, Part A* **2002,** *33,* 1311–1315. doi:10.1016/S1359-835X(02)00167-7
25. Barbakadze, N.; Enders, S.; Gorb, S.; Arzt, E. *J. Exp. Biol.* **2006,** *209,* 722–730. doi:10.1242/jeb.02065
26. Klein, M.-C. G.; Deuschle, J. K.; Gorb, S. N. *J. Comp. Physiol., A* **2010,** *196,* 659–668. doi:10.1007/s00359-010-0556-y
27. Fong, H.; Sarikaya, M.; White, S. N.; Snead, M. L. *Mater. Sci. Eng., C* **2000,** *7,* 119–128. doi:10.1016/S0928-4931(99)00133-2
28. Wang, R. Z.; Weiner, S. *J. Biomech.* **1997,** *31,* 135–141. doi:10.1016/S0021-9290(97)00131-0
29. Perez Goodwyn, P.; Peressadko, A.; Schwarz, H.; Kastner, V.; Gorb, S. *J. Comp. Physiol., A* **2006,** *192,* 1233–1243. doi:10.1007/s00359-006-0156-z
30. Gorb, S. N. Smooth attachment devices in insects. In *Advances in Insect Physiology: Insect Mechanics and Control;* Casas, J.; Simpson, S. J., Eds.; Elsevier Ltd., Academic Press: London, 2008; pp 81–116.

Beilstein Journal of Nanotechnology

Controlling mechanical properties of bio-inspired hydrogels by modulating nano-scale, inter-polymeric junctions

Seonki Hong[1], Hyukjin Lee[2] and Haeshin Lee[*1]

Full Research Paper

Open Access

Address:
[1]Department of Chemistry, Center for Nature-inspired Technology in KI NanoCentury, Korea Advanced Institute of Science and Technology (KAIST), 291, University Rd, Daejeon 305-701, South Korea and [2]College of Pharmacy, Graduate School of Pharmaceutical Sciences, Ewha Womans University, Seoul 120–750, South Korea

Email:
Haeshin Lee[*] - haeshin@kaist.ac.kr

* Corresponding author

Keywords:
catechols; hydrogels; poly(ethylene glycol)s; quinone tanning

Beilstein J. Nanotechnol. **2014,** *5,* 887–894.
doi:10.3762/bjnano.5.101

Received: 22 November 2013
Accepted: 29 May 2014
Published: 23 June 2014

This article is part of the Thematic Series "Biological and bioinspired adhesion and friction".

Guest Editor: S. N. Gorb

Abstract

Quinone tanning is a well-characterized biochemical process found in invertebrates, which produce diverse materials from extremely hard tissues to soft water-resistant adhesives. Herein, we report new types of catecholamine PEG derivatives, PEG-NH-catechols that can utilize an expanded spectrum of catecholamine chemistry. The PEGs enable simultaneous participation of amine and catechol in quinone tanning crosslinking. The intermolecular reaction between PEG-NH-catechols forms a dramatic nano-scale junction resulting in enhancement of gelation kinetics and mechanical properties of PEG hydrogels compared to results obtained by using PEGs in the absence of amine groups. Therefore, the study provides new insight into designing new crosslinking chemistry for controlling nano-scale chemical reactions that can broaden unique properties of bulk hydrogels.

Introduction

Water-resistant adhesives secreted by marine mussels, stiff cuticles synthesized by insects, and sharp beaks found in squids appear to be drastically different biomaterials (Figure 1a–c) [1-6]. Not only their mechanical properties, but also their biological functions are distinct: The adhesives anchor mussels in place for survival and colonization, the cuticles securely protect insects from predators, pathogens, and environmental stresses, and the beaks act as a non-mineralized knife for capturing prey. However, despite such differences in biological function, the molecular basis for the formation of the beaks, the cuticles, and the adhesives is similar. The process is called quinone tanning, which is defined by chemical crosslinking of proteins by a variety of reactive quinones. For mussel adhesives, DOPA-quinone is formed by oxidation of a catecholic amino acid, 3,4-dihydroxy-L-phenylalanine (DOPA). Subsequently, DOPA-quinone rapidly reacts with basic amino acids, such as lysine

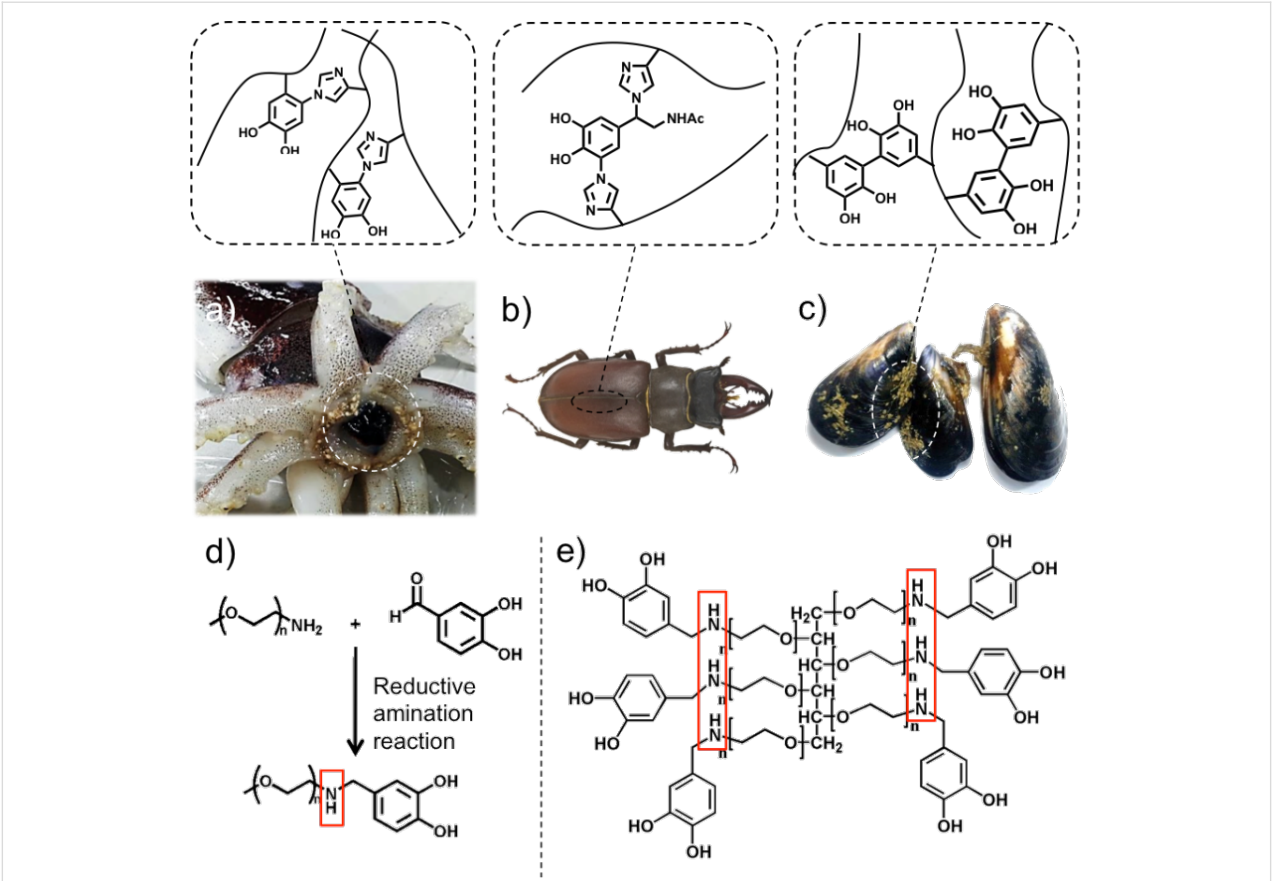

Figure 1: Biomaterials formed by quinone tanning processes found in (a) squid beaks, (b) insect cuticles, and (c) mussel adhesives. Representative chemical reactions were shown for each biomaterials (a,b,c top). Synthetic PEG derivatives that can mimic the natural catecholamine-involved quinone tanning due to the presence of secondary amine: (d) mPEG-NH-catechol for a model reaction, and (e) 6Arm-PEG-NH-catechol for hydrogels.

and/or histidine, forming covalent adducts of DOPA-DOPA, lysyl-DOPA, and/or histeinyl-DOPA [7-9]. For insect cuticles, the quinone tanning (i.e., sclerotization) occurs via crosslinking of cuticular proteins in which primary amines, secondary amines, and phenols from the proteins react with *N*-acetylcatecholamines [9-11]. For squid beaks, the reaction between the imidazole of histidine and DOPAquinone is the primary mechanism for mechanical hardening of the beaks (Figure 1a–c) [6].

The quinone tanning process has been a useful method to create chemically functionalized interfaces regardless of the chemistry of materials. Recently, we and other research groups have reported novel strategies for the functionalization of virtually any material surfaces by using synthetic catecholamine polymers such as poly(dopamine) [12], poly(norepinephrine) [13], and poly(ethylenimine)-catechol [14]. The surfaces modified by those catecholamines exhibited a variety of functionalities such as protein-immobilization [15], facilitating cell adhesion [16], attenuating in vivo toxicity [17], initiating bio-mineralization [18], graphene nano-composites [19], and bio-inspired adhesives [20,21]. In addition to the interface science and engineering, methods to prepare bulk materials such as poly(ethylene glycol) (PEG) and pluronic hydrogels have been reported [22-26]. However, most previous work utilized catechol–catechol crosslinking by using catechol end-functionalized polymers, which limits the control of important variables in hydrogels such as gelation kinetics and mechanical properties.

Herein, we report new types of PEG derivatives (linear mPEG-NH-catechol and branched 6Arm-PEG-NH-catechol) that offer an expanded spectrum of catecholamine chemistry. In the PEG derivatives, catechol and secondary amine coexist that can effectively mimic the chemical process of catecholamine-involved quinone tanning. The hydrogels produced by catecholamine crosslinking using 6Arm-PEG-NH-catechol exhibited enhanced mechanical properties and rapid gelation compared to the hydrogel prepared by PEGs that can only use catechol-catechol crosslinking. This study demonstrates that the chemical configuration by inserting both secondary amine and catechol expands the properties of PEG hydrogels, which can provide new insight into designing hydrogels prepared by other polymers using quinone tanning chemistry.

Results and Discussion

Quinone tanning reactions of catecholamine PEGs

Preparation of linear (5 kDa) and 6Arm-PEG-NH-catechol (15 kDa) was performed by a simple one-step reductive amination between 3,4-dihydroxybenzaldehyde (DHBA) and linear or 6Arm-PEG-NH_2 (Figure 1d and Figure 1e). Primary amines are difficult to be chemically tethered to PEG-catechol, because the typical reaction (i.e., EDC coupling) is the formation of an amide bond between the primary amine and the carboxyl group. Instead, we could easily generate secondary amines by using aldehyde chemistry, in other words reductive amination reaction, for the PEG-catechol to contain secondary amine groups. Secondary amines are also well-known to be reactive with catechol, which has been found in natural organisms [6]. The product was purified by dialysis (MWCO = 3 kDa for linear PEG and MWCO = 10 kDa for 6Arm-PEG) for two days and was subsequently lyophilized. White powders were obtained for both PEG derivatives. An absolute negative result from the ninhydrin test indicated that all amine groups of linear and 6Arm-PEGs had reacted with the catechol derivatives. Control polymers with the absence of secondary amines, linear and 6Arm-PEG-catechols, were prepared by an amide bond forming reaction using the BOP/HOBt/DIPEA coupling with 3,4-dihydroxyhydrocinnamic acid (DHCA) and linear or 6Arm-PEG-NH_2.

To investigate the effect of secondary amines on the results of quinone tanning, both linear PEG derivatives, mPEG-NH-catechol and mPEG-catechol, underwent the same crosslinking reactions in phosphate buffered saline (pH 8.0 with 0.3 mM $NaIO_4$) (Supporting Information File 1, Figure S6). Quantitative analysis of the crosslinked PEG products was performed by gel permeation chromatography (GPC). GPC results showed that the peak that appeared at 18 min of elution time is unreacted monomer (Standard data of unreacted monomer: Supporting Information File 1, Figure S5), and the other peaks eluted at around 17 min or earlier indicate multimers resulting from the quinone tanning reactions. The peak intensities of the multimers and the monomer were varied depending on the concentration of $NaIO_4$, which initiated the quinone tanning reaction. It was found that maximum intensity of the multimer peaks was obtained at 1.5 equiv $NaIO_4$ to catechols for both mPEG-NH-catechol (Supporting Information File 1, Figure S6, left) and mPEG-catechol (Supporting Information File 1, Figure S6, right). The entire range of $NaIO_4$ added to the reaction mixtures was 0.25–2 equiv to catechols. Amounts of $NaIO_4$ higher than 1.5 equiv no longer affected the results of the crosslinking. In fact, the intensity of the multimer peak for mPEG-NH-catechol was decreased, when 2 equiv of $NaIO_4$ were used. One equivalent of $NaIO_4$ to catechol is enough, but in practice a slight excess of $NaIO_4$ was found to be necessary for maximal crosslinking.

Quantitative analysis of crosslinked PEG products with GPC

One notable result was that the relative amounts and the molecular species of the multimers formed by quinone tanning reactions exhibited large differences between mPEG-NH-catechol and mPEG-catechol. For mPEG-NH-catechol, multimers were a major component (Figure 2a) but became a minor molecular species for mPEG-catechol. The monomer was dominant in the mPEG-catechol reaction mixture (Figure 2b).

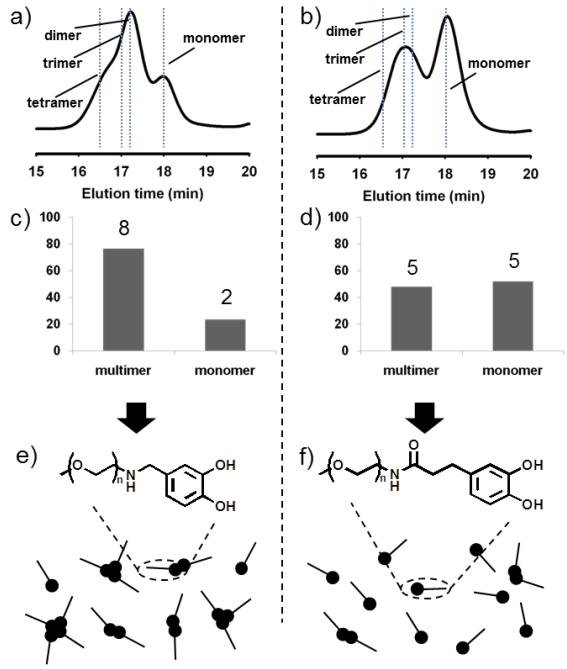

Figure 2: Comparative analysis of crosslinking products of mPEG-NH-catechol and mPEG-catechol. (a,b) GPC data obtained from crosslinking at a stoichiometric ratio of $NaIO_4$:catechol = 1.5:1. The dot lines indicate each elution time of PEG standards with molecular weight of 5, 10, 15, and 20 kDa. The quantitative multimeric and monomeric ratio of crosslinked mPEG-NH-catechol and mPEG-catechol were shown in (c) and (d). (e,f) Schematic results comparing nanoscale junctions formed by (e) mPEG-NH-catechol and (f) mPEG-catechol.

The molecular weight analysis of the GPC products showed that the multimer peak consisted of dimeric, trimeric, and tetrameric PEGs, composing up to about 80 percent of the total product in the mPEG-NH-catechol reaction mixture (Figure 2c). However, for mPEG-catechol, the GPC analysis showed that only dimeric and trimeric PEGs was formed. No indication of tetramers was found in the reaction mixture, and a large amount of unreacted monomer, about 50 percent, remained (Figure 2d). The lines in

Figure 2a and Figure 2b indicate the elution time of standard PEG compounds with known molecular weight and configuration. Linear mPEG-NH_2 5 kDa (18.0 min elution time), 10 kDa (17.2 min), 4Arm-PEG-NH_2 20 kDa (16.5 min) were used as standards (Supporting Information File 1, Figure S5). These results demonstrated that the quinone tanning reaction involved with amine and catechol simultaneously was more efficient than the reaction engaged only with catechol (Figure 2e and 2f). This result strongly suggests that one can control physicochemical properties of a wide variety of PEG-containing biomaterials by designing effective conjugation chemistry. We chose PEG hydrogels as an example.

Effect of the amine group in PEG gelation I: mechanical properties of hydrogels

To explore the effect of the amine group in PEG gelation, we prepared 6Arm-PEG-NH-catechol and 6Arm-PEG-catechol (control). Both were dissolved in PBS pH 8.0 with a final concentration of 3% (w/v). It is expected that the hydrogel formed by amine-catechol involved tanning (6Arm-PEG-NH-catechol) may exhibit faster gelation kinetics and stronger mechanical properties than the one formed by a catechol–catechol tanning (6Arm-PEG-catechol). We measured the mechanical modulus of the hydrogels by a rheometer. Frequency (0.01 to 10 Hz, Figure 3a) and strain (1 to 90%, Figure 3b) sweeps were performed for three times each on both 6Arm-PEG-NH-catechol and 6Arm-PEG-catechol hydrogels, after allowing time for complete gelation (10 min). The elastic modulus, G', and loss modulus, G", were found to be independent over a wide range of frequencies and strains, demonstrating that the gelation was successfully completed within 10 min. The elastic modulus of the hydrogel made of 6Arm-PEG-NH-catechol was about 1,000 Pa, but the G' of the hydrogel prepared by 6Arm-PEG-catechol was low, as expected (about 500 Pa). The two-times increase in the elastic modulus indicates that amine-catechol quinone tanning is more chemically efficient process compared to catechol–catechol tanning. Therefore, we understand that the amine–catechol tanning process has been chosen in nature to produce stiff biomaterials for the various invertebrates shown in Figure 1.

Effect of the amine group in PEG gelation II: differences in gelation kinetics

In rheology, gelation point is defined by the intersection of the elastic modulus (G') and the loss modulus (G"). We tried to measure the point by a rheometer, but it was found that gelation occurred within a minute in both hydrogels (6Arm-PEG-NH-catechol and 6Arm-PEG-catechol), preventing a direct measurement of the gelation time in a rheometer. There was, however, a difference in gelation kinetics: dropping the solu-

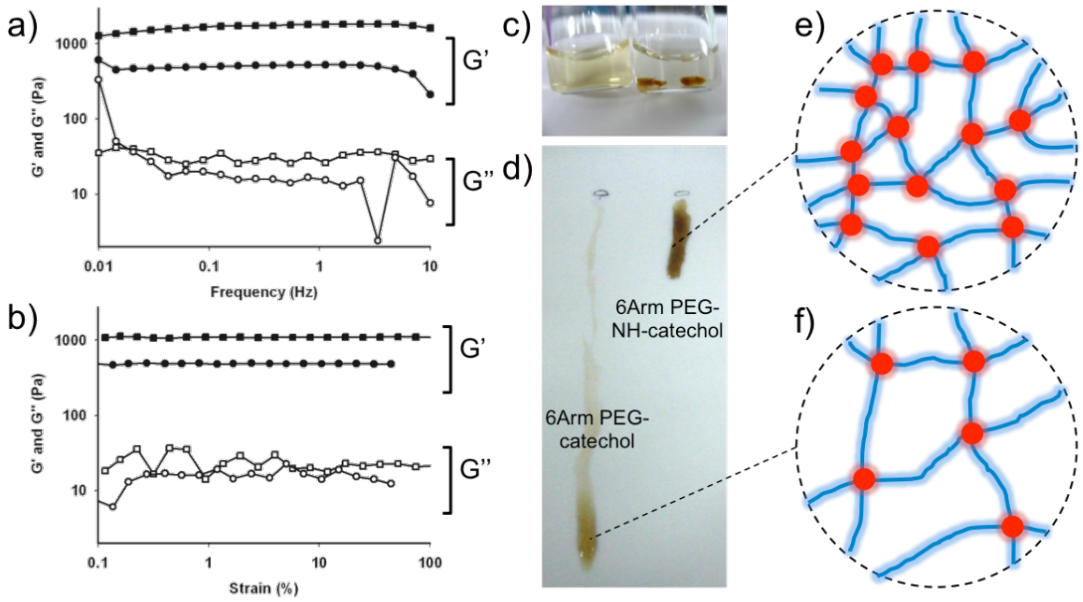

Figure 3: Rheological analysis data of quinone tanning inspired crosslinking hydrogels (a) frequency sweep and (b) strain sweep of 6Arm-PEG-NH-catechol (square) and 6Arm-PEG-catechol (circle). (n = 3 each) (c) Rapid quinone tanning of 6Arm-PEG-NH-catechol (right) in $NaIO_4$ (100 mM in DDW). A visible tanning reaction was not observed in 6Arm-PEG-catechol (left). (d) Measurement of gelation kinetics by dropping solutions of 6Arm-PEG-NH-catechol (right) and 6Arm-PEG-catechol (left) on a PTFE surface (45 deg slope). (e and f) Schematic results showing nano-scale junctions formed by (e) 6Arm-PEG-NH-catechol and (f) 6Arm-PEG-catechol.

tion of 6Arm-PEG-NH-catechol (3%, w/v) into a $NaIO_4$ solution (100 mM in DDW) immediately formed dark brown gel-like aggregates (Figure 3c, right bottle). In contrast, such rapid aggregates were not detected when dropping the 6Arm-PEG-catechol solution was dropped into the same solution (Figure 3c, left bottle). The PEG solution was dispersed in the $NaIO_4$ solution. This clear indication of differences in the gelation time led us to design a new, simple method for measuring this parameter. A poly(tetrafluoroethylene) (PTFE) surface was set up at a 45° slope angle, and drops of 6Arm-PEG-NH-catechol (Figure 3d, right) and 6Arm-PEG-catechol (Figure 3d, left) solutions were applied to observe the gelation time. The PEG solution flowed in the liquid phase but stopped in the gel phase. Immediate gelation of 6Arm-PEG-NH-catechol was observed within 2 s, but it took about 12 s for the 6Arm-PEG-catechol solution to become a hydrogel. This result, combined with the rheology data, indicates that amine–catechol tanning is an efficient process that is suitable for controlling a large number of chemical junctions in nanobiomaterials (Figure 3e and Figure 3f). Because the reaction occurs in aqueous conditions, many invertebrates utilize this process to produce a variety of biomaterials for their use in nature. The effective tanning process of catechol and amine demonstrated herein suggests a general approach for creating novel catecholaminergic derivatives of biopolymers such as alginate, hyaluronic acid, chitosan, dextran, and other synthetic or proteineous materials for a variety of applications.

Quinone, an oxidized form of catechol, is reactive to nucleophiles such as hydroxyl, amine, and quinone, which typically undergo the 1,4-Michael addition reactions [27]. Considering the molecular structures of PEGs studied herein, three quinone tanning reactions are possible: (i) catechol–catechol formation through C–C coupling between phenyl rings [27,28], (ii) C–O coupling at a C-4 position by the reaction between deprotonated hydroxyl anion and quinone [27,29], and (iii) C–N coupling at the same position by the secondary amine and quinone [7-11,27]. For PEG-catechol, the C–C and C–O couplings are the only possible quinone tanning mechanisms to form hydrogels (Figure 4a). However, for PEG-NH-catechol, another scenario of C–N coupling is added to the two previous tanning reactions (catechol–catechol and C–O couplings of

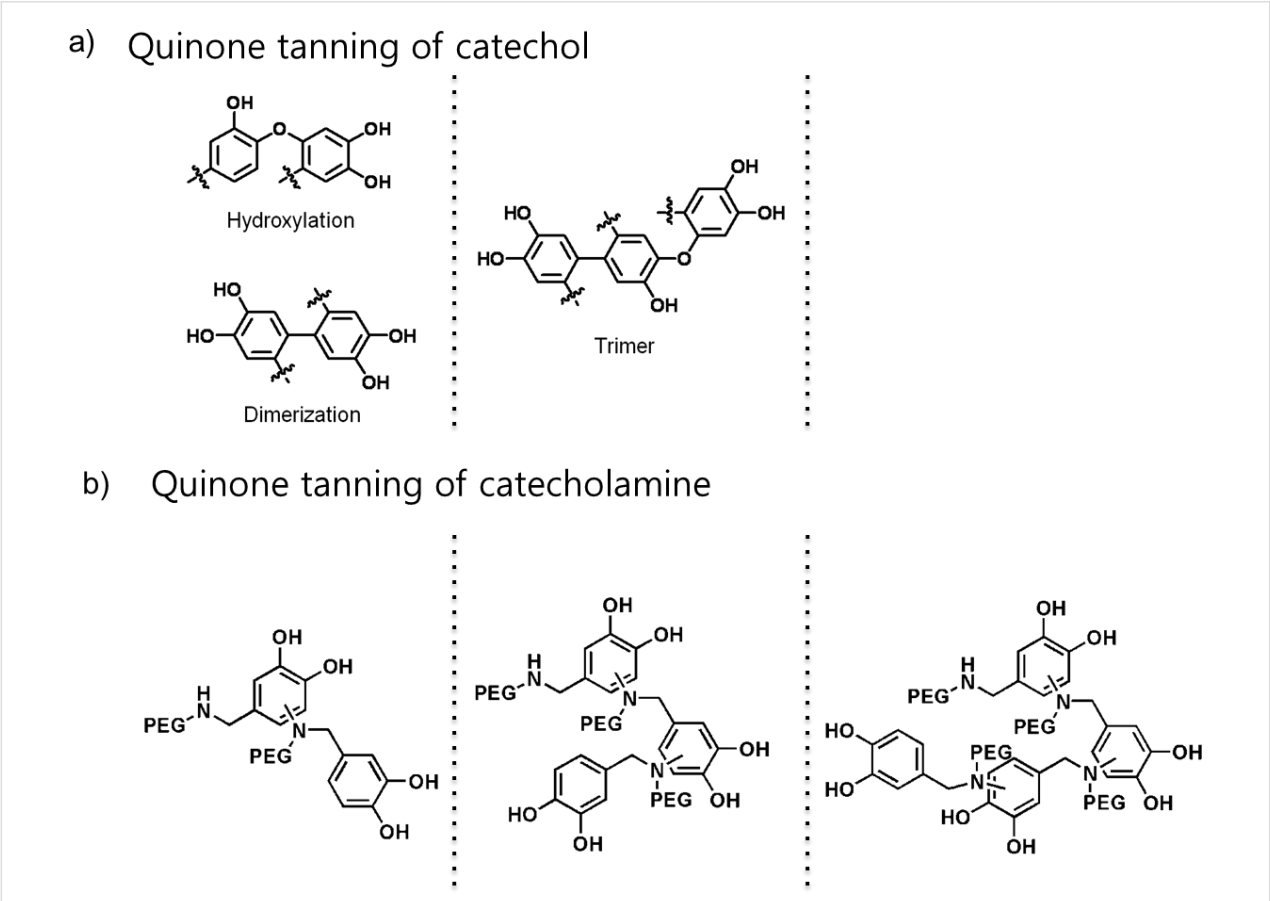

Figure 4: Proposed chemical structures of crosslinked products by quinone tanning reactions. (a) Catechol quinone tanning and (b) catecholamine quinone tanning. In catecholamine tanning, amine-involved crosslinking shown in (b) is more favorable than catechol tanning pathway shown in (a).

PEG-catechol) (Figure 4b). It is generally accepted that the nucleophilicity of amines is higher than that of a hydroxyl group. Thus, nature utilizes the amine-involved quinone tanning reactions for the formation of stiff insect cuticles [7-11,27] by a reaction between imidazole (side-chain of histidine) and catechol. So far, the majority of research was focused on catechol–catechol crosslinking [25,30,31], accidentally ignoring the importance of catecholamine quinone tanning. Thus, the results demonstrated herein can be a useful toolkit to further control physicochemical properties of biomaterials.

Conclusion

In summary, we demonstrated that the particular quinone tanning process simultaneously involved with catechol and amine was effective in crosslinking. The linear type of polymer mPEG-NH-catechol showed superior crosslinking result compared to mPEG-catechol, the polymer crosslinked via catechol-catechol tanning. Similar to the difference in crosslinking efficiency in linear PEG experiments, hydrogels formed by multi-armed PEGs showed that the hydrogel utilizing catechol–amine tanning, 6Arm-PEG-NH-catechol, showed fast in gelation kinetics (about 2 s) and strong in mechanical properties (G' > 1,000 Pa) compared to the hydrogel produced by 6Arm-PEG-catechol (about 12 s and about 500 Pa).

Experimental

Materials

6Arm-PEG-amine (PEG-$(NH_2)_4$, M_w = 15,000 Da) and methoxy-PEG-amine (mPEG-NH_2, M_w = 5,000 Da) were purchased from SunBio, Inc. (Walnut Creek, CA). Sodium periodate ($NaIO_4$), sodium cyanoborohydride ($NaBH_3CN$), *N*,*N*-diisopropylethylamine (DIPEA), 3,4-dihydroxyhydrocinnamic acid (DHCA) and 3,4-dihydroxybenzaldehyde (DHBA) were acquired from Sigma-Aldrich (St. Louis, MO). 1-Hydroxybenzotriazole (HOBt) hydrate was purchased from Peptides International (Louisville, KY) and benzotriazole-1-yl-oxy-tris-(dimethylamino)-phosphonium hexafluorophosphate (BOP) was acquired from Novabiochem (Germany).

Synthesis of catechol-conjugated PEG (1)

Synthesis of 6Arm-PEG-catechol and mPEG-catechol: 6Arm-PEG-amine (1 g, 0.067 mmol) was dissolved in 10 mL of NMP at 60 °C for 10 min. DHCA (0.8 mmol), BOP (0.8 mmol), HOBt (0.8 mmol) and DIPEA (0.8 mmol) were dissolved in 5 mL of NMP in a separate vial. The PEG and DHCA solutions were mixed and reacted at room temperature for 3–6 h. The reaction solution was purified by dialysis at acidic condition for 2 d and then lyophilized. (Dialysis conditions: 10 mL of polymer solution was added to 3 L of DDW for 3 h and the dialysate was exchanged for four times. MWCO = 5,000.) The content of catechol was confirmed by UV–vis spectroscopy at 280 nm. The UV–vis intensity of catechol modified polymer was calculated to the contents of catechol by using the standard curve made by the known concentration of dopamine solution versus the UV–vis intensity, demonstrating that all terminal amine groups were conjugated with DHCA. The catechol contents of catechol-modified PEG were double checked by the ninhydrin test. The ninhydrin test was performed by mixing 20 μL of catechol-modified PEG (1 mg mL^{-1} in DDW) with 20 μL of 2% ninhydrin reagent solution, followed by heating at 100 °C for 3 min. The heated solution was diluted to 700 μL of DDW and then the primary amine and secondary amine was confirmed by UV–vis spectrometer at 470 nm and 440 nm. ^{1}H NMR (300 MHz, $CDCl_3$, δ): 6.71–6.69 (m, 2H, $C_6HH_2(OH)_2$-), 6.52–6.49 (dd, 1H, $C_6H_2H(OH)_2$-), 3.79–3.33 (m, PEO), 2.81–2.76 (t, 2H, $C_6H_3(OH)_2$-CH_2-), 2.49–2.44 (t, 2H, CH_2-C(O)NH-). mPEG-catechol was prepared by using the same procedure described above with the amount of reagents used are the followings: mPEG-amine (200 mg, 0.04 mmol), DHCA (0.048 mmol), BOP (0.048 mmol), HOBt (0.048 mmol) and DIPEA (0.048 mmol). The Purity of synthetic PEGs was determined by ^{1}H NMR and GPC (Supporting Information File 1, Figure S2 and S4).

Synthesis of catechol-conjugated PEG (2)

6Arm-PEG-amine (200 mg, 0.013 mmol) was solved in 2 mL of NMP at 60 °C for 10 min. DHBA (33 mg, 0.24 mmol) in 1 mL of NMP was added to the PEG solution and stirred at room temperature for 1 h. $NaBH_3CN$ (38 mg, 0.6 mmol) in 100 μL of NMP was added to that solution and reacted at room temperature for overnight. The reaction solution was successively purified by dialysis at acidic condition for 2 d and then lyophilized. The content of catechol was confirmed by ultraviolet–visible spectroscopy at 280 nm, demonstrating that all terminal amine groups were conjugated with DHBA. (The dialysis condition and catechol content assay were the same as in the synthesis of 6Arm-PEG-catechol and mPEG-catechol.) ^{1}H NMR (300 MHz, $CDCl_3$, δ) 7.19 (s, 1H, $C_6H_2H(OH)_2$-), 6.81–6.88 (m, 2H, C_6HH_2-$(OH)_2$-), 4.09–4.05 (m, 2H, -NH-CH_2-$C_6H_3(OH)_2$-), 3.95–3.59 (m, PEO), 3.40–3.36 (t, 2H, PEO-CH_2-NH-). mPEG-NH-catechol was prepared by using the same procedure described above with the amount of reagents used being as follows: mPEG-amine (200 mg, 0.04 mmol), DHBA (17 mg, 0.12 mmol), $NaBH_3CN$ (38 mg, 0.6 mmol). The purity of synthetic PEGs was determined by ^{1}H NMR and GPC (Supporting Information File 1, Figure S1 and S3).

Quinone tanning reactions of catecholamine PEGs

Quinone tanning reactions of mPEG-NH-catechol and mPEG-catechol were performed by the addition of sodium periodate ($NaIO_4$) to PEG solutions (2 mg mL^{-1} in 10 mM phosphate

buffered saline, pH 8.5), and the resulting molecular weight of the crosslinked PEGs was determined by gel permeation chromatography (GPC). Two GPC columns (OHpak SB-806M HQ and SB-804 HQ, Shodex®, Munich, Germany) were connected in series and equilibrated with phosphate buffered saline (10 mM, pH 4.0). The detector for the PEG standard was a reflective index detector (Shodex, RI-71), and a UV–vis spectrometer (Hewlett Packard HP 8453 spectrophotometer, 190 nm to 1100 nm, integration time 0.5 sec, interval 1 nm, Deuterium lamp for UV and tungsten lamp for vis) was used for detecting the catechol modified polymers. The columns were characterized with various PEG standards: mPEG-amine (linear, 5 kDa), mPEG-amine (linear, 10 kDa), 4Arm-PEG-amine (star shaped, 20 kDa). The elution time of the PEG standards were 18 min for mPEG-NH_2 (linear, 5 kDa), 17.2 min for mPEG-amine (linear, 10 kDa), 16.5 min for 4Arm-PEG-NH_2 (star shaped, 20 kDa). Our GPC column approximately separated the 100 Da molecular weight after 30 min elution time, calculated by using a standard curve of 130 kDa, 30 kDa, 20 kDa, and 5 kDa molecular weight hyaluronic acid and PEGs. (Supporting Information File 1, Figure S5) The quinone tanning reaction was optimized by varying the amount of sodium periodate (0.1 to 2 equiv relative to mole of catechol). It was confirmed in our previous report that the chemical pathway of catechol crosslinking is exactly the same whether $NaIO_4$ is used or not, and $NaIO_4$ can effectively control the kinetics of catecholamine crosslinking without any additional byproducts [32].

Formation of PEG hydrogels

To form PEG hydrogels, 1.5 equiv of $NaIO_4$ (moles of catechol basis) was added to 3% PEG solution (30 mg mL^{-1} in phosphate-buffered saline, pH 8.0), and the subsequently determined gelation time through vial inversion method was typically 10–20 s. For a naccurate determination of the gelation time, we used PTFE plate setup with 45 degree slope and droplets of PEG solutions (10 μL) allowed to flow until the solutions stopped when became hydrogels.

Oscillatory rheometry

Oscillatory rheometry by using a rotating rheometer (Bohlin Advanced Rheometer with a parallel 20 mm plate, Malvern Instruments, UK) was used to determine the mechanical properties of the PEG hydrogels. Strain sweep was performed at 1 Hz and frequency sweep was carried out at a strain of 10% after 10 min from the gel formed. To perform rheology studies of the modified-PEG hydrogels, 1.5 equiv of $NaIO_4$ (moles of catechol basis) was added to 3% PEG solution (30 mg mL^{-1} in phosphate-buffered saline, pH 8.0) in 24 well-plate as a mold for rheology sample. The formed hydrogel was a cylinder shape with diameter of 16 mm and height of 1 mm. The time dependent rheology test showed that the sol–gel transition was finished within 1 min (data not shown). In order to test the mechanical properties of the hydrogels in a stable condition, we carried out the frequency and strain sweep test 10 min after the gel formed.

Supporting Information

Supporting Information File 1

Further experimental data.

The further experimental data describes ^1H NMR and GPC data for the purity of synthetic products, mPEG-catechol, mPEG-NH-catechol, 6Arm-PEG-catechol, and 6Arm-PEG-NH-catechol.

[http://www.beilstein-journals.org/bjnano/content/supplementary/2190-4286-5-101-S1.pdf]

Acknowledgements

The authors are grateful to the financial support from National Research Foundation: Mid-career Scientist Grant (2104002855) and Biomedical Technology Development Program (2012-0006085). World Premier Material (WPM) Program from the Ministry of Knowledge and Economy. This work is also supported in part by Development of Future Therapeutic Materials Program (A120170) from The Ministry of Health and Welfare.

References

1. Waite, J. H.; Andersen, N. H.; Jewhurst, S.; Sun, C. J. *J. Adhes.* **2005,** *81,* 297. doi:10.1080/00218460590944602
2. Deming, T. J. *Curr. Opin. Chem. Biol.* **1999,** *3,* 100. doi:10.1016/S1367-5931(99)80018-0
3. Waite, J. H.; Tanzer, M. L. *Science* **1981,** *212,* 1038. doi:10.1126/science.212.4498.1038
4. Sherald, A. F. *Experientia* **1980,** *36,* 143. doi:10.1007/BF01953696
5. Andersen, S. O. *Insect Biochem. Mol. Biol.* **2010,** *40,* 166. doi:10.1016/j.ibmb.2009.10.007
6. Miserez, A.; Schneberk, T.; Sun, C. J.; Zok, F. W.; Waite, J. H. *Science* **2008,** *319,* 1816. doi:10.1126/science.1154117
7. Waite, J. H. *Integr. Comp. Biol.* **2002,** *42,* 1172. doi:10.1093/icb/42.6.1172
8. Bittner, S. *Amino Acids* **2006,** *30,* 205. doi:10.1007/s00726-005-0298-2
9. Kramer, K. J.; Kanost, M. R.; Hopkins, T. L.; Jiang, H. B.; Zhu, Y. C.; Xu, R. D.; Kerwin, J. L.; Turecek, F. *Tetrahedron* **2001,** *57,* 385. doi:10.1016/S0040-4020(00)00949-2
10. Suderman, R. J.; Dittmer, N. T.; Kramer, K. J.; Kanost, M. R. *Insect Biochem. Mol. Biol.* **2010,** *40,* 252. doi:10.1016/j.ibmb.2010.02.008
11. Kerwin, J. L.; Turecek, F.; Xu, R. D.; Kramer, K. J.; Hopkins, T. L.; Gatlin, C. L.; Yates, J. R., III. *Anal. Biochem.* **1999,** *268,* 229. doi:10.1006/abio.1998.3069
12. Lee, H.; Dellatore, S. M.; Miller, W. M.; Messersmith, P. B. *Science* **2007,** *318,* 426. doi:10.1126/science.1147241
13. Kang, S. M.; Rho, J.; Choi, I. S.; Messersmith, P. B.; Lee, H. *J. Am. Chem. Soc.* **2009,** *131,* 13224. doi:10.1021/ja905183k

14. Lee, H.; Lee, Y.; Statz, A. R.; Rho, J.; Park, T. G.; Messersmith, P. B. *Adv. Mater.* **2008,** *20,* 1619. doi:10.1002/adma.200702378
15. Lee, H.; Rho, J.; Messersmith, P. B. *Adv. Mater.* **2009,** *21,* 431. doi:10.1002/adma.200801222
16. Ku, S. H.; Ryu, J.; Hong, S. K.; Lee, H.; Park, C. B. *Biomaterials* **2010,** *31,* 2535. doi:10.1016/j.biomaterials.2009.12.020
17. Hong, S.; Kim, K. Y.; Hwang, J. W.; Park, S. Y.; Lee, K. D.; Lee, D. Y.; Lee, H. *Nanomedicine* **2011,** *6,* 793. doi:10.2217/nnm.11.76
18. Ryu, J.; Ku, S. H.; Lee, H.; Park, C. B. *Adv. Funct. Mater.* **2010,** *20,* 2132. doi:10.1002/adfm.200902347
19. Kang, S. M.; Park, S.; Kim, D.; Ruoff, R. S.; Lee, H. *Adv. Funct. Mater.* **2010,** *21,* 108. doi:10.1002/adfm.201001692
20. Kaneko, D.; Kinugawa, S.; Matsumoto, K.; Kaneko, T. *Plant Biotechnol. (Tokyo, Jpn.)* **2010,** *27,* 293. doi:10.5511/plantbiotechnology.27.293
21. Kaneko, D.; Wang, S.; Matsumoto, K.; Kinugawa, S.; Yasaki, K.; Chi, D. H.; Kaneko, T. *Polym. J.* **2011,** *43,* 855. doi:10.1038/pj.2011.77
22. Huang, K.; Lee, B. P.; Ingram, D. R.; Messersmith, P. B. *Biomacromolecules* **2002,** *3,* 397. doi:10.1021/bm015650p
23. Lee, B. P.; Dalsin, J. L.; Messersmith, P. B. *Biomacromolecules* **2002,** *3,* 1038. doi:10.1021/bm025546n
24. Westwood, G.; Horton, T. N.; Wilker, J. J. *Macromolecules* **2007,** *40,* 3960. doi:10.1021/ma0703002
25. Lee, B. P.; Chao, C. Y.; Nunalee, F. N.; Motan, E.; Shull, K. R.; Messersmith, P. B. *Macromolecules* **2006,** *39,* 1740. doi:10.1021/ma0518959
26. Brubaker, C. E.; Kissler, H.; Wang, L. J.; Kaufman, D. B.; Messersmith, P. B. *Biomaterials* **2010,** *31,* 420. doi:10.1016/j.biomaterials.2009.09.062
27. Nematollahi, D.; Tammari, E.; Sharifi, S.; Kazemi, M. *Electrochim. Acta* **2004,** *49,* 591. doi:10.1016/j.electacta.2003.09.013
28. Rayn, M. D.; Yueh, A.; Wen-Yu, C. *J. Electrochem. Soc.* **1980,** *127,* 1489. doi:10.1149/1.2129936
29. Papouchado, L.; Petrie, G.; Adams, R. N. *J. Electroanal. Chem. Interfacial Electrochem.* **1972,** *38,* 389. doi:10.1016/S0022-0728(72)80349-8
30. Burke, S. A.; Jones, M. R.; Lee, B. P.; Messersmith, P. B. *Biomed. Mater.* **2007,** *2,* 203. doi:10.1088/1748-6041/2/4/001
31. Holowka, E. P.; Deming, T. J. *Macromol. Biosci.* **2010,** *10,* 496. doi:10.1002/mabi.200900390
32. Hong, S.; Na, Y. S.; Choi, S.; Song, I. T.; Kim, W. Y.; Lee, H. *Adv. Funct. Mater.* **2012,** *22,* 4711. doi:10.1002/adfm.201201156

License and Terms

Beilstein Journal of Nanotechnology

Direct observation of microcavitation in underwater adhesion of mushroom-shaped adhesive microstructure

Lars Heepe*, Alexander E. Kovalev and Stanislav N. Gorb

Full Research Paper

Open Access

Address:
Functional Morphology and Biomechanics, Zoological Institute, Kiel University, Am Botanischen Garten 1-9, 24118 Kiel, Germany

Email:
Lars Heepe* - lheepe@zoologie.uni-kiel.de

* Corresponding author

Keywords:
bio-inspired; biomimetic; cavitation; contact mechanics; gecko; interface; negative pressure; pull-off; surface; tribology

Beilstein J. Nanotechnol. **2014,** *5,* 903–909.
doi:10.3762/bjnano.5.103

Received: 07 April 2014
Accepted: 01 June 2014
Published: 25 June 2014

This article is part of the Thematic Series "Biological and bioinspired adhesion and friction".

Associate Editor: K. Koch

Abstract

In this work we report on experiments aimed at testing the cavitation hypothesis [Varenberg, M.; Gorb, S. *J. R. Soc., Interface* **2008,** *5,* 383–385] proposed to explain the strong underwater adhesion of mushroom-shaped adhesive microstructures (MSAMSs). For this purpose, we measured the pull-off forces of individual MSAMSs by detaching them from a glass substrate under different wetting conditions and simultaneously video recording the detachment behavior at very high temporal resolution (54,000–100,000 fps). Although microcavitation was observed during the detachment of individual MSAMSs, which was a consequence of water inclusions present at the glass–MSAMS contact interface subjected to negative pressure (tension), the pull-off forces were consistently lower, around 50%, of those measured under ambient conditions. This result supports the assumption that the recently observed strong underwater adhesion of MSAMS is due to an air layer between individual MSAMSs [Kizilkan, E.; Heepe, L.; Gorb, S. N. Underwater adhesion of mushroom-shaped adhesive microstructure: An air-entrapment effect. In *Biological and biomimetic adhesives: Challenges and opportunities*; Santos, R.; Aldred, N.; Gorb, S. N.; Flammang, P., Eds.; The Royal Society of Chemistry: Cambridge, U.K., 2013; pp 65–71] rather than by cavitation. These results obtained due to the high-speed visualisation of the contact behavior at nanoscale-confined interfaces allow for a microscopic understanding of the underwater adhesion of MSAMSs and may aid in further development of artificial adhesive microstructures for applications in predominantly liquid environments.

Introduction

During the past two decades, bio-inspired microstructured adhesives became a new class of adhesive materials with different potential applications (e.g., in robotic systems, medicine, and industrial pick-and-place processes), due to the reversible and residue-free character of the sticking mechanism [1-4]. So far, the most promising candidates for technical applications are

surface microstructures with mushroom-shaped contact geometry (see review [4]), which have been studied intensively under various loads (e.g., preload [5,6], shear [7,8], overload [9], and tilt [10,11]) and environmental conditions (e.g., dry in air [5-12], oil lubricated [13], on rough substrates [13-15], in vacuum [10,16-18], and underwater [19,20]). The origin of the high adhesion capability of the mushroom-shaped adhesive microstructures (MSAMSs) was attributed to the combination of intermolecular van der Waals forces and a particular failure mode at detachment, a consequence of an optimized homogeneous stress distribution in the contact interface during pull-off [21,22]: During detachment of an individual MSAMS from a substrate, a crack nucleates somewhere in the middle of the contact area and further propagates towards the outer edge while the perimeter remains still in contact until complete separation occurs. This type of failure mode, further called mode II [21], suggests the formation of a low-pressure zone in the contact area giving rise to a suction effect [9]. However, such effect at a dry interface was shown to contribute only marginally (at most ≈10%) to the overall measured pull-off forces [10,16-18].

In their recent work Varenberg and Gorb [19] have observed that the pull-off forces measured underwater were significantly higher (about 25%) compared to those measured under ambient conditions. This effect cannot be explained by intermolecular van der Waals forces. The authors hypothesized that the enhanced underwater adhesion may be a result of cavitation under each individual MSAMS when entrapped water in the contact area is subjected to a negative pressure (tension) during pull-off and the liquid water turns into vapor at a certain cavitation threshold [19]. This effect would make each individual MSAMS to act as a passive suction device [19].

In the present study, we report on underwater adhesion experiments with individual MSAMSs. The visualisation of the MSAMS interface using the combination of high speed video recording and reflection contrast microscopy under applied pull-off force aimed at testing the cavitation hypothesis, an effect that have never been experimentally observed in artificial bio-inspired microstructured adhesives.

Experimental

Experimental setup

In the experiments, two individual MSAMSs, denoted by sample 1 and sample 2, were detached from a smooth glass slide under different wetting conditions with simultaneous video recording of the failure dynamics with a setup similar to a reflection interference contrast microscope (RICM) [23,24]. Individual MSAMSs were cut off from the microstructured tape made from polyvinylsiloxane (PVS) with a thickness of the supporting polymer film of about 900 µm [5,11,22]. Pull-off forces were measured using a force measuring system (FMS) consisting of a tensometric force transducers FORT-10 (World Precision Instruments, Inc., Sarasota, Florida) fixed on a three-axis micromanipulator F-131.3SS (Physik Instrumente GmbH & Co. KG, Karlsruhe, Germany) [11]. The FMS was installed on an inverse light microscope Observer.A1 (Carl Zeiss MicroImaging GmbH, Göttingen, Germany) equipped with a "Plan-Neofluar 63×/1.25 Antiflex" oil-immersion objective (Carl Zeiss MicroImaging GmbH). The microscope was operated in the epi-illumination mode and the complete spectrum of the light source HXP 120 (Carl Zeiss MicroImaging GmbH) was used. Detachment behavior was recorded with an attached high-speed camera Photron Fastcam SA1.1 (VKT Video Kommunikation GmbH, Pfullingen, Germany) either with 54,000 frames/s or with 100,000 frames/s. Obtained high-speed video sequences were background corrected by using the average of at least 10 frames at the end of the sequences where MSAMSs were already detached.

Figure 1A shows the schematic of the experimental setup. In order to repeatedly attach and detach samples, individual MSAMSs were glued to the force transducer. To ensure parallel alignment between samples and the glass slide, first individual MSAMSs were attached manually to the glass slide using

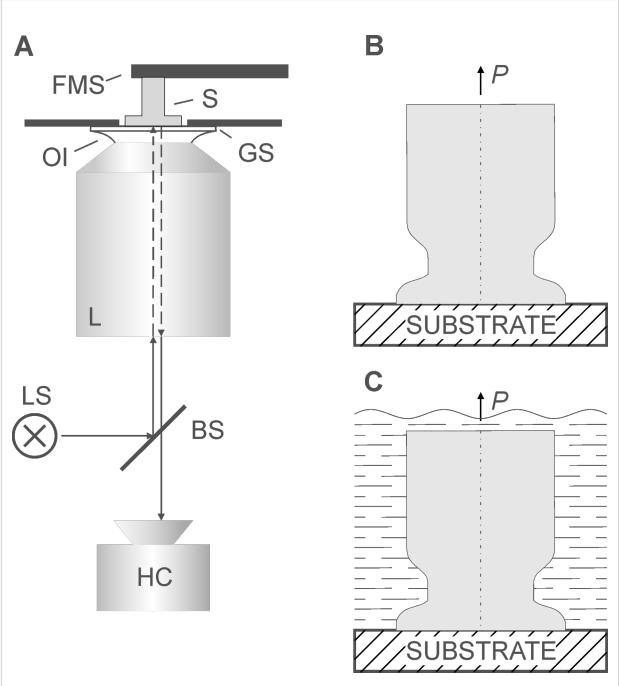

Figure 1: Schematic of the experimental setup (A). FMS, force measuring system; S, sample; GS, glass slide; OI, oil immersion; L, lens; LS, light source; BS, beam splitter; HC, high-speed camera. Individual MSAMS in contact with a substrate under ambient conditions (B) and submerged in water (C). *P* is the applied force.

tweezers while observing the proper contact via the microscope. Then, attached to the glass slide, samples were withdrawn at a retraction velocity of 10 µm/s in the direction normal to the surface of the glass slide. In order to test the cavitation hypothesis, pull-off forces were measured at detachment on individual MSAMS samples under different wetting conditions. For sample 1, the following measurement sequence was performed: 1. Pull-off forces were measured at ambient conditions, further called 'dry state' (Figure 1B). 2. After reattachment, i.e., contact formation in dry state, pull-off force was measured with the sample 1 submerged in water by applying a drop of deionized water onto the individual MSAMS with a syringe (Figure 1C), further called 'dry–wet' state. 3. Then, pull-off forces were measured after reattachment of the individual MSAMS under submerged conditions, further called 'wet' state (Figure 1C). For sample 2, only the dry state and the wet state could be compared.

Image formation and simulation

In order to reliably interpret the high-speed video sequences of the underwater detachment behavior of individual MSAMSs, we simulated the image formation obtained in the RICM experiments according to the theory described in [25]. Consider the case, when an individual MSAMS, submerged in water and partially detached from the glass substrate, where the detached regions are filled with water (Figure 2), is observed in epi-illumination as depicted in Figure 1A. Then, the incoming light with intensity I_0 is partially reflected at the glass–water interface (I_1) and superimposes with the reflected light I_2 from the water–PVS interface (Figure 2). Depending on the degree of coherence, roughly a measure of the ability to interfere, which is defined by the mutual coherence function Γ_{12}, the total reflected intensity I can be written in its general form

$$I = I_1 + I_2 + 2\sqrt{I_1 I_2}\,\Gamma_{12}\cos\left(2kh + \varphi\right) \tag{1}$$

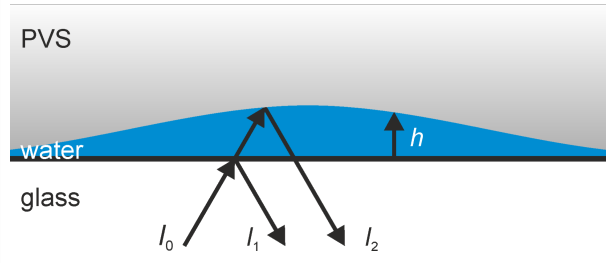

Figure 2: Schematic of the optical path in the RICM at the glass–water–PVS layers. The incoming beam with intensity I_0 is partially reflected at the glass-water interface (I_1) and at the water–PVS interface (I_2). The optical path difference between I_1 and I_2 depends on the distance h between glass and PVS, the angle of incidence, and on the refractive index of water.

where $k = 2\pi n_{water}/\lambda$ is the wave vector with n being the refractive index of the medium (here water) and λ the wavelength. The constant phase φ accounts for potential phase shifts of π at reflectance at an optical denser medium. For $\Gamma_{12} = 0$ (incoherent case), beam 1 and beam 2 cannot interfere and Equation 1 is reduced to $I = I_1 + I_2$. $\Gamma_{12} > 0$ corresponds to a partial coherence and $\Gamma_{12} = 1$ describes the fully coherent case. According to the van Cittert–Zernike theorem Γ_{12} is [25]

$$\Gamma_{12} = \frac{\sin y}{y} e^{iy}, \quad y = 2kh\sin^2\alpha/2 \tag{2}$$

where α is the maximum illumination angle. Substituting Equation 2 in Equation 1 yields, according to Rädler and Sackmann [25]

$$I(x,y) = 4\pi\sin^2\alpha/2\left[I_1 + I_2 + I_{12}\right]$$
$$I_{12} = 2\sqrt{I_1 I_2}\,\frac{\sin(y)}{y}\cos\left[2k\left(1-\sin^2\alpha/2\right)h(x,y) + \varphi\right] \tag{3}$$

here $h(x,y)$ denotes the distance between glass and PVS surface along the x and y direction. Since $n_{PVS} > n_{water}$ (see below) with n_{PVS} and n_{water} being the refractive index of PVS and water, respectively, beam I_2 undergoes a phase shift of π at the water–PVS interface (Figure 2). The intensities I_1 and I_2 can be calculated by

$$I_1 = R_{GW} I_0, \quad I_2 = \left(1 - R_{GW}\right)^2 R_{WP} \tag{4}$$

where R_{GW} and R_{WP} denote the reflectance at the glass–water and water–PVS interface, respectively. In general, the reflectance at an interface of medium 1 to medium 2 can be calculated from Fresnel's equations and takes, in the simplest case of normal incidence, the form [25]

$$R_{12} = \left(\frac{n_1 - n_2}{n_1 + n_2}\right)^2 \tag{5}$$

with $n_{1,2}$ being the refractive indices of medium 1 and 2. Since n_{PVS} is unknown we first determined the refractive index using the image A of Figure 3 where sample 1 was in dry contact with the glass. Incoming intensity I_0 was determined from the background using Equation 2 and Equation 3 at the glass-air interface. For numerical values of the refractive indices of glass and air see Table 1. Since no interference pattern is visible in the region under the thin contact plate (i.e., $\Gamma_{12} = 0$) and assuming intimate contact (i.e. glass-PVS interface) the total reflected intensity in that region is simply the sum $I = I_1 + I_2$, whereas I_2

is the second reflection at the PVS-air interface. The refractive index n_{PVS} was adjusted to match the measured intensity in that region. We found $n_{PVS} = 1.468$ to be a good estimate which is well in the range of refractive indices of silicon rubber [26]. Next we used the image B of Figure 3 to determine again I_0, but now for the underwater case. For simplicity, the distance $h(x,y)$ between the glass and PVS surface was modelled Gaussian-like by

$$h(x,y) = h_0 \exp\left[-\frac{(x-x_0)^2+(y-y_0)^2}{w^2}\right] \quad \text{for } \sqrt{(x-x_0)^2+(y-y_0)^2} < R, \tag{6}$$

where R is the radius of an individual MSAMS, (x_0, y_0) the origin of the circular contact of an individual MSAMS, w the width of the distribution, and h_0 the maximum height. Using Equation 3 and a reasonable set of parameter (see Table 1) a still image of the detachment of an individual MSAMS was simulated in order to interpret the experimentally obtained detachment sequences. Results were rounded to greyscale values between 0 (black) and 255 (white) in accordance to the 8-bit output of the high-speed camera. Finally, shot noise was added to the simulated image so that the standard deviation of the background is comparable to the noise obtained from Figure 3B.

Results and Discussion

We measured pull-off forces of individual MSAMSs on glass substrates under different wetting conditions (Figure 4). Pull-off forces were normalized with respect to those obtained in the dry state. Dry state pull-off forces were averaged over five individual measurements for both samples. For the sample 1, the median dry state pull-off force was ca. 570 µN ($N = 5$, min. value ca. 540 µN, and max. value ca. 590 µN). For the sample 2, the median dry state pull-off force was ca. 490 µN ($N = 5$, min. value ca. 440 µN, and max. value ca. 570 µN). In the dry–wet state, the pull-off force of sample 1 was about 55% of the dry state. In the wet state, the pull-off forces for both samples were both about 50% of the dry state, except for the second measurement of sample 1 in the wet state, which was about 25%. These values are in agreement with recent macroscopic adhesion measurements on arrays of MSAMSs completely wetted by water and submerged underwater [20]. For the first classification of these results we may consider the following two limiting cases in the underwater adhesion of MSAMS. In the first case, a thin water layer separates the glass–MSAMS contact. Then the van der Waals interaction strength, described by the Hamaker constant between glass and

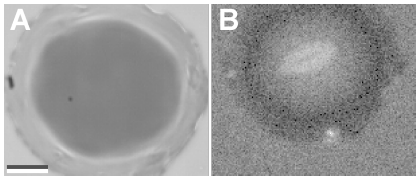

Figure 3: Sample 1 in dry contact with glass (A) and in contact with glass underwater (B). Scale bar, 10 µm.

Table 1: Parameter and its values used in the simulation.

parameter	value
grid size, $N \times N$	150 × 150
refractive index of air, n_{air}	1.000
refractive index of water, n_{water}	1.335
refractive index of glass, n_{glass}	1.526
refractive index of PVS, n_{PVS}	1.468
incoming light intensity, I_0	10462
light wavelength, λ	550 nm
radius of MSAMS, R	(N – 10)/2
width of distribution, w	0.375R
maximum height, h_0	150 nm
constant phase, φ	π
maximum illumination angle, α	25°

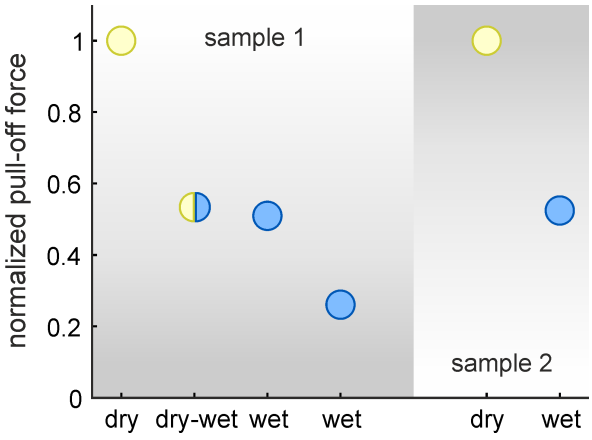

Figure 4: Pull-off forces, normalized by the average value of the dry state. Two individual MSAMS samples were measured on glass substrates for different wetting conditions: dry state (yellow circle), dry–wet state (yellow/blue circle), and wet state (blue circles). Dry state corresponds to measurements under ambient conditions. Dry–wet state corresponds to measurements where the sample has been brought into contact under dry conditions, but subsequently submerged in water. Wet state corresponds to measurements where the sample has been brought into contact when already submerged. For sample 1 the median dry state pull-off force was ca. 570 µN ($N = 5$, min. value ca. 540 µN, and max. value ca. 590 µN). For sample 2 the median dry state pull-off force was ca. 490 µN ($N = 5$, min. value ca. 440 µN, and max. value ca. 570 µN).

MSAMS, is expected to be reduced by about 86% [19]. In the second case, MSAMS and glass form a dry contact underwater. In this case, one would expect similar pull-off forces as observed in the dry state. However, the experimentally obtained results lie somewhere in between these two cases.

For each measurement also the detachment behavior was video recorded, in order to observe the actual failure process of the MSAMS detachment from the glass substrate. Figure 5 shows detachment sequences in the dry–wet state (A, sample 1) and in the wet states (B, sample 1 second measurement; C, sample 2). Images labelled with '0' correspond to equilibrium conditions right after the contact formation. Images with index '1' to '5' are still images of the actual detachment sequence. Frames set to $t \equiv 0$ ms (images with index '1') were arbitrarily chosen as a reference. For better comparability all images have the same scale. For comparison, detachment sequences in the dry state are shown in [4,9,11,17].

Let us first observe that during detachment, also in the dry–wet state (Figure 5A), water inclusions were present within the contact interface of MSAMS and glass (see white arrow heads in Figure 5). In order to confirm this observation we simulated an individual MSAMS partially detached from a glass substrate with the gap between the MSAMS and glass being filled with liquid water, not with air (for details see Experimental section: Image formation and simulation). The gap was, for simplicity, simulated as a Gaussian-like shape with its maximum separation of 150 nm in the middle of the contact. The result is shown in Figure 6. The light grey central region, which indicates the non-contact state, is clearly visible. Around the maximum separation in the middle of the contact the lower greyscale values (darker region) indicate a first-order interference minimum (zero order minimum corresponds to intimate contact) similar to what is observed in Figure 5A1. The red line in Figure 6 indicates the position with a separation between glass and MSAMS of about 25 nm. Note that with the particular noise level, heights below 25 nm cannot be clearly resolved even in the simulation. Thus, in that range, a contact region cannot be reliably distinguished from a non-contact region. The white square in Figure 6 was calculated assuming the gap being filled with air instead of water. We are thus very confident that we indeed observed water inclusions within the contact interface of MSAMSs and glass. This is particular interesting, especially in the case of dry contact formation (dry–wet state), since MSAMSs (hydrophobic) and glass (hydrophilic) form a Janus

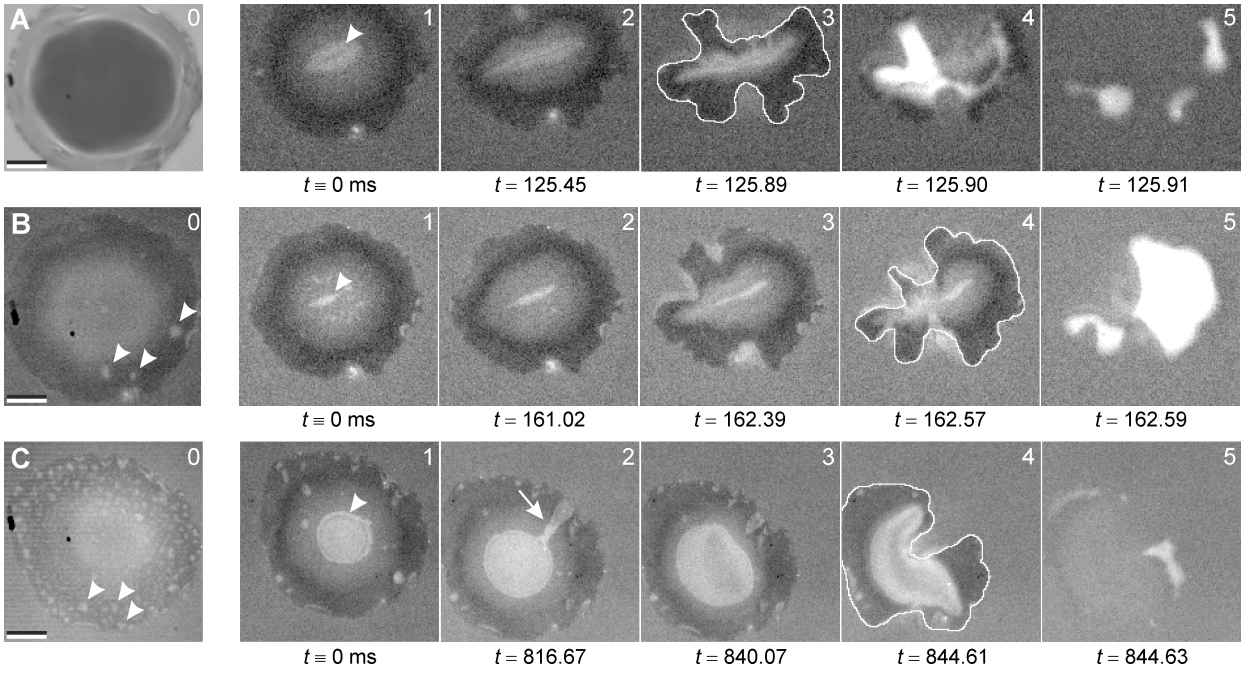

Figure 5: Detachment sequences of individual MSAMSs separating from a glass substrate for the sample 1 in the dry–wet state (A), second measurement of the sample 1 in the wet state (B), and the sample 2 in the wet state (C). Images labelled with '0' correspond to equilibrium conditions right after contact formation. Note, in (A) contact formation was under ambient conditions. Images with index '1' to '5' are still images of the actual detachment sequence. Frames set to $t \equiv 0$ ms (images with index '1') were arbitrarily chosen as a reference. All times are given in milliseconds (ms). During detachment water inclusions were present within the contact interface of MSAMS and glass (white arrowheads). In sequences (A) and (B) microcavitation was observed indicated by the white region in images A4–5 and B5. The white arrow (C2) indicates channel formation by interfacial crack propagation between the confined water within the contact interface and the surrounding water. The white traces in A3, B4, and C4 outline the contact area prior to detachment. For comparison, detachment sequences in the dry state are shown [4,9,11,17]. Scale bar, 10 µm.

interface in which confined water may exhibit non-trivial behavior [27]. However, in a recent experiment it has been confirmed that water can "leak" into a (dry) Janus interface formed by glass and MSAMSs [28]. During the further detachment process the contact area shrank to about 60% (Figure 5A) of the initial contact area (images labelled with '0') without losing contact. Then, at the very moment of detachment a sudden (within less than 20 µs) and significant change in contrast is observed (see white areas especially in Figure 5 A4–5 and B5). This dramatic change in contrast clearly indicates cavitation.

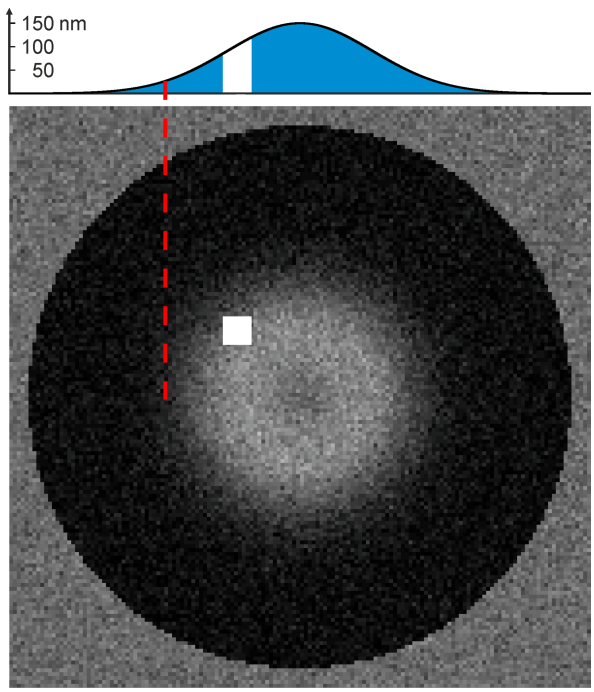

Figure 6: Simulated image of an individual MSAMS partially detached from a glass substrate submerged in water, for which the gap filled with liquid water was, for simplicity, chosen Gaussian-like with a maximum separation of 150 nm in the middle of the contact (see graph at top of the simulated image). The simulation parameters are given in Table 1. Note that around the maximum separation in the middle of the contact the lower greyscale values (darker region) indicate a first order interference minimum (zero order minimum corresponds to intimate contact) similar to what is observed in Figure 5A1. The red dashed line indicates separation of about 25 nm. Due to the noise level even in the simulation it is not possible to reliably distinguish between contact and non-contact region for a separation below 25 nm. The white square has been calculated assuming the gap being filled with air instead of water.

We can calculate the pull-off strength σ for all sequences dividing the obtained pull-off forces P by the contact area A_{det} right before complete separation and cavitation (area within white counters in Figure 5 A3, B4, C4). We obtain $\sigma_A \approx 430$ kPa, $\sigma_B \approx 180$ kPa, and $\sigma_C \approx 260$ kPa for sequences A–C, respectively. By using $P = \Delta p A_{det} = (p_{atm} - p_1)A_{det}$ with p_{atm} the atmospheric pressure and p_1 the pressure in the liquid, we estimate negative pressures subjected to the confined water of about −0.33 MPa, −0.08 MPa, and −0.16 MPa, for sequences A–C, respectively. These values are well in the range observed for mechanically stretched water and may indicate heterogeneous nucleation at gas residues (see [29,30]). One may also consider the role of the fluid viscosity, which may strongly affect the fluid motion [31] during contact formation and breakage between MSAMS and substrate. This may result in a viscous contribution to the observed pull-off stress. However, in a recent publication [17] the effect of a suction contribution to the adhesion of MSAMS was tested by comparing pull-off forces obtained at atmospheric and reduced pressure at different retraction velocities. It was shown that at a sufficiently low retraction velocity (100 µm/s) no suction contribution was observed [17]. At higher velocities (400 µm/s and 800 µm/s) a suction effect of about 10% contributed to the overall pull-off force [17]. This was explained by air being able to percolate through the contact interface (due to, e.g., surface roughness resulting in partial contact) and instantaneously balancing the pressure in the forming low pressure zone in the center of the contact area [17]. For water, the viscosity of which is much larger than the viscosity of air, such a 'critical' retraction velocity will be shifted towards lower values. We thus assume that the fluid volume which enters the contact interface during detachment from outside is very small and trapped water in the contact interface is effectively sealed from the outer environment.

Finally, it is important to mention a particularly interesting observation in sequence C (Figure 5C). During detachment the large amount of small water inclusions (Figure 5C0) accumulated to a large non-contact region in the middle of the contact area (Figure 5C1). At a certain load a channel formed (white arrow in Figure 5C2) by interfacial crack propagation balancing (at least partially) the pressure between the confined water within the contact interface and the surrounding water. Interestingly, the channel closed again before a complete separation occurred (Figure 5C3). Although not observed under dry conditions such channel formation may also be an additional explanation why at low retraction velocities no suction effect was found in the dry adhesion of MSAMS arrays [17].

Conclusion

We confirmed the cavitation hypothesis proposed in [19] in the underwater adhesion of individual MSAMSs. We found underwater pull-off forces consistently lower, approximately 50%, of those under ambient conditions which cannot be explained by one of the two limiting cases: (1) MSAMS and glass form a dry contact underwater, (2) MSAMS and glass are separated by (thin) water layer. Instead we observed that water inclusions

present at the interface are subjected to negative pressure (tension) during applied pull-off. However, for individual MSAMSs used in this work, we did not observe higher underwater adhesion, when compared to the dry state as reported in [19]. This supports the assumption that the observed enhanced underwater adhesion reported in [19] is probably an effect of the air retaining properties of MSAMS arrays, when submerged underwater [20]. Our results allow a microscopic understanding of the underwater adhesion of MSAMSs and may aid in further development of artificial adhesive microstructures for applications especially in liquid dominated environments.

Acknowledgements

The authors would like to thank the reviewers for constructive feedback. This work was supported by German Science Foundation (DFG, No. GO 995/10-1 and Project No. C-10 within SFB 677) and the Ministry of Economic Affairs, Employment, Transport, and Technology, Schleswig-Holstein, Germany within the programme „Zukunft Meer“.

References

1. Kamperman, M.; Kroner, E.; del Campo, A.; McMeeking, R. M.; Arzt, E. *Adv. Eng. Mater.* **2010,** *12,* 335–348. doi:10.1002/adem.201000104
2. Sameoto, D.; Menon, C. *Smart Mater. Struct.* **2010,** *19,* 103001. doi:10.1088/0964-1726/19/10/103001
3. Xue, L.; Steinhart, M.; Gorb, S. N. Biological and bioinspired micro- and nanostructured adhesives. In *Biomaterials Surface Science;* Taubert, A.; Mano, J. F.; Rodríguez-Cabello, J. C., Eds.; Wiley-VCH: Weinheim, Germany, 2013; pp 409–439. doi:10.1002/9783527649600.ch14
4. Heepe, L.; Gorb, S. *Annu. Rev. Mater. Res.* **2014,** *44,* in press. doi:10.1146/annurev-matsci-062910-100458
5. Gorb, S.; Varenberg, M.; Peressadko, A.; Tuma, J. *J. R. Soc., Interface* **2007,** *4,* 271–275. doi:10.1098/rsif.2006.0164
6. Kim, S.; Sitti, M. *Appl. Phys. Lett.* **2006,** *89,* 261911. doi:10.1063/1.2424442
7. Varenberg, M.; Gorb, S. *J. R. Soc., Interface* **2007,** *4,* 721–725. doi:10.1098/rsif.2007.0222
8. Kim, S.; Aksak, B.; Sitti, M. *Appl. Phys. Lett.* **2007,** *91,* 221913. doi:10.1063/1.2820755
9. Varenberg, M.; Gorb, S. *J. R. Soc., Interface* **2008,** *5,* 785–789. doi:10.1098/rsif.2007.1201
10. Murphy, M. P.; Aksak, B.; Sitti, M. *Small* **2009,** *5,* 170–175. doi:10.1002/smll.200801161
11. Heepe, L.; Carbone, G.; Pierro, E.; Kovalev, A. E.; Gorb, S. N. *Appl. Phys. Lett.* **2014,** *104,* 011906. doi:10.1063/1.4860991
12. del Campo, A.; Greiner, C.; Arzt, E. *Langmuir* **2007,** *23,* 10235–10243. doi:10.1021/la7010502
13. Kovalev, A. E.; Varenberg, M.; Gorb, S. N. *Soft Matter* **2012,** *8,* 7560–7566. doi:10.1039/c2sm25431j
14. Kasem, H.; Varenberg, M. *J. R. Soc., Interface* **2013,** *10,* 20130620. doi:10.1098/rsif.2013.0620
15. Cañas, N.; Kamperman, M.; Völker, B.; Kroner, E.; McMeeking, R. M.; Arzt, E. *Acta Biomater.* **2012,** *8,* 282–288. doi:10.1016/j.actbio.2011.08.028
16. Davies, J.; Haq, S.; Hawke, T.; Sargent, J. P. *Int. J. Adhes. Adhes.* **2009,** *29,* 380–390. doi:10.1016/j.ijadhadh.2008.07.009
17. Heepe, L.; Varenberg, M.; Itovich, Y.; Gorb, S. N. *J. R. Soc., Interface* **2011,** *8,* 585–589. doi:10.1098/rsif.2010.0420
18. Sameoto, D.; Sharif, H.; Menon, C. *J. Adhes. Sci. Technol.* **2012,** *26,* 2641–2652. doi:10.1080/01694243.2012.701463
19. Varenberg, M.; Gorb, S. *J. R. Soc., Interface* **2008,** *5,* 383–385. doi:10.1098/rsif.2007.1171
20. Kizilkan, E.; Heepe, L.; Gorb, S. N. Underwater adhesion of mushroom-shaped adhesive microstructure: An air-entrapment effect. In *Biological and biomimetic adhesives: Challenges and opportunities;* Santos, R.; Aldred, N.; Gorb, S. N.; Flammang, P., Eds.; The Royal Society of Chemistry: Cambridge, U.K., 2013; pp 65–71. doi:10.1039/9781849737135-00065
21. Carbone, G.; Pierro, E.; Gorb, S. N. *Soft Mater.* **2011,** *7,* 5545–5552. doi:10.1039/c0sm01482f
22. Heepe, L.; Kovalev, A. E.; Filippov, A. E.; Gorb, S. N. *Phys. Rev. Lett.* **2013,** *111,* 104301. doi:10.1103/PhysRevLett.111.104301
23. Curtis, A. S. G. *J. Cell Biol.* **1964,** *20,* 199–215. doi:10.1083/jcb.20.2.199
24. Ploem, J. S. Reflection-contrast microscopy as a tool for investigation of the attachment of living cells to a glass surface. In *Mononuclear phagocytes in immunity, infection and pathology;* Furth, R. V., Ed.; Blackwell Scientific Publications: Oxford, U.K., 1975; pp 405–421.
25. Rädler, J.; Sackmann, E. *J. Phys. II* **1993,** *3,* 727–748. doi:10.1051/jp2:1993163
26. Mark, J. E., Ed. *Physical properties of polymers handbook,* 2nd ed.; Springer: New York, NY, USA, 2007. doi:10.1007/978-0-387-69002-5
27. Zhang, X.; Zhu, Y.; Granick, S. *Science* **2002,** *295,* 663–666. doi:10.1126/science.1066141
28. Heepe, L.; Kovalev, A. E.; Gorb S. N. unpublished results.
29. Caupin, F.; Herbert, E. *C. R. Phys.* **2006,** *7,* 1000–1017. doi:10.1016/j.crhy.2006.10.015
30. Qian, J.; Gao, H. *Acta Biomater.* **2006,** *2,* 51–58. doi:10.1016/j.actbio.2005.08.005
31. Persson, B. N. J.; Mugele, F. *J. Phys.: Condens. Matter* **2004,** *16,* R295–R355. doi:10.1088/0953-8984/16/10/R01

License and Terms

Beilstein Journal of Nanotechnology

Molecular biology approaches in bioadhesion research

Marcelo Rodrigues, Birgit Lengerer, Thomas Ostermann and Peter Ladurner*

Review

Open Access

Address:
University of Innsbruck, Institute of Zoology and Center for Molecular Biosciences Innsbruck, Technikerstraße 25, A-6020 Innsbruck, Austria

Email:
Peter Ladurner* - peter.ladurner@uibk.ac.at

* Corresponding author

Keywords:
bioadhesion; differential gene expression; in situ hybridization; RNA interference; transcriptome

Beilstein J. Nanotechnol. **2014,** *5,* 983–993.
doi:10.3762/bjnano.5.112

Received: 31 December 2013
Accepted: 17 June 2014
Published: 08 July 2014

This article is part of the Thematic Series "Biological and bioinspired adhesion and friction".

Guest Editor: S. N. Gorb

Abstract

The use of molecular biology tools in the field of bioadhesion is still in its infancy. For new research groups who are considering taking a molecular approach, the techniques presented here are essential to unravelling the sequence of a gene, its expression and its biological function. Here we provide an outline for addressing adhesion-related genes in diverse organisms. We show how to gradually narrow down the number of candidate transcripts that are involved in adhesion by (1) generating a transcriptome and a differentially expressed cDNA list enriched for adhesion-related transcripts, (2) setting up a BLAST search facility, (3) perform an in situ hybridization screen, and (4) functional analyses of selected genes by using RNA interference knock-down. Furthermore, latest developments in genome-editing are presented as new tools to study gene function. By using this iterative multi-technologies approach, the identification, isolation, expression and function of adhesion-related genes can be studied in most organisms. These tools will improve our understanding of the diversity of molecules used for adhesion in different organisms and these findings will help to develop innovative bio-inspired adhesives.

Introduction

The capability of an organism to attach to a surface, either temporarily or permanently, is referred to as “bioadhesion”. Bioadhesion occurs in many living organisms that have designed ways to adhere to a range of surfaces [1-3]. Information on how animals solve problems of adhesion in diverse environments can lead to the development of novel bio-inspired adhesives [4] with major applicability in the fields of surface engineering and biomedicine. Molecular biology is helpful in bioadhesion research with respect to the isolation of genes, and the study of their expression and function (Figure 1). Methods in the field have advanced tremendously in recent years, largely due to the recent advances in DNA and RNA sequencing, and

protein analysis. These technologies allow research objectives to move from the analyses of single genes to the study of more complete sets of genes, or to examine all genes that are expressed at once. Now, functional genomics may reveal the transcriptional program of entire genomes by RNA sequencing.

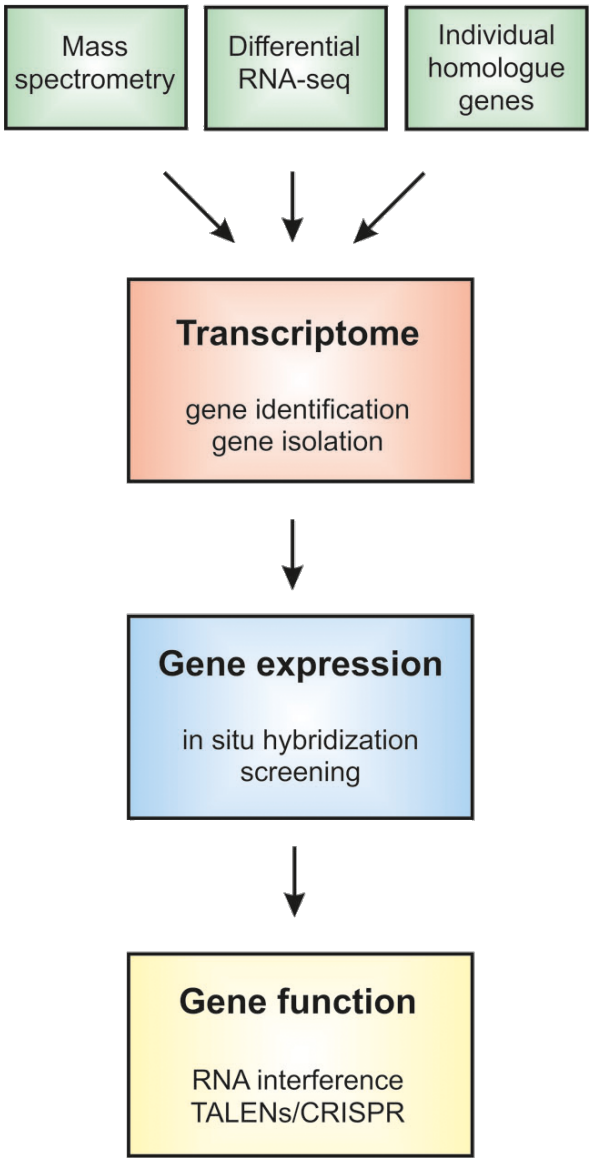

Figure 1: Flowchart showing the transcriptome as a central element to be searched by data generated from various sources, while downstream analyses also rely on the transcriptome.

The recent advances in molecular biology have made available a wide range of research tools and techniques that are of particular interest to researchers working on bioadhesion of organisms where no reference genome exists. Important prerequisites of bioadhesion research are based on techniques such as histology, biochemistry and mechanics [1,3] but gradually certain model systems are entering molecular biology such as mussels [5], barnacles [6,7], sandcastle worms [8], starfishes [9], and flatworms [10]. Efforts to develop bio-inspired adhesives are most effective when guided by a detailed understanding of the key features and mechanisms of natural adhesives [11]. Here, we intend to provide a general outline of cutting-edge methods in molecular biology from which researchers can explore the mechanism of biological adhesion. We know that no single protocol can be applied for every organism. Our goal is to offer a conceptual design of molecular biology tools for experimental analysis ranging from gene identification to gene function in bioadhesion.

The article is divided into three main sections: firstly, we describe the generation of a transcriptome and the use of the differential transcriptome in order to attain the full complement of transcripts (we refer to as bioinformatically assembled hypothetical complementary DNA originating from isolated messenger RNA) expressed in the region of the animal containing adhesive-producing cells; secondly, in situ hybridization (ISH) screening provides the (temporal and) spatial expression of target transcripts; thirdly, RNA interference (RNAi) allows for the elucidation of selected genes by their manipulation in vivo. These tools provide highly detailed molecular information about the adhesive-related proteins. This would impact mainly research on permanent adhesives made up of a combination of carbohydrates and proteins. Indeed, even temporary adhesives that contain a significant carbohydrate fraction usually also rely on proteins for adhesion.

Review

1. Transcriptome sequencing and differential gene expression

1.1 What is a transcriptome?

A transcriptome represents the entirety of RNA molecules expressed in an organism, a tissue or a certain cell type [12-15] (Figure 2). One has to be aware that this collection includes messenger RNA (mRNA), ribosomal RNA (rRNA), transfer RNA (tRNA), and non-coding RNAs [16,17]. For the identification of adhesion-related genes we are mostly interested in mRNA which comprises only 1–5% of all RNAs produced [18].

For simplicity, in the following sections, we refer to "transcriptome" as the full complement of mRNAs of our target organism, tissue or cell type of interest. We have to keep in mind that the representation of mRNAs in the transcriptome experiment depends on the developmental stage of the organism, its environmental condition, and the selected tissue or body region. Finally, after transcriptome sequencing is completed the researcher usually receives a FASTA file containing the cDNA sequences. A BLAST search facility can

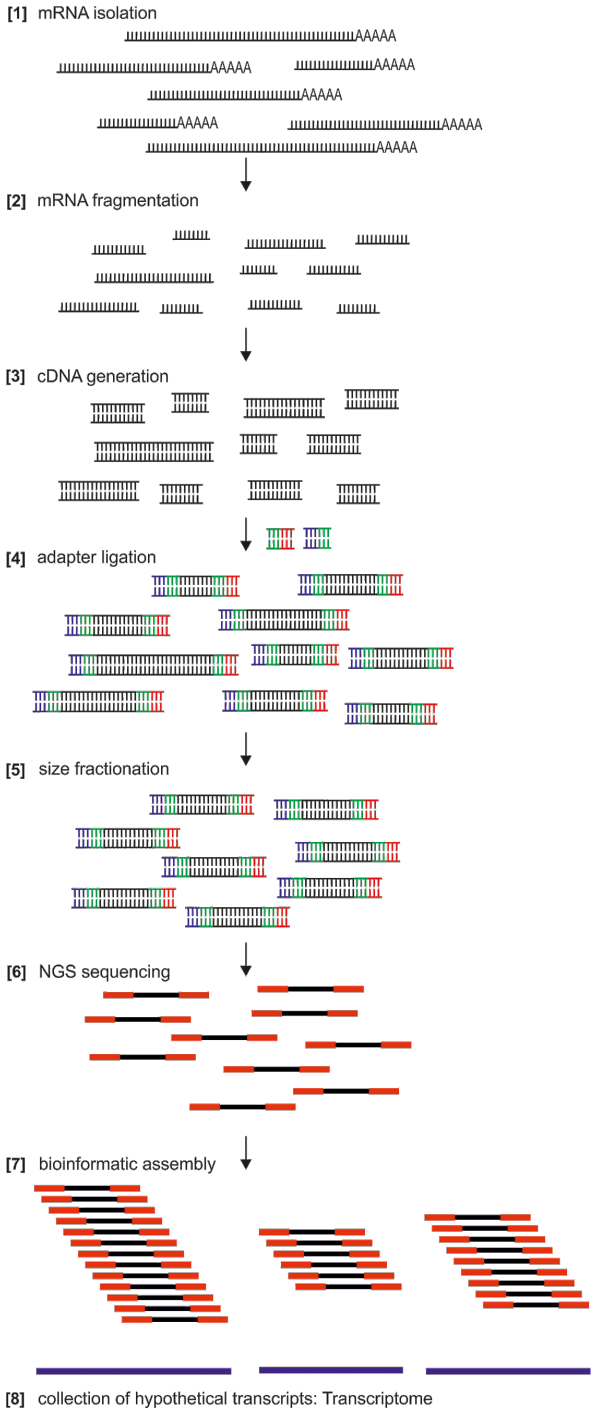

Figure 2: Next generation sequencing (NGS) is a massive sequencing technology, which enables hundreds of gigabases of data to be produced in a single sequencing run. Here, the consecutive steps for the generation of a transcriptome by NGS are illustrated. Depending on the input tissue from which RNA is isolated, a transcriptome of the whole organism or adhesion-related tissue can be generated. See text for details.

be set up (section 2) to search for homologue sequences. The significance of an available transcriptome cannot be overestimated. It can be seen as the cornerstone of downstream applications such as gene isolation, expression studies by ISH (section 3), and functional studies by RNAi (section 4).

1.2 Why transcriptome sequencing?

The identification of proteins involved in the adhesion of an organism will eventually require the isolation of the respective gene. Before next generation sequencing was available, gene isolation proved to be a laborious endeavor. The advent of modern sequencing technologies has changed gene isolation strategies away from approaches, which investigated a single gene at a time, towards an encompassing all-genes-at-once strategy. Therefore, the rationale for performing transcriptome sequencing – commonly referred to as RNA-seq – is based on the relative simplicity, nowadays, of obtaining a substantial collection of transcripts expressed in a specific tissue or an organism [19-23]. Current and future sequencing technologies allow for the generation of the transcriptome of a tissue or an organism of interest with a comparatively low burden on the research budget, and without in-depth bioinformatic expertise on the part of the commissioning researcher. In-house sequencing facilities of universities and institutes as well as commercial service providers will advise on the sequencing strategy. When using current technologies such as Illumina paired-end sequencing, an initial transcriptome will cost no more than a few thousand euros. Such a dataset will provide a reasonable coverage of the transcriptome in question. Depending on the requirement and the research goals, additional data can be produced and added later, e.g., by applying longer-reads strategies, stranded and/or rRNA removed libraries, and libraries of specific tissues.

1.3 Sequencing a transcriptome

With respect to the generation of a transcriptome that contains adhesion related genes of an organism, it can be favorable to only select the tissue that contains the adhesive organs. This can have several advantages: First, it will drastically reduce the complexity of the transcriptome when expressed genes of, e.g., the reproductive organs or the brain are not included. Second, the bioinformatic assembly of such a transcriptome will be facilitated. Third, the costs can be reduced since a higher coverage of bases, i.e., the frequency of how often a base of the transcriptome is sequenced, can more easily be achieved.

For the generation of a transcriptome, the following sequence of steps will usually be necessary (Figure 2): First, total RNA isolation. Sequencing facilities usually prefer to be provided with total RNA of good quality. Current technologies require only small amounts of total RNA (1 µg). Alternatively, tissue flash-frozen in liquid nitrogen and stored at −80 °C could be provided for RNA isolation to be performed at the sequencing facility or the commercial provider. RNA isolation can be

straightforward by using, e.g., Trizol or Tri Reagent procedures according to the manufacturers instructions. However, RNA isolation often requires the mechanical disruption and homogenization of the tissue. Total RNA can be stored at −80 °C and shipped on dry ice to the sequencing facility. The following steps are recommended to be performed at the sequencing facility or the commercial provider (see steps 2–8 of Figure 2): After poly (A) selection, RNA is fragmented into pieces of 200–300 bp and reverse transcribed into complementary DNA (cDNA). Next, sequencing adaptors are ligated by using a standard protocol. Alternatively, strand-specific sequencing can be performed [24,25]. Size range selection is performed (about 200 bp) followed by a PCR based amplification step before the library is subjected to next generation (NGS) sequencing. After the raw reads are obtained, bioinformatic data analysis including de-multiplexing, artefact removal and error correction is carried out [12,14]. Finally, the reads are assembled to hypothetical transcripts, which results in the transcriptome of the selected organism, tissue or cell type. This transcriptome consists of the reconstructed transcripts as simple text (FASTA) file format.

1.4 Differential RNA-seq

RNA-seq is transcriptome sequencing that reveals a quantitative portrait of mRNAs present within a certain tissue and/or at a certain time point. The basic idea behind differential RNA-seq is the comparison of two conditions to identify the differentially expressed genes [19,23,26-30]. For example, in adhesion research we are interested in the identification of transcripts specifically expressed in the adhesive cells or tissue. Therefore, the experiment needs to be designed in a way that allows the tissue to be obtained, both with and without the cells that produce the adhesive proteins. This can be achieved by amputation, regeneration, collection of different developmental stages, or manipulation of the cellular (for instance by RNAi, see section 4) or physiological conditions. Successful collection of the starting material completely relies on an in-depth knowledge of the morphology of the adhesive organ and the respective organism. A recommended starting point would be RNA isolation of biological triplicates (see ENCODE suggestions for RNA-seq: "Standards, Guidelines and Best Practices for RNA-Seq, The ENCODE Consortium") followed by standard sequencing library generation. In contrast to full transcriptome sequencing where we would aim for long paired-end reads to optimize transcriptome assembly, we would choose cheaper short (50 bp) single reads that would then be mapped to the existing transcriptome (Figure 3). The advantage of this strategy is that one does not need to generate an assembled transcriptome for each replicate of each condition, which would require massive paired-end sequencing and bioinformatic effort. Rather, we generate about 10 million 50 bp single reads of each replicate. Several consecutive steps allow for the identification of differentially expressed transcripts (numbering according to Figure 3): (1) sample preparation, (2) isolation of total RNA, (3) preparation of the NGS library, (4) sequencing of each library, (5) bioinformatic mapping of the reads to the corresponding gene of the transcriptome, (6) bioinformatic subtraction of transcript lists, and (7) generation of the candidate transcript list. Commonly we are faced with the following situation (Figure 3): (A) From the control samples containing all cells of the organism, including the adhesive cells, all reads will be mapped to the transcript present in the transcriptome in a quantitative manner, i.e., transcripts that are highly expressed will be sequenced more often and, therefore, a higher number of mapped reads will be obtained. (B) In samples that lack the adhesive cells the mRNAs of the adhesive proteins will not be represented in the library while all other mRNAs of the machinery of a cell will be present. Therefore, in the sample B, no mapped reads will be obtained for the adhesion-related transcripts whereas all other transcripts are covered with the respective short reads. Finally, the collection of transcripts without mapped reads constitutes the adhesive-transcript candidate list – a highly valuable collection of transcripts for downstream applications. Alternatively, (C) samples containing adhesive cells could be extracted. This sample will generate a library that contains all the mRNAs of the adhesive proteins, boosting the comparisons between samples (Figure 3).

2. Creating a local BLAST search facility

2.1 BLAST – basic local alignment search tool

Basic local alignment search tool (BLAST) is a software package to query sequence databases for homologues [31]. Statistical information helps to determine the significance of every alignment. BLAST is widely used to analyze sequencing data and to find candidate genes for further analysis using molecular approaches.

2.2 Establishment of a local BLAST search system

We recommend the software "SequenceServer" (http://www.sequenceserver.com/) to deploy a web-based system to share and query sequence data for similarities [32]. It uses all advantages of recent developments on the NCBI-BLAST+ package [33], is free of charge for academics and has an easy to use web interface.

The setup can be achieved by following the detailed documentation available at the SequenceServer homepage. Briefly, to comply with the requirements a computer or server running a Linux operating system (e.g., Debian GNU Linux; http://www.debian.org/) or MacOS is needed. Besides the NCBI-BLAST+ package, the Ruby scripting language (http://www.ruby-lang.org/) has to be installed. Most Linux distribu-

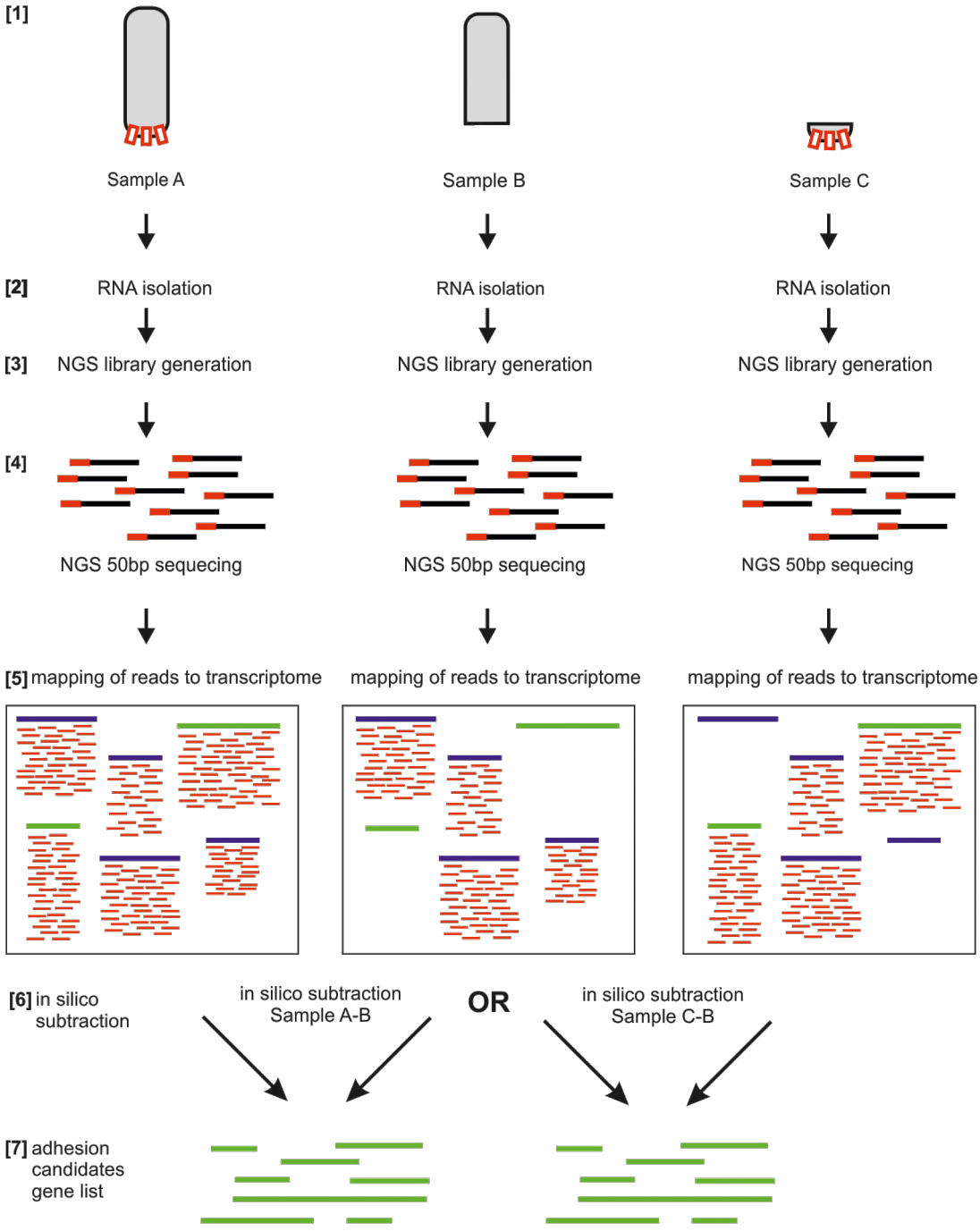

Figure 3: Generation of a differential transcriptome for obtaining a collection of candidate transcript enriched for adhesion-related transcripts. Note that "Sample A" (containing all cells including adhesives cells) minus "Sample B" as well as "Sample C" minus "Sample B" results in an adhesion-enriched candidate transcript list. For small organisms "Sample C" can be difficult to obtain. Therefore, the in silico subtraction of "Sample A" minus "Sample B" is a good option since tissue lacking adhesive organs might be easier to collect. Red rectangles in sample A and C illustrate the adhesive organs in a hypothetical organism. See text for details.

tions perform installation tasks by using a package-management system, e.g., aptitude). SequenceServer setup is performed by the Ruby package management framework rubygems. Further it is needed to define directory-paths to the NCBI-BLAST+ executables and the transcriptome-FASTA-file at the SequenceServer configuration file. SequenceServer is accessible using a web browser immediately after program start, because it uses Ruby's built in webserver Webrick (http://www.ruby-doc.org/stdlib-2.0/libdoc/webrick/rdoc/WEBrick.html).

Finally, any query sequence such as known adhesion-related transcripts of other organisms, mass spectrometry peptide sequences or candidate transcripts originated from a differential RNA-seq experiment can be compared to the established transcriptome database.

3. Spatial gene expression

3.1 Aim of in situ hybridization

For detecting the spatial (and temporal) expression of genes within a tissue, ISH is a widespread and straightforward method. The principle of ISH can be used to detect various types of nucleic acids [34-37]. In this review we will focus on the visualization of specific transcript expression in the form of mRNA in whole mount specimen and tissue sections. ISH provides a powerful tool to map candidate transcripts from a transcriptome dataset to a distinct tissue or cell type. In bioadhesion research, it can be used to identify and validate gene exclusively expressed in adhesion-related cells, like supportive cells [10] or secretory glands [6,38]. The method described below is based on the complementary binding of digoxigenin labelled nucleotide probes to endogenous mRNA [39] (Figure 4).

3.2 In situ hybridization set-up

Several ways to visualize the probes can be utilized – with fluorescent dyes, with alkaline phosphatase, or horseradish peroxidase reactions. We will present a widely used chromogenic visualization method, based on an alkaline phosphate reaction. The first step is the production of single-stranded RNA probes labelled with digoxigenin (DIG) (Figure 4). Gene specific primer pairs are designed and extended at their 5' end with a RNA polymerase T7, T3 or SP6 promoter sequence [40]. Regions for ISH probes must be selected carefully and should not have significant similarities to other endogenous transcripts (BLAST search). The size of the probes should range between 500 and 1000 nucleotides. Shorter probes can lead to weak staining results and/or less specificity. cDNA is used as a template for a standard PCR reaction with the gene-specific primers. The purified PCR product serves as a template for in vitro RNA probe synthesis. Depending on which primer (forward or reverse) the polymerase promoter sequence is located, sense or antisense RNA probes are produced. Antisense probes bind to the target mRNA and should lead to a specific ISH pattern, whereas sense probes are often used as a negative control. Purified RNA probes are stable for months at −80 °C.

For most model organisms standardized protocols for ISH are available [41-47]. To successfully stain other organisms, species-specific adaptations may be required. Critical steps are the fixation and the achievement of permeability of the tissue

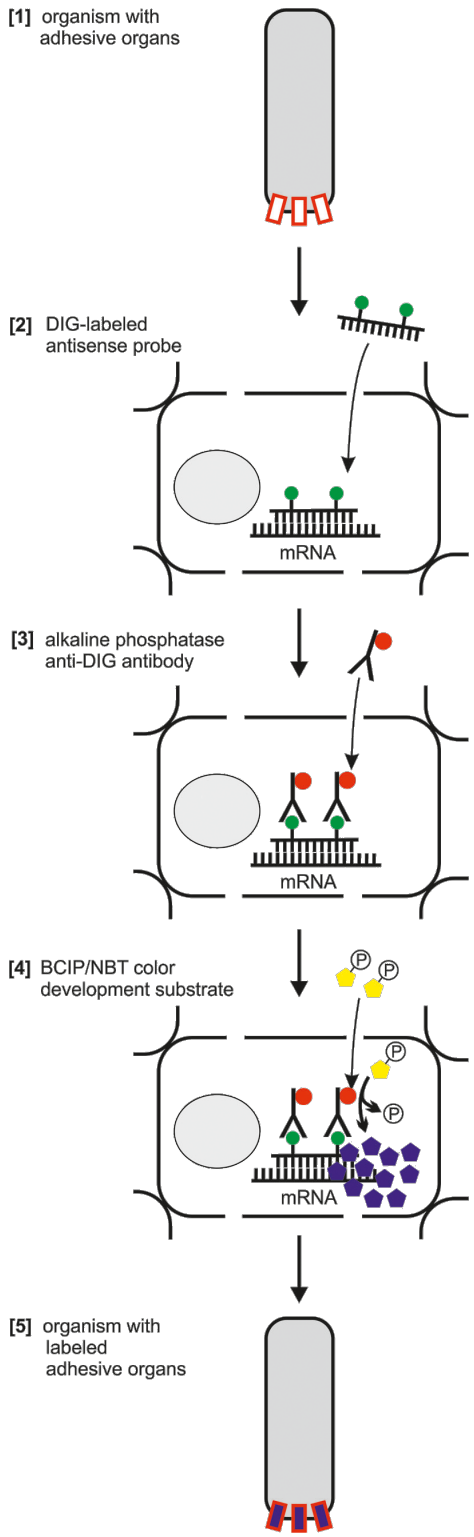

Figure 4: Principle of in situ hybridization. (1) Schematic organism with unstained adhesive organs. (2) The DIG-labelled RNA probe binds to the target mRNA and (3) is detected by an antibody conjugated with a phosphatase. (4) The former colorless substrate becomes dephosphorylated and turns blue. (5) The staining reveals the cells with target gene expression, in this case the adhesive organs.

without losing endogenous mRNA or structural tissue integrity. Usually, good results are achieved with a fixation using 4% paraformaldehyde and proteinase K treatment. Treatment times and concentrations vary depending on tissue hardness and size and must be empirically tested for every tissue. If permeability and transparency cannot be achieved in a whole mount specimen, it may be necessary to perform the ISH on tissue sections [48]. After pre-treatments of the tissue, the DIG-labelled RNA probe is added and hybridized to the complementary mRNA (Figure 4). The hybridization products are then detected with an anti-digoxigenin antibody conjugated to alkaline phosphatase. NBT/BCIP (NBT: nitro blue tretrazolium chloride, BCIP: 5-bromo-4-chloro-3-indolyl phosphate) is a colorless substrate that becomes a blue precipitate when it is dephosphorylated. When added to the samples NBT/BCIP leads to a stable blue staining in cells where the anti-digoxigenin antibody is bound (Figure 4). Endogenous phosphatase activity can lead to a false-positive staining. Therefore, it is essential to inhibit phosphatases during the pretreatments of the tissue and to perform valid negative-control experiments.

3.3 Large-scale expression screening

Once the ISH protocol for an organism is adjusted, it provides a powerful tool to perform large-scale expression screens. For example, it might be necessary to study and validate the expression of an adhesion-related candidate transcript list that resulted from previous mass spectrometry or differential gene expression experiments. For high-throughput approaches, in situ robots such as “InsituPro VSi” from Invatis AG are available. For medium scale ISH screenings, a manual 24-well plate system might be useful [10].

The knowledge of spatial and temporal expression patterns is crucial to elucidate the function of genes during development. Therefore, numerous high-throughput in situ screens have been performed in model organisms from developmental biology such as mouse [40,49-52], chicken [43,53,54], zebrafish [55], medaka fish [56,57], the fruit fly *Drosophila* [47,58], the frog *Xenopus* [59-62] and the ascidian *Ciona intestinalis* [63-66]. These screens demonstrate the potential of large-scale ISH for the discovery of new genes. In bioadhesion research, high-throughput expression analyses can be adapted for the identification of genes exclusively expressed in adhesive organs, providing a straightforward method to discover adhesion-related proteins.

4. Gene function analyses by RNA interference or TALENs/CRISPR

4.1 What is RNA interference?

In order to evaluate whether a transcript that is expressed in the adhesive organs of an animal indeed exhibits a role in adhesion, a functional analysis of the gene and its respective protein is necessary. There are several ways to identify the role of a gene, but RNAi offers a fast and direct way. By means of RNAi the mRNA of the gene of interest is broken down and the corresponding protein cannot be produced anymore. The lack of the protein will lead to a deficiency in the function of the cell (Figure 5). In the case of an adhesion-related protein, this could lead to a non-adhesive phenotype [10]. The degradation of the respective mRNA is achieved by the application of a several hundred base pairs long double-stranded RNA (dsRNA) corresponding to the gene sequence or commercially available and bioinformatically designed 20–25 base pairs (bp) small interfering RNAs (siRNAs).

The dsRNA uptake by the cell and gene knock-down results from a complex and multistep mechanism (Figure 5). The exogenous long dsRNA (usually 200–1000 bp in length) is transported to the cell cytoplasm, where it is recognized by a ribonuclease III-like enzyme (Dicer). The Dicer cleaves this long dsRNA in short fragments of 21–22 bp in length. These short fragments are known as siRNAs. Each siRNA is unwound into two single stranded components: The passenger strand, which is degraded, and the guide strand which is recruited by the RNAi-induced silencing complex (RISC). When the guide strand fits to a given complementary mRNA, a protein which makes part of the RISC, known as Argonaute, cleaves the mRNA resulting in its efficient degradation. To date, a standardized RNAi protocol is still not available for some organisms such as the fruit fly [67,68]. This is not the case for the nematode *Caenorhabditis elegans* [69], or planarians [70-72], for which straightforward RNAi protocols are established. The application of RNAi is limited by the efficiency of the uptake of dsRNA, which differs for different genes, organisms and developmental stages. Therefore, preliminary studies are required. RNAi is currently available in a range of different methodologies and is widely used for functional analysis in cellular, animal [73], and genome-wide studies [68,74]. In the context of bioadhesion research, RNAi might also be applied to check if the selected adhesion-related transcripts are actually carrying out the expected function.

4.2 The RNA interference experiment

The first step is the synthesis of the dsRNA. The full-length gene is usually not used for dsRNA synthesis (Figure 5), rather gene-specific sequences between 200 bp to 1000 bp are chosen. Special attention should be paid to the selection of the sequence of the transcript to be knocked-down and highly conserved domains that could also be present in other genes should be avoided. Therefore, for long dsRNA synthesis the sequence identity and uniqueness to the target transcript of the organism needs to be verified [67,68,75-77]. In order to generate the

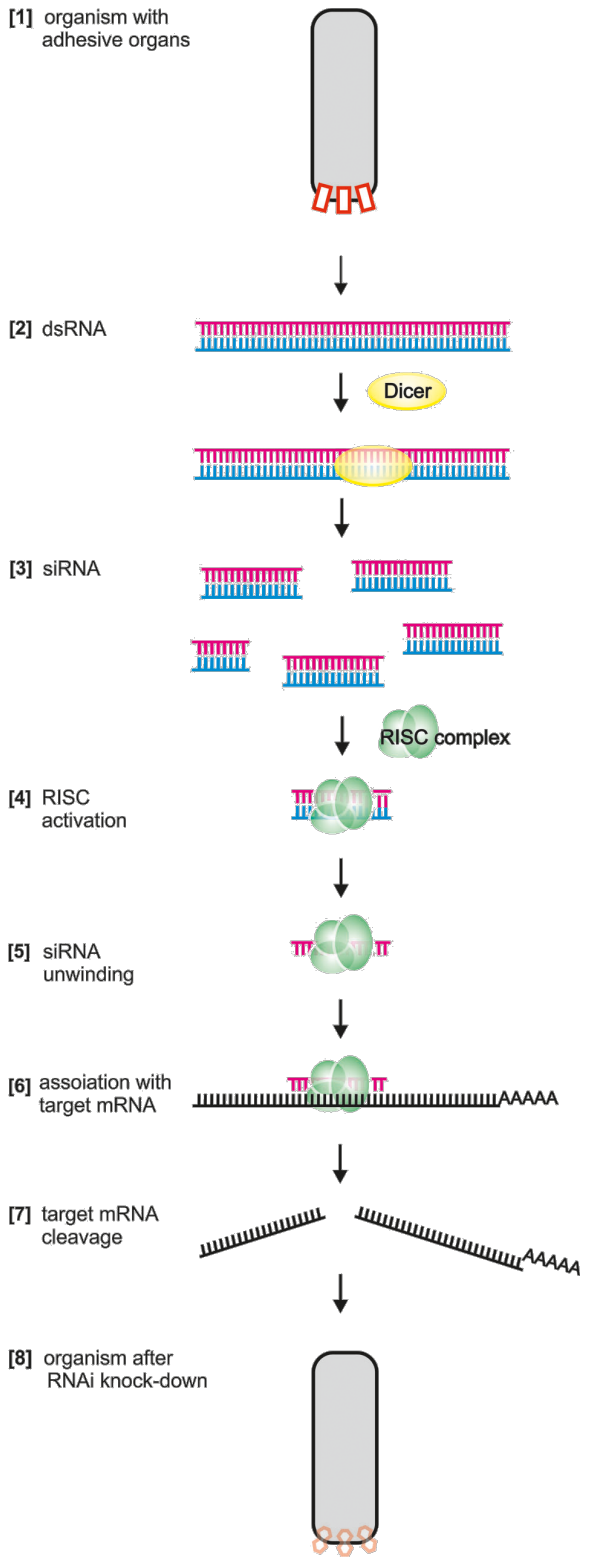

Figure 5: Functional analyses of an adhesion-related gene by RNAi. After the application of dsRNA the mRNA gets degraded. The lack of the corresponding protein affects the function of the adhesive structure and the organism is unable to attach if an essential adhesion-related gene has been targeted. See text for details.

dsRNA, we have frequently used the same primers with which ISH was previously performed. Templates can be generated by standard PCR amplification from cDNA, but this time, with the addition of a RNA polymerase promoter (T7, T3, or SP6) to the 5′ end of both primers (forward and reverse). It is highly recommended to clone and sequence the amplified fragments, however, for a high-throughput screening, the amplified PCR fragments might be used directly and verified only if an interesting phenotype is observed. Following PCR amplification a transcription reaction is performed in two independent reactions to synthesize the two complementary RNA transcripts from the template. Several commercial kits for RNA synthesis are available and can be used according to the manufacturer's instructions [78-81]. After annealing the RNA strands by in vitro transcription to form the dsRNA, the DNA and single-stranded RNA are removed through a nuclease digestion. After purification, dsRNA is checked for quality and concentration. Finally, aliquots containing the desirable concentrations of dsRNA can be stored at −80 °C or directly used for RNAi experiments.

The dsRNA can be delivered to the target organism by a variety of methods; the most common are soaking, ingestion and injection. In several aquatic organisms like *Hydra*, flatworms, planarians, nematodes, and shrimps, feeding or soaking are the most straightforward methodologies for delivering dsRNA. The organisms have to be immersed in a medium containing dsRNA. Another strategy is ingestion, by inducing target organisms to feed on other organisms like bacteria expressing the desirable dsRNA [69,82-84], or transgenic plants for feeding insects [85]. Also the combination of methods like the enrichment of natural diets, for example, liver paste and *Artemia* enriched with engineered bacteria to feed planarians and *Hydra* [72,86]. Lastly, microinjection has been applied in several species, like the harvestmen Opiliones [87] and tardigrades [88]. The suitability of each delivery method depends on the organism being studied. Experimental animals should be incubated or injected with dsRNA solution for an appropriate period of time. The incubation time is extremely variable and is dependent on cell turnover in the target tissue. Gene knock-down in biological adhesion has been achieved by using in vitro designed long dsRNA in the flatworm *Macrostomum lignano* [10].

Importantly, control experiments should include an RNAi molecule against a heterologous sequence absent from the genome of the target organism. For example, in the flatworm *M. lignano* a dsRNA of the firefly luciferase sequence of 1002 bp was used as negative control [78,80,81,89]. Regarding the validation of experiments, quantitative real-time PCR is the most straightforward way to direct evaluate if the mRNA was in fact knocked

down. Also, ISH against the target mRNA could provide a representation of the results when comparing treated samples and controls, albeit not in a quantitative manner.

4.3 New approaches: TALENs and CRISPR

Genome editing technologies offer a potential tool for bioadhesion research. The central idea is to specifically mutate the genomic region of the gene of interest to inhibit the production of functional mRNA and protein. While RNAi experiments are a robust and useful tool, the results of these experiments are temporary, preventing longer-term evaluations. Traditionally, zincfinger nucleases have been used for genome editing [90] but they have limitations in the freedom to select a particular genomic region, and they are expensive. Recently, two customised genome editors have become available and these have gained acceptance from the scientific community. First, the transcription activator like effector nucleases (TALENs) [91,92], cause the fusion of DNA binding domains derived from TALE proteins with the *Fok*I restriction endonuclease. Basically, TALENs induce DNA double-stranded breaks that stimulate the cellular DNA repair mechanisms enabling custom modifications [91,93]. The second genome editor is the clustered regulatory interspaced short palindromic repeat (CRISPR/Cas) [94-97], which uses a guide RNA and a protein called Cas9 endonuclease to enable a sequence-specific cleavage of homologous target double-stranded DNA. Both TALENs and CRISPR/cas genome-editing tools allow for gene knock-out, knock-in (when a desired gene is inserted) or the modification of genes, and represent a powerful method capable of providing conclusive information for evaluating gene function. However, these technologies require genomic information of the target organism or the gene of interest. Also, the microinjection delivering system in single-cell embryos are compulsory for these technologies. Nevertheless, TALENs and CRISPR appear to work in principle in most organisms and might be a useful tool to study gene function in diverse organisms.

Conclusion

The identification of adhesion-related genes and proteins is a challenging task. Certain organisms allow the collection of the glue and direct analyses by mass spectrometry or biochemistry. Small organisms can exhibit remarkable adhesive performance but their tiny size impedes the direct collection of the glue. Therefore, other approaches are necessary for identifying adhesive molecules. A molecular biological approach provides the means to identify adhesion-related transcripts in these organisms and allows their expression and function to be studied. Nowadays, even a small research group can use high-throughput sequencing platforms to generate a transcriptome of an organism. Differential gene expression can be highly useful to narrow down the number of candidate transcripts. In order to further confirm the expression of genes of the candidate list – which can also be derived from a mass spectrometry experiment – ISH needs to be employed. Next, the possible role of an adhesion-candidate transcript can be studied by adapting gene knock-down using RNAi or gene knock-out by TALENs or CRISPR for the respective organism. The need for new strategies in adhesion research demands efforts in key molecular biology technologies. Enhancing our ability to understand in vivo adhesive molecules is essential for exploring biomimetic approaches to synthesising new adhesive products. A molecular biology approach can help to facilitate the search for new adhesives across the animal phyla.

Acknowledgements

This work was supported by Austrian Science Fund (FWF): [P 25404-B25] to PL and COST Action TD 0906. MR is a recipient of a Marie-Curie FP7-PEOPLE-2013-IEF 626525 and BL of a DOC Fellowship of the Austrian Academy of Sciences ÖAW DOC 24020.

References

1. Smith, A. M.; Callow, J. A., Eds. *Biological Adhesives;* Springer-Verlag: Berlin, Heidelberg, 2007.
2. Gorb, S., Ed. *Adhesion and Friction in Biological Systems;* Springer, 2011.
3. von Byern, J.; Grunwald, I., Eds. *Biological Adhesive Systems: From Nature to Technical and Medical Application;* Springer: Vienna, Austria, 2011.
4. Yang, S. Y.; O'Cearbhaill, E. D.; Sisk, G. C.; Park, K. M.; Cho, W. K.; Villiger, M.; Bouma, B. E.; Pomahac, B.; Karp, J. M. *Nat. Commun.* **2013,** *4,* No. 1702. doi:10.1038/ncomms2715
5. Bai, Z.; Zheng, H.; Lin, J.; Wang, G.; Li, J. *PLoS One* **2013,** *8,* e53617. doi:10.1371/journal.pone.0053617
6. Chen, Z.-F.; Matsumura, K.; Wang, H.; Arellano, S. M.; Yan, X.; Alam, I.; Archer, J. A. C.; Bajic, V. B.; Qian, P.-Y. *PLoS One* **2011,** *6,* e22913. doi:10.1371/journal.pone.0022913
7. Lin, H.-C.; Wong, Y. H.; Tsang, L. M.; Chu, K. H.; Qian, P.-Y.; Chan, B. K. K. *Biofouling* **2014,** *30,* 169–181. doi:10.1080/08927014.2013.853051
8. Endrizzi, B. J.; Stewart, R. J. *J. Adhes.* **2009,** *85,* 546–559. doi:10.1080/00218460902996457
9. Hennebert, E.; Wattiez, R.; Waite, J. H.; Flammang, P. *Biofouling* **2012,** *28,* 289–303. doi:10.1080/08927014.2012.672645
10. Lengerer, B.; Pjeta, R.; Wunderer, J.; Rodrigues, M.; Arbore, R.; Schärer, L.; Berezikov, E.; Hess, M. W.; Pfaller, K.; Egger, B.; Obwegeser, S.; Salvenmoser, W.; Ladurner, P. *Front. Zool.* **2014,** *11,* No. 12. doi:10.1186/1742-9994-11-12
11. Stewart, R. J. *Appl. Microbiol. Biotechnol.* **2011,** *89,* 27–33. doi:10.1007/s00253-010-2913-8
12. Wilhelm, B. T.; Landry, J.-R. *Methods* **2009,** *48,* 249–257. doi:10.1016/j.ymeth.2009.03.016
13. Wang, Z.; Gerstein, M.; Snyder, M. *Nat. Rev. Genet.* **2009,** *10,* 57–63. doi:10.1038/nrg2484
14. McGettigan, P. A. *Curr. Opin. Chem. Biol.* **2013,** *17,* 4–11. doi:10.1016/j.cbpa.2012.12.008

15. Mutz, K.-O.; Heilkenbrinker, A.; Lönne, M.; Walter, J.-G.; Stahl, F. *Curr. Opin. Biotechnol.* **2013,** *24,* 22–30. doi:10.1016/j.copbio.2012.09.004
16. Atkins, J. F.; Gesteland, R. F.; Cech, T. R. *RNA Worlds: From Life's Origins to Diversity in Gene Regulation;* Cold Spring Harbor Laboratory Press: New York, 2011.
17. Elliott, D. *Molecular Biology of RNA;* Oxford University Press: Hampshire, U.K., 2011.
18. Darnell, J. *RNA: Life's Indispensable Molecule,* 1st ed.; Cold Spring Harbor Laboratory Press: New York, 2011.
19. Martin, J. A.; Wang, Z. *Nat. Rev. Genet.* **2011,** *12,* 671–682. doi:10.1038/nrg3068
20. Lovén, J.; Orlando, D. A.; Sigova, A. A.; Lin, C. Y.; Rahl, P. B.; Burge, C. B.; Levens, D. L.; Lee, T. I.; Young, R. A. *Cell* **2012,** *151,* 476–482. doi:10.1016/j.cell.2012.10.012
21. Strickler, S. R.; Bombarely, A.; Mueller, L. A. *Am. J. Bot.* **2012,** *99,* 257–266. doi:10.3732/ajb.1100292
22. Liu, Y.; Zhou, J.; White, K. P. *Bioinformatics* **2014,** *30,* 301–304. doi:10.1093/bioinformatics/btt688
23. Van Verk, M. C.; Hickman, R.; Pieterse, C. M. J.; Van Wees, S. C. M. *Trends Plant Sci.* **2013,** *18,* 175–179. doi:10.1016/j.tplants.2013.02.001
24. Levin, J. Z.; Yassour, M.; Adiconis, X.; Nusbaum, C.; Thompson, D. A.; Friedman, N.; Gnirke, A.; Regev, A. *Nat. Methods* **2010,** *7,* 709–715. doi:10.1038/nmeth.1491
25. Borodina, T.; Adjaye, J.; Sultan, M. *Methods Enzymol.* **2011,** *500,* 79–98. doi:10.1016/B978-0-12-385118-5.00005-0
26. Oshlack, A.; Robinson, M. D.; Young, M. D. *Genome Biol.* **2010,** *11,* No. 220. doi:10.1186/gb-2010-11-12-220
27. Tarazona, S.; Garcia-Alcalde, F.; Dopazo, J.; Ferrer, A.; Conesa, A. *Genome Res.* **2011,** *21,* 2213–2223. doi:10.1101/gr.124321.111
28. Kao, D.; Felix, D.; Aboobaker, A. *BMC Genomics* **2013,** *14,* No. 797. doi:10.1186/1471-2164-14-797
29. Soneson, C.; Delorenzi, M. *BMC Bioinf.* **2013,** *14,* No. 91. doi:10.1186/1471-2105-14-91
30. Trapnell, C.; Hendrickson, D. G.; Sauvageau, M.; Goff, L.; Rinn, J. L.; Pachter, L. *Nat. Biotechnol.* **2013,** *31,* 46–53. doi:10.1038/nbt.2450
31. Altschul, S. F.; Gish, W.; Miller, W.; Myers, E. W.; Lipman, D. J. *J. Mol. Biol.* **1990,** *215,* 403–410. doi:10.1016/S0022-2836(05)80360-2
32. Priyam, A.; Woodcroft, B. J.; Wurm, Y. *In preparation.*
33. Camacho, C.; Coulouris, G.; Avagyan, V.; Ma, N.; Papadopoulus, J.; Bealer, K.; Madden, T. L. *BMC Bioinf.* **2009,** *10,* No. 421. doi:10.1186/1471-2105-10-421
34. Jiang, J.; Gill, B. S. *Genome* **2006,** *49,* 1057–1068. doi:10.1139/g06-076
35. de Planell-Saguer, M.; Rodicio, M. C.; Mourelatos, Z. *Nat. Protoc.* **2010,** *5,* 1061–1073. doi:10.1038/nprot.2010.62
36. Javelle, M.; Timmermans, M. C. P. *Nat. Protoc.* **2012,** *7,* 533–541. doi:10.1038/nprot.2012.006
37. Chen, A. Y.-Y.; Chen, A. *J. Invest. Dermatol.* **2013,** *133,* e8. doi:10.1038/jid.2013.120
38. Wang, C. S.; Stewart, R. J. *J. Exp. Biol.* **2012,** *215,* 351–361. doi:10.1242/jeb.065011
39. Tautz, D.; Pfeifle, C. *Chromosoma* **1989,** *98,* 81–85. doi:10.1007/BF00291041
40. Eichele, G.; Diez-Roux, G. *Methods* **2011,** *53,* 417–423. doi:10.1016/j.ymeth.2010.12.020
41. Satou, Y.; Takatori, N.; Yamada, L.; Mochizuki, Y.; Hamaguchi, M.; Ishikawa, H.; Chiba, S.; Imai, K.; Kano, S. *Development* **2001,** *128,* 2893–2904.
42. Hargrave, M.; Bowles, J.; Koopman, P. *Methods Mol. Biol. (N. Y., NY, U. S.)* **2006,** *326,* 103–113. doi:10.1385/1-59745-007-3:103
43. Darnell, D. K.; Kaur, S.; Stanislaw, S.; Davey, S.; Konieczka, J. H.; Yatskievych, T. A.; Antin, P. B. *Cytogenet. Genome Res.* **2007,** *117,* 30–35. doi:10.1159/000103162
44. Jones, C. M.; Smith, J. C. *Methods Mol. Biol. (N. Y., NY, U. S.)* **2008,** *461,* 697–702. doi:10.1007/978-1-60327-483-8_47
45. Thisse, C.; Thisse, B. *Nat. Protoc.* **2008,** *3,* 59–69. doi:10.1038/nprot.2007.514
46. Pearson, B. J.; Eisenhoffer, G. T.; Gurley, K. A.; Rink, J. C.; Miller, D. E.; Sánchez Alvarado, A. *Dev. Dyn.* **2009,** *238,* 443–450. doi:10.1002/dvdy.21849
47. Weiszmann, R.; Hammonds, A. S.; Celniker, S. E. *Nat. Protoc.* **2009,** *4,* 605–618. doi:10.1038/nprot.2009.55
48. Tsai, C.-J.; Harding, S. A. *Methods Cell Biol.* **2013,** *113,* 339–359. doi:10.1016/B978-0-12-407239-8.00016-1
49. Neidhardt, L.; Gasca, S.; Wertz, K.; Obermayr, F.; Worpenberg, S.; Lehrach, H.; Hermann, B. G. *Mech. Dev.* **2000,** *98,* 77–93. doi:10.1016/S0925-4773(00)00453-6
50. Yoshikawa, T.; Piao, Y.; Zhong, J.; Matoba, R.; Carter, M. G.; Wang, Y.; Goldberg, I.; Ko, M. S. H. *Gene Expression Patterns* **2006,** *6,* 213–224. doi:10.1016/j.modgep.2005.06.003
51. Lein, E. S.; Hawrylycz, M. J.; Ao, N.; et al. *Nature* **2007,** *445,* 168–176. doi:10.1038/nature05453
52. Visel, A.; Carson, J.; Oldekamp, J.; Warnecke, M.; Jakubcakova, V.; Zhou, X.; Shaw, C. A.; Alvarez-Bolado, G.; Eichele, G. *PLoS Genet.* **2007,** *3,* e178. doi:10.1371/journal.pgen.0030178
53. Thut, C. J.; Rountree, R. B.; Hwa, M.; Kingsley, D. M. *Dev. Biol.* **2001,** *231,* 63–76. doi:10.1006/dbio.2000.0140
54. Bell, G. W.; Yatskievych, T. A.; Antin, P. B. *Dev. Dyn.* **2004,** *229,* 677–687. doi:10.1002/dvdy.10503
55. Bertrand, S.; Thisse, B.; Tavares, R.; Sachs, L.; Chaumot, A.; Bardet, P.-L.; Escrivà, H.; Duffraisse, M.; Marchand, O.; Safi, R.; Thisse, C.; Laudet, V. *PLoS Genet.* **2007,** *3,* e188. doi:10.1371/journal.pgen.0030188
56. Quiring, R.; Wittbrodt, B.; Henrich, T.; Ramialison, M.; Burgtorf, C.; Lehrach, H.; Wittbrodt, J. *Mech. Dev.* **2004,** *121,* 971–976. doi:10.1016/j.mod.2004.03.031
57. Deyts, C.; Candal, E.; Joly, J.-S.; Bourrat, F. *Dev. Dyn.* **2005,** *234,* 698–708. doi:10.1002/dvdy.20465
58. Tomancak, P.; Beaton, A.; Weiszmann, R.; Kwan, E.; Shu, S.; Lewis, S. E.; Richards, S.; Ashburner, M.; Hartenstein, V.; Celniker, S. E.; Rubin, G. M. *Genome Biol.* **2002,** *3,* RESEARCH0088. doi:10.1186/gb-2002-3-12-research0088
59. Pollet, N.; Niehrs, C. *Methods Mol. Biol. (N. Y., NY, U. S.)* **2001,** *175,* 309–321. doi:10.1385/1-59259-235-X:309
60. Thisse, B.; Heyer, V.; Lux, A.; Alunni, V.; Degrave, A.; Seiliez, I.; Kirchner, J.; Parkhill, J.-P.; Thisse, C. *Methods Cell Biol.* **2004,** *77,* 505–519. doi:10.1016/S0091-679X(04)77027-2
61. Pollet, N.; Muncke, N.; Verbeeck, B.; Li, Y.; Fenger, U.; Delius, H.; Niehrs, C. *Mech. Dev.* **2005,** *122,* 365–439. doi:10.1016/j.mod.2004.11.009
62. Parain, K.; Mazurier, N.; Bronchain, O.; Borday, C.; Cabochette, P.; Chesneau, A.; Colozza, G.; El Yakoubi, W.; Hamdache, J.; Locker, M.; Gilchrist, M. J.; Pollet, N.; Perron, M. *Dev. Neurobiol.* **2012,** *72,* 491–506. doi:10.1002/dneu.20973
63. Imai, K. S.; Hino, K.; Yagi, K.; Satoh, N.; Satou, Y. *Development* **2004,** *131,* 4047–4058. doi:10.1242/dev.01270

64. Imai, K. S.; Levine, M.; Satoh, N.; Satou, Y. *Science* **2006,** *312,* 1183–1187. doi:10.1126/science.1123404
65. Miwata, K.; Chiba, T.; Horii, R.; Yamada, L.; Kubo, A.; Miyamura, D.; Satoh, N.; Satou, Y. *Dev. Biol.* **2006,** *292,* 546–554. doi:10.1016/j.ydbio.2006.01.024
66. Kobayashi, K.; Yamada, L.; Satou, Y.; Satoh, N. *Genesis* **2013,** *51,* 647–659. doi:10.1002/dvg.22413
67. Miller, S. C.; Miyata, K.; Brown, S. J.; Tomoyasu, Y. *PLoS One* **2012,** *7,* e47431. doi:10.1371/journal.pone.0047431
68. Li, H.; Jiang, W.; Zhang, Z.; Xing, Y.; Li, F. *PLoS One* **2013,** *8,* e65931. doi:10.1371/journal.pone.0065931
69. McEwan, D. L.; Weisman, A. S.; Hunter, C. P. *Mol. Cell* **2012,** *47,* 746–754. doi:10.1016/j.molcel.2012.07.014
70. Wang, Y.; Stary, J. M.; Wilhelm, J. E.; Newmark, P. A. *Genes Dev.* **2010,** *24,* 2081–2092. doi:10.1101/gad.1951010
71. Forsthoefel, D. J.; James, N. P.; Escobar, D. J.; Stary, J. M.; Vieira, A. P.; Waters, F. A.; Newmark, P. A. *Dev. Cell* **2012,** *23,* 691–704. doi:10.1016/j.devcel.2012.09.008
72. Rouhana, L.; Weiss, J. A.; Forsthoefel, D. J.; Lee, H.; King, R. S.; Inoue, T.; Shibata, N.; Agata, K.; Newmark, P. A. *Dev. Dyn.* **2013,** *242,* 718–730. doi:10.1002/dvdy.23950
73. Mohr, S. E.; Perrimon, N. *Wiley Interdiscip. Rev.: RNA* **2012,** *3,* 145–158. doi:10.1002/wrna.110
74. Mohr, S.; Bakal, C.; Perrimon, N. *Annu. Rev. Biochem.* **2010,** *79,* 37–64. doi:10.1146/annurev-biochem-060408-092949
75. Reynolds, A.; Leake, D.; Boese, Q.; Scaringe, S.; Marshall, W. S.; Khvorova, A. *Nat. Biotechnol.* **2004,** *22,* 326–330. doi:10.1038/nbt936
76. Whangbo, J. S.; Hunter, C. P. *Trends Genet.* **2008,** *24,* 297–305. doi:10.1016/j.tig.2008.03.007
77. Huvenne, H.; Smagghe, G. *J. Insect Physiol.* **2010,** *56,* 227–235. doi:10.1016/j.jinsphys.2009.10.004
78. Pfister, D.; De Mulder, K.; Hartenstein, V.; Kuales, G.; Borgonie, G.; Marx, F.; Morris, J.; Ladurner, P. *Dev. Biol.* **2008,** *319,* 146–159. doi:10.1016/j.ydbio.2008.02.045
79. De Mulder, K.; Kuales, G.; Pfister, D.; Willems, M.; Egger, B.; Salvenmoser, W.; Thaler, M.; Gorny, A.-K.; Hrouda, M.; Borgonie, G.; Ladurner, P. *BMC Dev. Biol.* **2009,** *9,* No. 89. doi:10.1186/1471-213X-9-69
80. De Mulder, K.; Pfister, D.; Kuales, G.; Egger, B.; Salvenmoser, W.; Willems, M.; Steger, J.; Fauster, K.; Micura, R.; Borgonie, G.; Ladurner, P. *Dev. Biol.* **2009,** *334,* 198–212. doi:10.1016/j.ydbio.2009.07.019
81. Kuales, G.; De Mulder, K.; Glashauser, J.; Salvenmoser, W.; Takashima, S.; Hartenstein, V.; Berezikov, E.; Salzburger, W.; Ladurner, P. *Dev. Biol.* **2011,** *357,* 117–132. doi:10.1016/j.ydbio.2011.06.030
82. Fire, A.; Xu, S.; Montgomery, M. K.; Kostas, S. A.; Driver, S. E.; Mello, C. C. *Nature* **1998,** *391,* 806–811. doi:10.1038/35888
83. Hinas, A.; Wright, A. J.; Hunter, C. P. *Curr. Biol.* **2012,** *22,* 1938–1943. doi:10.1016/j.cub.2012.08.020
84. Jose, A. M.; Kim, Y. A.; Leal-Ekman, S.; Hunter, C. P. *Proc. Natl. Acad. Sci. U. S. A.* **2012,** *109,* 14520–14525. doi:10.1073/pnas.1201153109
85. Mao, Y.-B.; Cai, W.-J.; Wang, J.-W.; Hong, G.-J.; Tao, X.-Y.; Wang, L.-J.; Huang, Y.-P.; Chen, X.-Y. *Nat. Biotechnol.* **2007,** *25,* 1307–1313. doi:10.1038/nbt1352
86. Chera, S.; de Rosa, R.; Miljkovic-Licina, M.; Dobretz, K.; Ghila, L.; Kaloulis, K.; Galliot, B. *J. Cell Sci.* **2006,** *119,* 846–857. doi:10.1242/jcs.02807
87. Sharma, P. P.; Schwager, E. E.; Giribet, G.; Jockusch, E. L.; Extravour, C. G. *Evol. Dev.* **2013,** *15,* 228–242. doi:10.1111/ede.12029
88. Tenlen, J. R.; McCaskill, S.; Goldstein, B. *Dev. Genes Evol.* **2013,** *223,* 171–181. doi:10.1007/s00427-012-0432-6
89. Sekii, K.; Salvenmoser, W.; De Mulder, K.; Scharer, L.; Ladurner, P. *BMC Dev. Biol.* **2009,** *9,* No. 62. doi:10.1186/1471-213X-9-62
90. Wood, A. J.; Lo, T.-W.; Zeitler, B.; Pickle, C. S.; Ralston, E. J.; Lee, A. H.; Amora, R.; Miller, J. C.; Leung, E.; Meng, X.; Zhang, L.; Rebar, E. J.; Gregory, P. D.; Urnov, F. D.; Meyer, B. J. *Science* **2011,** *333,* 307. doi:10.1126/science.1207773
91. Miller, J. C.; Tan, S.; Qiao, G.; Barlow, K. A.; Wang, J.; Xia, D. F.; Meng, X.; Paschon, D. E.; Leung, E.; Hinkley, S. J.; Dulay, G. P.; Hua, K. L.; Ankoudinova, I.; Cost, G. J.; Urnov, F. D.; Zhang, H. S.; Holmes, M. C.; Zhang, L.; Gregory, P. D.; Rebar, E. J. *Nat. Biotechnol.* **2011,** *29,* 143–148. doi:10.1038/nbt.1755
92. Mussolino, C.; Morbitzer, R.; Lütge, F.; Dannemann, N.; Lahaye, T.; Cathomen, T. *Nucleic Acids Res.* **2011,** *39,* 9283–9293. doi:10.1093/nar/gkr597
93. Mussolino, C.; Cathomen, T. *Curr. Opin. Biotechnol.* **2012,** *23,* 644–650. doi:10.1016/j.copbio.2012.01.013
94. Wiedenheft, B.; Sternberg, S. H.; Doudna, J. A. *Nature* **2012,** *482,* 331–338. doi:10.1038/nature10886
95. Cong, L.; Ran, F. A.; Cox, D.; Lin, S.; Barretto, R.; Habib, N.; Hsu, P. D.; Wu, X.; Jiang, W.; Marraffini, L. A.; Zhang, F. *Science* **2013,** *339,* 819–823. doi:10.1126/science.1231143
96. Friedland, A. E.; Tzur, Y. B.; Esvelt, K. M.; Colaiácovo, M. P.; Church, G. M.; Calarco, J. A. *Nat. Methods* **2013,** *10,* 741–743. doi:10.1038/nmeth.2532
97. Mali, P.; Yang, L.; Esvelt, K. M.; Aach, J.; Guell, M.; DiCarlo, J. E.; Norville, J. E.; Church, G. M. *Science* **2013,** *339,* 823–826. doi:10.1126/science.1232033

License and Terms

BEILSTEIN JOURNAL OF NANOTECHNOLOGY

Insect attachment on crystalline bioinspired wax surfaces formed by alkanes of varying chain lengths

Elena Gorb*[1], Sandro Böhm[1], Nadine Jacky[1], Louis-Philippe Maier[1], Kirstin Dening[1], Sasha Pechook[2], Boaz Pokroy[2] and Stanislav Gorb[1]

Full Research Paper

Open Access

Address:
[1]Department of Functional Morphology and Biomechanics, Zoological Institute, Kiel University, Am Botanischen Garten 9, D-24098 Kiel, Germany and [2]Department of Material Science and Engineering and the Russell Berrie Nanotechnology Institute, Technion – Israel Institute of Technology, 32000 Haifa, Israel

Email:
Elena Gorb* - egorb@zoologie.uni-kiel.de

* Corresponding author

Keywords:
Coccinella septempunctata; insect–plant interactions; plant waxes; pull-off force; traction force

Beilstein J. Nanotechnol. **2014,** *5,* 1031–1041.
doi:10.3762/bjnano.5.116

Received: 31 March 2014
Accepted: 18 June 2014
Published: 14 July 2014

This article is part of the Thematic Series "Biological and bioinspired adhesion and friction".

Associate Editor: K. Koch

Abstract

The impeding effect of plant surfaces covered with three-dimensional wax on attachment and locomotion of insects has been shown previously in numerous experimental studies. The aim of this study was to examine the effect of different parameters of crystalline wax coverage on insect attachment. We performed traction experiments with the beetle *Coccinella septempunctata* and pull-off force measurements with artificial adhesive systems (tacky polydimethylsiloxane semi-spheres) on bioinspired wax surfaces formed by four alkanes of varying chain lengths ($C_{36}H_{74}$, $C_{40}H_{82}$, $C_{44}H_{90}$, and $C_{50}H_{102}$). All these highly hydrophobic coatings were composed of crystals having similar morphologies but differing in size and distribution/density, and exhibited different surface roughness. The crystal size (length and thickness) decreased with an increase of the chain length of the alkanes that formed these surfaces, whereas the density of the wax coverage, as well as the surface roughness, showed an opposite relationship. Traction tests demonstrated a significant, up to 30 fold, reduction of insect attachment forces on the wax surfaces when compared with the reference glass sample. Attachment of the beetles to the wax substrates probably relied solely on the performance of adhesive pads. We found no influence of the wax coatings on the subsequent attachment ability of beetles. The obtained data are explained by the reduction of the real contact between the setal tips of the insect adhesive pads and the wax surfaces due to the micro- and nanoscopic roughness introduced by wax crystals. Experiments with polydimethylsiloxane semi-spheres showed much higher forces on wax samples when compared to insect attachment forces measured on these surfaces. We explain these results by the differences in material properties between polydimethylsiloxane probes and tenent setae of *C. septempunctata* beetles. Among wax surfaces, force experiments showed stronger insect attachment and higher pull-off forces of polydimethylsiloxane probes on wax surfaces having a higher density of wax coverage, created by smaller crystals.

Introduction

During their locomotion, insects use different structures for attachment, depending on the texture of the substrate. They usually apply their claws to interlock with surface irregularities on rough surfaces, when the diameter of the claw tip is smaller than the dimensions of typical surface asperities or cavities [1]. On smooth and microrough substrates, many insects use highly specialised adhesive pads, which may be located on different parts of the leg and are of two different types: smooth and setose (hairy) [2,3]. Due to the material flexibility of smooth pads and fine fibrillar surface microstructures (tenent setae) that cover hairy pads, both pad types can maximize the possible contact area with various substrate profiles (reviews [2,4,5]). Additionally, insect pads release a secretory fluid, which is most probably a micro-emulsion containing water-soluble and lipid-soluble fractions, onto a contact zone [2,6-8]. Due to such an elaborate system, insects are able to attach successfully and move efficiently on a variety of substrates (e.g., [9-11]) by using a broad range of physical interactions.

In nature, most insect species are associated with plants. During the long period of co-evolution between plants and insects, plants have developed surfaces that enable pollinators and symbiotic insects to attach to and walk on, as well as surface structures that reduce insect attachment [11]. The impeding effects of plant surfaces on insect attachment ability depend on the concrete plant–insect system and may serve as a defence mechanism against herbivores and nectar robbers or as a mechanism preventing the escape of insects from traps of carnivorous plants and kettle trap flowers. Plant surface features such as particular cell arrangements, shapes, and orientation, as well as the presence of some types of trichomes, acting mainly at the macroscopic level, hinder the interlocking of insect claws. Additionally, plant-produced wet films on the surface, microscopic cuticular folds and epicuticular (deposited onto the plant cuticle) wax crystals reduce the adhesion of insect attachment pads (reviews [11,12]). In the present study, we consider the effect of wax crystal dimension on insect attachment.

Three-dimensional projections, called wax crystals throughout the text, emerge from a two-dimensional film of cuticular lipids (waxes), representing the hydrophobic component of the plant cuticle [13]. Both projections and films exhibit a crystalline nature [14,15]. Wax crystals range in size from 0.5 to 100 μm and show various morphologies, such as platelets, rodlets, tubules, threads etc. [16,17], which originate from the self-assembly of specific molecules (e.g., [14,18-21]). The morphology of crystals is coherent with the chemical composition of the wax, representing a complex mixture of long-chain aliphatic and cyclic hydrocarbons, fatty acids, aldehydes, ß-diketones, primary and secondary alcohols, and is usually determined by the dominating chemical compound or compound class [16,22,23].

The effect of plant surfaces covered by wax crystals on insect attachment has been examined experimentally using different approaches in numerous previous studies (e.g., [10,24-44]). It has been demonstrated that such surfaces can greatly reduce the insect attachment ability when compared to wax free substrates. Not only the presence of wax crystals, but also their size and density affect insect attachment. The effect of the length and density of crystals has been observed in the case of *Cryptolaemus montrouzieri* beetles moving on the leaflets of the *Pisum sativum* plants covered with wild-type waxes and plant mutants with reduced wax coverage [40]. It has been found that the force reduction correlated with the increasing crystal length and the decreasing density of individual wax crystals. However, plant surfaces used also differed in the shape of the crystals in addition to their variability of dimension and density.

The aim of this study was to examine the effect of different parameters of crystalline wax coverage on insect attachment. To avoid the possible influence of chemical diversity and crystal shape, we decided, instead of using native plant wax surfaces, to use bioinspired wax surfaces covered by crystals having a similar morphology. Bioinspired surfaces were made of long-chain hydrocarbons, which can be dominating chemical constituents in plant waxes [22]. Four *n*-alkanes of varying chain lengths ($C_{36}H_{74}$, $C_{40}H_{82}$, $C_{44}H_{90}$, and $C_{50}H_{102}$) were used to form crystalline wax coatings having a different size and density of crystals. Different alkanes created different roughness on the surface [45,46].

Insect attachment ability was studied in traction experiments with adult seven-spotted ladybird beetles *Coccinella septempunctata* (Coleoptera, Coccinellidae) walking on five different substrates: four wax surfaces plus a hydrophilic smooth glass used as a reference sample. Two main questions were addressed. (i) Do insects perform differently on smooth glass and wax coated samples? (ii) How do different characteristics of crystalline wax surfaces influence the attachment? We also measured adhesion (pull-off) forces of artificial adhesive systems on these surfaces. Here, tacky and deformable polydimethylsiloxane (PDMS) semi-spheres, having elasticity moduli similar to those of insect adhesive pads were used as probes [47]. Results obtained in different types of force tests were compared and discussed from the perspective of insect attachment.

Results

Bioinspired wax surfaces formed by alkanes of varying chain lengths ($C_{36}H_{74}$, $C_{40}H_{82}$, $C_{44}H_{90}$, and $C_{50}H_{102}$), referred to as C_{36}, C_{40}, C_{44}, and C_{50}, respectively, throughout the text, were regularly covered with submicroscopic plate-like wax crystals (Figure 1). The size of the wax crystals (Table 1) gradually decreased as the alkane chain length increased, showing a significant difference between surfaces (length: $H_{3,499} = 336.512$; thickness: $H_{3,499} = 366.532$; both $P < 0.001$, Kruskal–Wallis one way ANOVA on ranks). Also, pairwise comparisons of samples demonstrated significant differences in both morphometrical variables, with the exception of C_{44} vs

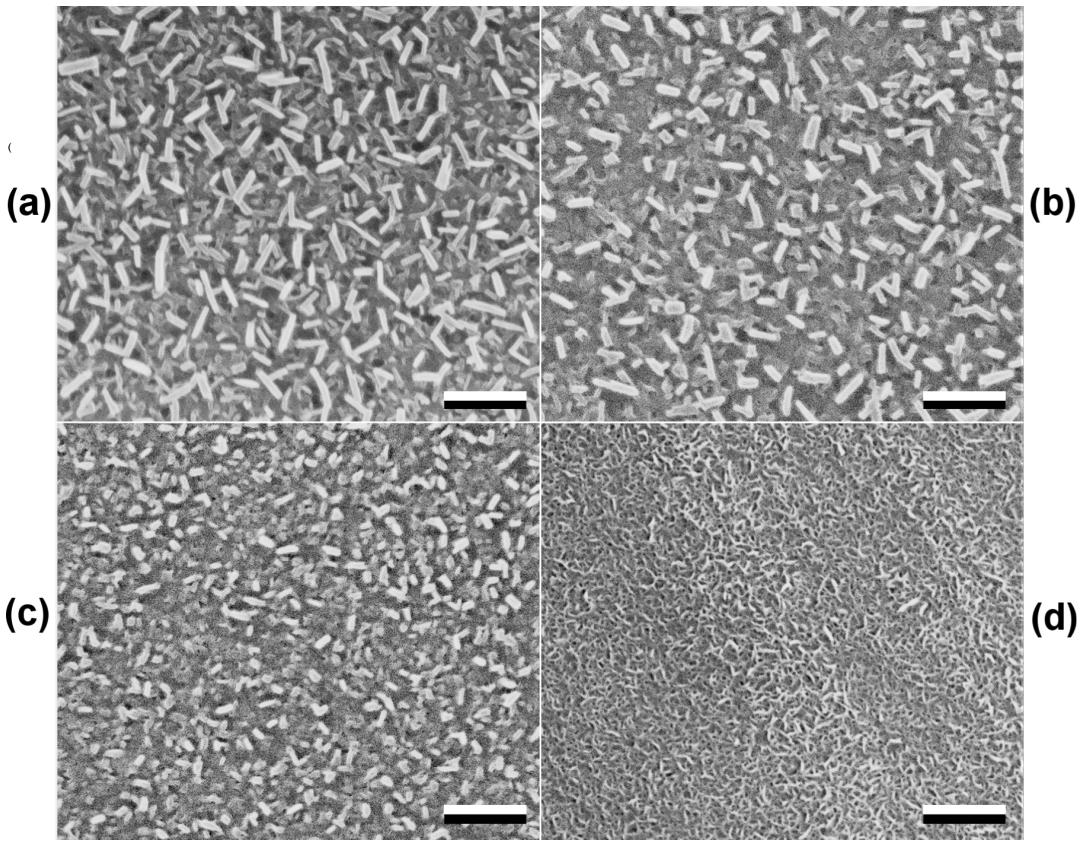

Figure 1: Scanning electron microscopy (SEM) micrographs of wax surfaces formed by alkanes of varying chain lengths: $C_{36}H_{74}$ (a), $C_{40}H_{82}$ (b), $C_{44}H_{90}$ (c), and $C_{50}H_{102}$ (d). Scale bars = 2 µm.

Table 1: Morphometrical variables of crystals, surface roughness, and wetting properties of wax samples.[a]

sample	CL, µm	CT, µm	CD, µm	R_a, nm	r.m.s., nm	CA, °
C_{36}	0.713 ± 0.213 *n* = 125	0.170 ± 0.032 *n* = 125	5.460 ± 0.617 *n* = 4	973.66 *n* = 1	1024.46 *n* = 1	165.6 ± 1.5 *n* = 15
C_{40}	0.483 ± 0.133 *n* = 125	0.166 ± 0.032 *n* = 125	4.956 ± 0.269 *n* = 4	695.92 *n* = 1	737.55 *n* = 1	163.4 ± 1.1 *n* = 15
C_{44}	0.301 ± 0.727 *n* = 125	0.118 ± 0.022 *n* = 125	8.386 ± 2.030 *n* = 3	622.97 *n* = 1	651.30 *n* = 1	161.3 ± 1.9 *n* = 15
C_{50}	0.279 ± 0.078 *n* = 125	0.077 ± 0.013 *n* = 125	27.786 ± 1.251 *n* = 4	134.70 *n* = 1	137.42 *n* = 1	160.0 ± 2.2 *n* = 15

[a]CA, apparent contact angle of water; CD, density of crystals; CL, crystal length; CT, crystal thickness; *n*, number of individual measurements; R_a, mean roughness; r.m.s., root mean square of roughness.

C_{50} for the crystals length and C_{36} vs C_{40} for the crystals thickness (Table 2). On the contrary, the density of crystals on the surface (Table 1) showed a significant, up to five-fold, increase with an increased chain length ($F_{3,14}$ = 359.201, P < 0.001, one way ANOVA). However, the density was similar in C_{36} and C_{40} (Table 2).

Table 2: Results of statistical analyses (Tukey test performed after Kruskal–Wallis one way ANOVA on ranks and one way ANOVA) of morphometrical variables of wax crystals between different wax samples.[a]

comparison	*q*	*P*	significantly different
length			
C_{36} vs C_{40}	7.909	<0.05	yes
C_{36} vs C_{44}	20.146	<0.05	yes
C_{36} vs C_{50}	22.541	<0.05	yes
C_{40} vs C_{44}	12.237	<0.05	yes
C_{40} vs C_{50}	14.631	<0.05	yes
C_{44} vs C_{50}	2.395	>0.05	no
thickness			
C_{36} vs C_{40}	1.000	>0.05	no
C_{36} vs C_{44}	12.954	<0.05	yes
C_{36} vs C_{50}	23.364	<0.05	yes
C_{40} vs C_{44}	11.955	<0.05	yes
C_{40} vs C_{50}	22.264	<0.05	yes
C_{44} vs C_{50}	10.409	<0.05	yes
density			
C_{36} vs C_{40}	0.884	>0.05	no
C_{36} vs C_{44}	4.760	<0.05	yes
C_{36} vs C_{50}	39.101	<0.05	yes
C_{40} vs C_{44}	5.578	<0.05	yes
C_{40} vs C_{50}	49.987	<0.05	yes
C_{44} vs C_{50}	31.443	<0.05	yes

[a]*P*, probability value; *q*, Tukey test statistics; yes, significantly different; no, no significant difference.

Wax crystals created a microscopic and nanoscopic roughness of surfaces (Figure 2, Table 1). Values of the surface roughness parameters dropped by factors of 7–9, when C_{36} was compared with C_{50}. Both middle-chain alkanes created surfaces with relatively similar mid-range roughness. All four wax samples showed superhydrophobic properties: apparent contact angles of water ranged from ca. 160 to 166° (Table 1).

The traction forces generated by beetles *Coccinella septempunctata* in the first and second tests on glass did not differ in either of the experimental sets with various wax surfaces (Table 3). Force values obtained on the glass sample were up to 30 times higher compared to those obtained on wax surfaces (Figure 3a, inset) and showed highly significant differences with the latter (Kruskal–Wallis one way ANOVA on ranks: $H_{4,159}$ = 121.922, P < 0.001; Table 3). Traction forces measured on wax surfaces ranged from 0.224 ± 0.053 to 0.418 ± 0.301 mN. Comparisons between these samples revealed a trend toward an increase of force values in the order of surfaces C_{36}–C_{40}–C_{44}–C_{50} (Figure 3a): Forces on the C_{50} surface were significantly higher compared to those on C_{36} and C_{40} surfaces, whereas forces in other surface pairs were similar (Table 3).

Table 3: Results of statistical analyses (*t*-test, Mann–Whitney rank sum test, and Dunn's method performed after Kruskal–Wallis one way ANOVA on ranks) of traction force values obtained on different samples.[a]

comparison	d.f.	test statistics	*P*	significantly different
glass: 1 vs 2				
C_{36}	38	t = 0.048	0.962	no
C_{40}	—	T = 428	0.636	no
C_{44}	38	t = 0.580	0.565	no
C_{50}	—	T = 4040	0.862	no
glass vs wax				
C_{36}	—	Q = 7.203	<0.05	yes
C_{40}	—	Q = 7.743	<0.05	yes
C_{44}	—	Q = 6.938	<0.05	yes
C_{50}	—	Q = 5.734	<0.05	yes
between wax				
C_{36} vs C_{40}	38	t = 1.105	0.312	no
C_{36} vs C_{44}	—	T = 396	0.715	no
C_{36} vs C_{50}	—	T = 319	0.015	yes
C_{40} vs C_{44}	—	T = 362	0.198	no
C_{40} vs C_{50}	—	T = 299	0.003	yes
C_{44} vs C_{50}	—	T = 340	0.062	no

[a]d.f., degrees of freedom; *P*, probability value; *Q*, Dunn's method statistics; *t*, t-test statistics; *T*, Mann–Whitney rank sum test statistics; yes, significantly different; no, no significant difference.

Pull-off forces measured using PDMS semi-spherical probes were either significantly lower in cases of shorter-chain alkanes or similar in cases of longer-chain alkanes, when compared with forces obtained on the glass sample (Figure 3b, Table 4). Among the wax surfaces, we observed a trend of rising pull-off forces in the following order of samples C_{36}–C_{40}–C_{44}–C_{50} (Figure 3b): the lowest force was measured on C_{36} (0.800 ± 0.712 mN) and the highest one on C_{50} (3.092 ± 1.094 mN). However, significant differences in force values were found only in C_{50} vs C_{36} and C_{50} vs C_{40} (Table 4). In other pairs of surfaces, differences were non-significant (Table 4).

Correlations between forces and different wax surface parameters (crystal length, crystal thickness, density of crystals, mean roughness, and root mean square of roughness) were examined.

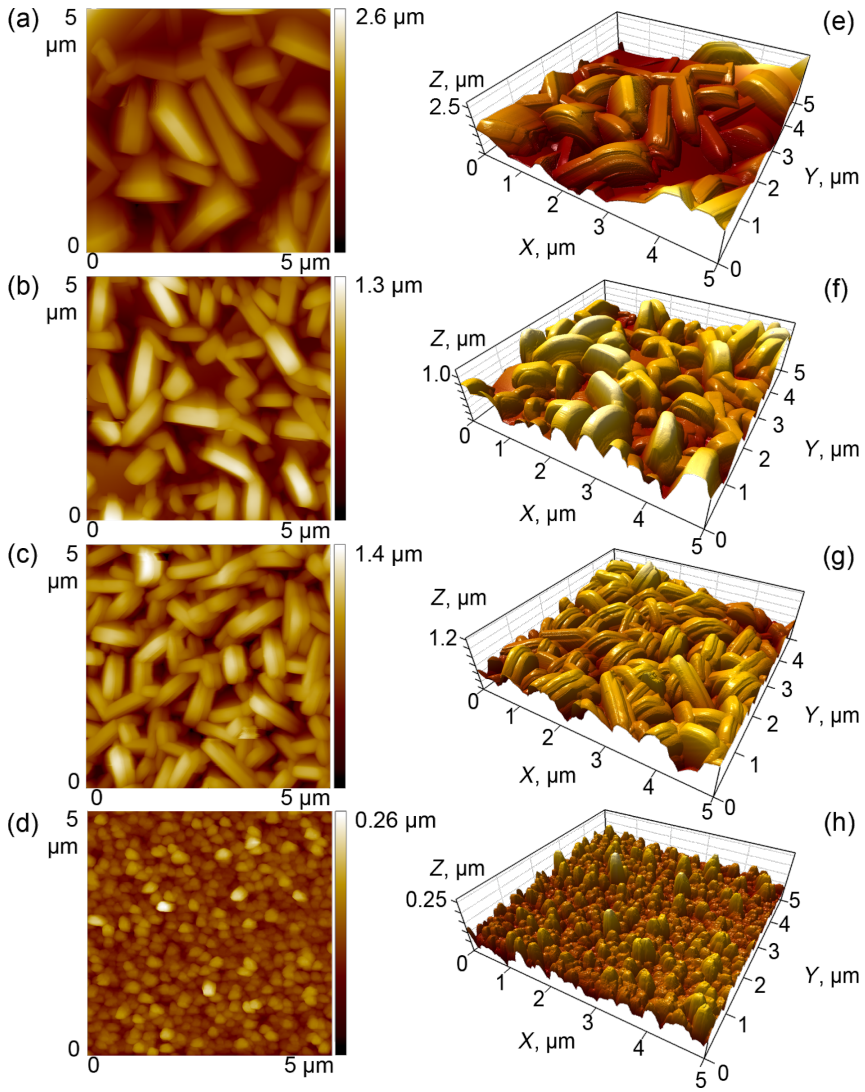

Figure 2: Atomic force microscopy (AFM) height images used for estimating the surface roughness parameters R_a and r.m.s. (a–d) and three-dimensional projections (e–h) of wax surfaces created by alkanes of varying chain lengths: $C_{36}H_{74}$ (a,e), $C_{40}H_{82}$ (b,f), $C_{44}H_{90}$ (c,g), and $C_{50}H_{102}$ (d,h).

We found a significant positive correlation between the traction force and crystal density (P = 0.002, linear regression; Figure 4a). The pull-off force showed significant negative correlations with the crystal thickness (P = 0.011, linear regression; Figure 4b), mean roughness R_a (P = 0.034, linear regression; Figure 4c), and root mean square of roughness r.m.s. (P = 0.032, linear regression; Figure 4d). Other correlations between forces and wax surface parameters were non-significant (P > 0.05, linear regression).

Discussion

Using *n*-alkanes of varying chain lengths ($C_{36}H_{74}$, $C_{40}H_{82}$, $C_{44}H_{90}$, and $C_{50}H_{102}$), we obtained surfaces with crystalline wax coatings composed of crystals having similar plate-like shapes. Wax crystals were either of the same dimensions as epicuticular crystals in plants [16,17] or even smaller, because we used alkanes with the same or longer chain lengths, when comparing to plant wax compounds (20 to 40 carbons [22,23]). Microscopy studies of our bioinspired wax surfaces showed differences in both crystal size and density among the samples: The length and thickness of the crystals decreased with an increase of the chain length of the alkanes that formed these surfaces, whereas the density of the wax coverage showed an opposite relationship. These differences in the wax coverage micromorphology caused distinctions in the surface roughness. Samples bearing looser coverage were composed of larger (longer and thicker) crystals and were rougher than samples with smaller (shorter and thinner) crystals covering the surface more densely. Since the surface roughness dropped in the order of surfaces C_{36}–C_{40}–C_{44}–C_{50}, it demonstrated a similar

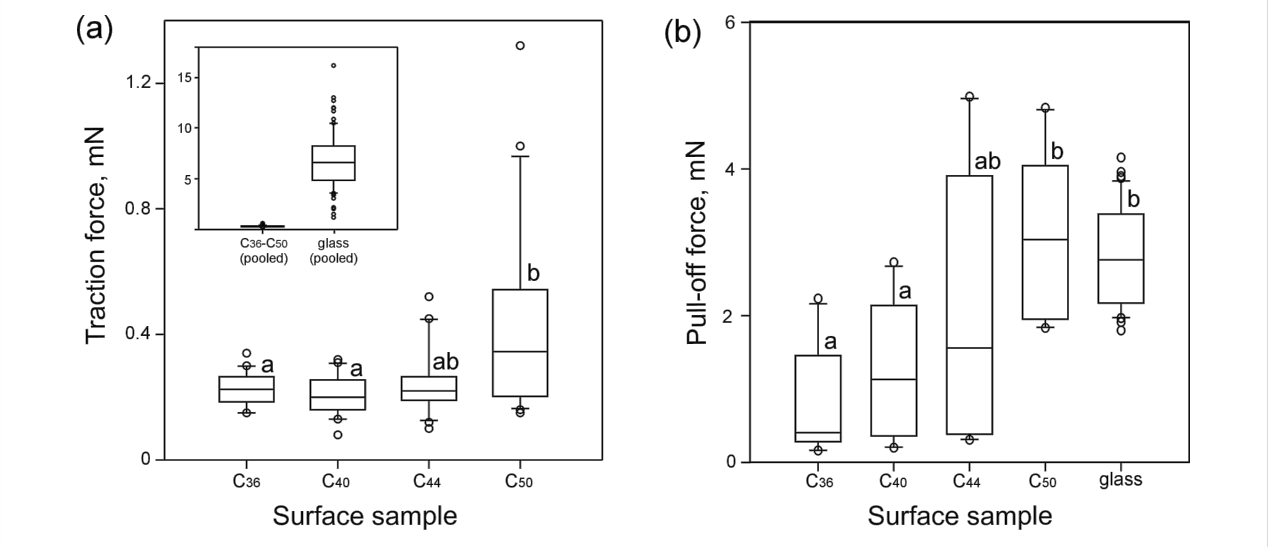

Figure 3: Traction forces of male beetles *Coccinella septempunctata* (a) and pull-off forces of PDMS semi-spheres (b) on different surfaces. According to the *t*-test and Mann–Whitney rank sum test (Table 3 and Table 4), means/medians with different letters differ significantly from each other.

Table 4: Results of statistical analyses (*t*-test and Mann–Whitney rank sum test) of pull-off force values obtained on different samples.

comparison	d.f.	test statistics	*P*	significantly different
glass vs wax				
C_{36}	48	$t = 8.733$	<0.001	yes
C_{40}	48	$t = 6.317$	<0.001	yes
C_{44}	—	$T = 197$	0.163	no
C_{50}	—	$T = 268$	0.762	no
between wax				
C_{36} vs C_{40}	18	$t = -1.252$	0.226	no
C_{36} vs C_{44}	—	$T = 81$	0.076	no
C_{36} vs C_{50}	—	$T = 58$	<0.001	yes
C_{40} vs C_{44}	—	$T = 92$	0.345	no
C_{40} vs C_{50}	18	$t = -4.082$	<0.001	yes
C_{44} vs C_{50}	18	$t = -1.467$	0.160	no

d.f., degrees of freedom; *P*, probability value; *t*, t-test statistics; *T*, Mann–Whitney rank sum test statistics; yes, significantly different; no, no significant difference.

dependence on the chain length as did the morphometrical variables of crystals. Interestingly, the values of surface roughness parameters measured using AFM on the crystalline epicuticular wax in the pitcher of the *Nepenthes alata* plant ($R_a = 0.254 \pm 0.035$ µm, r.m.s. = 0.317 ± 0.045 µm [48]) were in the range of those measured in our bioinspired samples, to be exact between those of C_{44} and C_{50} samples. The fine microroughness of bioinspired surfaces covered by hydrophobic wax material led to very high values of the apparent contact angle of water, which were very close to those measured on plant surfaces bearing three-dimensional waxes (e.g., [49-51]).

The tarsal attachment system of the *C. septempunctata* beetle used in this study has been previously described in detail by Gorb et al. [52]. The tarsus bears two ventrally curved claws with a claw tip diameter of about 4 µm [42] and hairy adhesive pads situated on the ventral side of the two first proximal tarsomeres (Figure 5a). Pads are covered with numerous tiny setae having various tip shapes, from sharp-pointed to spatula-like, ranging in width from ca. 1.8 to 3.5 µm (Figure 5b–d). Male beetles additionally have large areas (up to a half of the total pad area) covered by setae with discoid terminal elements having an average diameter of 8 µm (Figure 5a,e). These setae are adapted for holding strongly on to females for a long time during mating [53,54].

As the studied substrates were lacking surface structures suitable for claw interlocking (larger than 4 µm according to [1]), we assume that insect attachment relied solely on the performance of adhesive pads. Traction force tests demonstrated a great reduction in beetle attachment on microstructured crystalline wax surfaces compared to smooth glass ($R_a = 0.007 \pm 0.001$ µm, r.m.s. = 0.009 ± 0.001 µm [47]). These results are in line with previous experimental data obtained for different insect species on three-dimensional plant waxes vs smooth surfaces (see Introduction). The good performance of the beetles during the second run on glass, which followed the test on each bioinspired wax surface, indicated no influence of the wax coatings on the subsequent attachment ability of insects. This may also suggest that there was no contamination of insect adhesive organs by wax crystals in our experiments, although a contaminating effect caused by plant crystalline waxes has been repeatedly reported previously (e.g., [25,38,55-

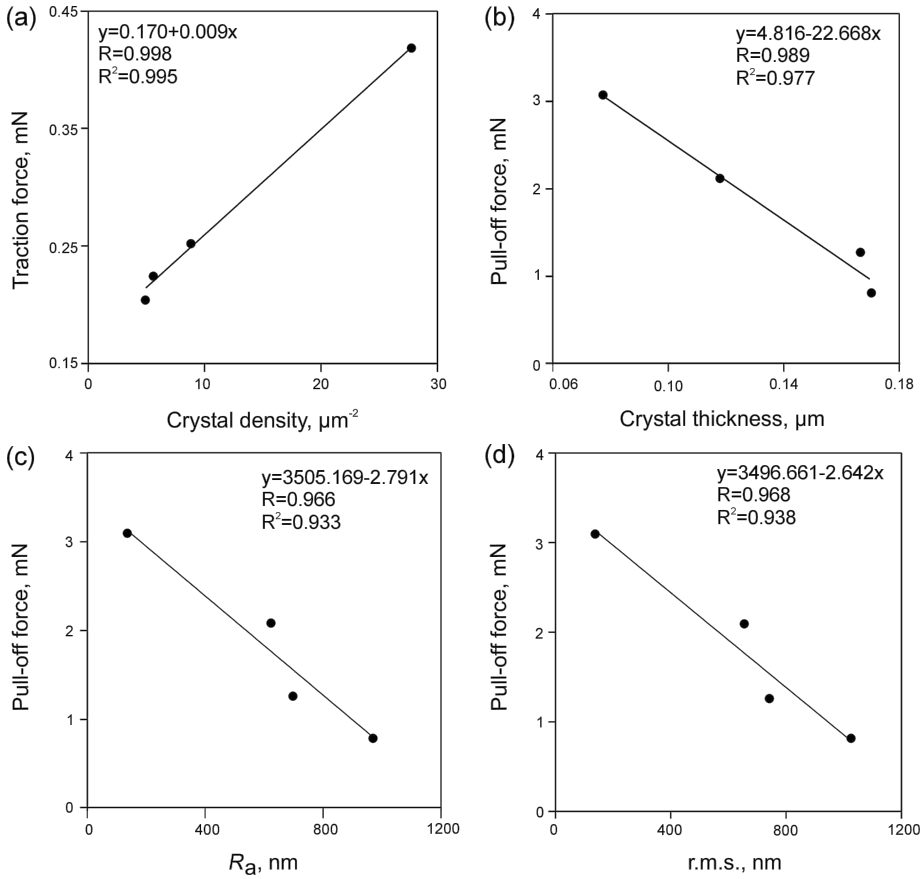

Figure 4: Traction forces of male beetles *Coccinella septempunctata* vs crystal densities (a) and pull-off forces of PDMS semi-spheres vs crystals thickness (b), mean roughness R_a (c), and root mean square of roughness r.m.s. (d). Lines indicate linear regressions.

57]). Therefore, we did not consider contamination as a mechanism for the reduction of beetle attachment on bioinspired wax surfaces studied (see hypotheses proposed for plant waxes [10]). The obtained data may be primarily explained by the inability of relatively large setal tips to make full contact with these surfaces: The real contact area was highly reduced presumably due to the micro- and nanoscopic roughness introduced by wax crystals (roughness hypothesis according to [10]). The impact of the surface roughness on insect adhesion has been shown in a number of experimental studies demonstrating a greatly reduced adhesion on the surface roughness of specific microscopic dimensions in comparison to smooth substrate [2,58-60]. Also, an adsorption of the secretion from insect adhesive pads by the bioinspired wax coverage and/or wax dissolving in the pad secretion leading to hydroplaning cannot be completely excluded (adsorption hypothesis and wax dissolving hypothesis [10]).

Using PDMS semi-spheres as artificial adhesive systems, we obtained much higher forces on wax samples compared to insect attachment forces measured on these surfaces. These force values were either close or equal to those measured on glass. We explain these results by differences in the material properties between PDMS and tenent setae of *C. septempunctata* beetles. The PDMS probes exhibited elastic properties (effective E-modulus of ca. 70 kPa), which were in the range of those in smooth adhesive pads of insects (27 kPa in *Tettigonia viridissima* [61] and 12–625 kPa in *Carausius morosus* [62]). Due to high deformability of the material, PDMS probes were able to make good contact with the substrates. Similar force values obtained on glass and on both C_{50} and C_{44} suggest a similar real contact area between the probes and these three surfaces. The material in the hairy adhesive pads of *C. septempunctata* is much stiffer: The lowest E-modulus recently measured at the setal tip is 1 MPa [63]. Therefore, the pressing in of less deformable pad material into cavities between the wax crystals probably did not occur, resulting in a smaller real contact area and, consequently, lower traction forces. Also, the lack of pressing in will not lead to the mechanical interlocking at the interface and will not contribute to increase of traction forces.

Among the bioinspired wax surfaces, the highest attachment force was measured on C_{50}. It significantly correlated with the

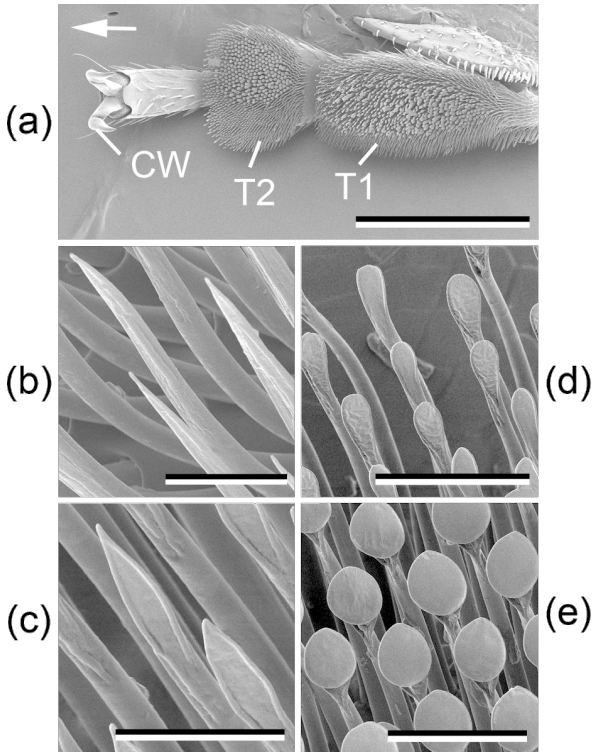

Figure 5: SEM micrographs of tarsal attachment devices in the male beetle *Coccinella septempunctata*: tarsus of the foreleg (a) and different types of tenent setae (b–e). Arrow in (a) shows the distal direction. CW, claw; T1, first proximal tarsomere; T2, second proximal tarsomere. Scale bars = 500 µm (a), 20 µm (d,e), 10 µm (b,c). Adapted from [52].

densest coverage, created by the smallest crystals. These results are not in line with our previous findings showing the opposite effects of the crystal size and density on insect attachment [40]. The discrepancy may be due to differences in the micromorphology of the crystals between the surfaces used in these studies. Here, all wax surfaces were uniformly covered with platelet-like crystals, whereas previous data were obtained on real plant surfaces bearing crystals of diverse shapes (platelets, combination of scales with ribbons, and combination of filaments with ribbons and rodlets).

Pull-off force measurements performed on bioinspired wax surfaces with artificial adhesive systems also showed the highest force on the C_{50} surface. Force values grew with a decrease in both crystal sizes (thickness) and surface roughness. The latter result is in accordance with data of previous studies on rubber surfaces, where the highest forces were recorded on substrates with the finest microroughness [47,64,65]. In these cases, as well as in C_{50}, the small dimensions of the surface structures together with their dense distribution on the surface resulted in a rather smooth surface topography. Such substrate profiles can be replicated by very deformable material down to a micro- or even nanometer scale due to high flexibility of one of the contact partners (substrate or probe).

Conclusion

By using *n*-alkanes of varying chain lengths, we obtained highly hydrophobic surfaces with wax coatings composed of crystals having similar shapes, but differing in size and distribution/density. Insect attachment on these substrates probably relied solely on the performance of adhesive pads. Force experiments showed stronger insect attachment ability and higher pull-off forces of PDMS probes on the wax surface with a higher density of wax coverage, created by smaller (thinner) crystals. At this (sub)microscopic range of roughness, adhesion grew with an increase of the substrate smoothness.

Experimental

Wax surfaces were prepared through self-assembly of *n*-alkane hexatriacontane $C_{36}H_{74}$ (98%), tetracontane $C_{40}H_{82}$ (≥95%), tetratetracontane $C_{44}H_{90}$ (99%), and pentacontane $C_{50}H_{102}$ (≥97%) (Sigma-Aldrich, France). The waxes were deposited by thermal evaporation using a Bio-Rad Polaron Division Coating System, in a vacuum chamber at 10^{-4} mbar on a holder placed 10–12 cm above a crucible loaded with 40–50 mg of wax. The wax was evaporated at a crucible temperature of about 200 °C by applying pulses of an electrical current. After evaporation, the specimens were kept at room temperature (25 °C).

Surface imaging was performed by using SEM (FEI E-SEM Quanta 200, FEI Company, Hillsboro, OR, USA). Morphometrical variables of wax crystals (length CL and thickness CW) and density of crystals (CD) covering the surface of bioinspired wax samples were measured from digital images using the image analysis software SigmaScan Pro 5.0.0 (SPSS Inc., Chicago, IL, USA).

The topography of wax surfaces was examined using the AFM (Typ NanoWizard, JPK Instruments AG, Berlin, Germany). On each sample, areas of 5 µm × 5 µm were scanned in intermittent contact mode with a supersharp silicon non-contact cantilever (SSS-NCH, Nanoworld, Neuchâtel, Switzerland). The scanned area was comparable with the size of setal tips in adhesive pads of the beetle *C. septempunctata* [52]. The images obtained were processed with the scanning probe image processing software (SPIP, Version 5.1.2, Image Metrology A/S, Hørsholm, Danemark) for evaluation of roughness parameters, such as R_a (mean roughness) and r.m.s. (root mean square of roughness). Prior to roughness analyses, the images were plane corrected. The scanning tip geometry was characterized by scanning on a mica disc covered with colloidal gold particles (5.5, 9.3, and 14.4 nm in diameter) (Pelco AFM Gold

standard Kit Product No. 16205, TED Pella Inc., Redding, CA, USA). Using the SPIP software, the radius of 13 nm was determined via blind tip reconstruction.

Measurements of contact angles of double-distilled water on wax surfaces were performed by using a high-speed optical contact angle measuring device OCAH 200 (DataPhysics Instruments GmbH, Filderstadt, Germany) according to the needle-in sessile drop method. For a detailed description of the method, see [50]. We applied 1 µL drops and ellipse fitting for evaluation of apparent contact angles. On each surface, the contact angles of 15 drops were measured. Altogether, 60 measurements were executed.

To measure the attachment forces of *Coccinella septempunctata* beetles on different substrates, traction experiments with tethered walking male insects were carried out by using a load cell force transducer (10 g capacity, Biopac Systems Ltd, Santa Barbara, CA, USA) as described in [52]. Insects were collected from plants along roadsides near Kronshagen (Germany). The experimental design includes three successive force tests with the same beetle: first on hydrophilic smooth glass (glass 1), then on one of the wax surfaces, and once more on glass (glass 2). Each insect individual was tested on all wax surfaces. We used 20 male beetles and carried out 240 traction tests in total.

Pull-off forces were measured in indentation experiments with the micro-tribometer Basalt 01 (Tetra GmbH, Ilmenau, Germany), which has been described in detail in [66]. We applied a recently developed technique for testing surfaces with very low adhesive capability by using elastic (effective E-modulus of ca. 70 kPa) PDMS semi-spheres as probes [47]. With each probe, pull-off force measurements were conducted at an applied normal force of ca. 1 mN on two samples: (1) hydrophilic smooth glass and (2) one of the wax surfaces. The order of samples was not randomized. We used 40 probes (20 for each wax surface) and performed 80 pull-off force measurements in all.

All experiments were carried out at room temperature (20–25 °C) and a relative ambient humidity of 30–42%. Values are presented in the text as "mean ± standard deviation". Data obtained were statistically analysed with the SigmaStat 3.5 software (SPSS Inc., Chicago, IL, USA). One way ANOVA and Kruskal–Wallis one way ANOVA on ranks were used to evaluate differences in the morphometrical variables of the crystals between wax surfaces. We applied Kruskal–Wallis one way ANOVA on ranks for comparison of traction force values on glass and wax surfaces. To compare traction forces and pull-off forces obtained on pairs of different substrates, data were analysed with *t*-test and Mann–Whitney rank sum test. Correlations between forces and different wax surface parameters (crystal length CL, crystal thickness CT, density of crystals CD, mean roughness $R_{a,}$ and root mean square of roughness r.m.s.) were examined by using linear regression.

Acknowledgements

Figure 5 was prepared by using Figure 4 from [52]. We are thankful to Ms. V. Kastner (Tuebingen, Germany) for linguistic corrections of the manuscript. This study was partly supported by the SPP 1420 of the German Science Foundation 'Biomimetic Materials Research: Functionality by Hierarchical Structuring of Materials' (project GO 995/9-2) to SG.

References

1. Dai, Z.; Gorb, S. N.; Schwarz, U. *J. Exp. Biol.* **2002,** *205,* 2479–2488.
2. Gorb, S. N. *Attachment Devices of Insect Cuticle;* Kluwer Academic Publishers: Dordrecht, The Netherlands, 2001.
3. Beutel, R. G.; Gorb, S. N. *J. Zool. Syst. Evol. Res.* **2001,** *39,* 177–207. doi:10.1046/j.1439-0469.2001.00155.x
4. Federle, W. *J. Exp. Biol.* **2006,** *209,* 2611–2621. doi:10.1242/jeb.02323
5. Gorb, S. N. *Adv. Insect Physiol.* **2007,** *33,* 81–115. doi:10.1016/S0065-2806(07)34002-2
6. Vötsch, W.; Nicholson, G.; Müller, R.; Stierhof, Y.-D.; Gorb, S.; Schwarz, U. *Insect Biochem. Mol. Biol.* **2002,** *32,* 1605–1613. doi:10.1016/S0965-1748(02)00098-X
7. Federle, W.; Riehle, M.; Curtis, A. S. G.; Full, R. J. *Integr. Comp. Biol.* **2002,** *42,* 1100–1106. doi:10.1093/icb/42.6.1100
8. Peisker, H.; Gorb, S. N. *J. Exp. Biol.* **2012,** *215,* 1266–1271. doi:10.1242/jeb.065722
9. Stork, N. E. *J. Exp. Biol.* **1980,** *88,* 91–107.
10. Gorb, E. V.; Gorb, S. N. *Entomol. Exp. Appl.* **2002,** *105,* 13–28. doi:10.1046/j.1570-7458.2002.01028.x
11. Gorb, E. V.; Gorb, S. N. Anti-adhesive Surfaces in Plants and their Biomimetic Potential. In *Materials Design Inspired by Nature: Function through Inner Architecture;* Fratzl, P.; Dunlop, J. W. C.; Weinkamer, R., Eds.; RSC Publishing: Cambridge, U.K., 2013; pp 282–309. doi:10.1039/9781849737555-00282
12. Poppinga, S.; Koch, K.; Bohn, H. F.; Barthlott, W. *Funct. Plant Biol.* **2010,** *37,* 952–961. doi:10.1071/FP10061
13. Jeffree, C. E. The Fine Structure of the Plant Cuticle. In *Biology of the Plant Cuticle;* Riederer, M.; Müller, C., Eds.; Annual Plant Reviews, Vol. 23; Blackwell: Oxford, U.K., 2006; pp 11–125. doi:10.1002/9780470988718.ch2
14. Meusel, I.; Neinhuis, C.; Markstädter, C.; Barthlott, W. *Plant Biol. (Berlin, Ger.)* **2000,** *2,* 462–470. doi:10.1055/s-2000-5961
15. Ensikat, H. J.; Boese, M.; Mader, W.; Barthlott, W.; Koch, K. *Chem. Phys. Lipids* **2006,** *144,* 45–59. doi:10.1016/j.chemphyslip.2006.06.016
16. Barthlott, W.; Neinhuis, C.; Cutler, D.; Ditsch, F.; Meusel, I.; Theisen, I.; Wilhelmi, H. *Bot. J. Linn. Soc.* **1998,** *126,* 237–260. doi:10.1111/j.1095-8339.1998.tb02529.x
17. Koch, K.; Bhushan, B.; Barthlott, W. Multifunctional Plant Surfaces and Smart Materials. In *Handbook of Nanotechnology;* Bhushan, B., Ed.; Springer: Heidelberg, Germany, 2010; pp 1399–1436. doi:10.1007/978-3-642-02525-9_41
18. Jeffree, C. E.; Baker, E. A.; Holloway, P. J. *New Phytol.* **1975,** *75,* 539–549. doi:10.1111/j.1469-8137.1975.tb01417.x

19. Jetter, R.; Riederer, M. *Planta* **1994,** *195,* 257–270. doi:10.1007/BF00199686
20. Jetter, R.; Riederer, M. *Bot. Acta* **1995,** *108,* 111–120. doi:10.1111/j.1438-8677.1995.tb00840.x
21. Koch, K.; Ensikat, H.-J. *Micron* **2008,** *39,* 759–772. doi:10.1016/j.micron.2007.11.010
22. Jetter, R.; Kunst, L.; Samuels, A. L. Composition of Plant Cuticular Waxes. In *Biology of the Plant Cuticle;* Riederer, M.; Müller, C., Eds.; Annual Plant Reviews, Vol. 23; Blackwell: Oxford, U.K., 2006; pp 145–181. doi:10.1002/9780470988718.ch4
23. Bargel, H.; Koch, K.; Cerman, Z.; Neinhuis, C. *Funct. Plant Biol.* **2006,** *33,* 893–910. doi:10.1071/FP06139
24. Way, M. J.; Murdie, G. *Ann. Appl. Biol.* **1965,** *56,* 326–328. doi:10.1111/j.1744-7348.1965.tb01245.x
25. Stork, N. E. *Entomol. Exp. Appl.* **1980,** *28,* 100–107. doi:10.1111/j.1570-7458.1980.tb02992.x
26. Edwards, P. B. *Aust. J. Ecol.* **1982,** *7,* 347–352. doi:10.1111/j.1442-9993.1982.tb01309.x
27. Stork, N. E. The Form of Plants Waxes: A Mean of Preventing Insect Attachment. In *Insects and the Plantt Surface;* Juniper, B. E.; Southwood, T. R. E., Eds.; Edward Arnold: London, U.K., 1986; pp 346–347.
28. Federle, W.; Maschwitz, U.; Fiala, B.; Riederer, M.; Hölldobler, B. *Oecologia* **1997,** *112,* 217–224. doi:10.1007/s004420050303
29. Eigenbrode, S. D.; Kabalo, N. N. *Entomol. Exp. Appl.* **1999,** *91,* 125–130. doi:10.1046/j.1570-7458.1999.00474.x
30. Eigenbrode, S. D.; Castognola, T.; Roux, M.-B.; Steljes, L. *Entomol. Exp. Appl.* **1996,** *81,* 335–343. doi:10.1046/j.1570-7458.1996.00104.x
31. Eigenbrode, S. D.; Kabalo, N. N.; Stoner, K. A. *Entomol. Exp. Appl.* **1999,** *90,* 225–235. doi:10.1046/j.1570-7458.1999.00443.x
32. Eigenbrode, S. D.; Rayor, L.; Chow, J.; Latty, P. *Entomol. Exp. Appl.* **2000,** *97,* 161–166. doi:10.1046/j.1570-7458.2000.00726.x
33. Federle, W.; Rohrseitz, K.; Hölldobler, B. *J. Exp. Biol.* **2000,** *203,* 505–512.
34. Brennan, E. B.; Weinbaum, S. A. *Aust. J. Entomol.* **2001,** *40,* 270–277. doi:10.1046/j.1440-6055.2001.00229.x
35. Eigenbrode, S. D.; Jetter, R. *Integr. Comp. Biol.* **2002,** *42,* 1091–1099. doi:10.1093/icb/42.6.1091
36. Gaume, L.; Gorb, S.; Rowe, N. *New Phytol.* **2002,** *156,* 479–489. doi:10.1046/j.1469-8137.2002.00530.x
37. Rutledge, C. E.; Eigenbrode, S. D. *Can. Entomol.* **2003,** *135,* 93–101. doi:10.4039/n02-044
38. Gorb, E.; Haas, K.; Henrich, A.; Enders, S.; Barbakadze, N.; Gorb, S. *J. Exp. Biol.* **2005,** *208,* 4651–4662. doi:10.1242/jeb.01939
39. Voigt, D.; Gorb, E.; Gorb, S. *Arthropod-Plant Interact.* **2007,** *1,* 221–243. doi:10.1007/s11829-007-9021-4
40. Gorb, E.; Voigt, D.; Eigenbrode, S. D.; Gorb, S. *Arthropod-Plant Interact.* **2008,** *2,* 247–259. doi:10.1007/s11829-008-9049-0
41. Eigenbrode, S. D.; Snyder, W. E.; Clevenger, G.; Ding, H.; Gorb, S. N. Variabale Attachment to Plant Surface Waxes by Predatory Insects. In *Functional Surfaces in Biology (II);* Gorb, S. N., Ed.; Springer: Heidelberg, Germany, 2009; pp 157–181. doi:10.1007/978-1-4020-6695-5_7
42. Gorb, E. V.; Gorb, S. N. *Beilstein J. Nanotechnol.* **2011,** *2,* 302–310. doi:10.3762/bjnano.2.35
43. Prüm, B.; Seidel, R.; Bohn, H. F.; Speck, T. *J. R. Soc. Interface* **2012,** *9,* 127–135. doi:10.1098/rsif.2011.0202
44. Prüm, B.; Seidel, R.; Bohn, H. F.; Speck, T. *Beilstein J. Nanotechnol.* **2012,** *3,* 57–64. doi:10.3762/bjnano.3.7
45. Pechook, S.; Pokroy, B. *Adv. Funct. Mater.* **2012,** *22,* 745–750. doi:10.1002/adfm.201101721
46. Pechook, S.; Pokroy, B. *Soft Matter* **2013,** *9,* 5710–5715. doi:10.1039/c3sm27484e
47. Purtov, J.; Gorb, E. V.; Steinhart, M.; Gorb, S. N. *Appl. Phys. A* **2013,** *111,* 183–189. doi:10.1007/s00339-012-7520-3
48. Scholz, I.; Bückins, M.; Dolge, L.; Erlinghagen, T.; Weth, A.; Hischen, F.; Mayer, J.; Hoffmann, S.; Riederer, M.; Riedel, M.; Baumgartner, W. *J. Exp. Biol.* **2010,** *213,* 1115–1125. doi:10.1242/jeb.035618
49. Neinhuis, C.; Barthlott, W. *Ann. Bot. (Oxford, U. K.)* **1997,** *79,* 667–677. doi:10.1006/anbo.1997.0400
50. Gorb, E. V.; Gorb, S. N. *Plant Biol. (Berlin, Ger.)* **2006,** *8,* 841–848. doi:10.1055/s-2006-923929
51. Koch, K.; Bhushan, B.; Barthlott, W. *Soft Matter* **2008,** *4,* 1943–1963. doi:10.1039/b804854a
52. Gorb, E. V.; Hosoda, N.; Miksch, C.; Gorb, S. N. *J. R. Soc. Interface* **2010,** *7,* 1571–1579. doi:10.1098/rsif.2010.0081
53. Stork, N. E. *Zool. J. Linn. Soc.* **1980,** *68,* 173–306. doi:10.1111/j.1096-3642.1980.tb01121.x
54. Stork, N. E. *J. Nat. Hist.* **1983,** *17,* 583–597. doi:10.1080/00222938300770481
55. Juniper, B. E.; Burras, J. K. *New Sci.* **1962,** *269,* 75–77.
56. Gaume, L.; Perret, P.; Gorb, E.; Gorb, S.; Labat, J.-J.; Rowe, N. *Arthropod Struct. Dev.* **2004,** *33,* 103–111. doi:10.1016/j.asd.2003.11.005
57. Gorb, E.; Gorb, S. Do Plant Waxes Make Insect Attachment Structures Dirty? Experimental Evidence for the Contamination Hypothesis. In *Ecology and Biomechanics – A Mechanical Approach to the Ecology of Animals and Plants;* Herrel, A.; Rowe, N. P.; Speck, T., Eds.; CRC Press: Boca Raton, FL, USA, 2006; pp 147–162. doi:10.1201/9781420001594.ch7
58. Peressadko, A.; Gorb, S. Surface Profile and Friction Force Generated by Insects. In *Proceedings of the 1st International Industrial Conference Bionik 2004,* Boblan, I.; Bannasch, R., Eds.; VDI Verlag: Düsseldorf, Germany, 2004; pp 257–263.
59. Voigt, D.; Schuppert, J. M.; Dattinger, S.; Gorb, S. N. *J. Insect Physiol.* **2008,** *54,* 765–776. doi:10.1016/j.jinsphys.2008.02.006
60. Bullock, J. M. R.; Federle, W. *Insect Sci.* **2011,** *18,* 298–304. doi:10.1111/j.1744-7917.2010.01369.x
61. Gorb, S.; Jiao, Y.; Scherge, M. *J. Comp. Physiol., A* **2000,** *186,* 821–831. doi:10.1007/s003590000135
62. Scholz, I.; Baumgartner, W.; Federle, W. *J. Comp. Physiol., A* **2008,** *194,* 373–384. doi:10.1007/s00359-008-0314-6
63. Peisker, H.; Michels, J.; Gorb, S. N. *Nat. Commun.* **2013,** *4,* No. 1661. doi:10.1038/ncomms2576
64. Fuller, K. N. G.; Tabor, D. *Proc. R. Soc. London, Ser. A* **1975,** *345,* 327–342. doi:10.1098/rspa.1975.0138
65. Briggs, G. A. D.; Briscoe, B. J. *J. Phys. D* **1977,** *10,* 2453–2466. doi:10.1088/0022-3727/10/18/010
66. Scherge, M.; Gorb, S. N. *Biological Micro- and Nanotribology;* Springer: Heidelberg, Germany, 2001.

BEILSTEIN JOURNAL OF NANOTECHNOLOGY

Dry friction of microstructured polymer surfaces inspired by snake skin

Martina J. Baum*[1], Lars Heepe[1], Elena Fadeeva[2] and Stanislav N. Gorb[1]

Full Research Paper

Open Access

Address:
[1]Functional Morphology and Biomechanics, Zoological Institute, Kiel University, Am Botanischen Garten 1–9, Kiel 24098, Germany and [2]Laser Zentrum Hannover e.V. (LZH), Hollerithallee 8, Hannover 30419, Germany

Email:
Martina J. Baum* - mbaum@zoologie.uni-kiel.de

* Corresponding author

Keywords:
biomimetics; dry friction; microstructure; polymer; snake skin

Beilstein J. Nanotechnol. **2014,** *5,* 1091–1103.
doi:10.3762/bjnano.5.122

Received: 03 April 2014
Accepted: 25 June 2014
Published: 21 July 2014

This article is part of the Thematic Series "Biological and bioinspired adhesion and friction".

Associate Editor: K. Koch

Abstract

The microstructure investigated in this study was inspired by the anisotropic microornamentation of scales from the ventral body side of the California King Snake (*Lampropeltis getula californiae*). Frictional properties of snake-inspired microstructured polymer surface (SIMPS) made of epoxy resin were characterised in contact with a smooth glass ball by a microtribometer in two perpendicular directions. The SIMPS exhibited a considerable frictional anisotropy: Frictional coefficients measured along the microstructure were about 33% lower than those measured in the opposite direction. Frictional coefficients were compared to those obtained on other types of surface microstructure: (i) smooth ones, (ii) rough ones, and (iii) ones with periodic groove-like microstructures of different dimensions. The results demonstrate the existence of a common pattern of interaction between two general effects that influence friction: (1) molecular interaction depending on real contact area and (2) the mechanical interlocking of both contacting surfaces. The strongest reduction of the frictional coefficient, compared to the smooth reference surface, was observed at a medium range of surface structure dimensions suggesting a trade-off between these two effects.

Introduction

Owing to the lack of extremities, the ventral body side of snakes is in almost continuous contact with the substrate. In spite of this, snakes are one of the most successful animal groups in occupying niches on all continents, except for Antarctica [1-3]. From a tribology point of view, their ventral skin surface has to fulfil two opposite functions: (1) to support body propulsion during locomotion by generating high friction in contact with the substrate and (2) to reduce skin material abrasion by generating low friction in forward sliding along the substrate [4]. Anisotropic frictional properties of the snake skin were previously shown by several tribological studies using various techniques at the macro scale [5-9], meso scale [10], and nano scale [11]. These properties must be kept up over a longer period of time until new skin is moulted.

Frictional properties of snake skin in contact with a solid partner depend on (i) the surface energy, (ii) material properties, and (iii) surface topography of the tribo-pair [12,13]. The surface energy of snake skin has been mostly assumed according to the chemical analysis of the skin material [14-18]. Only Lillywhite et al. [19] directly measured contact angles of the snake skin and showed its hydrophobic properties. The mechanical properties of the skin have been investigated in great detail by Klein and Gorb [20]. They revealed a depth gradient in stiffness: the skin consists of a hard, robust, inflexible outer surface and softer, flexible inner layers [20]. The topography of the skin is well known for many snake species [4,6,8,11,18,21-34]. Some of the previous authors suggested that the microstructure of the ventral surface could be of high relevance for the snake locomotion [6,8,10,11,34].

Lampropeltis getula californiae, the California King Snake (Figure 1a) was recently chosen as biotribological model, because this snake lives in habitats with a relatively wide variety of substrates and therefore the skin modifications are presumably adapted for locomotion not just for one type of substrate. The microstructures on ventral scales are regular tooth-like shaped caudally-oriented (parallel to the body axis of the snake, see Figure 1b) with anisotropic frictional properties [10]. However, the complexity of the microstructure of this species is limited to the extent that it is suitable for transfer in artificial epoxy resin surfaces. Such artificial surfaces were used in this study for closer frictional characterization.

Due to the fact that controlled variation of the surface microstructure of the biological model is not possible, the investigation of the influence of the microstructure on the frictional properties is almost impossible, because of the absence of a control surface made of the same material. By using epoxy resin polymer surfaces for tribological investigations, we gained the opportunity to transfer the snake skin microstructure and other types of surface topographies into a well defined material by using two-step moulding technique [35]. Snake-inspired microstructured polymer surface (SIMPS) was developed in cooperation with the company Leonhard Kurz Group Stiftung & Co (Fürth, Germany). Its geometry is based on that of the ventral snake scales of *L. g. californiae* [10] (Figure 1c).

In the previous study, we have characterised frictional properties of shed snake skin from *L. g. californiae* and the influence of the stiffness of the underlying skin layers and the surface roughness of the substrate on the frictional coefficient [10]. In the present study, we used a similar experimental setup to characterise frictional properties of the SIMPS. Additionally, frictional properties of a broad variety of epoxy surfaces with different types and dimensions of the microstructure were characterised to understand the influence of two general tribological phenomena on friction: (1) molecular interaction depending on the real contact area between surfaces and (2) the interlocking of surface asperities of both contacting surfaces [36-38]. This approach of investigating the contribution of different geometries and dimensions of microstructures to the friction coefficient was chosen, because the complex phenomenon of friction cannot be reduced to a single mechanism: It is rather a result of various simultaneously acting mechanisms at different scales [39-41] and this approach opens up opportunities (i) to draw conclusions on the influence of the microstructure of the snake skin on frictional properties and thereby to extend the knowledge on specific surface modifications due to the legless locomotion of snakes and (ii) to evaluate which particular features (shape, dimension, orientation) of the snake skin are worth of mimicking for technological applications.

Results

Surface morphology

The morphology of the SIMPS' microstructure is much alike the biological model regarding the structural wavelength and

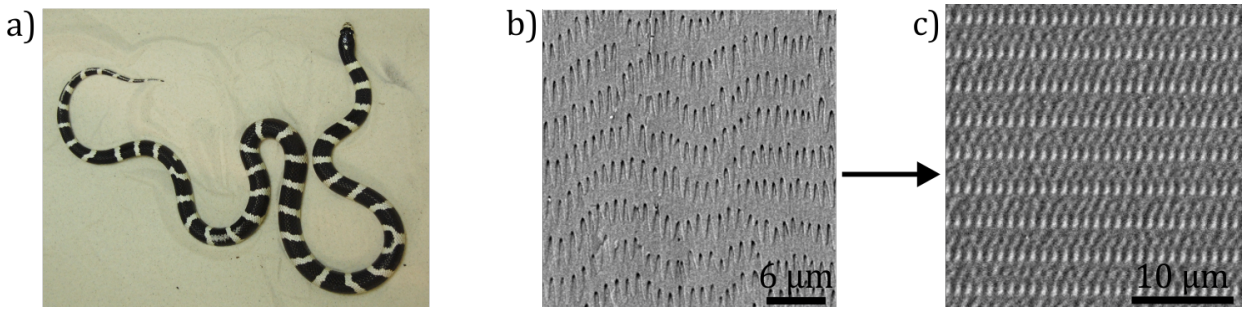

Figure 1: From the snake skin microstructure to the SIMPS. a) Photograph of the California King Snake (*Lampropeltis getula californiae*). SEM-micrographs of the snake skin of a ventral scale (b) and the SIMPS made of epoxy resin (c).

the mean width of denticulations. The length of the denticulations on SIMPS is shorter than that of the snake surface, but the overall dimensions of the microstructures are comparable (Table 1). The geometrical anisotropy in form of slopes is present (Figure 2a). The angle in the direction of the measurement along the SIMPS' microstructure is 47°, in the opposite direction 62°, and in lateral direction 55° (Table 2, Figure 2a).The quality of the moulded polymer surfaces was inspected by SEM and AFM (Figure 3). To ensure the absence of abrasion on the surface of the probe (a smooth glass ball), its surface was repeatedly examined by white light interferometer (data not shown).

As an indication for the maximum contact area occurring in our measurements we estimated the Hertzian contact area [42] of the glass sphere in contact with flat substrate according to the following parameters. The radius of the glass sphere was R_S = 0.5 mm. For the glass sphere, an elastic modulus of 70 GPa and a Poisson's ratio of 0.2 were assumed [43]. The elastic modulus of the epoxy resin was estimated to be 7 GPa and the Poisson's ratio to be 0.5 [43]. The geometric deformation between the sphere and flat surface under an applied normal force F was characterised by the indentation depth d and indentation radius a (Figure 4).

Table 2: Frictional coefficients (mean values and standard deviations) measured on SIMPS and angles of microstructure. Arrows show sliding directions of each individual measurement.

surface type	frictional coefficient, μ	angle
SIMPS - along the microstructure	0.165 ± 0.010	47°
SIMPS - against the microstructure	0.245 ± 0.019	62°
SIMPS - lateral to the microstructure	0.250 ± 0.018	55°

The contact radius a can be described by [37]:

$$a = \sqrt{Rd}\ . \tag{1}$$

Table 1: Dimensions of the microstructures of the ventral scales of the snake *L. g. californiae* and the SIMPS.

	structural wavelength of the microstructure [μm]	length of the denticulations [μm]	mean width of the denticulations [μm]
L. g. californiae	1.1 ± 0.1	2.5 ± 0.5	0.6 ± 0.1
SIMPS	1.2 ± 0.1	1.1 ± 0.2	0.7 ± 0.2

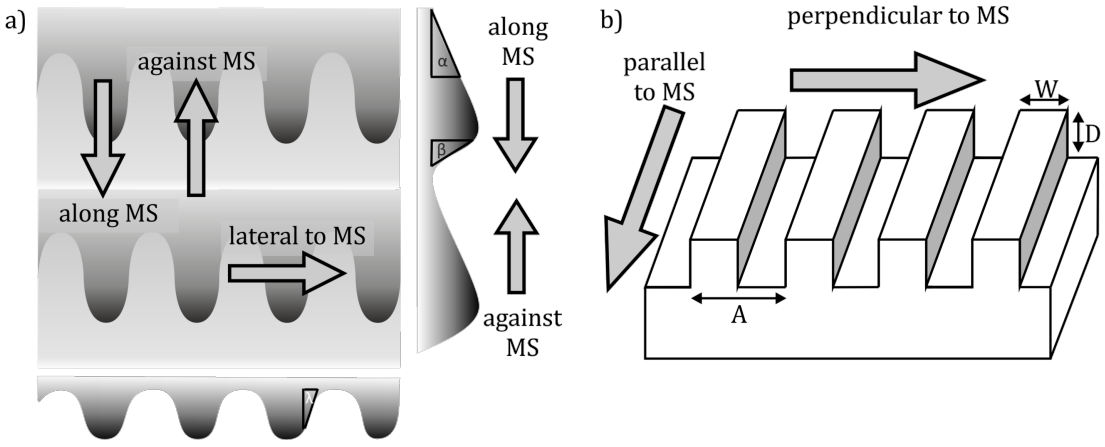

Figure 2: Scheme of the directionality of frictional measurements on polymer surfaces and its geometry. a) Directions of measurement relative to the topography of the SIMPS and angles of the microstructure depending on the measurement directions: α: along, β: against and λ: lateral to the microstructure. b) Diagram of the periodic groove-like profile. MS: microstructure, *A*: periodicity of the structure, *W*: width of the structure and *D*: depth of the grooves.

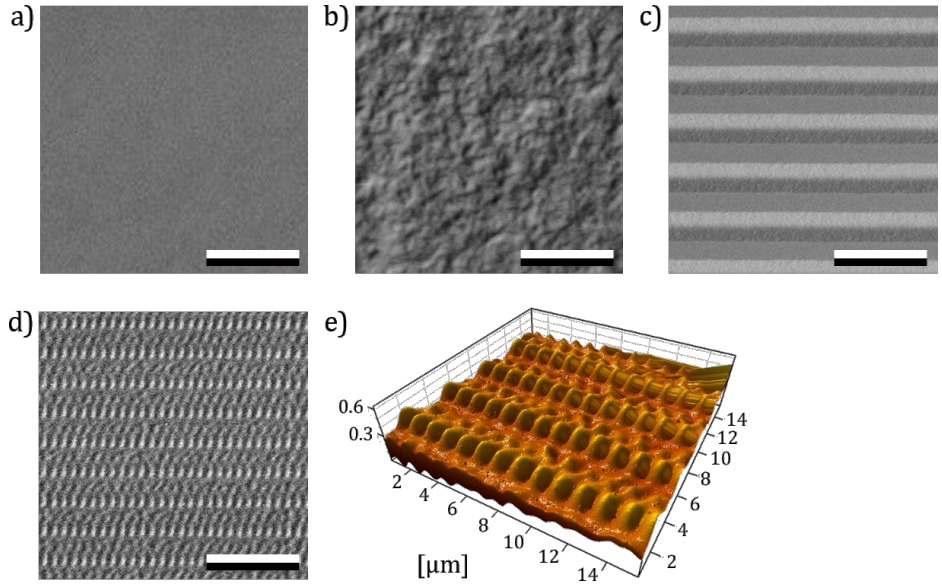

Figure 3: SEM (a–d) and AFM (e) micrographs of epoxy resin polymer moulds of different types of surfaces used in experiments. a) Smooth surface. b) Randomly rough surface with a grain size of 0.3 µm. c) Surface with periodically groove-like microstructures with a structural wavelength of 5 µm. d) SIMPS. Scale bars = 10 µm. e) 3D surface profile of the SIMPS.

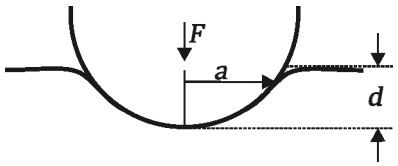

Figure 4: Contact area between sphere and flat elastic surface. *F*: Normal force. *a*: indentation radius. *d*: Indentation depth. Image modified after Popov [37].

The relationship between applied force and geometrical deformation can be described by the following formula [37]:

$$F = \frac{4}{3} E^* \times \sqrt{R} \sqrt[3]{d} \,, \tag{2}$$

where

$$\frac{1}{E^*} = \frac{1-\nu_S^2}{E_S} + \frac{1-\nu_F^2}{E_F} \,. \tag{3}$$

The calculated contact area between the tribo-pair on smooth and flat surfaces was 40 µm^2 corresponding to a contact radius of 3.5 µm and an indentation depth of 25 nm. The actual contact areas in case of the microstructured surfaces were indeed smaller. The following calculations are dealing with the geometric dimensions between the periodicity of the microstructures and the glass ball as counterpart, without applying a normal force (Figure 5). Detailed calculations are only possible for groove-like microstructure polymer surfaces (PGMS) due to the regular and well defined surface microstructures. Information on the exact geometry of PGMS topography is listed in Table 3. The measured details are described in Figure 2.

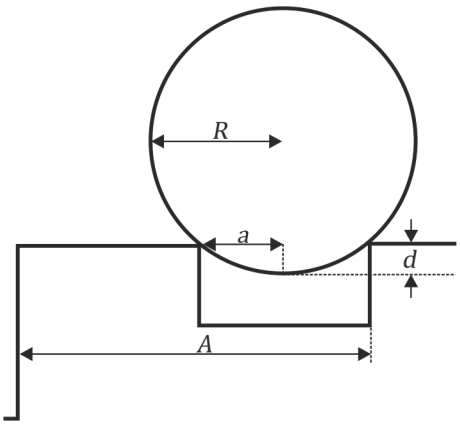

Figure 5: Geometric interaction between sphere and PGMS. *R*: sphere radius. *a*: indentation radius. *d*: indentation depth. The elastic response of the materials is excluded. Image modified after Sondhauß et al. [38].

The indentation depth h of the glass sphere was calculated according to the following formula modified after Sondhauß et al. [38]. With the indentation radius a and the periodicity of the structure A.

Table 3: Exact geometry of each PGMS pattern (mean values and standard deviations) measured by white-light interferometer. λ: pitch dimension, *A*: periodicity of the structure, *W*: width of the structure and *D*: depth of the grooves.

sample	*A* [µm]	*W* [µm]	*D* [µm]
PGMS - λ = 5 µm	5.3 ± 0.5	2.2 ± 0.1	2.2 ± 0.3
PGMS - λ = 25 µm	24.9 ± 1.8	13.1 ± 1.1	5.2 ± 0.4
PGMS - λ = 50 µm	50.0 ± 0.3	23.8 ± 2.3	17.7 ± 0.4
PGMS - λ = 100 µm	100.4 ± 1.9	49.4 ± 2.6	34.2 ± 1.2

$$a = \frac{A}{4} \tag{4}$$

and

$$r = \frac{a^2 + h^2}{2h}. \tag{5}$$

The calculated indentation depth of the glass ball into the microstructures without material deformation is listed in Table 4. It is necessary to emphasise that this theoretical indentation depth means the depth of penetration of the spherical cap just by geometry. The real indentation depth of the glass ball into the microstructures under a certain applied normal force is a combination of the material deformation and geometric conditions. Hence, this calculated penetration depth describes the minimal penetration depth between the tribo-pair.

It is necessary to notice that the spacial resolution of the microtribometer for cantilever deflection in normal direction is too low to detect the deflection due to the penetration of the glass ball into microstructures of pitch dimensions of 5 µm and 25 µm (Table 4). Conclusions can be drawn on the interaction between the glass sphere and the geometries of the other microstructured surfaces due to the comparison of surface roughness of the investigated surfaces (Table 5). Referring to

Table 4: Calculated indentation of the glass ball into the PGMS depending on their pitch dimension. The calculated values, which lay beyond the spacial resolution of the system in normal direction (50 nm), are highlighted in bold.

	PGMS - 5 µm	PGMS - 25 µm	PGMS - 50 µm	PGMS - 100 µm
indentation depth [µm]	**0.002**	**0.039**	0.156	0.625

Table 5: Surface roughness (R_a) of all investigated polymer surfaces. λ: pitch dimension. SD: standard deviation. For PGMS, the surface roughness was measured perpendicular to the microstructure for each type of pitch dimension. In parallel direction to the PGMS microstructures, the roughness was averaged over all pitch dimensions.

sample			R_a ± SD [µm]
	periodic groove-like microstructure	PGMS - λ = 5 µm	0.18 ± 0.022
	periodic groove-like microstructure	PGMS - λ = 25 µm	4.95 ± 0.369
	periodic groove-like microstructure	PGMS - λ = 50 µm	21.75 ± 0.262
	periodic groove-like microstructure	PGMS - λ = 100 µm	42.50 ± 1.465
	periodic groove-like microstructure	PGMS – on line	0.03 ± 0.005
	randomly rough surface	RRS - 0.3 µm	0.23 ± 0.004
	randomly rough surface	RRS - 1 µm	0.41 ± 0.013
	randomly rough surface	RRS - 3 µm	1.11 ± 0.106
	randomly rough surface	RRS - 9 µm	2.39 ± 0.072
	randomly rough surface	RRS - 12 µm	7.64 ± 0.127
	snake-inspired microstructured surface	SIMPS	0.10 ± 0.130
	smooth surface	smooth surface	0.02 ± 0.007

the threshold of detectable microstructure dimensions and the corresponding roughness value, it can be concluded that the interaction between the investigated surfaces (except for PGMS - 50 µm and PGMS - 100 µm) and the sphere is not exclusively caused by a vertical interlocking due to indenting into the microstructure.

Frictional measurements

The microtribological measurements on the rough polymer surfaces (Figure 6) showed the lowest frictional coefficient (0.192 ± 0.007) at a grain size of 9 µm. Comparing this with the one measured on the smooth polymer surface (0.318 ± 0.024), a reduction in friction of about 40% was observed. The frictional coefficients decreased from the highest value on the smooth surface to the minimum at a specific grain size of 9 µm and further increased at a grain size of 12 µm. All frictional coefficients differed significantly from each other, except between surfaces with grain sizes of 0.3 µm/1 µm, 1 µm/12 µm, and 3 µm/9 µm (Figure 6b).

The frictional measurements on the periodical groove-like microstructure polymer surfaces (PGMS) were performed in two perpendicular sliding directions. The measurements perpendicular to the orientation of the microstructure with structural wavelength dimensions of 25 µm, 50 µm, and 100 µm revealed a lower frictional coefficient, if compared to the smooth polymer surface. The coefficient, measured for a structural wavelength of 5 µm, was very similar to the one of the smooth polymer surface. A minimum of friction was observed at a wavelength dimension of 25 µm. In this case, the frictional coefficient was 49% lower than that for the smooth surface (Figure 7).

If it is compared to the smooth surface, a reduction in friction of 44% was observed when measuring parallel to microstructure of the PGMS with a structural wavelength of 100 µm, but no minimum of frictional coefficient was detected within the parallel measurements (Figure 7). There was no statistically significant difference between the surfaces with different wavelengths. An interlocking effect, like the one detected in perpendicular direction, was not observed in parallel measurements. Nevertheless, any type of microstructure provided a statistically significant reduction in frictional coefficient, if compared with the smooth control surface (Figure 7b).

Frictional measurements on SIMPS showed anisotropic frictional properties and a reduction of the frictional coefficient of 48% measured along the microstructures, if it is compared to the smooth surface. There was significant difference between frictional coefficients on the smooth surface and the measurements against to the microstructure of the SIMPS and in the lateral directions (Figure 8). A statistically significant anisotropy was found between the measurement directions (i) “along” versus “against” the microstructure and (ii) “along”

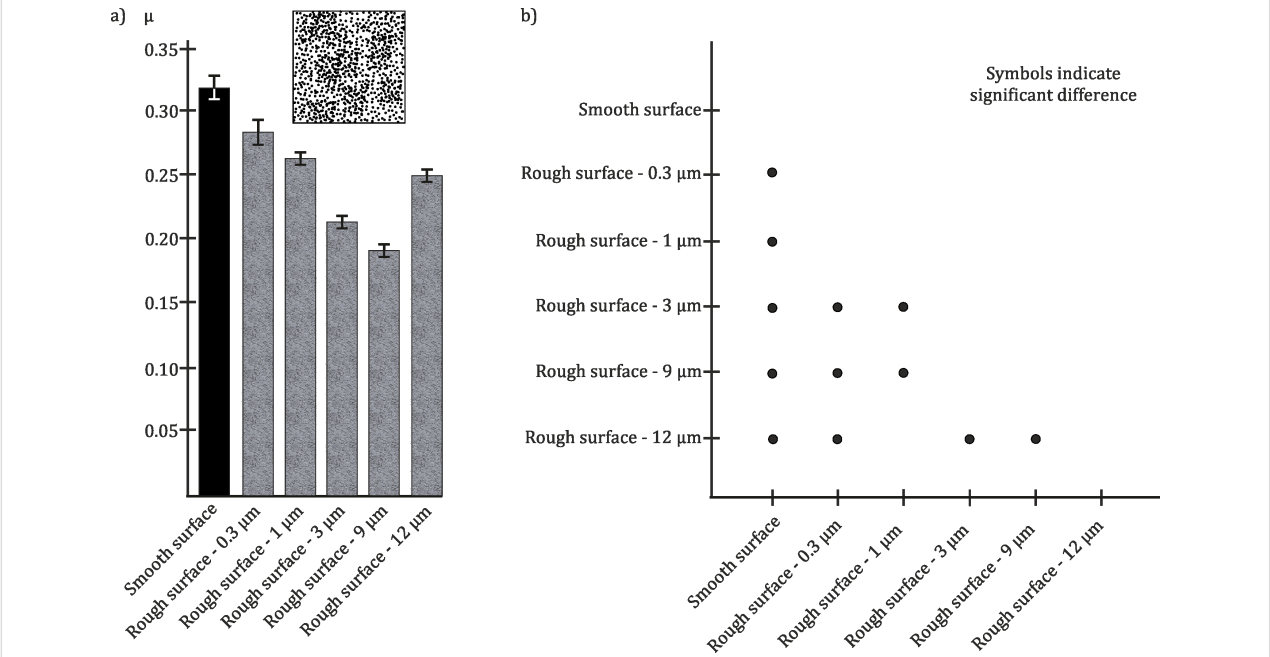

Figure 6: a) Results of tribological characterization of microstructured polymer surfaces in contact with a smooth glass ball. Average frictional coefficients (µ) and standard deviations are shown. Black column: smooth surface as reference. Gray columns: epoxy resin moulds of randomly rough surface with different grain size (R_a: 0.3 µm, 1 µm, 3 µm, 9 µm, and 12 µm). b) Multiple comparison graph of the results presented in a). Dots indicate statistically significant differences between samples.

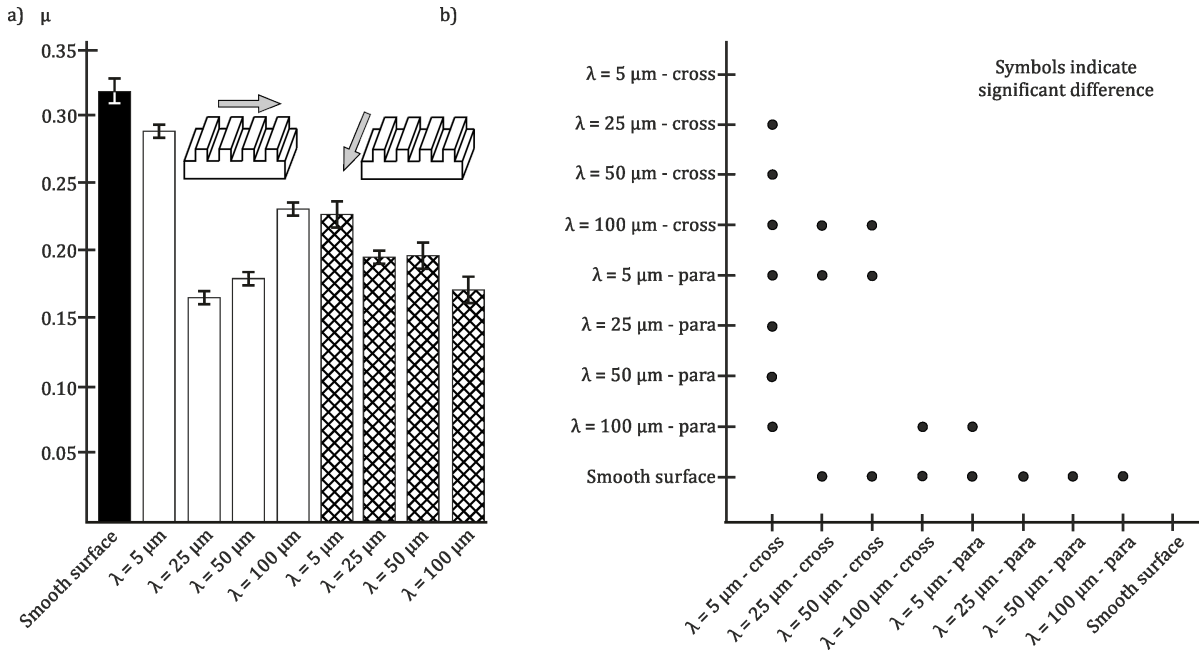

Figure 7: a) Results of tribological measurements of PGMS with different wavelengths (λ) in contact with a glass ball. The dimensions (structural wavelengths) of microstructures are 5 μm, 25 μm, 50 μm, and 100 μm, respectively. To investigate the influence of the geometry of the microstructure on frictional properties, measurements were performed in two perpendicular sliding directions. Black column: smooth surface as reference. White columns: sliding direction perpendicular to the groove pattern. Patterned columns: sliding direction parallel to the grooves. Average frictional coefficients (μ) and standard deviations are shown. b) Multiple comparison graph of the results presented in a). Dots indicate statistically significant differences between samples.

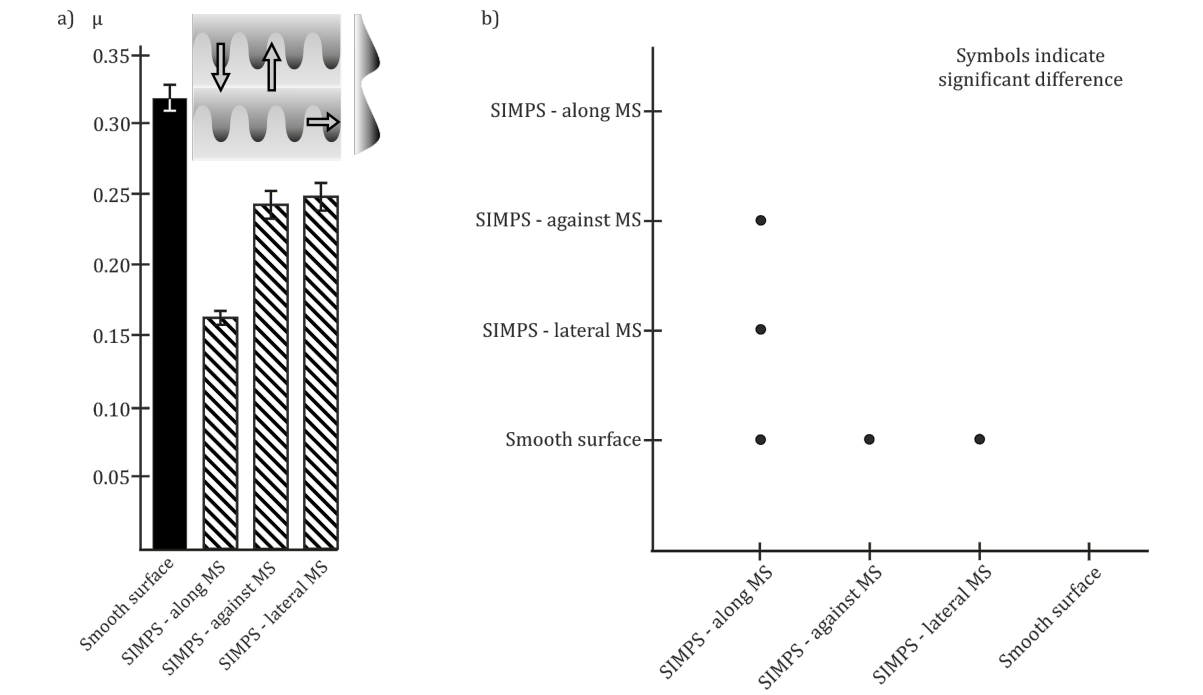

Figure 8: a) Results of tribological measurements of SIMPS in contact with a glass ball. Black column: smooth surface as reference. Hatched columns: SIMPS. To investigate the influence of the anisotropic geometry of the microstructure on frictional properties, measurements were performed in three different sliding directions. MS: microstructure. Average frictional coefficients (μ) and standard deviations are shown. b) Multiple comparison graph of the results presented in a). The dots indicate statistically significant differences between samples.

versus “lateral” to the microstructure orientation (frictional coefficient was reduced by 33% and 34%, respectively). All results of frictional measurements are listed in Table 6.

Table 6: Frictional coefficients (mean values and standard deviations) of all examined polymer surfaces. The arrows show the sliding directions of each individual measurement.

surface type	frictional coefficient, μ
smooth surface	0.318 ± 0.024
randomly rough surface - 0.3 μm	0.284 ± 0.027
randomly rough surface - 1 μm	0.264 ± 0.008
randomly rough surface - 3 μm	0.214 ± 0.011
randomly rough surface - 9 μm	0.192 ± 0.007
randomly rough surface - 12 μm	0.250 ± 0.013
 SIMPS - along the microstructure	0.165 ± 0.010
 SIMPS - against the microstructure	0.245 ± 0.019
 SIMPS - lateral to the microstructure	0.250 ± 0.018
 λ = 5 μm	0.290 ± 0.006
 λ = 25 μm	0.167 ± 0.008
 λ = 50 μm	0.181 ± 0.006
 λ = 100 μm	0.232 ± 0.006
 λ = 5 μm	0.228 ± 0.016
 λ = 25 μm	0.196 ± 0.011
 λ = 50 μm	0.198 ± 0.022
 λ = 100 μm	0.172 ± 0.024

Discussion

SIMPS with their anisotropic microstructure geometry exhibited anisotropic frictional properties similar to those of the biological model [5,8,10,11]. Additionally, SIMPS demonstrated a considerable reduction of the frictional coefficient, if compared to the same polymer with smooth surface.

Different kinds of microstructured surfaces with isotropic and anisotropic microstructure geometry of different dimensions were examined to gain a deeper understanding of how frictional properties are influenced by surface topography. The results obtained can be explained by mechanical interactions between surfaces at two scales: at a nano scale by the influence of the real contact area, and at a micro scale by an interlocking of the probe with the valleys of the structured counter surface. These findings indicate that the dimension of the best friction minimizing microstructure reduces the real contact area with the tribo-pair as far as possible without enabling mechanical interlocking. Nevertheless, as Baum et al. [44] have shown, frictional behaviour in respect to stick–slip behaviour is strongly influenced by the dimension of surface microstructures even when no mechanical interlocking occurs. One possible explanation for this phenomenon is that the microornamentation causes a critical stiction length, which leads to a periodical variation in real contact area between the tribo-pair causing friction-induced vibrations. Baum et al. [44] investigated this effect by fast Fourier transformation in detail and have shown that frictional behaviour is strongly influenced by real contact area, the possibility of mechanical interlocking, but beyond these parameters, also a critical stiction length due to microstructure dimension is of importance. Furthermore Sondhauß et al. [38] investigated the influence of microstructures in a smaller dimension on frictional properties. By using a friction force microscope, they have shown that the macroscopic interlocking of the probe tip and the surface microstructure leads to an increase of the frictional coefficient in a dry sliding system. This increase is caused by the interlocking, when the probe tip leaves the valleys of the microstructure and “climbs up” its edge. Hazel et al. [11] found a comparable situation for the skin surface of snakes. Sondhauß et al. [38] reported a 50% reduction in friction coefficient measured for the contact pair sphere–microstructure, when interlocking was not possible. A similar reduction in friction was also found in our experiments for frictional measurements on PGMS in perpendicular direction to the microstructure at a dimension of 25 μm. Sondhauß et al. [38] and Baum et al. [44] concluded that the frictional response is dominated by the geometry of the tribo-pair. Based on these assumptions they stated that moderate modification of surface roughness can improve the tribological performance of meso scale contacts.

The influence of surface roughness and thereby the contact area between the tribo-pair have been controversially discussed in literature for a long period of time. Based on Amontons' friction law [36,37,39-41,45], it is stated, that friction is proportional to the normal force and independent of contact area, thereby the influence of the roughness of the friction is minor, as long, as the roughness is low. This assumption can be confirmed for macroscopic frictional contacts [36,37,39,41,45]. Later it was stated that the real contact area between a tribo-pair

is formed by multi-asperity contacts that enable a molecular interaction of the surface molecules and constitutes only a small percentage of the macroscopic contact area [36,37,39,45,46]. These close contacts are called junctions and the sum of all junctions forms the real contact area. This theory also explains the correlation between frictional coefficient and applied normal force, because an increase of normal force leads to an increase of the area of each asperity in contact and thereby to an increase of the molecular interaction between the surfaces. The degree to which the real contact area is influence by the load force depends strongly on material properties [41,46-48]. These properties are also affected by the surface geometry [49]. There are numerous experimental studies on the roughness effect on friction of technical surfaces. Etsion [50] and Kovalchenko et al. [51] investigated the role of the microstructuring with regular circular holes in micrometer dimensions on friction and concluded that artificial microstructuring of surfaces is a possibility to enhance the control of frictional system behaviour. They showed that a higher density of dimples lead to a stronger abrasive wear on the tribo-pair. Nevertheless by such kind of surface modification, they were able to reduce the frictional coefficient. A comparison of these finding with the results of our study is only possible in a limited way, because they used for their investigation a different machinery type (pin-on-disk friction machine), the micro dimples were much bigger than our microstructures (diameter: 58–78 µm) and they investigated a lubricated system. The observation of the effect that a specific surface roughness leads to the enhancement of the friction coefficient is congruent with ours, nevertheless it is necessary to notice that their ratio between spherical probe and line width (sphere diameter: 2.3 µm and 7.9 µm and line width: 0.5 µm to 3.5 µm) is different from our sphere/line width ratio (sphere diameter: 1 mm, line width: 5 µm to 100 µm).

Marchetto et al. [52] reported a reduction of the frictional coefficient measured perpendicular to linearly-grooved microstructured surfaces to about 36% in comparison to a smooth surface. Frictional measurements in two different directions (parallel and perpendicular to the line-grooved microstructure) showed equivalent values, meaning there were no anisotropic frictional properties. The reduction in friction is in accordance to our findings, but it is necessary to mention, that the contact geometry in Marchetto et al. [52] is different to our experimental setup, because they used a cut-off AFM cantilever tip. One can assume that a decrease in frictional coefficient is due to the reduction of adhesive components of the frictional mechanisms [51,52]. Another approach to explain the reduction in frictional coefficient on many microstructured surfaces could be the possibility of trapping of loose wear particles within the microstructures and thereby the avoidance of further surface ploughing by these wear particles [38,48,50,53].

The gap between biologically and artificially microstructured surfaces can be closed by interpreting the microstructure of the SIMPS as lines and spaces, in which the lines are periodically interrupted by the elevated tips (denticulations). The SIMPS microstructure is based on shapes and dimensions of the microornamentation of the biological model, the ventral scales of the snake *L. g. californiae*. For the biological model, it was previously assumed, that the caudal tips of denticulations are elevated, so the snake can generate propulsion due to the interlocking of its microstructure with surface asperities. The results of the study of the snake skin's microstructure by using atomic force microscopy (AFM) and confocal laser scanning microscopy (CLSM) showed that the anisotropic geometry of the surface structure is not dominated by the elevation of the caudal tips of the denticulations as previously found on *Boa constrictor* skin [11], but rather by depressions located cranially between the denticulations [10]. The dimension of the microstructure on the SIMPS is quite similar to those of the ventral scales of the investigated snake species, but there is a difference in topography: In SIMPS, the caudal tips are slightly elevated, whereas in *L. g. californiae* they are not.

In the present study, SIMPS showed a similar level of frictional anisotropy as the uncushioned snake skin [10], enforcing the hypothesis that the snake-like surface microstructure contributes to the frictional anisotropy. Previous studies have demonstrated that frictional coefficients can be controlled by using different kinds of microstructures on technical surfaces [38,50-52,54] the specific geometry of the microstructure was investigated by Wang et al. [55], Galda et al. [56], Yu et al. [57], Prodanov et al. [58], Gachot et al. [59] and Filippov and Gorb [60]. The role of the specific geometry of the microstructure and its angle in relation to the direction of sliding was in focus of Abdel-Aal [61]. Anisotropic frictional properties, shown in the present paper, can be explained by mechanical interlocking of multiple micro asperities and by the variation of the contact area depending on the angle of the microstructure. This statement is strengthened by the following observation. The angle along the microstructure is 25% smaller than in the opposite and 17% smaller than in lateral direction. The frictional measurements on SIMPS showed a similar distribution of the frictional coefficients measured along and against the microstructure, but not in lateral direction compared to both other directions (Table 6). Despite the fact that frictional anisotropy is not completely congruent to the angle distribution, it can be derived, that the slope of surface topography influences frictional properties, as proposed by, e.g., Abdel-Aal [61], Persson [36] and Popov [37].

Our experiments reveal an influence of the surface roughness on the friction of dry polymeric systems in contact with smooth

surface: In general, we recorded lower values on rough surfaces, if compared to the smooth reference surface. It can be primarily explained by the lower real contact area between the tribo-pair. The data on surfaces with different roughness show a decrease of frictional coefficient with growing grain size until a minimum friction is reached at 9 μm. The observed effect of a decreasing frictional coefficient, μ, with increasing roughness is reversed at 12 μm grain size presumably by another type of tribo-pair interaction. While the decreasing part of the curve can be explained by the reduction of the contact area of the tribo-pair, the increasing part is rather due to the interlocking between the sphere and large surface asperities. The indentation radius of the glass ball on the polymer surface was 3.5 μm, which should be sufficient for interlocking with a rough surface having a grain size of 12 μm and a roughness (R_a) of 7.64 μm. The interlocking effect is presumably rather strong here and obviously reverses the friction minimizing effect due to the decreased contact area of rough surfaces. These effects have been described by various authors investigating frictional behaviour of technical surfaces [38,52,54] or biological surfaces [6,11].

In order to understand the influence of the periodic anisotropic surface roughness, further frictional measurements on periodically groove-like microstructured polymer surfaces were performed here. Frictional measurements perpendicular to the periodical groove-like microstructure showed a maximal reduction of μ to 49% at a structural wavelength of 25 μm, if compared to the smooth reference. The results obtained on PGMS with a structural wavelength of 5 μm were similar to those on the smooth surface. We assume that frictional behaviour of the latter contact pair can be explained by the relatively big real contact area. At λ = 25 μm, the contact area is presumably much smaller than at λ = 5 μm. Measurements on PGMS with larger λ (50 and 100 μm) showed an increase of the frictional coefficient. Similar to the experiments on polymer surfaces with different roughness (see above), these differences in frictional behaviour result from the interplay between two effects: (1) the decreasing of the real contact area at small λ and (2) the increasing of the mechanical interlocking between the sphere and surface topography at large λ (Figure 7).

Measurements in the direction parallel to the microstructure excluded the possibility of interlocking and were dominated by the real contact area effect, which was rather constant for samples with different wavelengths. The data do not show statistically significant differences of μ with an increasing wavelength. By comparing the results obtained in measurements perpendicular and parallel to the PGMS, it is possible to consider both physical phenomena which influence the friction in a dry polymeric system: the real contact area and mechanical interlocking between the tribo-pair. By comparison of the results obtained in both directions within the different wavelength of microstructures, a significant difference was detected only for λ = 5 μm. It can be deduced that interlocking with the microstructure occurs, but its effect on frictional coefficient is minor (no significant difference, but variations in absolute frictional coefficient). In a comparable experimental setup, Yu and Wang [57] investigated whether anisotropic frictional properties do change with topographic parameters, and, thereby, whether the modification of microstructures is a way to modulate friction. They used groove-textured surfaces and performed frictional measurement on two different combinations of sphere and microstructure dimension. For the combination of a tungsten carbide sphere (diameter = 800 μm) and a microstructured silica surface (λ = 278 nm) the frictional coefficient parallel to the microstructure was higher, than in the perpendicular direction. The second investigated frictional pair was a steel ball (diameter = 800 μm) in contact with a microstructured tungsten carbide surface (λ = 220 μm). For this combination, the frictional coefficients in both directions were similar, but in the perpendicular direction they were slightly higher. Similar experiments were done by Marchetto et al. [38], during which they also observed the absence of anisotropy on periodically groove-like microstructure, but the influence of different dimensions of microstructures on this effect was not investigated.

Our above experiments have demonstrated dimensional effects of microstructure on friction and strong effect of their shape. There is a trend for the reduction of friction with increasing dimensions of the microstructure until the interlocking effects start to occur. It has been previously shown that the attachment ability of insects [62-65] and geckos [66] is strongly dependent on the surface roughness. Yu et al. [67] demonstrated that surface roughness also strongly affects the performance of gecko-inspired adhesives. All these authors have shown that there is a critical roughness, on which the attachment ability (both adhesion and friction) is strongly reduced. The interlocking effect, contributing to the friction increase, was observed taking place at larger dimensions of the microstructure, as shown for frictional measurements perpendicular to the PGMS with a structural wave length of both 50 μm and 100 μm.

A global comparison of all samples studied shows that minimal frictional coefficients were obtained (1) perpendicular to the PGMS with a structural wavelength of 25 μm, (2) on a surface grain size of 9 μm, (3) on SIMPS measured along the microstructure and (4) parallel to the PGMS with a structural wavelength of 100 μm. What do these microstructured surfaces have in common? Most of them (1)–(3) possess a meso scale surface roughness, resulting in the best compromise between a

reduction of the real contact area (and therefore reduction of adhesion) and the prevention of the interlocking effect. The only exception (4) was the measurement parallel to the PGMS with a structural wavelength of 100 µm, because here geometrical interlocking was not possible. In this case, it would be most interesting to investigate in the future, if a further minimization of the frictional coefficient would be possible, if the periodicity of the microstructures would be so wide that the sphere would only be in contact in between two lines (something similar to the effect of micro rails).

We showed that the reduction of the real contact area leads to a minimization of the frictional coefficient, but this possibility of optimisation is limited by an interlocking of surface structures. This conclusion is in accordance to Marchetto et al. [52] and Sondhauß et al. [38]. Because the frictional optimisation in a dry sliding frictional system strongly depends on the dimension and shape of surface asperities of the tribo-pair, an optimisation of the frictional surfaces by surface texturing must be done individually for each type of friction contact pair, as previously proposed [50]. However, the present work provides some ideas for the implementation of surface microstructures of particular dimensions and shape for the reduction of friction of polymeric systems. Additionally, we have clearly shown that the use of inspiration from sliding biological tribosystems, such as snake skin, may provide a short cut to development of novel tribologically optimised polymer surfaces. However, in long term experiments, the geometry of the surface microstructure can undergo some evolution due to abrasive wear, and therefore enhanced frictional properties can change due to the degeneration of surfaces [50,51]. However, the wear of the SIMPS was not in the focus of this study, but should be done in future investigations.

Experimental

Microstructured surfaces

Friction measurements were performed on four different types of microstructured surfaces. The first type of surfaces (control) originated from the mould of a smooth glass surface (Figure 3a). The second type of surfaces originated from moulds of polishing paper (FibrMet Discs, Buehler GmbH, Düsseldorf, Germany) with different grain sizes (R_a: 0.3 µm, 1 µm, 3 µm, 9 µm, and 12 µm) (Figure 3b). The master for the third type of surfaces was produced from zirconium oxide surface microstructured by femtosecond laser ablation. Structuring was performed with a commercially available amplified Ti:Sapphire femtosecond laser system (Femtopower Compact Pro, Femtolasers GmbH, Austria). The systems delivers sub-30-fs pulses at a central wavelength of 800 nm with a pulse energy of up to 1 mJ, and a repetition rate of 1 kHz. An x–y motorized translation stage (Physik Instrumente GmbH, Germany) was used for sample positioning and translation. A computer controlled LCD element was used for setting the laser pulse energy. It features periodic groove-like microstructures (PGM) with different structural wavelengths of 5 µm, 25 µm, 50 µm, and 100 µm (Figure 3c). The fourth type of surfaces was inspired by the microornamentation of the ventral scales of the snake *L. g. californiae* (snake-inspired microstructured polymer surface, SIMPS) (Figure 3d). The masters were produced by the Leonhard Kurz Group Stiftung & Co. (Fürth, Germany) by using e-beam greytone lithography with a negative photoresist. Afterwards nickel copies were manufactured through an electroplating process.

Replication of the microstructures was performed by using a two-step moulding technique according to Gorb [35]. The surface that ought to be replicated was used as a master and, in the first step, was covered with fluid polyvinylsiloxane (PVS), a two-component silicone, which polymerizes within minutes at room temperature (Coltène President light body, Coltène Whaledent Dentalvertriebs Ltd., Constance, Germany). The obtained negative cast was filled out by Spurr's low-viscosity resin [68]. The polymerization of the resin took place overnight at 70° C. The resin (Polysciences Inc., Eppelheim, Germany) consists of nonenyl succinic anhydride (NSA) (61.3%), 3,4-epoxycyclohexylmethyl-3,4-epoxycyclohexylcarboxylate (ERL 4221) (23.6%), diglycidyl ether of polypropyleneglycol (D.E.R. 736) (14.2%) and *N*,*N*-dimethylaminoethanol (DMAE) (0.9%).

Visualization

The microstructure of the obtained polymer surfaces were visualized by means of a scanning electron microscope (SEM). The SEM investigations were performed with a Hitachi S-4800 (Hitachi High-Technologies Corporation, Tokyo, Japan) at an acceleration voltage of 2–3 kV and a Hitachi TM3000 (Hitachi High-Technologies Corporation, Tokyo, Japan) at an acceleration voltage of 5 kV. Prior to visualization, the material was fixed to the aluminium stub with a carbon-bearing adhesive pad and sputter-coated with a 20 nm thick gold-palladium (4:1) layer by using a high vacuum sputter coater Leica EM SCD500 (Leica Microsystems GmbH, Wetzlar, Germany). Additionally, for quick 3D surface observations a white-light interferometer (New View 6000, ZygoLOT, Darmstadt, Germany) without the sputter coating was used.

As described in [44], the detailed characterization of the surface topography was performed by a NanoWizard® atomic force microscope (JPK Instruments), mounted on an inverted light microscope (Zeiss Axiovert 135, Carl Zeiss MicroImaging GmbH). The SIMPS were imaged by using the intermittent contact mode of the AFM. The error channel (also known as the amplitude channel) visualizes the change in damping of the

cantilever amplitude while scanning the surface. Only images obtained with the error channel are shown, because this visualization method is helpful to gain a more vivid imaging of the surface topography. Scans were carried out at a 1 Hz scan rate and a resolution of 1024 × 1024 pixels with an intermittent contact mode cantilever (c = 50 N·m^{-1}, NST-NCHF, Nascatec GmbH, Stuttgart, Germany), at ambient conditions (room temperature 24° C, relative humidity 41%). NanoWizard® SPM software 3.3.23 (JPK Instruments) was used to obtain AFM images and NanoWizard® image processing software 3.3.25 was applied to extract 3D surface profiles. The variables of microstructured surfaces were measured from digital images by means of the image analysis software SigmaScanPro 5.0 (SPSS Inc., Chicago, USA).

Frictional measurements

Frictional coefficients, μ, were defined according to the Amontons' friction law: $\mu = F_t/F_n$ (F_t: tangential force; F_n: normal force). The experimental parameters of the frictional measurements were chosen as described before [10], except for the usage of a rough glass ball. The E-moduli of the polymerized Spurr resin and the glass ball were 7 GPa and 70 GPa, respectively [43]. The maximum contact area between the glass ball and a smooth polymer under the given load was estimated according to the Hertz model [42].

To characterise frictional properties of the SIMPS, the measurements were performed in three different sliding directions: along the anisotropic microstructure (i), against the anisotropic microstructure (ii), and in the lateral direction, perpendicular to both other directions (iii) (Figure 2). The frictional properties of the periodic groove-like patterned surface (PGMS) were characterised in two different directions only: parallel to the microstructure (i) and perpendicular to the microstructure (ii) (Figure 2b).

Individual measurements were repeated 15 times on each micro patterned surface and on the smooth reference surface. The other surfaces were tested five times each. Each measurement was performed on a new area of the surface to minimize the influence of abrasion. Obtained data were statistically analysed with SigmaPlot 11.0 software (SPSS Inc., Chicago, USA). Kruskal–Wallis one way ANOVAs followed by Holm–Sidak tests with a significance level of $p < 0.05$ were performed.

Acknowledgements

The authors are thankful to Alexander Kovalev for fruitful discussions, Henrik Peisker and Kirstin Dening for technical support while using the AFM. This work was funded by the Federal Ministry of Education and Research, Germany within the BIONA program (01 RB 0812A) to SNG.

References

1. Mattison, C. *The encyclopedia of snakes;* Facts on File: New York, USA, 1995.
2. Mattison, C. *Schlangen;* Dorling Kindersley Publishing: London, UK, 1999.
3. Greene, H. W. *Snakes: the evolution of mystery in nature;* University of California: London, UK, 1997.
4. Renous, S.; Gasc, J. P.; Diop, A. *Fortschr. Zool.* **1985,** *30,* 487–489.
5. Gray, J.; Lissmann, H. W. *J. Exp. Biol.* **1950,** *26,* 354–367.
6. Berthé, R. A.; Westhoff, G.; Bleckmann, H.; Gorb, S. N. *J. Comp. Physiol., A* **2009,** *195,* 311–318. doi:10.1007/s00359-008-0408-1
7. Marvi, H.; Hu, D. L. *J. R. Soc., Interface* **2012,** *9,* 3067–3080. doi:10.1098/rsif.2012.0132
8. Abdel-Aal, H. A.; Vargiolu, R.; Zahouani, H.; El Mansori, M. *Wear* **2012,** *290–291,* 51–60. doi:10.1016/j.wear.2012.05.015
9. Hu, L.-D.; Nirody, J.; Scott, T.; Shelley, M. J. *Proc. Natl. Acad. Sci. U. S. A.* **2009,** *106,* 10081–10085. doi:10.1073/pnas.0812533106
10. Baum, M. J.; Kovalev, A. E.; Michels, J.; Gorb, S. N. *Tribol. Lett.* **2014,** *54,* 139–150. doi:10.1007/s11249-014-0319-y
11. Hazel, J.; Stone, M.; Grace, M. S.; Tsukruk, V. V. *J. Biomech.* **1999,** *32,* 477–484. doi:10.1016/S0021-9290(99)00013-5
12. Bowden, F. P.; Tabor, D. *The friction and lubrication of solids;* Clarendon Press: Oxford, 1986.
13. Scherge, M.; Gorb, S. N. *Biological micro- and nanotribology;* Springer: Berlin, 2001. doi:10.1007/978-3-662-04431-5
14. Landmann, L. *J. Morphol.* **1979,** *162,* 93–125. doi:10.1002/jmor.1051620107
15. Landmann, L.; Stolinski, C.; Martin, B. *Cell Tissue Res.* **1981,** *215,* 369–382. doi:10.1007/BF00239121
16. Lillywhite, H. B.; Maderson, P. F. A. Skin structure; permeability. In *Biology of the Reptilia;* Gans, C.; Pough, F. H., Eds.; Physiology C, Physiological Ecology, Vol. 12; Academic Press: New York, USA, 1982; pp 379–442.
17. Lillywhite, H. B. *J. Exp. Biol.* **2005,** *209,* 202–226. doi:10.1242/jeb.02007
18. Alibardi, L. *J. Morphol.* **2005,** *264,* 178–190. doi:10.1002/jmor.10326
19. Lillywhite, H. B.; Menon, J. G.; Menon, G. K.; Sheehy, C. M.; Tu, M. C. *J. Exp. Biol.* **2009,** *212,* 1921–1929. doi:10.1242/jeb.028704
20. Klein, M.-C. G.; Gorb, S. N. *J. R. Soc., Interface* **2012,** *9,* 3140–3155. doi:10.1098/rsif.2012.0479
21. Leydig, F. *Arch. Mikrosk. Anat.* **1873,** *9,* 753–794. doi:10.1007/BF02956189
22. Picado, C. *Bull. Antivenin Inst. Am.* **1931,** *4,* 104–105.
23. Hoge, A. R.; Santos, P. S. *Science* **1953,** *118,* 410–411. doi:10.1126/science.118.3067.410
24. Maderson, P. F. A. *Br. J. Herpetol.* **1964,** *3,* 151–154.
25. Maderson, P. F. A. The structure; development of the squamate epidermis. In *The biology of the skin and hair growth;* Lyne, A. G.; Short, B. F., Eds.; Angus Robertson: Sydney, Australia, 1965; pp 129–153.
26. Maderson, P. F. A. *Am. Zool.* **1972,** *12,* 159–171.
27. Price, R. M. *J. Herpetol.* **1982,** *16,* 294–306. doi:10.2307/1563721
28. Bea, A.; Fontarnau, R. The study of the sloughing cycle in snakes by means of scanning electron microscopy. In *Studies in herpetology;* Robek, Z., Ed.; Charles University: Prague, Czechoslovakia, 1968; pp 373–376.
29. Irish, F. J.; Williams, E. E.; Seling, E. *J. Morphol.* **1988,** *197,* 105–126. doi:10.1002/jmor.1051970108

30. Chiasson, R. B.; Lowe, C. H. *J. Herpetol.* **1989,** *23,* 109–118. doi:10.2307/1564016
31. Price, R. M.; Kelly, P. *J. Herpetol.* **1989,** *23,* 244–261. doi:10.2307/1564446
32. Arnold, E. N. *J. Morphol.* **2002,** *252,* 145–169. doi:10.1002/jmor.1096
33. Gower, D. J. *J. Morphol.* **2003,** *258,* 249–268. doi:10.1002/jmor.10147
34. Schmidt, C. V.; Gorb, S. N. In *Snake Scale Microstructure: Phylogenetic Significance and Functional Adaptations;* Paulus, H. F., Ed.; Zoologica, Vol. 157; Schweizerbart Science Publishers: Stuttgart, Germany, 2012.
35. Gorb, S. N. *Microsc. Today* **2007,** *3,* 44–46.
36. Persson, B. N. J. *Sliding friction: physical principles and applications,* 2nd ed.; Springer-Verlag: New York, USA, 2000. doi:10.1007/978-3-662-04283-0
37. Popov, V. L. *Contact mechanics and friction – Physical principles and Applications;* Springer-Verlag: Berlin, Heidelberg, Germany, 2010. doi:10.1007/978-3-642-10803-7
38. Sondhauß, J.; Fuchs, H.; Schirmeisen, A. *Tribol. Lett.* **2011,** *42,* 319–324. doi:10.1007/s11249-011-9776-8
39. Bowden, F. P.; Tabor, D. *The friction and lubricating of solids;* Clarendon Press: Oxford, UK, 1950.
40. Bhushan, B. *Introduction to Tribology;* Wiley: New York, USA, 2002.
41. Nosonovsky, M.; Bhushan, B. *Mater. Sci. Eng., R* **2007,** *58,* 162–193. doi:10.1016/j.mser.2007.09.001
42. Hertz, H. *J. Reine Angew. Math.* **1881,** *92,* 156–171.
43. Peisker, H.; Gorb, S. N. *J. Exp. Biol.* **2010,** *213,* 3457–3462. doi:10.1242/jeb.043661
44. Baum, M. J.; Heepe, L.; Gorb, S. N. *Beilstein J. Nanotechnol.* **2014,** *5,* 83–97. doi:10.3762/bjnano.5.8
45. Lorenz, B.; Persson, B. N. J.; Dieluweit, S.; Tada, T. *Eur. Phys. J. E* **2011,** *34,* 129. doi:10.1140/epje/i2011-11129-1
46. Persson, B. N. J. *J. Phys.: Condens. Matter* **2012,** *24,* 095008. doi:10.1088/0953-8984/24/9/095008
47. Carbone, G.; Mangialardi, L.; Persson, B. N. J. *Phys. Rev. B* **2004,** *70,* 125407. doi:10.1103/PhysRevB.70.125407
48. Popov, V. L.; Filippov, A. É. *Tech. Phys. Lett.* **2010,** *36,* 525–527. doi:10.1134/S1063785010060118
49. Yu, C.; Wang, Q. J. *Sci. Rep.* **2012,** *2,* No. 988. doi:10.1038/srep00988
50. Etsion, I. *J. Tribol.* **2005,** *127,* 248–253. doi:10.1115/1.1828070
51. Kovalchenko, A.; Ajayi, O.; Erdemir, A.; Fenske, G. *Wear* **2011,** *271,* 1719–1725. doi:10.1016/j.wear.2010.12.049
52. Marchetto, D.; Rota, A.; Calabri, L.; Gazzadi, G. C.; Menozzi, C.; Valeri, S. *Wear* **2008,** *265,* 577–582. doi:10.1016/j.wear.2007.12.010
53. Suh, N. P.; Mosleh, M.; Howard, P. S. *Wear* **1994,** *175,* 151–158. doi:10.1016/0043-1648(94)90178-3
54. Ando, Y.; Ino, J. *Sens. Actuators* **1996,** *57,* 83–89. doi:10.1016/S0924-4247(97)80098-2
55. Wang, X.; Liu, W.; Zhou, F.; Zhu, D. *Tribol. Int.* **2009,** *42,* 1118–1123. doi:10.1016/j.triboint.2009.03.012
56. Galda, L.; Pawlus, P.; Sep, J. *Tribol. Int.* **2009,** *42,* 1505–1512. doi:10.1016/j.triboint.2009.06.001
57. Yu, H.; Wang, X.; Zhou, F. *Tribol. Lett.* **2010,** *37,* 123–130. doi:10.1007/s11249-009-9497-4
58. Prodanov, N.; Gachot, C.; Rosenkranz, A.; Mücklich, F.; Müser, M. H. *Tribol. Lett.* **2013,** *50,* 41–48. doi:10.1007/s11249-012-0064-z
59. Gachot, C.; Rosenkranz, A.; Reinert, L.; Ramos-Moore, E.; Souza, N.; Müser, M. H.; Mücklich, F. *Tribol. Lett.* **2012,** *49,* 193–202. doi:10.1007/s11249-012-0057-y
60. Filippov, A.; Gorb, S. N. *Sci. Rep.* **2013,** *3,* No. 1240. doi:10.1038/srep01240
61. Abdel-Aal, H. A. *J. Mech. Behav. Biomed. Mater.* **2013,** *22,* 115–135. doi:10.1016/j.jmbbm.2012.09.014
62. Peressadko, A. G.; Gorb, S. N. Surface profile and friction force generated by insects. International Industrial Conference Bionik, Hannover, April 22, 2004; Boblan, I.; Bannasch, R., Eds.; VDI Verlag: Düsseldorf, Germany, 2004; pp 257–263.
63. Voigt, D.; Schuppert, J. M.; Dattinger, S.; Gorb, S. N. *J. Insect Physiol.* **2008,** *54,* 765–776. doi:10.1016/j.jinsphys.2008.02.006
64. Bullock, J. M. R.; Federle, W. *Insect Sci.* **2011,** *18,* 298–304. doi:10.1111/j.1744-7917.2010.01369.x
65. Wolff, J. O.; Gorb, S. N. *J. Exp. Biol.* **2012,** *215,* 179–184. doi:10.1242/jeb.061507
66. Huber, G.; Gorb, S. N.; Hosada, N.; Spolenak, R.; Arzt, E. *Acta Biomater.* **2007,** *3,* 607–610. doi:10.1016/j.actbio.2007.01.007
67. Yu, J.; Chary, S.; Das, S.; Tamelier, J.; Turner, K. L.; Israelachvili, J. N. *Langmuir* **2012,** *28,* 11527–11534. doi:10.1021/la301783q
68. Spurr, A. R. *J. Ultrastruct. Res.* **1969,** *26,* 31–43. doi:10.1016/S0022-5320(69)90033-1

License and Terms

BEILSTEIN JOURNAL OF NANOTECHNOLOGY

Physical principles of fluid-mediated insect attachment - Shouldn't insects slip?

Jan-Henning Dirks

Review

Open Access

Address:
Department of New Materials and Biosystems, Max Planck Institute for Intelligent Systems, Stuttgart, Germany

Email:
Jan-Henning Dirks - dirks@is.mpg.de

Keywords:
adhesion; friction; insect biomechanics; tribology

Beilstein J. Nanotechnol. **2014,** *5,* 1160–1166.
doi:10.3762/bjnano.5.127

Received: 06 February 2014
Accepted: 27 June 2014
Published: 28 July 2014

This article is part of the Thematic Series "Biological and bioinspired adhesion and friction".

Guest Editor: S. N. Gorb

Abstract

Insects use either hairy or smooth adhesive pads to safely adhere to various kinds of surfaces. Although the two types of adhesive pads are morphologically different, they both form contact with the substrate via a thin layer of adhesive fluid. To model adhesion and friction forces generated by insect footpads often a simple "wet adhesion" model is used, in which two flat undeformable substrates are separated by a continuous layer of fluid. This review summarizes the key physical and tribological principles that determine the adhesion and friction in such a model. Interestingly, such a simple wet-adhesion model falls short in explaining several features of insect adhesion. For example, it cannot predict the observed high static friction forces of the insects, which enable them to cling to vertical smooth substrates without sliding. When taking a closer look at the "classic" attachment model, one can see that it is based on several simplifications, such as rigid surfaces or continuous layers of Newtonian fluids. Recent experiments show that these assumptions are not valid in many cases of insect adhesion. Future tribological models for insect adhesion thus need to incorporate deformable adhesive pads, non-Newtonian properties of the adhesive fluid and/or partially "dry" or solid-like contact between the pad and the substrate.

Review

How do insects adhere to surfaces?

More than 80% of the animal species in the world are arthropods [1], and amongst them insects can be considered probably the evolutionarily most successful group. For hundreds of millions of years they are inhabiting almost every part of the world, and different species have developed adaptations to environments with a wide range of temperatures, humidities and substrates.

For a long time the ability of insects and other arthropods to effortlessly walk up and down all kinds of natural and artificial

surfaces has fascinated scientists and the underlying mechanisms have been debated since the early days of light microscopy. From “gluten-filled sponges”, the interlocking of fine hairs, suction cups and adhesive secretions, many hypotheses about insect adhesion have been proposed over the last two centuries [2-7].

In recent years more elaborate microscopes and better analytical tools have become available and the interest of biologists and engineers in biological and biomimetic adhesives has increased [8-13]. Imaging techniques such as atomic force microscopy (AFM) and various different types of scanning electron microscopy (SEM) now allow biologists to analyse sensitive biological samples on a nanometre scale. Nevertheless, the detailed mechanisms allowing insects to safely adhere to surfaces are still not fully understood.

In a previous paper we have discussed the general principles of insect adhesion and highlighted recent advances and open questions [14]. This review will focus on summarizing the key physical principles that are thought to determine the attachment forces. We will discuss in which aspects a commonly used simple “wet adhesion” model is sufficient and, in particular, in which it falls short in explaining the forces generated by the adhesive pads of insects.

Hairy and smooth adhesive organs of insects

One of the most basic biological micro-scale structures for mechanical interlocking to a substrate seems to be a claw. However, the potential use of claws is limited to compliant surfaces in which the claws can insert, or rough surfaces with asperities larger than the diameter of the claw tip [15]. Hence, to stick to smooth and stiff natural substrates, such as stones or leaves, insects and other arthropods have to use adhesive pads (Figure 1).

In general, the hairy adhesive pads on the feet of flies, beetles and spiders are densely covered with dense arrays of flexible setae (see Figure 1A) [16-22]. Although the setae of some beetles branch towards the tip, they only end in a single terminal element in most insects. These terminal elements can vary in shape and size, even within one tarsus or between the sexes of one species [23]. Recently it has been shown that in beetles the setae show a decreasing stiffness of the cuticle towards the tip of the setae [24]. Similar “hairy” structures can be found in many other biological adhesive pads such as lizards and spiders [25], indicating a general “favourable” design [8].

Despite the large number of species, only two types of adhesive systems have evolved in insects and other arthropods: “hairy” (fibrillar) and “smooth” pads [26]. Both systems provide attach-

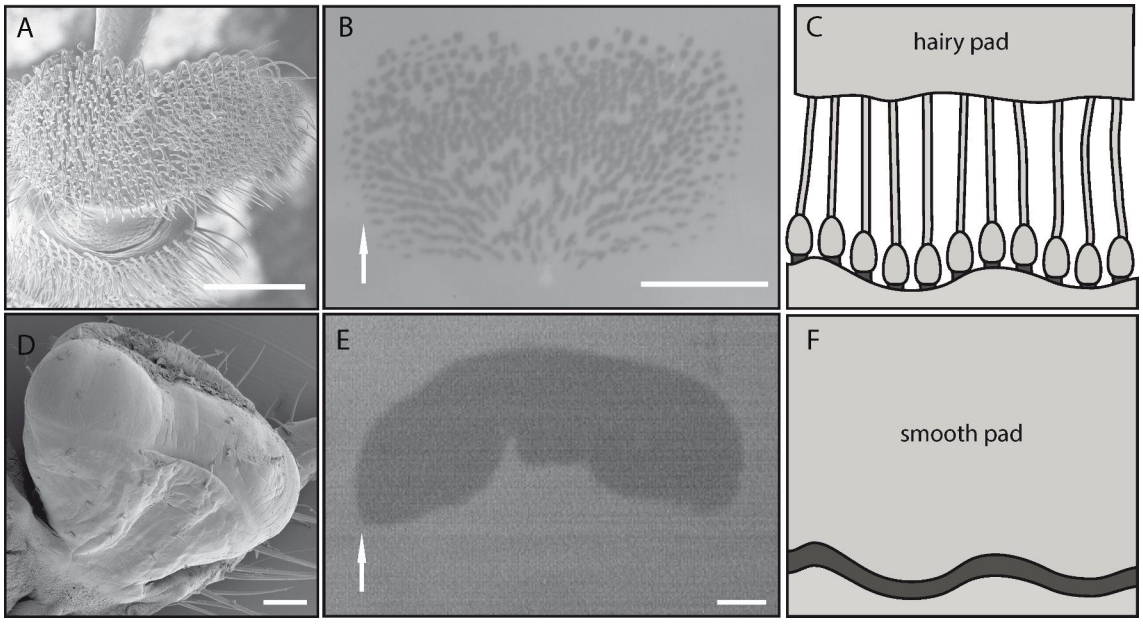

Figure 1: Adhesive pad morphology of a male dock beetle (*Gastrophysa viridula*, A) and an Indian stick insect (*Carausius morosus*, D). Epi-illumination can be used to visualise the contact area of the adhesive pad in contact with glass (B, E). Arrows indicate distal direction. Subfigures C and F show a schematic view of the close contact of the hairy and smooth pads to a rough substrate. Note that in both cases the contact zone is mediated by an adhesive fluid (dark). Images A, B, D and E adapted with kind permission of [16]. Copyright (2008) The Company of Biologists Ltd. All scale bars represent 100 µm.

ment to rough and smooth surfaces by maximizing the contact area and achieving close contact [27,28]. In contrast to the hairy adhesives, smooth pads of insects increase the contact area by adapting as a whole to the surface roughness (Figure 1F, [29-32]). Smooth adhesive organs can be found in many insect groups such as ants, bees, stick insects, grasshoppers, true bugs and cockroaches. The larger number of insect groups with smooth pads, compared to the smaller number of groups with hairy pads, led to the suggestion that smooth pads probably appeared earlier in insect evolution and represent a more "basic" evolutionary adhesive structure [22]. In addition, the structural diversity of the smooth pads in different insect orders has lead to the suggestion that smooth adhesive pads have independently evolved several times [27,33]. Recently it has been shown that insects with smooth adhesive pads can also possess hairy "friction pads" with special morphological adaptations [34].

Despite their different morphology, hairy and smooth adhesive pads of insects have in common that they both secrete an adhesive fluid into the contact zone [14,16]. For the smooth pads of stick-insects, cockroaches and ants it has been shown that this adhesive fluid is a two-phasic microemulsion consisting of a hydrophilic, volatile dispersive phase within a hydrophobic, persistent continuous phase [30,35]. In hairy pads, with notably smaller contact points of each seta (and thus an even more complicated analysis of the foot secretion [36]), the detailed chemical composition is still a subject of investigation. Although it has been shown that the composition of the lipophilic phase of the secretion is similar to the composition of the cuticular hydrocarbon layer [37].

To understand the physical principles that enable the attachment of such fluid-mediated insect foot pads onto various substrates, one has to start with a simple model. In general, the fluid-mediated smooth and hairy adhesive organs of insects have to generate both adhesion forces perpendicular to the substrate and friction forces parallel to the substrate. The tribological models for both "types" of attachment forces will be considered separately in the following.

Fluid-mediated adhesion

For simplicity, the contact zones of both smooth and hairy adhesive pads are often modeled by using a "wet-adhesion model" consisting of a smooth, undeformable disk and substrate with a mediating continuous fluid-layer (see Figure 2 and [30,38-42]).

In this simple model, the total adhesive force is basically the sum of three components: the surface tension of the fluid, the Laplace pressure (both often combined as "capillary forces") and the viscous forces, often called "Stefan adhesion" [43,44] (see below in Table 1).

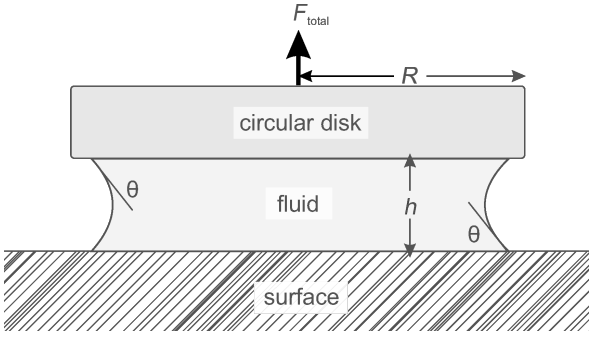

Figure 2: Schematic illustration of a simple fluid-mediated attachment model. The contact of a circular rigid disk (radius *R*) and a plane rigid surface is mediated by a thin fluid layer (height *h*). The contact angle of the fluid to the surface and the disk θ is assumed to be identical in this case.

$$F_{adh} = \underbrace{F_{surface\ tension} + F_{Laplace\ pressure}}_{capillary\ forces} + F_{viscous\ forces} \quad (1)$$

Based on a few assumptions and further simplifications (such as equal contact angles θ of the mediating fluid layer to the surface and the disk), the adhesive forces generated by such a "wet adhesion" model in Equation 1 can be estimated by using

$$F_{adh} = \underbrace{2\pi\gamma \cdot R}_{surface\ tension} + \underbrace{\pi\gamma\left(\frac{2\cos\theta}{h} - \frac{1}{R}\right)\cdot R^2}_{Laplace\ pressure} + \underbrace{\frac{dh}{dt}\frac{3\pi\eta}{2h^3}\cdot R^4}_{viscous\ forces} \quad (2)$$

By using a few experimentally accessible parameters such as mediating fluid height, viscosity, and contact angle (for a more detailed review on the challenges on measuring these parameters see [14]), this model can then be used to discuss and qualitatively predict a few characteristic "features" of insect adhesion (see Table 1). For example, looking only at the Laplace term in Equation 2

$$F_{Laplace} = \pi\gamma\left(\frac{2\cos\theta}{h} - \frac{1}{R}\right)\cdot R^2 \quad (3)$$

one can predict that an increasing fluid height *h* between adhesive pad and surface would result in decreasing capillary adhesive forces. As a consequence, insects and all organisms with fluid-mediated attachment organs should minimize the secretion of adhesive fluid into the contact area to increase capillary adhesion on smooth surfaces.

However, and this is where the simple "wet adhesion model" starts to fall short when used to model insect attachment, only very few natural surfaces are actually smooth. Experimental studies indeed show that the adhesive fluid actually plays a more important role in increasing adhesion on rough surfaces by filling gaps between the pad and the surface, thereby maximizing contact area and adhesion to rough substrates [45,46]. This has been shown by studies in which adhesive fluid was either experimentally accumulated or depleted. In smooth and hairy adhesive systems an additional fluid volume decreased friction and adhesive forces on smooth surfaces, as predicted by the simple model. When forces were measured on rough surfaces however, accumulating adhesive fluid increased adhesion, as the additional fluid compensated the surface roughness and thus increased the effective contact area [16,46]. In addition, the presence of adhesive fluid has been shown to improve the self-cleaning of the adhesive pads in comparison to dry adhesive pads [47,48].

Besides the "smooth vs rough" limitation, the simple model also bears several additional notable problems, in particular in light of the stiffness and deformability of the adhesive pads. For example, the capillary term in Equation 2 is only valid in the case of rigid, stiff surfaces in contact. In the case of insect (and tree frog) attachment, with very smooth and adaptable pads [49,50], it is very questionable whether this assumption is justified. In fact, recent and more comprehensive tribological models show that for certain ratios of adhesive pad size and stiffness, the Young's modulus of the adhesive pad can play an important role in determining the capillary adhesion [51,52]. In these models the overall capillary force is taken as the sum of the capillary attraction and the counter-acting elastic repulsion of the deformed pad/substrate (which depends on the elastic modulus). In simple terms, a softer adhesive pad/substrate (with a lower elasticity) deforms more easily at a given external force, resulting in a larger contact area. This larger contact area again increases the radius of the mediating meniscus of the liquid (the liquid is pressed towards the outside of the pad), which then increases the capillary force. This extended capillary model might add an explanation why some insects (and tree frogs) have soft toe pads [51].

It should also be noted that in particular in the context of insect adhesion the mechanics described by the third viscous forces, or "Stefan adhesion" term, are a rather substantial simplification of the processes determining the viscous adhesion between the adhesive pad and the substrate. The mechanism proposed by Stefan also assumes undeformable surfaces and uniform centripetal flow of the mediating fluid [53]. Both assumptions are very likely to be violated in the case of the very compliant smooth insect adhesive pads on micro-rough substrates [26,54]. Hence, in this context the term "Stefan adhesion" should only be used with great care. Also, it is important to note that according to the model, the forces generated by the viscous properties of the mediating fluid volume should decline over time. In a static adhesive pad with a Newtonian fluid, only the (negligible) surface tension and the small Laplace pressure would thus determine the overall adhesive force of the insect foot (Table 1).

Fluid-mediated friction forces

In a fluid mediated system with a continuous Newtonian fluid film, the friction forces between the substrates can in general be described by using two basic principles: the surface tension of the mediating fluid and the laws of hydrodynamic lubrication [55,56].

Table 1: Summary of physical principles often used to model the attachment forces generated by the adhesive feet of insects. However, based on this simple model (besides other limitations discussed in detail in the text), insects should not be able to generate sufficient static friction forces to prevent slipping.

	fluid-based attachment				
	adhesion			friction	
factor	"surface tension"	"Laplace pressure"	viscous force	"surface tension"	hydrodynamic lubrication
contact area	×	×	×	×	×
fluid height	—	×	×	—	×
contact angle	×	×	—	—	—
surface tension	×	×	—	×	—
Viscosity	—	—	×	—	×
dynamics	—	—	change of fluid height	—	sliding velocity

Surface tension

The contribution of the surface tension of the mediating fluid to friction forces can be estimated by using a simple model of a mercury thread moving through a glass tube [55]. For a simplified model with a circular contact area with radius r, and α_1 and α_2 as the leading and trailing edge contact angles [57], the retentive "friction" force F acting on the mercury can be described by using

$$F = 2\pi r\gamma_{\text{fluid}}\left(\cos\alpha_1 - \cos\alpha_2\right). \quad (4)$$

However, the contribution of surface tension towards the generation of friction forces is very limited. Looking at the adhesive fluid secreted by the Indian stick insect *Carausius morosus* with an estimated surface tension of 27 mNm^{-1} [58] and a contact area of 0.1 mm^2 [16], the maximal possible shear stress before sliding occurs (with $\cos\alpha_1 - \cos\alpha_2 \leq 2$) would be only approx. 0.38 kPa. This value (and the corresponding value for smaller contact areas) is several orders of magnitude smaller than the shear stresses measured in smooth adhesive pads of the stick insects, cockroaches and ants [16,46,57,59]. Surface tension alone is thus unlikely to explain the high friction forces generated by the adhesive pads of insects.

Hydrodynamic or boundary lubrication?

Similar to the viscous forces in adhesion, the "hydrodynamic lubrication" friction model takes into account the viscosity of the mediating fluid layer. Two parallel smooth surfaces with a distance of h sliding at a velocity v relative to each other generate the friction force

$$F_{\text{F}} = \eta_{\text{eff}} A\frac{v}{h} \quad (5)$$

where η_{eff} is the effective viscosity of the mediating fluid layer and A the size of the contact area. Again, similar to the time-dependent viscous adhesion (Equation 2), the v/h-term in Equation 5 shows that a simple fluid mediated system at rest should not be able to generate any static friction. Based on viscosity estimations from dewetting processes (40 to 150 mPa), Federle et al. showed that the hydrodynamic friction forces generated by a continuous fluid film of 90 nm height would be one order of magnitude smaller than the shear stresses observed in adhesive organs [30]. Thus it is not yet clear how insects with a fluid-mediated adhesive pad generate the observed friction forces preventing them from sliding down smooth vertical substrates. As a quick look at the nearest window pane can confirm, insects can actually safely adhere to smooth vertical substrates. This indicates that a simple "continuous" and Newtonian fluid-layer model is not a valid model for the friction forces of insect pads [57]. Indeed, experimental results suggest that thixotropic (shear-thinning) non-Newtonian properties of the secretion could explain the presence of high static friction forces [46,60].

A second, yet to be tested, hypothesis to explain the observed high friction forces is the formation of local "dry" rubber like direct contacts between the adhesive pad and the substrate [61]. The classic hydrodynamic model only describes the friction observed with relatively "thick" layers of lubricant (≥0.5 μm, [62]), where neither the specific surface properties (roughness, surface energy) nor Amonton's law are involved [63]. Friction forces generated by fluid layers thinner than 5 to 10 molecular layers are usually modeled by using the more complex boundary lubrication theory, in which a decreasing film height and increasing number and area of direct contacts between the two substrates actually increase the friction coefficient [56,64,65]. The range between the hydrodynamic model and the boundary lubrication model, in which the mediating fluid layer is still lubricating the contact, however allows a weak interaction between the surfaces, is mostly referred to as elasto-hydrodynamic lubrication (Figure 3 and [66,67]). Within this range, the mediating fluid film can become unstable and areas with "dry" solid-like contact can form as a result of local "dewetting" and increased friction forces. Indeed, a similar mechanism has been proposed for the fluid-mediated adhesive toes found in tree frogs, for which force measurements and interference reflection microscopy results indicate that boundary friction might be responsible for the friction [49,68]. However, although first results indicate that the mediating fluid layer in insect pads might be thinner than previous estimates

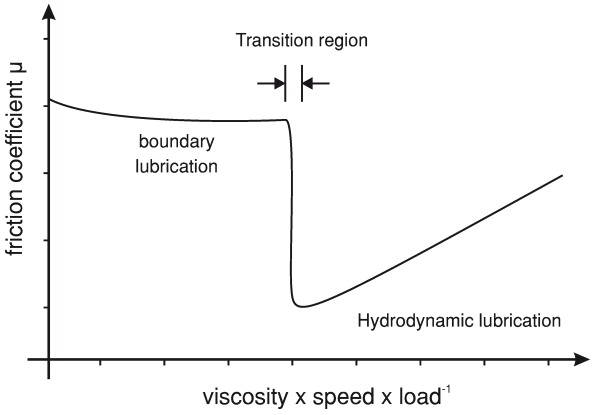

Figure 3: Regions of hydrodynamic and boundary lubrication of two fluid mediated smooth surfaces (Stribeck curve). With decreasing sliding velocity and increasing load the mediating fluid film becomes thinner, allowing regions of direct contact between the two surfaces. Within the transition region the friction coefficient rapidly increases, usually to a value smaller than unlubricated surfaces. This region is also referred to as elasto-hydrodynamic lubrication. It is not yet fully understood in which of the two "regions" the adhesive organs of insects operate.

[69], so far there is no experimental evidence for the occurrence of dewetting or direct contacts between adhesive pad and surface in smooth or hairy adhesive organs of insects [14,30,31,46].

Conclusion

Even after many years of research, several of the fundamental physical properties enabling insects to safely adhere to surfaces are still not fully understood. Although simple fluid-mediated models based on capillary and viscosity are still often used to estimate the attachment forces generated by insect feet, newer experimental data and more comprehensive tribological models suggest that many aspects of these classic "microscopic" attachment models fall short in fully explaining the forces generated by the fluid-mediated adhesive pads of insects.

To fully understand the physical principles of insect adhesion, one thus has to extend (or even replace) the "classic" models of friction and adhesion to incorporate for example deformable pads or non-Newtonian properties of the adhesive fluid. In particular in respect to friction forces one has also take into account possible more complex nano-tribological models, with boundary lubrication or other mechanisms resulting in points of "dry" contact between the pad and the surface.

Further fundamental experimental work, in particular a more accurate in vivo measurement of the height of the mediating fluid and high-resolution single-leg force measurements on smooth substrates with well known physical properties are required to answer these questions [14].

Acknowledgements

The author would like to acknowledge many helpful discussions with Walter Federle and the members of the Insect Biomechanics Workgroup, Department or Zoology, University of Cambridge. This study was supported by the Max Planck Society.

References

1. May, R. *Science* **1988,** *241,* 1441–1449. doi:10.1126/science.241.4872.1441
2. Power, H. *Experimental Philosophy;* Martin and Allestry: London, UK, 1664.
3. Hooke, R. *Micrographia;* John Bowles: London, UK, 1665.
4. Burmeister, H. *Handbuch der Entomologie;* G. Reimer: Berlin, 1832.
5. Blackwall, J. *Extracts from the Minute-Book of the Linnean Society* **1833,** *21,* 767.
6. Dewitz, H. *Zool. Anz.* **1884,** *7,* 400–405.
7. West, T. *Trans. Linnean Soc.* **1861,** *23,* 393–421. doi:10.1111/j.1096-3642.1860.tb00139.x
8. Federle, W. *J. Exp. Biol.* **2006,** *209,* 2611–2621. doi:10.1242/jeb.02323
9. Waite, J. H.; Andersen, N.; Jewhurst, S.; Sun, C. *J. Adhes.* **2005,** *81,* 297–317. doi:10.1080/00218460590944602
10. Geim, A. K.; Dubonos, S. V.; Grigorieva, I. V.; Novoselov, K. S.; Zhukov, A. A.; Shapoval, S. Yu. *Nat. Mater.* **2003,** *2,* 461–463. doi:10.1038/nmat917
11. Seidl, T.; Vidoni, R. Adhesion to Flat Surfaces: From Spiders to Stickers. *Spider ecophysiology;* Springer, 2013; pp 463–473. doi:10.1007/978-3-642-33989-9_35
12. Zhou, M.; Pesika, N.; Zeng, H.; Tian, Y.; Israelachvili, J. *Friction* **2013,** *1,* 114–129. doi:10.1007/s40544-013-0011-5
13. Kovalev, A. E.; Varenberg, M.; Gorb, S. N. *Soft Matter* **2012,** *8,* 7560–7566. doi:10.1039/c2sm25431j
14. Dirks, J.-H.; Federle, W. *Soft Matter* **2011,** *7,* 11047–11053. doi:10.1039/C1SM06269G
15. Dai, Z.; Gorb, S.; Schwarz, U. *J. Exp. Biol.* **2002,** *205,* 2479–2488.
16. Bullock, J. M. R.; Drechsler, P.; Federle, W. *J. Exp. Biol.* **2008,** *211,* 3333–3343. doi:10.1242/jeb.020941
17. Arzt, E.; Gorb, S.; Spolenak, R. *Proc. Natl. Acad. Sci. U. S. A.* **2003,** *100,* 10603–10606. doi:10.1073/pnas.1534701100
18. Betz, O. *J. Morphol.* **2003,** *255,* 24–43. doi:10.1002/jmor.10044
19. Spolenak, R.; Gorb, S.; Gao, H.; Arzt, E. *Proc. R. Soc. A* **2005,** *461,* 305–319. doi:10.1098/rspa.2004.1326
20. Stork, N. E. *J. Nat. Hist.* **1983,** *17,* 829–835. doi:10.1080/00222938300770641
21. Stork, N. E.; Evans, M. E. G. *Int. J. Insect Morphol. Embryol.* **1976,** *5,* 219–221. doi:10.1016/0020-7322(76)90006-4
22. Gorb, S. N. *Adv. Insect Physiol.* **2008,** *34,* 81–115. doi:10.1016/S0065-2806(07)34002-2
23. Bullock, J. M. R.; Federle, W. *J. Exp. Biol.* **2009,** *212,* 1876–1888. doi:10.1242/jeb.030551
24. Peisker, H.; Michels, J.; Gorb, S. N. *Nat. Commun.* **2013,** *4,* 1661. doi:10.1038/ncomms2576
25. Stork, N. E. *J. Nat. Hist.* **1983,** *17,* 583–597. doi:10.1080/00222938300770481
26. Gorb, S. *Attachment devices of insect cuticle;* Kluwer Academic Publishers: Dordrecht, Boston, 2001.
27. Beutel, R. G.; Gorb, S. N. *J. Zool. Syst. Evol. Res.* **2001,** *39,* 177–207. doi:10.1046/j.1439-0469.2001.00155.x
28. Gorb, S. N.; Beutel, R. G.; Gorb, E. V.; Jiao, Y. K.; Kastner, V.; Niederegger, S.; Popov, V. L.; Scherge, M.; Schwarz, U.; Vötsch, W. *Integr. Comp. Biol.* **2002,** *42,* 1127–1139. doi:10.1093/icb/42.6.1127
29. Gorb, S.; Jiao, Y.; Scherge, M. *J. Comp. Physiol., A* **2000,** *186,* 821–831. doi:10.1007/s003590000135
30. Federle, W.; Riehle, M.; Curtis, A. S. G.; Full, R. J. *Integr. Comp. Biol.* **2002,** *42,* 1100–1106. doi:10.1093/icb/42.6.1100
31. Labonte, D.; Federle, W. *PLoS One* **2013,** *8,* e81943. doi:10.1371/journal.pone.0081943
32. Clemente, C. J.; Dirks, J.-H.; Barbero, D. R.; Steiner, U.; Federle, W. *J. Comp. Physiol., A* **2009,** *195,* 805–814. doi:10.1007/s00359-009-0457-0
33. Beutel, R. G.; Gorb, S. N. *Arthropod Syst. Phylog.* **2006,** *64,* 3–25.
34. Labonte, D.; Williams, J. A.; Federle, W. *J. R. Soc., Interface* **2014,** *11,* 20140034. doi:10.1098/rsif.2014.0034
35. Dirks, J.-H.; Federle, W. *J. R. Soc., Interface* **2011,** *8,* 952–960. doi:10.1098/rsif.2010.0575
36. Abou, B.; Gay, C.; Laurent, B.; Cardoso, O.; Voigt, D.; Peisker, H.; Gorb, S. *J. R. Soc., Interface* **2010,** *7,* 1745–1752. doi:10.1098/rsif.2010.0075
37. Geiselhardt, S. F.; Federle, W.; Prüm, B.; Geiselhardt, S.; Lamm, S.; Peschke, K. *J. Insect Physiol.* **2010,** *56,* 398–404. doi:10.1016/j.jinsphys.2009.11.016

38. Walker, G.; Yulf, A. B.; Ratcliffe, J. *J. Zool., Ser. A* **1985,** *205,* 297–307. doi:10.1111/j.1469-7998.1985.tb03536.x
39. Lees, A. D.; Hardie, J. *J. Exp. Biol.* **1988,** *136,* 209–228.
40. Walker, G. *Int. J. Adhes. Adhes.* **1993,** *13,* 3–7. doi:10.1016/0143-7496(93)90002-Q
41. Scherge, M.; Gorb, S. *Biological Micro- and Nanotribology: Nature's Solutions;* NanoScience and Technology; Springer: Berlin Heidelberg, 2001.
42. Langer, M. G.; Ruppersberg, J. P.; Gorb, S. *Proc. R. Soc. London, Ser. B* **2004,** *271,* 2209–2215. doi:10.1098/rspb.2004.2850
43. Emerson, S. B.; Diehl, D. *Biol. J. Linn. Soc.* **1980,** *13,* 199–216. doi:10.1111/j.1095-8312.1980.tb00082.x
44. Hanna, G.; Jon, W.; Barnes, W. J. P. *J. Exp. Biol.* **1991,** *155,* 103–125.
45. Baier, R. E.; Shafrin, E. G.; Zisman, W. A. *Science* **1968,** *162,* 1360–1368. doi:10.1126/science.162.3860.1360
46. Drechsler, P.; Federle, W. *J. Comp. Physiol., A* **2006,** *192,* 1213–1222. doi:10.1007/s00359-006-0150-5
47. Clemente, C. J.; Bullock, J. M. R.; Beale, A.; Federle, W. *J. Exp. Biol.* **2010,** *213,* 635–642. doi:10.1242/jeb.038232
48. Clemente, C. J.; Federle, W. *Bioinspiration Biomimetics* **2012,** *7,* 046001. doi:10.1088/1748-3182/7/4/046001
49. Federle, W.; Barnes, W. J. P.; Baumgartner, W.; Drechsler, P.; Smith, J. M. *J. R. Soc., Interface* **2006,** *3,* 689–697. doi:10.1098/rsif.2006.0135
50. Barnes, W. J. P.; Goodwyn, P. J. P.; Nokhbatolfoghahai, M.; Gorb, S. N. *J. Comp. Physiol., A* **2011,** *197,* 969–978. doi:10.1007/s00359-011-0658-1
51. Butt, H.-J.; Barnes, W. J. P.; del Campo, A.; Kappl, M.; Schönfeld, F. *Soft Matter* **2010,** *6,* 5930–5936. doi:10.1039/c0sm00455c
52. Wexler, J. S.; Heard, T. M.; Stone, H. A. *Phys. Rev. Lett.* **2014,** *112,* 066102. doi:10.1103/PhysRevLett.112.066102
53. Smith, A. M. *Integr. Comp. Biol.* **2002,** *42,* 1164–1171. doi:10.1093/icb/42.6.1164
54. Dirks, J.-H.; Li, M.; Kabla, A.; Federle, W. *Acta Biomater.* **2012,** *8,* 2730–2736. doi:10.1016/j.actbio.2012.04.008
55. West, G. D. *Proc. R. Soc. London, Ser. A* **1911,** *86,* 20–25. doi:10.1098/rspa.1911.0076
56. Israelachvili, J. *Intermolecular, surface forces;* Academic Press: London, 1992.
57. Federle, W.; Baumgartner, W.; Hölldobler, B. *J. Exp. Biol.* **2004,** *207,* 67–74. doi:10.1242/jeb.00716
58. Hasenfuss, I. *Zoomorphology* **1999,** *119,* 143–162. doi:10.1007/s004350050088
59. Clemente, C. J.; Federle, W. *Proc. R. Soc. B* **2008,** *275,* 1329–1336. doi:10.1098/rspb.2007.1660
60. Dirks, J.-H.; Clemente, C. J.; Federle, W. *J. R. Soc., Interface* **2010,** *7,* 587–593. doi:10.1098/rsif.2009.0308
61. Brochard-Wyart, F.; Daillant, J. *Can. J. Phys.* **1990,** *68,* 1084–1088. doi:10.1139/p90-151
62. Roberts, A. D. *J. Phys. D: Appl. Phys.* **1971,** *4,* 433–440.
63. Adamson, A. W.; Gast, A. *Physical Chemistry of Surfaces,* 6th ed.; Wiley-Interscience: New York, 1997.
64. Spikes, H. A. *Langmuir* **1996,** *12,* 4567–4573. doi:10.1021/la950899b
65. Spikes, H. *Proc. Inst. Mech. Eng., Part C* **2000,** *214,* 23–37. doi:10.1243/0954406001522787
66. Kendall, K. *Molecular adhesion, its applications: The sticky universe;* Kluwer Academic/Plenum Publishers: New York, USA, 2001.
67. Persson, B. N. J.; Volokitin, A. I. *Phys. Rev. B* **2002,** *65,* 134106. doi:10.1103/PhysRevB.65.134106
68. Endlein, T.; Ji, A.; Samuel, D.; Yao, N.; Wang, Z.; Barnes, W. J. P.; Federle, W.; Kappl, M.; Dai, Z. *J. R. Soc., Interface* **2012,** *10,* 20120838. doi:10.1098/rsif.2012.0838
69. Federle, W.; Dirks, J.-H. A8.79: Thin fluid films and insect adhesion - Interference reflection microscopy of the pad contact. In *SEB Annual Main Meeting 2010,* Society for Experimental Biology, 2010; pp 158 ff.

License and Terms

BEILSTEIN JOURNAL OF NANOTECHNOLOGY

Model systems for studying cell adhesion and biomimetic actin networks

Dorothea Brüggemann*[1,2], Johannes P. Frohnmayer[1,2] and Joachim P. Spatz[1,2]

Review

Open Access

Address:
[1]Department of New Materials and Biosystems, Max Planck Institute for Intelligent Systems, Heisenbergstr. 3, D-70569 Stuttgart, Germany and [2]Department of Biophysical Chemistry, University of Heidelberg, INF 253, D-69120 Heidelberg, Germany

Email:
Dorothea Brüggemann* - brueggemann@is.mpg.de

* Corresponding author

Keywords:
actin network; cell adhesion; giant unilamellar vesicle; integrin; lipid bilayer; synthetic cell; protein reconstitution; talin

Beilstein J. Nanotechnol. **2014,** *5,* 1193–1202.
doi:10.3762/bjnano.5.131

Received: 30 January 2014
Accepted: 25 June 2014
Published: 01 August 2014

This article is part of the Thematic Series "Biological and bioinspired adhesion and friction".

Guest Editor: S. N. Gorb

Abstract

Many cellular processes, such as migration, proliferation, wound healing and tumor progression are based on cell adhesion. Amongst different cell adhesion molecules, the integrin receptors play a very significant role. Over the past decades the function and signalling of various such integrins have been studied by incorporating the proteins into lipid membranes. These proteolipid structures lay the foundation for the development of artificial cells, which are able to adhere to substrates. To build biomimetic models for studying cell shape and spreading, actin networks can be incorporated into lipid vesicles, too. We here review the mechanisms of integrin-mediated cell adhesion and recent advances in the field of minimal cells towards synthetic adhesion. We focus on reconstituting integrins into lipid structures for mimicking cell adhesion and on the incorporation of actin networks and talin into model cells.

Review

Introduction

Since Hooke first described a biological cell in 1665 tremendous progress has been made in understanding the basic functions of living cells including signalling pathways, gene regulation and the molecular structure of cellular components. However, with each new discovery it becomes clearer that cells are very complex, active systems with many parts interlinked to each other. This complexity makes it very difficult to selectively study a single aspect of natural cells. In recent years, minimal cells with reduced molecular complexity have gained increasing importance as model systems for living cells. Such synthetic cells often consist of lipid vesicles with various incorporated proteins, which are used to study biochemical reactions and self-assembly processes in a controlled environment with reduced molecular complexity [1,2]. We here review previous

advances in the development of model cells with reconstituted integrin and incorporated actin networks. We also report on the fundamental mechanisms of integrin-mediated cell adhesion and the interaction of talin with lipid vesicles.

1. The role of integrins in cell adhesion

Cellular adhesion is an important mechanism, which enables cells to bind to the extracellular matrix and to surrounding cells. This process is crucial in regulating cell shape and for maintaining cell viability, migration, and tissue integrity [3]. Cell–cell and cell–substrate adhesion are mediated by different proteins, the cell adhesion molecules (CAMs). A very important group of CAMs is the integrin family, which functions both as cell–substrate and cell–cell adhesion receptors [4]. All connective tissues are supported by an extracellular protein structure, the extracellular matrix (ECM). For the first time, in 1986 an integrin was reported to link the intracellular cytoskeleton with the ECM. The name "integrins" was given to these receptors to denote their integral membrane nature and importance for the integrity of the cytoskeleton–ECM linkage [5]. Integrins are heterodimeric transmembrane glycoproteins consisting of noncovalently associated α and β subunits. In humans 24 different αβ permutations of such heterodimers exist, each of which can bind to a wide variety of specific ligands in the ECM [6-8]. Integrins contain short cytoplasmic tails and large extracellular domains, which enable the bi-directional transmission of forces across the plasma membrane [9]. Besides their anchorage function, integrins also provide spatial information on the environment and the adhesive state of the cell by transmitting chemical signals into the cytoplasm [10,11]. In addition to this outside-in signalling process integrins can undergo conformational changes, which are called inside-out activation. These changes are primarily induced by talin, a major actin-binding protein, which binds to the cytoplasmic β tails of integrins, thus activating the molecule (Figure 1). When integrin is present in its activated state it shows a higher affinity for ligands on the extracellular side of the cell membrane [12-15]. Many of these protein ligands in the ECM, for instance fibronectin, vitronectin, fibrinogen or laminin, contain the tripeptide sequence arginine-glycine-aspartic acid (RGD), which is specifically recognised by most integrins [3,7,8]. The affinity as well as the specificity of integrins to bind to their ligands in the ECM can also be increased by the presence of divalent ions such as manganese or calcium [16].

Cellular adhesion strength is mostly controlled by the intermolecular spacing of the adhesion receptors rather than by their density [17]. This result was obtained from different studies using highly ordered gold nanoparticles, which were functionalised with RGD peptides. The adhesive gold nanoparticles had a diameter below 8 nm, which allowed the binding of one integrin molecule per RGD-functionalised nanoparticle [18]. If the distance between adjacent integrin-binding gold nanoparticles was less than 70 nm, cell adhesion was found to be reinforced [17]. With nanoparticle spacings above 90 nm, focal contact formation and cell spreading were inhibited [19]. For a large variety of cells a universal length scale of 58 to 73 nm was found, which provided integrin clustering and activation, hence leading to effective cell adhesion [18]. These results showed that integrin signalling enables cells to amplify small environmental differences in adhesive cues to large differences in adhesion strength.

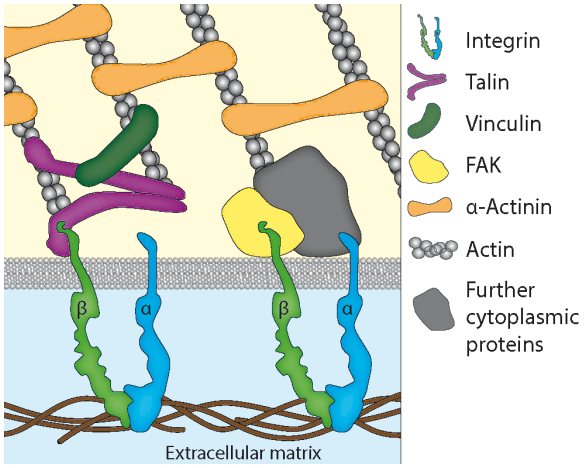

Figure 1: Schematic view of active integrin molecules linking the ECM to the actin cytoskeleton. The heads of the integrin molecules attach directly to their ligand molecules in the ECM; the intracellular tail of integrin binds to proteins like talin and FAK. On the intracellular side, active talin dimers also bind to filamentous actin. Other proteins like FAK form an indirect linkage to the actin cortex together with further cytoplasmic proteins. These intracellular anchor proteins, which include vinculin and α-actinin, help to regulate and reinforce the actin–integrin linkage.

As the cortical cytoskeleton of all cells is formed by the assembly of actin microfilaments, their linkage to adhesion-mediating proteins like integrin is important for cell shape and migration. The actin-based motility of cells is driven by myosin, a molecular motor, which converts chemical energy in the form of ATP to mechanical energy, thus generating force and movement [20]. When integrins have created a cell–ECM contact they cluster and recruit the cytoplasmic protein focal adhesion kinase (FAK), which generates stable anchoring cell–matrix junctions, the focal adhesions. These adhesion sites are crucial for the cytoskeleton, environmental sensing and cellular motility [6,21,22]. Besides talin, several other proteins including vinculin and α-actinin are well known to form integrin–actin linkages [23]. To date, the signalling network of potential integrin–actin linkages contains 156 components and

690 interactions, which have been summarised in a functional atlas of the integrin adhesome (http://www.adhesome.org) by Geiger and co-workers [24,25].

Further fundamental roles of integrin molecules in signalling and other cellular functions have been studied by using various knockdown animal models [7,26-28]. Studies on the molecular structure of integrins over the past 28 years have revealed that these adhesion molecules do not only have a vital function in cell health. They also contribute to the progression of many diseases, in which cell adhesion and migration are impaired due to alterations in the expression of integrins and their functionality. To date, integrins have already been identified as key factors in inflammation, thrombosis, cancer, fibrosis, autoimmune disorders, and infectious diseases [29-31]. These discoveries have brought integrins into the focus of pharmacological research for the development of anti-integrin drugs. At least three different integrins have been identified as therapeutic targets, and around 260 anti-integrin drugs have already entered clinical trials to date [30].

Lipid vesicles with incorporated integrin are a valuable model system to study the complex processes involved in cell adhesion with reduced molecular complexity. Talin is important for the activation of integrin and also creates a stable linkage between integrin and the cytoskeletal protein actin. Hence, these three proteins are important candidates to be incorporated into minimal cells, which mimic cell adhesion and shape.

2. Integrin reconstitution into lipid membranes

Membrane proteins and their specific impact on cell adhesion can be difficult to study in their natural environment due to the complexity of native cell membranes and interfering interactions with other membrane components and the cellular environment [32]. Over the past years, research on cell adhesion mechanisms has strongly benefited from the possibility to isolate membrane proteins, such as integrin, from cells and to embed them into lipid structures ranging from planar bilayers and small liposomes to giant unilamellar vesicles. This procedure has enabled studies on the functional properties of membrane proteins in a defined environment with reduced molecular complexity. We here review recent advances on integrin reconstitution in lipid structures and the significance of these model systems for understanding integrin-mediated cell adhesion.

2.1 Integrin incorporation into small lipid vesicles and planar bilayers

The successful reconstitution of functional integrins into small phospholipid vesicles was first achieved in 1985 by Parise et al. They worked with integrin $\alpha_{IIb}\beta_3$, which they purified from blood platelets [33,34]. This transmembrane glycoprotein is a major receptor of the platelet plasma membrane, which is required for platelet aggregation and has been well characterised. The liposomes, into which the integrins were incorporated, had diameters of 40 ± 8 nm and can be characterised as small liposomes. Integrin reconstitution was carried out by a detergent-dialysis method. During reconstitution the purified integrins were solubilized in octyl glucoside and added to different nitrogen dried phospholipids. Afterwards, the protein–lipid mixture was dialysed against a 1000 fold excess of the integrin buffer without octyl glucoside [34]. This procedure yielded proteoliposomes with functional integrin for the first time, as it was confirmed by specific binding to fibrinogen [33].

Triton X-100 is another detergent that is widely used for the reconstitution of numerous membrane proteins into liposomes since the 1980s [32,35,36]. This detergent has the tendency to form large micelles, which cannot be removed by dialysis. An efficient way of removing Triton X-100 is to use non-polar Bio-Beads, which are macroporous divinylbenzene cross-linked polystyrene beads. Detergents adsorb to these porous beads by hydrophobic bonds and can be removed from the protein solution in this way [37,38]. Müller and co-workers were the first to use this detergent removal method for reconstituting integrin $\alpha_{IIb}\beta_3$ from blood platelets and $\alpha_1\beta_1$ from chicken gizzard into lipid vesicles. Successful integrin incorporation into liposomes of 100 to 200 nm in diameter was confirmed by negative staining in cryoelectron microscopy (Figure 2). Proteoliposomes with integrin $\alpha_{IIb}\beta_3$ were also used to form planar lipid bilayers by vesicle fusion. With these planar integrin–lipid bilayers Müller et al. provided evidence that the binding of integrin $\alpha_{IIb}\beta_3$ to fibrinogen is a biphasic process consisting of a reversible first and a second irreversible step [39].

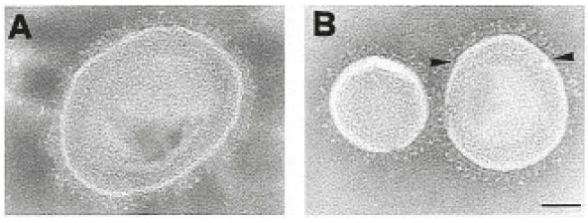

Figure 2: Cryoelectron micrographs of negatively stained DMPG/DMPC vesicles containing integrin $\alpha_{IIb}\beta_3$. Negatively stained vesicles with (A) high and (B) low surface density of integrin $\alpha_{IIb}\beta_3$. The scale bar represents 100 nm. (Reprinted with permission from [40]. Copyright (1997) American Chemical Society.)

Erb and Engel later showed by cryoelectron and fluorescence microscopy that activated integrin $\alpha_{IIb}\beta_3$ reconstituted into liposomes and planar bilayers was present in a nonclustered state and was equally distributed within the membrane. When

fibrinogen was bound to the proteolipid structures the integrins became immobile and transformed into clusters, thus passing into the previously observed irreversibly bound state [40]. Detailed protocols for the reconstitution of functional integrin into liposomes and planar bilayers of Erb and Engel have been summarised later together with several methods to analyse proteoliposome formation [41]. Recently, the activation of integrin $\alpha_{IIb}\beta_3$ reconstituted into liposomes was also studied by cryoelectron tomography [42]. With this technique it was possible to show that integrin activation with Mn^{2+} does not result in a height change of the integrin molecule. This observation was not as predicted by the switchblade model and is more consistent with the deadbolt model.

Goennenwein et al. reconstituted integrin $\alpha_{IIb}\beta_3$ into supported lipid bilayers to measure their adhesion force against RGD-peptide carrying giant vesicles. With this setup a simple and powerful tool was found to quantify the binding energy of different integrin–ligand pairs under bioanalogue conditions [43]. This system was developed further to facilitate the mobility of the integrin receptors within the supported lipid bilayer. Thus, it was shown that integrin mobility controls the force-induced growth of cell adhesion domains, which play an important role in mechanosensing of living cells [44].

In a study by Sinner et al. the integrins $\alpha_V\beta_3$ and $\alpha_1\beta_1$ were incorporated into planar lipid membranes, which were obtained by vesicle spreading. With surface plasmon-enhanced fluorescence spectroscopy and surface plasmon spectroscopy the structural and functional integrity of the embedded receptors could be confirmed over a time period of three days [45]. In binding experiments with various ECM ligands hardly any nonspecific binding was observed. Furthermore, Sinner and co-workers succeeded in regenerating the binding capacity of the artificial membranes by dissociating the integrin–ECM ligand complexes with ethylenediaminetetraacetate (EDTA). They concluded that integrin-functionalised membranes are well qualified as sensing devices for the detection of sensible ligand–receptor interactions.

2.2 Giant unilamellar vesicles with reconstituted membrane proteins

A model system that is much closer to natural cells than planar lipid membranes and small liposomes are giant unilamellar vesicles (GUVs). GUVs have diameters of 1 to 100 μm and enclose an aqueous medium. Their shell consists of only one lipid bilayer, like the membrane of natural cells. With these attributes GUVs have gained increasing importance as bottom-up model systems in synthetic biology over the past years. GUVs can be used to study cellular functions and the interplay between various proteins, which are incorporated in the lipid structures [1,2]. Other attempts in synthetic biology aim at building artificial cell systems from polymersomes. Although protocells prepared from polymer membranes have a higher stability than lipid vesicles they lack biorelevance. Furthermore, polymer membranes are much thicker than lipid bilayers, which are only 4 nm thick [46]. For the preparation of GUVs several methods exist, amongst which are electroformation on platinum wires or indium tin oxide (ITO) electrodes as well as spontaneous swelling. The specifics of GUVs, their detailed preparation methods and wide ranging applications are reviewed by P. Walde et al. [47].

Several membrane proteins have already been incorporated into GUVs over the past years. Girard and co-workers first reconstituted Ca^{2+}-ATPase from the sarcoplasmic reticulum and the H^+ pump bacteriorhodopsin into liposomes of 0.1 to 0.2 μm in size [48]. The liposomes were partially dried; the subsequent electroformation process on ITO yielded protein-GUVs with diameters between 5 and 100 μm. Both membrane proteins were homogeneously incorporated in the membranes and biologically active as demonstrated by Ca^{2+} or H^+ pumping. Functionally active aquaporins have also been embedded into GUV membranes either by mixing protein-reconstituted liposomes of 0.1 to 0.2 μm diameter with a lipid-containing oil phase (lipid cosolvent method) [49] or by swelling of a tissue-like giant vesicle film [50]. For the first time, Dezi et al. recently incorporated different transmembrane proteins like bacteriorhodopsin and the ferrichrome transport protein FhuA into GUVs with lipid mixtures representative of cellular plasma membranes [51]. Reconstitution was either performed with proteins solubilised in detergent micelles, with proteoliposomes or purified native membranes. This method proved to be highly versatile and can in future be applied to a large range of other transmembrane proteins, such as integrins.

Despite the large variety of complex membrane proteins, which have already been incorporated into GUVs, such as functional ion channels [52,53], the only existing work of integrin reconstitution in GUVs to date was published in 2008. Streicher et al. developed a novel biomimetic system based on giant vesicles that mimicked the first steps of integrin-mediated cell adhesion [54]. GUVs were produced from small liposomes by electroformation and had a diameter of 20 to 40 μm. The successful incorporation of partly fluorescently labelled integrin $\alpha_{IIb}\beta_3$ into the GUVs was confirmed by confocal microscopy. Binding experiments of integrin-GUVs on surfaces and quantum dots coated with RGD ligands revealed that the incorporated integrins were biologically active. In reflection interference contrast microscopy (RICM) experiments (Figure 3) it was observed that integrin-GUVs adhered to fibrinogen surfaces in a two-step spreading process without any enrichment of integrins in the

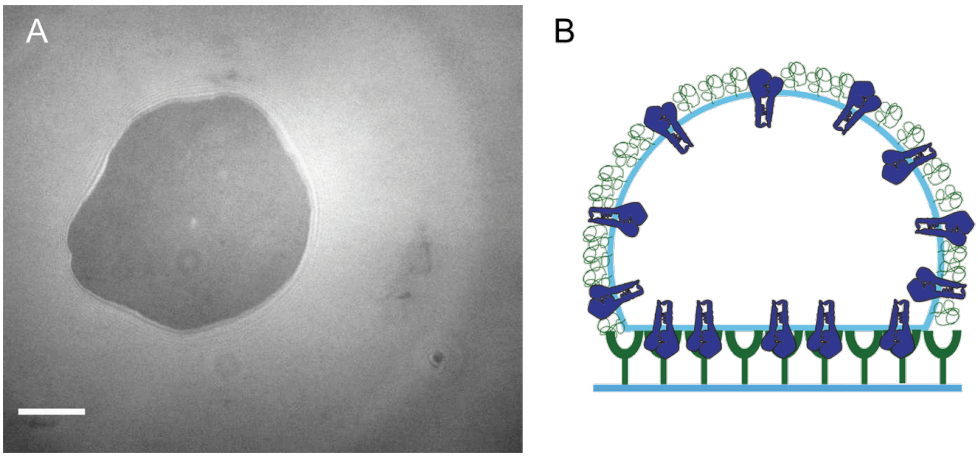

Figure 3: GUVs containing integrins interacting with a fibrinogen-coated substrate: (A) adhesion is detected with RICM (black patch), (B) Scheme of the minimal cell system. The scale bar represents 10 µm (Reprinted with permission from [54]. Copyright (2009) Elsevier Ltd.)

adhesive patches. From these observations Streicher et al. concluded that the role of the actin cytoskeleton in natural cells is to stabilise more integrins in the adhesion zones to form focal adhesion spots by recruiting FAK and other cytoplasmic proteins.

3. Biomimetic actin cortices in lipid vesicles

Due to the importance of actin in cell adhesion several studies have already been presented on the incorporation of this protein into liposomes and GUVs to build a biomimetic system that mimics cell adhesion, the formation of a cytoskeleton and spontaneous motion. The first study towards such a synthetic cell model was already performed in 1989 by Cortese et al. They encapsulated actin filaments and actin-binding proteins, such as filamin, into GUVs of 20 µm diameter. K^+ ions were introduced into the vesicles by ionophores, thus triggering actin polymerisation. This polymerisation process was observed to induce morphological changes of the initially spherical vesicles towards irregular, asymmetric shapes [55]. Sackmann and co-workers later studied GUVs with enclosed actin networks, which were formed by spontaneous swelling in a buffer containing actin monomers. They also observed shape transitions in these model cells following actin polymerisation, but osmotic effects due to the addition of $MgCl_2$ were also found to account for these changes [56]. In a subsequent study, self-assembly of thin actin shells beneath the lipid membranes of GUVs was accomplished. Buckling and blister formation of the composite actin–lipid shells were observed, which are typical shape changes in natural cell membranes, too [57]. The binding of actin filaments to positively charged lipid monolayers was further investigated by film balance in combination with neutron reflectivity. Filamentous actin adsorbed well to lipid membranes, whereas no binding was detected for monomeric actin. In dependence of the salt concentration and surface charge density of the lipid monolayer the adsorbed, filamentous actin film had a thickness between 69 and 84 Å [58].

When self-assembled actin networks were encaged in electro-formed GUVs, different actin cortex structures were obtained in dependence of the GUV size: for vesicle diameters smaller than the persistence length of actin (≤ 15 µm) a fuzzy cortex formed while larger vesicles yielded a homogeneous network as confirmed by magnetic tweezers [59]. With actin cortices in GUVs, which were cross-linked by α-actinin and filamin, randomly linked networks were observed at 25 °C. For temperatures below 15 °C a transformation into spiderweblike or ring-like networks was observed (Figure 4) [60]. This polymorphism was also found to depend on the vesicle size.

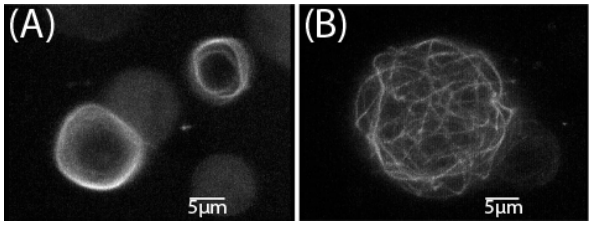

Figure 4: Dependence of actin/α-actinin network structures on the vesicle size. The 3D reconstructions of networks by confocal fluorescence microscopy (at a temperature of 4 °C). (A) Examples of rings obtained in vesicles of diameter $d < 12$ µm. (B) Spiderweblike networks formed in vesicles with diameter $d > 12$ µm (Reprinted with permission from [60]. Copyright (2002) American Physical Society.)

Pautot et al. developed an inverted emulsion technique, which assembles two independently formed lipid monolayers into unilamellar vesicles with a high yield [61]. By using this „droplet transfer“ approach, actin could be efficiently encapsu-

lated in unilamellar vesicles with sizes ranging from 100 nm to 1 μm. Actin polymerisation was induced by the addition of magnesium, and the polymerisation kinetics were unaffected by the encapsulation. Later, inverted emulsion was used to polymerise actin at the inner membrane of larger vesicles with sizes between 1 and 8 μm. This approach preserved the integrity of actin, and polymerisation was triggered by ATP and high salt concentrations [62]. When a continuous actin shell formed at the inner lipid membrane the spreading behaviour of these proteoliposomes on histidine-coated glass slides was reminiscent of a natural cell. The mechanical properties of the actin containing vesicles were found to be mainly governed by the density of the cortical shell [63]. Recently, the droplet transfer technique was extended further to encapsulate filaments of bacterial cytoskeletal proteins, such as MreB and FtsZ, into liposomes [64,65]. Compared to other vesicle preparation techniques, this approach offers a high encapsulation efficiency and good control over protein entrapment without a loss of activity [47].

Later, dynamic, branched actin networks were reconstituted on the outside of GUVs by Liu et al. With this model system they demonstrated that actin triggers both temporal and spatial rearrangement of components in the lipid bilayer, thus acting as a membrane domain switch [66]. This study was taken further by assembling dendritic actin networks inside GUVs to study the interaction between actin network growth and deformation of membranes [67]. It was observed that actin-based protrusions formed inside the GUVs, which showed a strong resemblance to cellular filopodia (Figure 5). Liu and co-workers concluded that the lipid membrane also plays an active part in organising actin networks. Already in 1999, Miyata et al. had observed similar protrusive formations at the outside of GUVs with encaged actin filaments. These protrusions developed within 30 to 100 s after KCl was introduced into the GUVs by electroporation and were also evoked by the inner actin polymerisation [68].

Actin filaments have also been encapsulated in giant liposomes together with the molecular motor heavy meromyosin. Without myosin, actin filaments were distributed homogeneously in the liposomes in an unordered manner. In the presence of actin-cross-linking proteins, self-organised actin structures emerged, which were similar to those in living motile cells [69,70]. The liposomes, which incorporated these actin networks, exhibited nonspherical shapes. Experimental protocols on preparing giant liposomes with encapsulated actin, myosin and other cross-linking proteins are discussed in more detail by Takiguchi et al. [69]. In a later study, actomyosin cortices were anchored to the outside or inside of cell-sized liposomes. This arrangement also resulted in shape changes of the biomimetic system. The regulation of morphological changes in such synthetic cells was explained by a balance of actomyosin cortical tension and mechanical resistance to rupture [71].

For the functional encapsulation of cytoskeletal proteins into lipid vesicles high physiological salt levels are mandatory and the fabrication method should only take a short period of time. These parameters cannot be fulfilled with conventional electroformation, which requires low salt concentrations and takes several hours. Recently, two novel methods were introduced, which overcome these problems of conventional vesicle formation and can incorporate biologically active proteins into GUVs. Gentle hydration of hybrid lipid-agarose films in solutions of cytoskeletal proteins yielded uniform actin and actomyosin networks enclosed in vesicles of 10 to 20 μm diameter (Figure 6) [72]. Actin filaments could also be specifically anchored to the GUV membrane by biotin-streptavidin linkages. This anchorage resulted in the formation of a cortex-like actin structure within the GUVs. However, the GUVs in this study were contaminated by agarose, which adhered to the lipid membrane. A very similar approach for growing GUVs with embedded biomolecules was later presented by Weinberger et al. Lipid precursor films were spread onto polyvinyl alcohol (PVA) films and placed in a swelling buffer containing different

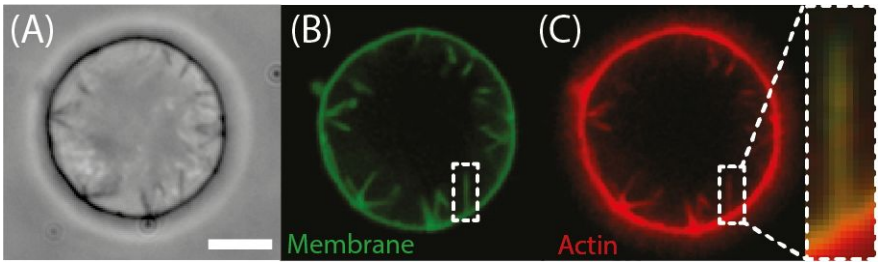

Figure 5: Thin actin protrusions emerge from dendritic actin networks. Phase-contrast (A) and spinning-disc confocal images (B) of lipid membrane (green) and (C) actin (red) show multiple protrusions in the lumen of a GUV. Overlay of the fluorescence images confirms that the membrane protrusions are supported by actin filaments. The scale bar represents 5 μm. (Reprinted with permission from [67]. Copyright (2008) Nature Publishing Group.)

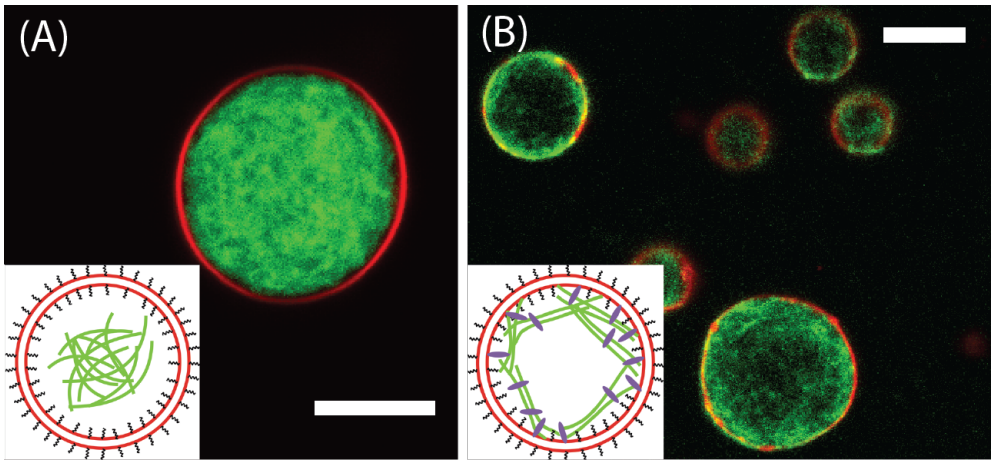

Figure 6: Confocal fluorescence micrographs of giant actin-filled liposomes. Lipid membranes are labelled with rhodamine (red); actin is labelled with AlexaFluor 488 (green). Insets indicate the nature of the actin-membrane interaction. (A) The actin filament solution inside a liposome with an inert membrane (containing PEG-lipids) is homogeneous and displays a depletion zone underneath the membrane. (B) Liposomes, which contain biotinylated lipids, encapsulate networks of biotinylated actin filaments that are coupled to the membrane via biotin–streptavidin bonds. The scale bars represent 10 µm. (Adapted with permission from [72]. Copyright (2011) American Chemical Society.)

biorelevant molecules such as actin. This gel-assisted electroformation of GUVs enabled the fast growth of polymer-free vesicles with high yields. Actin filaments were observed to incorporate into the GUVs, and bundles formed when additional cross-linkers were added to the swelling buffer [73].

4. Talin at liposomal membranes

As previously described, talin is a major actin-binding protein, which is a key player in integrin signalling. Moreover, talin anchors the actin microfilament system to the cell membrane and promotes actin polymerisation. With these functions talin can also play a crucial role in the development of synthetic cells from lipid membranes.

Reconstitution of talin into lipid membranes by self-assembly was first achieved by Heise et al. in 1991. Talin was purified from blood platelets and incorporated into vesicles by cyclic freeze-thawing of co-dispersions containing vesicles and talin. This technique yielded a uniform orientation of platelet talin with its large head group pointing to the outer vesicle side [74]. The reconstitution procedure did not change the lipid composition of the vesicles. Charged lipids were found to increase the solubility of talin in the membrane drastically, thus indicating an electrostatic interaction of talin with lipid bilayers. Based on these findings, reconstituted talin in lipid vesicles was later employed to study its interaction with actin filaments. Using fluorescence imaging it could be visualised for the first time that reconstituted talin is able to anchor actin at lipid membranes. Talin was also observed to nucleate actin filaments and to promote growth, as it was reflected by an increase in filament number at the lipid interface [75].

Furthermore, the lipid vesicle model system with reconstituted talin was employed in a study on the function of talin-vinculin complexes. When talin was present, an increase of the actin polymerisation rate was observed, which occurred independently of the presence of vinculin. In calorimetric measurements it was also found that talin, like vinculin, partially inserts into the hydrophobic region of negatively charged lipid bilayers [76]. This finding was later confirmed by light scatter techniques, which yielded a value of 3.3×10^5 M^{-1} for the molar affinity of talin to lipid vesicles [77]. The insertion behaviour of talin into negatively charged lipid bilayers was investigated in more detail by the film balance method combined with fluorescence imaging. With this technique, Sackmann and co-workers showed that fluorescently labelled as well as native talin interacts with negatively charged lipid monolayers [78]. These observations were in good agreement with previous results from differential scanning calorimetry and Fourier transform infrared spectroscopy [74]. Binding assays of talin on lipid membranes later revealed that the protein interacts simultaneously via its 47 kDa polypeptide domain with lipid bilayers and via its 200 kDa domain with actin [79]. Moreover, talin was found to trigger vesicle membrane fusion, which could be monitored using cryoelectron microscopy [80]. Hence, talin is of major importance for understanding cytoskeletal assembly and membrane targeting.

Further research on the influence of talin on lipid membranes was carried out by Takiguchi and co-workers, who studied the effects of adding talin to liposome solutions. They discovered a membrane-breaking function of talin: Lipid membranes were found to open stable holes and transform into cup-shaped lipo-

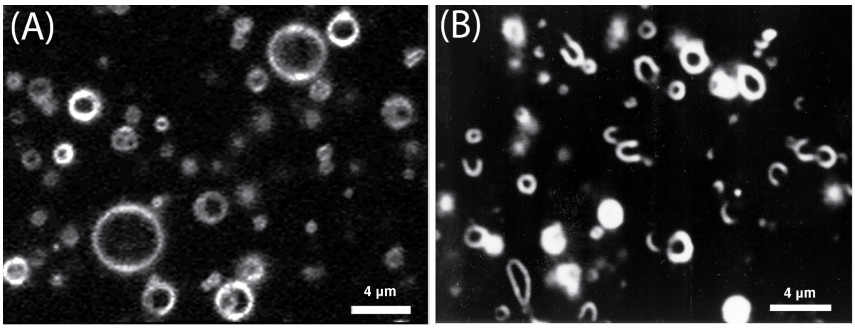

Figure 7: Transformed liposomes observed by dark-field microscopy in the presence of talin. Liposomes used were prepared from phosphatidylethanolamine and phosphatidylglycerol (1:1, mol:mol). (A) Closed spherical liposomes obtained in the absence of talin. (B) Cup-shaped liposomes observed in the presence of 0.4 mM talin. Image courtesy of K. Takiguchi (unpublished).

somes, which finally turned into lipid bilayers (Figure 7) [81]. Reversion of these morphological changes could be achieved by diluting talin in the surrounding medium, which resulted in the lipid bilayers to transform back into closed liposomes. In future, talin can also be a useful tool for controlled manipulation of liposome morphology, which can play an important role in the development of synthetic cells.

Since the early 2000's, research on talin reconstituted in lipid bilayers has not been pursued anymore although many fundamental results on cellular functions have previously been obtained from this model system. Nevertheless, small talin head domains have recently been employed to study physiological integrin activation. Ye and co-workers incorporated integrin into liposomes and added talin head domains, which have a size of only 50 kDa. With this reconstituted model system the physiological activation of integrin could be reconstructed in vitro for the first time [82].

Conclusion

Current research activities on biomimetic model cells with reduced molecular complexity have given fundamental insight into many cellular processes and signalling pathways. In particular incorporating integrins, actin filaments and talin into lipid vesicles has contributed to the current understanding of integrin-mediated cell adhesion and actomyosin-driven motility. Many obstacles in the reconstitution of biologically active membrane proteins into lipid bilayers and the functional encapsulation of actin filaments into vesicles have already been overcome in the past. Yet, there are still many open questions in the field of minimal cellular life, for instance how to incorporate further cytoplasmic proteins, including talin, into giant lipid vesicles. Future research in synthetic cells will certainly pave the way for model systems with tailored properties, which can also play an important role in targeted drug delivery or the development of novel implant materials.

Acknowledgements

We thankfully acknowledge Erich Sackmann for fruitful discussions on synthetic cell systems. This work was supported by an ERC Advanced Grant.

References

1. Fenz, S. F.; Sengupta, K. *Integr. Biol.* **2012,** *4,* 982–995. doi:10.1039/c2ib00188h
2. Stano, P. *Biotechnol. J.* **2011,** *6,* 850–859. doi:10.1002/biot.201100079
3. Ruoslahti, E.; Pierschbacher, M. D. *Science* **1987,** *238,* 491–497. doi:10.1126/science.2821619
4. Albelda, S. M.; Buck, C. A. *FASEB J.* **1990,** *4,* 2868–2880.
5. Tamkun, J. W.; DeSimone, D. W.; Fonda, D.; Patel, R. S.; Buck, C.; Horwitz, A. F.; Hynes, R. O. *Cell* **1986,** *46,* 271–282. doi:10.1016/0092-8674(86)90744-0
6. Hynes, R. O. *Trends Cell Biol.* **1999,** *9,* M33–M37. doi:10.1016/S0962-8924(99)01667-0
7. Barczyk, M.; Carracedo, S.; Gullberg, D. *Cell Tissue Res.* **2010,** *339,* 269–280. doi:10.1007/s00441-009-0834-6
8. Humphries, J. D.; Byron, A.; Humphries, M. J. *J. Cell Sci.* **2006,** *119,* 3901–3903. doi:10.1242/jcs.03098
9. Evans, E. A.; Calderwood, D. A. *Science* **2007,** *316,* 1148–1153. doi:10.1126/science.1137592
10. Hynes, R. O. *Cell* **2002,** *110,* 673–687. doi:10.1016/S0092-8674(02)00971-6
11. Huttenlocher, A.; Horwitz, A. R. *Cold Spring Harbor Perspect. Biol.* **2011,** *3,* a005074. doi:10.1101/cshperspect.a005074
12. Calderwood, D. A. *Biochem. Soc. Trans.* **2004,** *32,* 434–437. doi:10.1042/BST0320434
13. Calderwood, D. A. *J. Cell Sci.* **2004,** *117,* 657–666. doi:10.1242/jcs.01014
14. Critchley, D. R.; Gingras, A. R. *J. Cell Sci.* **2008,** *121,* 1345–1347. doi:10.1242/jcs.018085
15. Wang, J.-H. *Cell Res.* **2012,** *22,* 1512–1514. doi:10.1038/cr.2012.103
16. Gailit, J.; Ruoslahti, E. *J. Biol. Chem.* **1988,** *263,* 12927–12932.
17. Selhuber-Unkel, C.; López-García, M.; Kessler, H.; Spatz, J. P. *Biophys. J.* **2008,** *95,* 5424–5431. doi:10.1529/biophysj.108.139584
18. Arnold, M.; Cavalcanti-Adam, E. A.; Glass, R.; Blümmel, J.; Eck, W.; Kantlehner, M.; Kessler, H.; Spatz, J. P. *ChemPhysChem* **2004,** *5,* 383–388. doi:10.1002/cphc.200301014

19. Selhuber-Unkel, C.; Erdmann, T.; López-García, M.; Kessler, H.; Schwarz, U. S.; Spatz, J. P. *Biophys. J.* **2010,** *98,* 543–551. doi:10.1016/j.bpj.2009.11.001
20. Hartman, M. A.; Spudich, J. A. *J. Cell Sci.* **2012,** *125,* 1627–1632. doi:10.1242/jcs.094300
21. Mitra, S. K.; Hanson, D. A.; Schlaepfer, D. D. *Nat. Rev. Mol. Cell Biol.* **2005,** *6,* 56–68. doi:10.1038/nrm1549
22. Geiger, B.; Spatz, J. P.; Bershadsky, A. D. *Nat. Rev. Mol. Cell Biol.* **2009,** *10,* 21–33. doi:10.1038/nrm2593
23. Parsons, J. T.; Horwitz, A. R.; Schwartz, M. A. *Nat. Rev. Mol. Cell Biol.* **2010,** *11,* 633–643. doi:10.1038/nrm2957
24. Zaidel-Bar, R.; Geiger, B. *J. Cell Sci.* **2010,** *123,* 1385–1388. doi:10.1242/jcs.066183
25. Zaidel-Bar, R.; Itzkovitz, S.; Ma'ayan, A.; Iyengar, R.; Geiger, B. *Nat. Cell Biol.* **2007,** *9,* 858–867. doi:10.1038/ncb0807-858
26. Srichai, M. B.; Zent, R. Integrin Structure and Function. In *Cell-Extracellular Matrix Interactions in Cancer;* Zent, R.; Pozzi, A., Eds.; Springer: New York, 2010; pp 19–41. doi:10.1007/978-1-4419-0814-8_2
27. Grzesiak, J. J.; Tran Cao, H. S.; Burton, D. W.; Kaushal, S.; Vargas, F.; Clopton, P.; Snyder, C. S.; Deftos, L. J.; Hoffman, R. M.; Bouvet, M. *Int. J. Cancer* **2011,** *129,* 2905–2915. doi:10.1002/ijc.25942
28. Barczyk, M. M.; Gullberg, D.; Bolstad, A. I. *Methods Mol. Biol. (N. Y., NY, U. S.)* **2012,** *887,* 49–57. doi:10.1007/978-1-61779-860-3_6
29. Cox, D.; Brennan, M.; Moran, N. *Nat. Rev. Drug Discovery* **2010,** *9,* 804–820. doi:10.1038/nrd3266
30. Goodman, S. L.; Picard, M. *Trends Pharmacol. Sci.* **2012,** *33,* 405–412. doi:10.1016/j.tips.2012.04.002
31. Huveneers, S.; Truong, H.; Danen, E. H. J. *Int. J. Radiat. Biol.* **2007,** *83,* 743–751. doi:10.1080/09553000701481808
32. Rigaud, J. L.; Pitard, B.; Levy, D. *Biochim. Biophys. Acta* **1995,** *1231,* 223–246. doi:10.1016/0005-2728(95)00091-V
33. Parise, L. V.; Phillips, D. R. *J. Biol. Chem.* **1985,** *260,* 10698–10707.
34. Parise, L. V.; Phillips, D. R. *J. Biol. Chem.* **1985,** *260,* 1750–1756.
35. Rigaud, J.-L.; Lévy, D. *Methods Enzymol.* **2003,** *372,* 65–86. doi:10.1016/S0076-6879(03)72004-7
36. Levy, D.; Bluzat, A.; Seigneuret, M.; Rigaud, J.-L. *Biochim. Biophys. Acta* **1990,** *1025,* 179–190. doi:10.1016/0005-2736(90)90096-7
37. Holloway, P. W. *Anal. Biochem.* **1973,** *53,* 304–308. doi:10.1016/0003-2697(73)90436-3
38. Rigaud, J.-L.; Levy, D.; Mosser, G.; Lambert, O. *Eur. Biophys. J.* **1998,** *27,* 305–319. doi:10.1007/s002490050138
39. Müller, B.; Zerwes, H. G.; Tangemann, K.; Peter, J.; Engel, J. *J. Biol. Chem.* **1993,** *268,* 6800–6808.
40. Erb, E.-M.; Tangemann, K.; Bohrmann, B.; Müller, B.; Engel, J. *Biochemistry* **1997,** *36,* 7395–7402. doi:10.1021/bi9702187
41. Erb, E.-M.; Engel, J. Reconstitution of Functional Integrin into Phopsholipid Vesicles and Planar Lipid Bilayers. In *Extracellular Matrix Protocols;* Streuli, C.; Grant, M., Eds.; Humana Press: New York, NY, USA, 2000; pp 71–82. doi:10.1385/1-59259-063-2:71
42. Ye, F.; Liu, J.; Winkler, H.; Taylor, K. A. *J. Mol. Biol.* **2008,** *378,* 976–986. doi:10.1016/j.jmb.2008.03.014
43. Goennenwein, S.; Tanaka, M.; Hu, B.; Moroder, L.; Sackmann, E. *Biophys. J.* **2003,** *85,* 646–655. doi:10.1016/S0006-3495(03)74508-1
44. Smith, A.-S.; Sengupta, K.; Goennenwein, S.; Seifert, U.; Sackmann, E. *Proc. Natl. Acad. Sci. U. S. A.* **2008,** *105,* 6906–6911. doi:10.1073/pnas.0801706105
45. Sinner, E.-K.; Reuning, U.; Kök, F. N.; Saccà, B.; Moroder, L.; Knoll, W.; Oesterhelt, D. *Anal. Biochem.* **2004,** *333,* 216–224. doi:10.1016/j.ab.2004.05.022
46. Kamat, N. P.; Katz, J. S.; Hammer, D. A. *J. Phys. Chem. Lett.* **2011,** *2,* 1612–1623. doi:10.1021/jz200640x
47. Walde, P.; Cosentino, K.; Engel, H.; Stano, P. *ChemBioChem* **2010,** *11,* 848–865. doi:10.1002/cbic.201000010
48. Girard, P.; Pécréaux, J.; Lenoir, G.; Falson, P.; Rigaud, J.-L.; Bassereau, P. *Biophys. J.* **2004,** *87,* 419–429. doi:10.1529/biophysj.104.040360
49. Hansen, J. S.; Vararattanavech, A.; Vissing, T.; Torres, J.; Emnéus, J.; Hélix-Nielsen, C. *ChemBioChem* **2011,** *12,* 2856–2862. doi:10.1002/cbic.201100537
50. Hansen, J. S.; Thompson, J. R.; Hélix-Nielsen, C.; Malmstadt, N. *J. Am. Chem. Soc.* **2013,** *135,* 17294–17297. doi:10.1021/ja409708e
51. Dezi, M.; Di Cicco, A.; Bassereau, P.; Lévy, D. *Proc. Natl. Acad. Sci. U. S. A.* **2013,** *110,* 7276–7281. doi:10.1073/pnas.1303857110
52. Betaneli, V.; Petrov, E. P.; Schwille, P. *Biophys. J.* **2012,** *102,* 523–531. doi:10.1016/j.bpj.2011.12.049
53. Aimon, S.; Manzi, J.; Schmidt, D.; Poveda Larrosa, J. A.; Bassereau, P.; Toombes, G. E. S. *PLoS One* **2011,** *6,* e25529. doi:10.1371/journal.pone.0025529
54. Streicher, P.; Nassoy, P.; Bärmann, M.; Dif, A.; Marchi-Artzner, V.; Brochard-Wyart, F.; Spatz, J.; Bassereau, P. *Biochim. Biophys. Acta* **2009,** *1788,* 2291–2300. doi:10.1016/j.bbamem.2009.07.025
55. Cortese, J. D.; Schwab, B., III; Frieden, C.; Elson, E. L. *Proc. Natl. Acad. Sci. U. S. A.* **1989,** *86,* 5773–5777. doi:10.1073/pnas.86.15.5773
56. Bärmann, M.; Käs, J.; Kurzmeier, H.; Sackmann, E. A New Cell Model – Actin Networks Encaged by Giant Vesicles. In *The Structure and Conformation of Amphiphilic Membranes;* Lipowsky, R.; Richter, D.; Kremer, K., Eds.; Springer: Berlin, Heidelberg, 1992; pp 137–143. doi:10.1007/978-3-642-84763-9_26
57. Häckl, W.; Bärmann, M.; Sackmann, E. *Phys. Rev. Lett.* **1998,** *80,* 1786–1789. doi:10.1103/PhysRevLett.80.1786
58. Demé, B.; Hess, D.; Tristl, M.; Lee, L.-T.; Sackmann, E. *Eur. Phys. J. E* **2000,** *2,* 125–136. doi:10.1007/s101890050046
59. Limozin, L.; Barmann, M.; Sackmann, E. *Eur. Phys. J. E: Soft Matter Biol. Phys.* **2003,** *10,* 319–330.
60. Limozin, L.; Sackmann, E. *Phys. Rev. Lett.* **2002,** *89,* 168103. doi:10.1103/PhysRevLett.89.168103
61. Pautot, S.; Frisken, B. J.; Weitz, D. A. *Langmuir* **2003,** *19,* 2870–2879. doi:10.1021/la026100v
62. Pontani, L.-L.; van der Gucht, J.; Salbreux, G.; Heuvingh, J.; Joanny, J.-F.; Sykes, C. *Biophys. J.* **2009,** *96,* 192–198. doi:10.1016/j.bpj.2008.09.029
63. Murrell, M.; Pontani, L.-L.; Guevorkian, K.; Cuvelier, D.; Nassoy, P.; Sykes, C. *Biophys. J.* **2011,** *100,* 1400–1409. doi:10.1016/j.bpj.2011.01.038
64. Cabré, E. J.; Sánchez-Gorostiaga, A.; Carrara, P.; Ropero, N.; Casanova, M.; Palacios, P.; Stano, P.; Jiménez, M.; Rivas, G.; Vicente, M. *J. Biol. Chem.* **2013,** *288,* 26625–26634. doi:10.1074/jbc.M113.491688
65. Maeda, Y. T.; Nakadai, T.; Shin, J.; Uryu, K.; Noireaux, V.; Libchaber, A. *ACS Synth. Biol.* **2012,** *1,* 53–59. doi:10.1021/sb200003v
66. Liu, A. P.; Fletcher, D. A. *Biophys. J.* **2007,** *92,* 697. doi:10.1529/biophysj.106.0900151
67. Liu, A. P.; Richmond, D. L.; Maibaum, L.; Pronk, S.; Geissler, P. L.; Fletcher, D. A. *Nat. Phys.* **2008,** *4,* 789–793. doi:10.1038/nphys1071

68. Miyata, H.; Nishiyama, S.; Akashi, K.; Kinosita, K., Jr. *Proc. Natl. Acad. Sci. U. S. A.* **1999,** *96,* 2048–2053. doi:10.1073/pnas.96.5.2048
69. Takiguchi, K.; Yamada, A.; Negishi, M.; Honda, M.; Tanaka-Takiguchi, Y.; Yoshikawa, K. *Methods Enzymol.* **2009,** *464,* 31–53. doi:10.1016/S0076-6879(09)64003-9
70. Takiguchi, K.; Yamada, A.; Negishi, M.; Tanaka-Takiguchi, Y.; Yoshikawa, K. *Langmuir* **2008,** *24,* 11323–11326. doi:10.1021/la802031n
71. Carvalho, K.; Tsai, F.-C.; Lees, E.; Voituriez, R.; Koenderink, G. H.; Sykes, C. *Proc. Natl. Acad. Sci. U. S. A.* **2013,** *110,* 19969. doi:10.1073/pnas.1320628110
72. Tsai, F.-C.; Stuhrmann, B.; Koenderink, G. H. *Langmuir* **2011,** *27,* 10061–10071. doi:10.1021/la201604z
73. Weinberger, A.; Tsai, F.-C.; Koenderink, G. H.; Schmidt, T. F.; Itri, R.; Meier, W.; Schmatko, T.; Schröder, A.; Marques, C. *Biophys. J.* **2013,** *105,* 154–164. doi:10.1016/j.bpj.2013.05.024
74. Heise, H.; Bayerl, T.; Isenberg, G.; Sackmann, E. *Biochim. Biophys. Acta* **1991,** *1061,* 121–131. doi:10.1016/0005-2736(91)90276-E
75. Kaufmann, S.; Käs, J.; Goldmann, W. H.; Sackmann, E.; Isenberg, G. *FEBS Lett.* **1992,** *314,* 203–205. doi:10.1016/0014-5793(92)80975-M
76. Goldmann, W. H.; Niggli, V.; Kaufmann, S.; Isenberg, G. *Biochemistry* **1992,** *31,* 7665–7671. doi:10.1021/bi00148a030
77. Goldmann, W. H.; Senger, R.; Kaufmann, S.; Isenberg, G. *FEBS Lett.* **1995,** *368,* 516–518. doi:10.1016/0014-5793(95)00678-3
78. Dietrich, C.; Goldmann, W. H.; Sackmann, E.; Isenberg, G. *FEBS Lett.* **1993,** *324,* 37–40. doi:10.1016/0014-5793(93)81527-7
79. Niggli, V.; Kaufmann, S.; Goldmann, W. H.; Weber, T.; Isenberg, G. *Eur. J. Biochem.* **1994,** *224,* 951–957. doi:10.1111/j.1432-1033.1994.00951.x
80. Isenberg, G.; Doerhoefer, S.; Hoekstra, D.; Goldmann, W. H. *Biochem. Biophys. Res. Commun.* **2002,** *295,* 636–643. doi:10.1016/S0006-291X(02)00714-3
81. Saitoh, A.; Takiguchi, K.; Tanaka, Y.; Hotani, H. *Proc. Natl. Acad. Sci. U. S. A.* **1998,** *95,* 1026–1031. doi:10.1073/pnas.95.3.1026
82. Ye, F.; Hu, G.; Taylor, D.; Ratnikov, B.; Bobkov, A. A.; McLean, M. A.; Sligar, S. G.; Taylor, K. A.; Ginsberg, M. H. *J. Cell Biol.* **2010,** *188,* 157–173. doi:10.1083/jcb.200908045

License and Terms

BEILSTEIN JOURNAL OF NANOTECHNOLOGY

Surface topography and contact mechanics of dry and wet human skin

Alexander E. Kovalev*[1], Kirstin Dening[1], Bo N. J. Persson[2] and Stanislav N. Gorb[1]

Full Research Paper

Open Access

Address:
[1]Department of Functional Morphology and Biomechanics, Zoological Institute, University of Kiel, Am Botanischen Garten 1-9, D-24098 Kiel, Germany and [2]IFF, FZ-Jülich, 52425 Jülich, Germany

Email:
Alexander E. Kovalev* - akovalev@zoologie.uni-kiel.de

* Corresponding author

Keywords:
contact mechanics; interface fluid; roughness power spectrum; skin tribology

Beilstein J. Nanotechnol. **2014,** *5,* 1341–1348.
doi:10.3762/bjnano.5.147

Received: 18 April 2014
Accepted: 28 July 2014
Published: 22 August 2014

This article is part of the Thematic Series "Biological and bioinspired adhesion and friction".

Associate Editor: K. Koch

Abstract

The surface topography of the human wrist skin is studied by using optical and atomic force microscopy (AFM) methods. By using these techniques the surface roughness power spectrum is obtained. The Persson contact mechanics theory is used to calculate the contact area for different magnifications, for the dry and wet skin. The measured friction coefficient between a glass ball and dry and wet skin can be explained assuming that a frictional shear stress $\sigma_f \approx 13$ MPa and $\sigma_f \approx 5$ MPa, respectively, act in the area of real contact during sliding. These frictional shear stresses are typical for sliding on surfaces of elastic bodies. The big increase in friction, which has been observed for glass sliding on wet skin as the skin dries up, can be explained as result of the increase in the contact area arising from the attraction of capillary bridges. Finally, we demonstrated that the real contact area can be properly defined only when a combination of both AFM and optical methods is used for power spectrum calculation.

Introduction

The tribology of human skin is of great importance in sports, medicine, and cosmetics [1,2]. It is a rather complex topic due to the layered morphology and the viscoelastic–plastic nature of the human skin. A modern view about this topic is presented in [3].

The top-layer of the skin (*stratum corneum*, about 20 μm thick) has a Young's modulus of $E \approx 1$–3 GPa, which is similar to rubber in the glassy region. It is well know that the effective elastic modulus of *stratum corneum* may decrease by a factor of 100–1000 with increasing water content down to values of the order of $E \approx 5$–10 MPa in the wet state, which is comparable to rubber in the rubbery region [3,4].

The tissues beneath *stratum corneum* are very soft. This has been demonstrated in indentation experiments on the inner

forearm by using a macroscopic indentor (a ball with a diameter of about 1 cm). The measurements are explained well by using the Hertzian contact theory. The effective elastic modulus was found to be 10–40 kPa [3]. In a first approximation, a two layers model, with a thin stiff layer on top of a thick soft layer, is sufficient for a satisfactory description of the contact mechanics between the skin and the indentor.

The change of skin morphology and elastic modulus in the wet state contributes to the high friction of the wet human skin. However, the pattern of channels on the human skin surface, which is similar to the pattern on channels on the tree frogs toe pads [5], facilitates the fluid removal from the contact regions between skin and countersurface, increases the friction and enhances the grip between a fluid covered object and the human skin [3]. The strong reduction in the elastic modulus of the wet *stratum corneum*, e.g., due to sweating, results in a further increase of the contact area and of the friction, which may be crucially important in emergency situations.

In an earlier publication we have analyzed the frictional properties of skin by using the Persson contact mechanics theory. In [6] the surface topography of skin was measured by using an optical method with a resolution of the order of 1 μm. In this paper we report on AFM measurements at a higher resolution. From both optical and AFM data we have obtained the surface roughness power spectrum over all relevant length scales. This enabled us to perform a more accurate theoretical contact mechanics study of the frictional properties of skin, which we will report on in this paper.

Experimental

The topography of human wrist skin was analyzed in dry and wet states in the same way as described in [6]. The skin was washed with ethanol, wiped and dried for two minutes. To bring the skin in a wet state, a wet napkin was placed on the skin surface for 10 min. Afterwards, the skin was wiped and dried for two minutes. A two-component dental wax (President light body, Coltene, Switzerland) was used to prepare a negative mold of the skin. The negative mold was filled with Spurr's low-viscosity resin and polymerized overnight at 70 °C. The images of positive epoxy replicas coated with gold–palladium (6 nm layer thickness) were obtained by using a Hitachi TM3000 tabletop electron microscope (Hitachi High-Technologies Corp., Tokyo, Japan) at an accelerating voltage of 3 kV (Figure 1). 3D surface profiles of the positive replicas were acquired by using a white light interferometer NewView 6k (Zygo, Middlefield, CT, USA) with 5× and 50× magnifications (Figure 2). The data obtained at low magnification are considerably discontinuous. Exact height could not be defined in white areas, Figure 2a. Besides, a speckle-like high-amplitude noise appear at low magnification. At high magnification the height may be properly defined almost in entire field of view, Figure 2b.

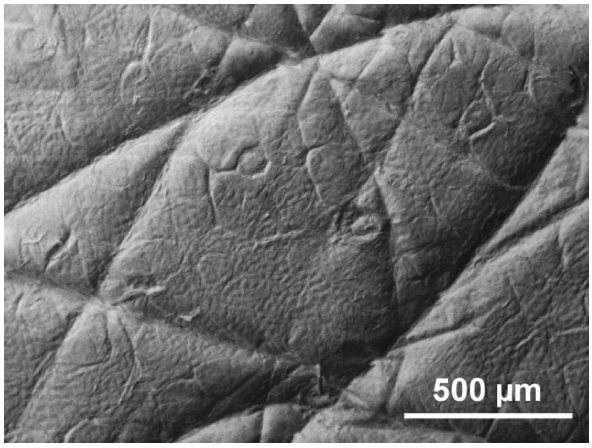

Figure 1: Scanning electron microscopy picture of a mould of wet human wrist skin.

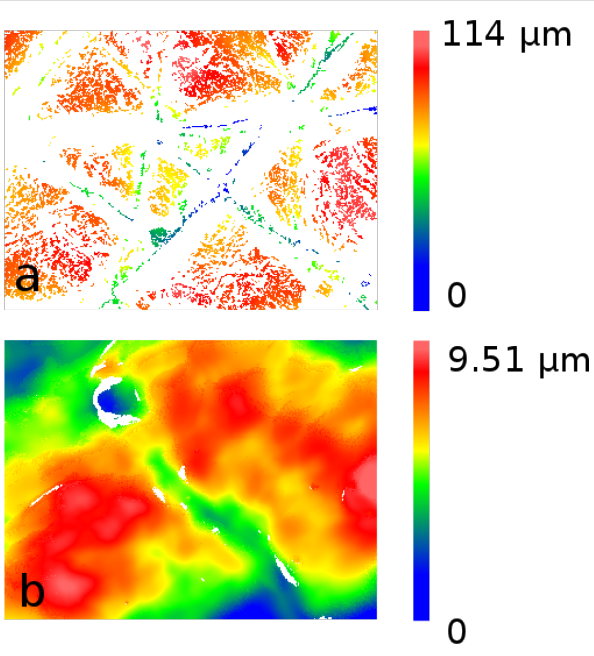

Figure 2: 3D surface profiles of a mould of wet human wrist skin obtained by using white light interferometry at low (a) and high (b) resolution (only the measured raw data are presented). The image width is 1.4 mm in (a) and 140 μm in (b).

For the AFM measurements a fragment of human wrist skin immediately after dissection was immersed in Ringer solution and placed on a Polysine™ slide (Gerhard Menzel GmbH, Braunschweig, Germany). The AFM measurements were performed with a NanoWizard® AFM system (JPK Instruments AG, Berlin, Germany) equipped with a high density carbon tip

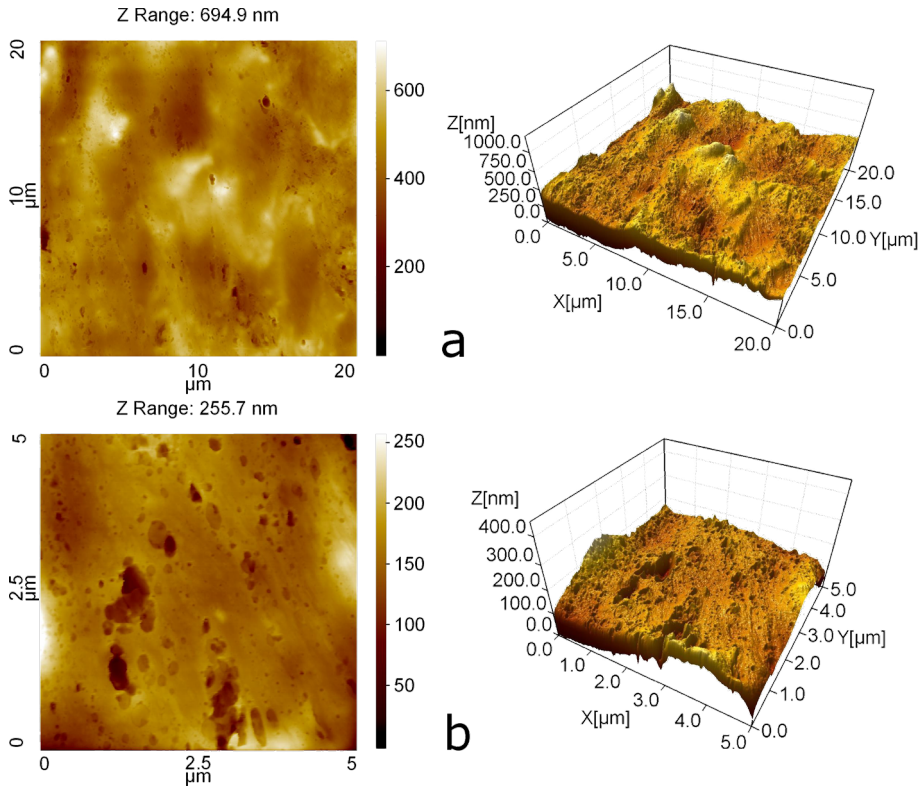

Figure 3: AFM images of a mould of wet human skin taken at (a) lower and (b) higher resolution.

(0.2 N/m, NanoWorld AG, Neuchâtel, Switzerland) in contact mode at 1024 × 1024 pixels resolution and 0.5 Hz scanning rate. Figure 3 was produced by using the software SPIP 5.1.2 (Image Metrology, Denmark).

Contact angles of water on skin were measured 5 times at different locations for each state of the skin by using a contact angle measurement device OCA20 (Dataphysics Instruments, Filderstadt, Germany). According to our measurements the advancing water contact angle on human wrist skin is (112.9 ± 1)° (mean ± s.e.m., n = 10) on dry skin and (121.4 ± 1.6)° (n = 9) on wet skin. The larger contact angle on wet skin could reflect either a change in the skin surface chemistry, or more likely may be due to the increase in the surface roughness of wet skin. The receding contact angle was not measured but it would be smaller than the advancing contact angle. In the literature, the values of the water contact angle on human skin range from 80 to 110° [7].

Results and Discussion

Surface roughness power spectrum of skin

Similar to [6] the measured height profiles $z = h(\mathbf{x})$ were used to calculate the surface roughness power spectrum defined by [8,9]:

$$C(\mathbf{q}) = \frac{1}{(2\pi)^2}\int d^2x \left\langle h(\mathbf{x})h(\mathbf{0})\right\rangle e^{-i\mathbf{q}\cdot\mathbf{x}}, \qquad (1)$$

where $\mathbf{x} = (x,y)$ is the in-plane coordinate, <... > stands for the ensemble average, $\mathbf{q} = (q_x,q_y)$ is a two-dimensional wavevector of a particular cosines surface-roughness component with wavelength $\lambda = 2\pi/q$ and orientation (in the x–y-plane) determined by the direction of $\mathbf{q}$. $C(\mathbf{q})$ depends only on $|\mathbf{q}|$ for surfaces with statistically isotropic roughness.

Figure 4 shows the power spectra obtained from the AFM topography data, Figure 3, as a function of the wave vector ($\log_{10}$–$\log_{10}$ scale). The red and blue lines are calculated using the surface topography data from Figure 10 in [3] for dry and wet skin, respectively. The green lines in Figure 4 are calculated for wet skin with AFM data taken into account.

In Figure 5 we show the power spectra over a larger wavevector range including both the results from the white light interferometry [6] and the AFM measurements from Figure 4. The dashed line denoted by **b** is the power spectra used in the calculations presented below in Figure 9), and correspond to a self-affine fractal surface with a fractal dimension of $D_f = 3 - H = 2.14$ in

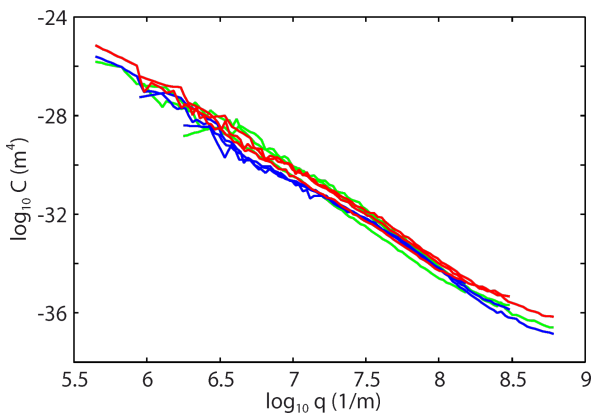

Figure 4: The power spectra as a function of the wave vector ($\log_{10}$–$\log_{10}$ scale), based on AFM topography data (green lines). The red lines are for dry skin, the blue lines for wet skin (calculated without AFM measurements).

the AFM region, a total surface area of $A_{tot} = 1.3A_0$ (where A_0 is the nominal or projected surface area) and an rms slope of 0.9. The smallest surface roughness wavevector is $q_0 = 10^3$ m^{-1} and the largest (cut-off) wavevector is $q_1 = 10^{10}$ m^{-1}. The dashed line denoted **a** was used in the study presented in [6] and corresponds to a surface with the total surface area of $A_{tot} = 2.7A_0$ and an rms slope of 2.8. Both power spectra correspond to surfaces with an rms roughness amplitude of ca. 22 μm.

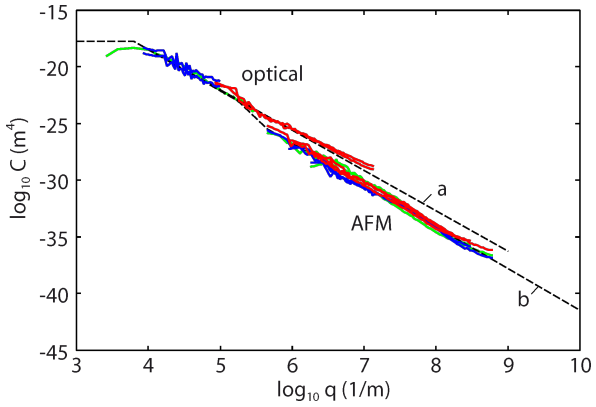

Figure 5: The power spectra as a function of the wave vector ($\log_{10}$–$\log_{10}$ scale). The dashed line denoted by **b** is the power spectra used in the calculations and correspond to a surface with the surface area $A_{tot} = 1.3A_0$ and rms slope 0.9.

Contact mechanics of dry and wet skin

The model of the skin used in the calculations is presented in Figure 6. The elastic modulus of the bulk skin is E_1 = 20 kPa and the Poisson ratio is $\nu_1 = 0.5$. The 20 μm thick layer of *stratum corneum* has a Young's modulus of E_0 = 7 MPa in the wet state and of E_0 = 1 GPa in the dry state with a Poisson ratio of $\nu_0 = 0.5$. Plastic deformation must be taken into account for the dry skin, because of the the high contact pressure. In the following calculations the plastic yield stress (or penetration hardness) of human skin was taken as σ_Y = 50 MPa [10], which is similar to the yield stress of most polymers, which are of the order of 100 MPa. We note that the yield stress of the skin is about 5% of its Young's modulus, which is typical for many materials, e.g., for dry cellulose fibers. In fact, cellulose fibers exhibit elastoplastic properties very similar to the *stratum corneum*: Both absorb water strongly and swell by wetting, both have elastic moduli of the order of 10 MPa in the wet state and of the order of 1 GPa in the dry state [11]. The swelling (and elastic softening) of the skin in water take place while the water fills the multiple intracellular cisternae in *stratum corneum* [12]. The elastoplastic parameters given above are in agreement with experimental measurements [3,10], but a large spread of the parameter values is observed in different measurements.

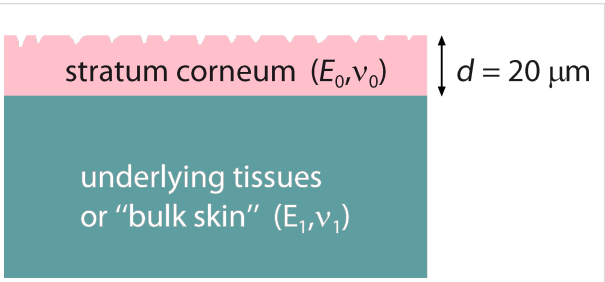

Figure 6: The model of the skin used in the calculations. The elastic modulus of the bulk skin is E_1 = 20 kPa, and the Poisson ratio is $\nu_1 = 0.5$. The 20 μm thick top layer (*stratum corneum*) has a Young's modulus of E_0 = 7 MPa, in the wet state and of E_0 = 1 GPa, in the dry state with a Poisson ratio of $\nu_0 = 0.5$. A penetration hardness of 50 MPa was assumed for dry skin.

We have used the Persson contact mechanics theory to analyze the contact between skin and a flat hard countersurface [6]. Shortly, when the interface is studied at a magnification ζ for which the surface roughness with wavevector $q > q_0\zeta$ cannot be detected, the observed surface area is given by [9,13]

$$\frac{A(\zeta)}{A_0} = \mathrm{erf}\left(\frac{1}{2\sqrt{G}}\right) \tag{2}$$

where erf(x) is the error function and

$$G(\zeta) = \pi\int_{q_0}^{\zeta q_0} dq\, q\, |\sigma_0 M_{zz}(q)|^{-2}\, C(q) \tag{3}$$

where $\sigma_0 = p_0$ is the applied stress or pressure. The linear response function M_{zz} relates (in wavevector space) the surface displacement normal to the surface to the stress acting normal to

the surface: $M_{zz}(q) = u_z(q)/\sigma_z(q)$. For a layered material of the type shown in Figure 6 it is given by $M_{zz} = -2S(q)/(qE_0^*)$, where $E_0^* = E_0/(1-\nu_0^2)$ and [14-16]

$$S(q) = \frac{1 + 4mqde^{-2qd} - mne^{-4qd}}{1 - \left(m + n + 4mq^2d^2\right)e^{-2qd} + mne^{-4qd}}, \qquad (4)$$

where

$$m = \frac{G_0/G_1 - 1}{G_0/G_1 + 3 - 4\nu_0},$$

$$n = 1 - \frac{4(1-\nu_0)}{1 + (G_0/G_1)(3-4\nu_1)},$$

where $G_0 = E_0/2(1+\nu_0)$ and $G_1 = E_1/2(1+\nu_1)$ are the shear moduli for solid 0 and solid 1, respectively.

In all the calculations presented below we have assumed a squeezing pressure $F_N/A_0 = p_0 = 6.83$ kPa, which is the average nominal contact pressure in the experiments reported on in Figure 7. Figure 8 shows the area of contact (in units of the nominal contact area A_0) as a function of the magnification ζ of the highest roughness components included in the calculation ($\log_{10}$–$\log_{10}$ scale). The blue and red curves in Figure 8 are for wet and dry skin, respectively. The solid and dashed blue curves use the surface power spectra denoted by **b** and **a** in Figure 5, respectively. For dry skin plastic yielding occurs already for small wavevector values (corresponding to long-wavelength roughness), for which the two power spectra with/without AFM data are identical. For this reason the contact mechanics for dry surfaces are the same using the two different power spectra. However, for the wet skin the power spectrum **a** result in a much smaller contact area than the power spectrum **b**. The reason is that the rms slope ξ (which is determined mainly by the large wavevector region of the power spectrum) of the surface in **a** is much larger than that in **b**, and the contact area is approximately proportional to $1/\xi$.

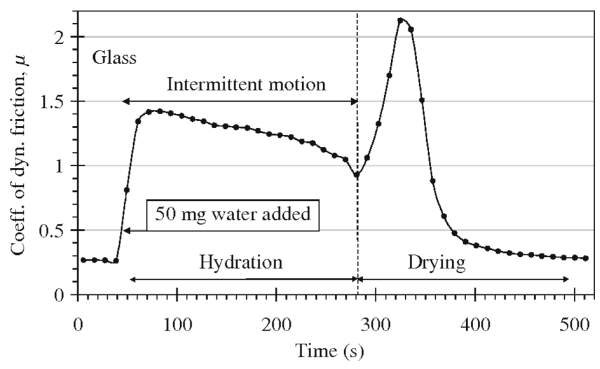

Figure 7: The friction coefficient of skin for a glass ball (R = 0.8 cm) at a sliding velocity of 0.8 cm/s and a normal load of 0.5 N during wetting/drying. Adopted from [3] with the permission of the authors.

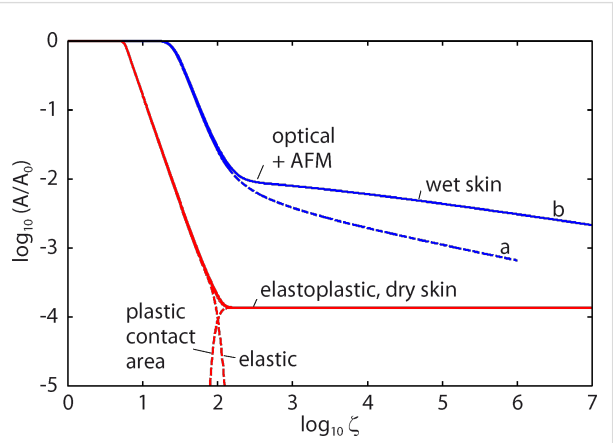

Figure 8: The ratio of the contact area A to the area of the nominal contact area A_0 as a function of the lower scale magnification ζ included in the calculation in a $\log_{10}$–$\log_{10}$ scale. The blue and the red curves correspond to wet and dry skin. The solid and dashed blue curves use the surface power spectra denoted by **b** (optical and AFM data pooled together) and **a** (optical data only) in Figure 5, respectively. The skin model shown in Figure 6 is used in the calculations. The squeezing pressure was assumed as $F_N/A_0 = p_0 = 6.83$ kPa.

The resolution of the instrument used to study surfaces determines the apparent contact area. Determination of the real contact area can be achieved only with an instrument having atomic resolution, such as AFM. Measurements based on the standard microscopy techniques, such as white light interferometry) have a resolution limited by the wavelength of the used light. Therefore, regions smaller than some fraction of the wavelength of light would appear as being in full contact and the contact area will be overestimated. At the highest magnification using the power spectra **b** the contact area is $A/A_0 = 2.15 \times 10^{-3}$ for wet skin and 1.37×10^{-4} for dry skin. For dry skin complete plastic yielding occurs in all contact regions so that $A/A_0 = \sigma_N/\sigma_Y = 1.37 \times 10^{-4}$. Plastic deformation starts at $q \geq 10^5$ m^{-1} corresponding to a wavelength of $\lambda \leq 2\pi/q \approx 60$ μm. The values of the friction coefficients, $\mu \approx 0.25$ for dry skin and $\mu \approx 1.4$ for wet skin, could be explained by frictional shear stresses of about 13 MPa for the dry surface and of about 5 MPa for the wet surface. These values are very similar to the frictional shear stresses for sliding on polymers [17], or for many thin (ca. 1 nm) confined fluid layers between hard surfaces [18]. They are also similar to the frictional shear stresses in the area of contact for tread rubber sliding on different surfaces [19], during which for sliding velocities of the order of cm/s the frictional shear stress is typically of the order of 2–8 MPa.

Capillary adhesion

In this section we evaluate different factors determining the tribological behaviour of wet skin, which is described in [3], following the line presented in [6]. The sliding friction of a glass ball was measured at a sliding velocity of 0.8 cm/s and a normal load of 0.5 N (Figure 7). At $t \approx 30$ s, a water droplet, $\Delta V = 50$ μL, was added to the sliding track. This corresponds to an average water film thickness on the track of the order of $\Delta V/LD \approx 90$ μm, where $L \approx 8$ cm is the stroke length and $D \approx 0.8$ cm the width of the (nominal) Hertzian contact region. A uniform water film of thickness $\Delta d = 90$ μm evaporates in about 500 s at room temperature, 50% relative humidity, and an evaporation rate of $\dot{d} \approx 1.7 \times 10^{-7}$ m/s (see below). This is exactly the time period necessary for the friction to return to the dry state value (Figure 7). The sharp increase of the friction coefficient that appears as the water evaporates, Figure 7, might result from the increase in the area of real contact arising from the attractive force of capillary bridges. We can take into account capillary bridges in an approximate way as described in detail in [20]. That is, water is placed at the interface between the skin and the glass surface in all regions where the separation is less than the water layer thickness:

$$d_{\mathrm{K}} = -r_{\mathrm{K}}\left(\cos\theta_1 + \cos\theta_2\right). \tag{5}$$

The negative Laplace pressure in the regions covered by water is described by

$$p_{\mathrm{K}} \approx -\gamma / r_{\mathrm{K}}\ , \tag{6}$$

where γ is the surface tension of water. If ΔA is the surface area occupied by the capillary bridges then the attractive force is

$$F_{\mathrm{a}} = \left|p_{\mathrm{K}}\right| \Delta A \tag{7}$$

The contact area and the distribution of interfacial separations are determined by using the Persson contact mechanics model with the external pressure p_0 replaced by the total pressure $p = p_0 + p_{\mathrm{a}}$, where $p_{\mathrm{a}} = F_{\mathrm{a}}/A_0$. In this mean-field approximation the force from the non-uniform distribution of capillary bridges is replaced by a uniform pressure or stress p_{a}. Note that to calculate ΔA one has to know the pressure $p = p_0 + p_{\mathrm{a}}$. Since p_{a} depends on ΔA [9] there is an implicit equation for ΔA or p_{a}, which can be solved, e.g., by iteration.

The area of real contact in thousandths of A_0 is shown in Figure 9 as a function of the average water film thickness d. The solid and dashed curves use the surface power spectra denoted by **b** and **a** in Figure 5, respectively. Note that the surface with the smaller rms slope (corresponding to the power spectra **b**) results in the largest contact area. For $d > 12$ μm the water covers all the interface (flooded condition). We have assumed a contact angle of 0° for water on glass and of 80° for water on skin. The increase in the contact area for an average water film thickness between 0 and about 10 μm is due to the formation of capillary bridges. Since the contact area is small compared to the nominal contact area, the area of real contact is proportional to the effective squeezing force $p_0 + p_{\mathrm{a}}$. Therefore, at the point where the contact area is maximal, $p_{\mathrm{a}} \approx p_0$, i.e., the attractive capillary pressure is of similar magnitude as the (nominally) applied pressure $p_0 \approx 7$ kPa. The width (in seconds) of the friction peak observed in Figure 7 corresponds to a change in the average water film thickness (due to evaporation) of ca. 10 μm, which is in beautiful agreement with the width of our predicted friction peak.

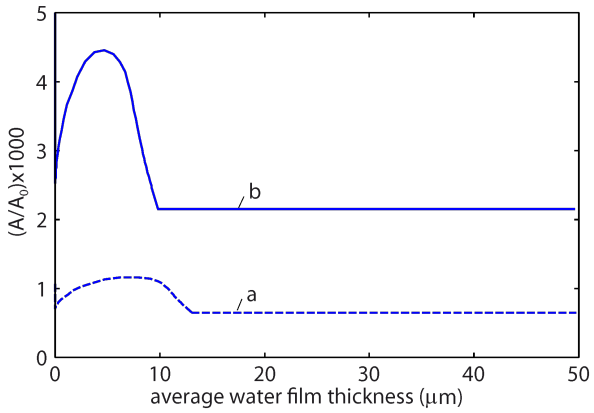

Figure 9: The area of real contact (in thousandths of the nominal contact area, A_0) as a function of the average water film thickness d. For $d > 12$ μm water fills the whole interface. The solid and dashed curves use the surface power spectra denoted by **b** and **a** in Figure 5, respectively. In the calculations we have used the skin model shown in Figure 6 and assumed a contact angle of 0° for water on glass and of 80° for water on skin. The squeezing pressure is $p_0 = F_{\mathrm{N}}/A_0 = 6.83$ kPa.

The water evaporation rate $\dot{d}$ (change per unit time of the fluid film thickness d) is given by the empirical formula [21]

$$\dot{d} \approx -\left(p_{\mathrm{w}} - p_{\mathrm{a}}\right) \times \left(a + bv\right) / Y\ , \tag{8}$$

where p_{w} is the water saturation vapor pressure at the water (surface) temperature, p_{a} is the water vapor pressure in the air (which is the product of the relative humidity and the saturation water pressure at the air temperature and air pressure), and v the velocity of the air (some distance from the water surface) over the water surface. Y is the latent heat of evaporation (for water $Y \approx 2272$ kJ/kg) and the coefficients a and b are

$a = 8.9 \times 10^{-5}$ m^4/(kg·s) and $b = 7.8 \times 10^{-5}$ m^3/kg, respectively. If the water on the skin has a temperature close to the body temperature, say $T = 35$ °C, then $p_w = 5.6$ kPa. The experiments were performed at room temperature ($T = 20$ °C) and a relative humidity of 50% giving $p_a = 0.5 \times 2.3$ kPa = 1.15 kPa. Hence, since $v << 1$ m/s, we get $\dot{d} \approx 1.7 \times 10^{-7}$ m/s. Thus it takes $\Delta t = \Delta d/\dot{d} \approx 60$ s for the water film thickness to decrease by $\Delta d \approx 10$ μm, which according to the theory is the film thickness range over which the capillary attraction between the surfaces is effective. This is in beautiful agreement with the experimental data (see Figure 7).

We have assumed that the thermodynamic water–skin contact angle is $\theta_1 \approx 80°$, and the water–glass contact angle $\theta_2 \approx 0°$. Thus $\cos\theta_1 + \cos\theta_2 \approx 1 > 0$ so that the interface is hydrophilic and attractive capillary bridges can form. In a second friction experiment Adams et al. [3] used a polypropylene sphere and in this case no increase in the friction was observed during drying. This is consistent with the fact that the water–polypropylene contact angle $\theta_2 \approx 102°$ so that $\cos\theta_1 + \cos\theta_2 \approx -0.03 < 0$. Hence, the interface may be slightly hydrophobic resulting in a negligible interaction between the counterpart bodies during drying. For more strongly hydrophobic interfaces, e.g., skin in contact with Teflon in water, a dewetting transition may occur resulting in a dry contact area and an effective attraction between the skin and the countersurface [22].

Conclusion

We studied the contact mechanics and friction for dry and water-lubricated human skin. The surface topography is studied by using two different methods, white light interferometry and AFM, which in combination allowed us to obtain the complete surface roughness power spectrum. The Persson contact mechanics theory is used to calculate the dependency of the apparent contact area on the magnification for both dry and wet skin. It was shown, that the proper estimation of the real contact area and attraction force is possible only if both types of surface profile measurements, AFM and white light interferometry, are used for the calculation of the roughness power spectrum. For dry skin plastic yielding becomes important and will determine the area of real contact at the highest magnification. The measured friction coefficient on both dry and wet skin can be explained assuming that a frictional shear stress $\sigma_f \approx 10$ MPa acts in the area of real contact during sliding. This frictional shear stress is typical for sliding on elastomeric surfaces, and for nanometer thick confined fluid films. The big increase in friction, which has been observed for glass sliding on wet skin as the skin dries up, can be explained by the increase in the contact area arising from the attraction of capillary bridges. This effect is predicted to operate as long as the water layer is thinner than ca. 10 μm.

References

1. Warman, P.; Ennos, A. *J. Exp. Biol.* **2009,** *212,* 2016–2022. doi:10.1242/jeb.028977
2. Derler, S.; Gerhardt, L.-C. *Tribol. Lett.* **2012,** *45,* 1–27. doi:10.1007/s11249-011-9854-y
3. Adams, M. J.; Briscoe, B. J.; Johnson, S. A. *Tribol. Lett.* **2007,** *26,* 239–253. doi:10.1007/s11249-007-9206-0
4. Park, A. C.; Baddiel, C. B. *J. Soc. Cosmet. Chem.* **1972,** *23,* 471–479.
5. Federle, W.; Barnes, W. J. P.; Baumgartner, W.; Drechsler, P.; Smith, J. M. *J. R. Soc., Interface* **2006,** *3,* 689–697. doi:10.1098/rsif.2006.0135
6. Persson, B. J. N.; Kovalev, A.; Gorb, S. N. *Tribol. Lett.* **2013,** *50,* 17. doi:10.1007/s11249-012-0053-2
7. Ginn, M. E.; Noyes, C. M.; Jungermann, E. *J. Colloid Interface Sci.* **1968,** *26,* 146–151. doi:10.1016/0021-9797(68)90306-8
8. Persson, B. J. N.; Albohr, O.; Tartaglino, U.; Volokitin, A. I.; Tosatti, E. *J. Phys.: Condens. Matter* **2005,** *17,* R1. doi:10.1088/0953-8984/17/1/R01
9. Persson, B. N. J. *Surf. Sci. Rep.* **2006,** *61,* 201–227. doi:10.1016/j.surfrep.2006.04.001
10. Kendall, M. A. F.; Carter, F. V.; Mitchell, T. J.; Bellhouse, B. J. Comparison of the transdermal ballistic delivery of micro-particles into the human and porcine skin. In *Proceedings of the 23rd Annual EMBS International Conference,* IEEE, 2001; pp 2991–2994. http://www.dtic.mil/dtic/tr/fulltext/u2/a410062.pdf
11. Persson, B. J. N.; Ganser, C.; Schmied, F.; Teichert, C.; Schennach, R.; Gilli, E.; Hirn, U. *J. Phys.: Condens. Matter* **2013,** *25,* 045002. doi:10.1088/0953-8984/25/4/045002
12. Warner, R. R.; Stone, K. J.; Boissy, Y. L. *J. Invest. Dermatol.* **2003,** *120,* 275–284. doi:10.1046/j.1523-1747.2003.12046.x
13. Persson, B. N. J. *J. Chem. Phys.* **2001,** *115,* 3840. doi:10.1063/1.1388626
14. O'Sullivan, T. C.; King, R. B. *J. Tribol.* **1988,** *110,* 235–240. doi:10.1115/1.3261591
15. Persson, B. N. J. *J. Phys.: Condens. Matter* **2012,** *24,* 095008. doi:10.1088/0953-8984/24/9/095008
16. Carbone, G.; Lorenz, B.; Persson, B. N. J.; Wohlers, A. *Eur. Phys. J. E* **2009,** *29,* 275–284. doi:10.1140/epje/i2009-10484-8
17. Sivebaek, I. M.; Samoilov, V. N.; Persson, B. N. J. *Eur. Phys. J. E: Soft Matter Biol. Phys.* **2008,** *27,* 37–46. doi:10.1140/epje/i2008-10349-8
18. Sivebaek, I. M.; Samoilov, V. N.; Persson, B. N. J. *Phys. Rev. Lett.* **2012,** *108,* 036102. doi:10.1103/PhysRevLett.108.036102
19. Lorenz, B.; Persson, B. N. J., in press. *Unpublished*, in press.
20. Persson, B. N. J. *J. Phys.: Condens. Matter* **2008,** *20,* 315007. doi:10.1088/0953-8984/20/31/315007
21. *ASHRAE Handbooks*; Technical Organization American Society of Heating, Refrigerating and Air- Conditioning Engineers, Inc. (ASHRAE), 2013. This Handbook is considered the practical repository of knowledge on the various topics that form the field of heating, ventilation, air-conditioning, and refrigeration.
22. Persson, B. N. J.; Volokitin, A. I.; Tosatti, E. *Eur. Phys. J. E: Soft Matter Biol. Phys.* **2003,** *11,* 409–413. doi:10.1140/epje/i2003-10054-2

BEILSTEIN JOURNAL OF NANOTECHNOLOGY

Influence of the PDMS substrate stiffness on the adhesion of *Acanthamoeba castellanii*

Sören B. Gutekunst[1], Carsten Grabosch[1], Alexander Kovalev[2], Stanislav N. Gorb[2] and Christine Selhuber-Unkel[*1]

Full Research Paper

Open Access

Address:
[1]Institute for Materials Science, Dept. Biocompatible Nanomaterials, Christian-Albrechts-Universität zu Kiel, Kaiserstr. 2, D-24143 Kiel, Germany and [2]Zoological Institute, Dept. Functional Morphology and Biomechanics, Christian-Albrechts-Universität zu Kiel, Am Botanischen Garten 9, D-24118 Kiel, Germany

Email:
Christine Selhuber-Unkel[*] - cse@tf.uni-kiel.de

* Corresponding author

Keywords:
acanthamoeba; cell adhesion; elastic substrates; mechanosensing; silicones

Beilstein J. Nanotechnol. **2014,** *5,* 1393–1398.
doi:10.3762/bjnano.5.152

Received: 28 February 2014
Accepted: 06 August 2014
Published: 28 August 2014

This article is part of the Thematic Series "Biological and bioinspired adhesion and friction".

Associate Editor: K. Koch

Abstract

Background: Mechanosensing of cells, particularly the cellular response to substrates with different elastic properties, has been discovered in recent years, but almost exclusively in mammalian cells. Much less attention has been paid to mechanosensing in other cell systems, such as in eukaryotic human pathogens.

Results: We report here on the influence of substrate stiffness on the adhesion of the human pathogen *Acanthamoebae castellanii (A. castellanii)*. By comparing the cell adhesion area of *A. castellanii* trophozoites on polydimethylsiloxane (PDMS) substrates with different Young's moduli (4 kPa, 29 kPa, and 128 kPa), we find significant differences in cell adhesion area as a function of substrate stiffness. In particular, the cell adhesion area of *A. castellanii* increases with a decreasing Young's modulus of the substrate.

Conclusion: The dependence of *A. castellanii* adhesion on the elastic properties of the substrate is the first study suggesting a mechanosensory effect for a eukaryotic human pathogen. Interestingly, the main targets of *A. castellanii* infections in the human body are the eye and the brain, i.e., very soft environments. Thus, our study provides first hints towards the relevance of mechanical aspects for the pathogenicity of eukaryotic parasites.

Introduction

The adhesion of many cell types, including fibroblasts, myocytes, and neurons, depends on the mechanical properties of the cellular microenvironment [1-3]. In particular, cells prefer to adhere to materials, which have mechanical properties similar to the ones found in their natural biological environments. Cells can even adapt their direction of migration on ma-

terials with gradually changing stiffness, a phenomenon known as mechanotaxis [4,5]. This adaptation is presumably due to an active probing of the cellular microenvironment by nanobiomechanical mechanisms in cells, allowing them to reorient and position themselves [6]. Once grown on a substrate with defined elasticity, cells adapt their own elasticity to the elasticity of their environment [7]. But not only differentiated cells are influenced by substrate stiffness. For stem cells it has been demonstrated that their differentiation is directed towards certain cell types if their adhesion substrate has similar mechanical properties as the natural tissue of the differentiated cell [8], probably mediated by stress-fibre polarization [9]. Even the adhesion of tumor cells is controlled by substrate stiffness [10]. However, not only substrate stiffness plays a decisive role for controlling cell adhesion on soft substrates, but also the specific mechanical anchorage of adhesion molecules [11]. The mechanosensory function of cells is supposed to be closely linked to the mechanisms of active force generation in cells. Analyzing cellular traction forces on elastic substrates has led to substantial information on the forces that cells are able to exert [12,13]. Taken together, there is evidence for the existence of mechanosensors in mammalian cells, yet the detailed mechanisms of mechanosensing are still under investigation. Currently, there are several molecules, such as talin and vinculin as well as ion channels under discussion to serve as possible candidates involved in sensing the mechanical properties of the cellular microenvironment [14-16].

In contrast to mammalian cells, for eukaryotic protists, such as amoebae, there is still only very little knowledge about their ability to sense the elastic properties of their extracellular microenvironments. Only for intracellular mechanosensing, a recent study discusses the signficiant role of myosin-II motor proteins in mechanosensing of the social amoeba *Dictyostelium discoideum* [17]. A medically highly relevant amoeba species are acanthamoebae. *Acanthamoeba spp.* are free-living protists, which are frequently found in water reservoirs such as lakes, swimming-pools, and even in tap water [18]. Some acanthamoeba species are pathogenic to humans, such as *A. culbertsoni* and *A. castellanii* [19,20]. Whereas both *A. culbertsoni* and *A. castellanii* can cause granulomatous amoebic encephalitis (GAE), a chronic and severe disease of the central nervous system [21], *A. castellanii* is more feared for its potential to infect contact lens users and cause a painful and hardly treatable keratitis in their eyes [22]. Such an acanthamoeba keratitis is often related to wrong contact lens care, e.g., due to nonsatisfactory contact lens disinfection [23].

In the study presented here we investigated the influence of substrate stiffness on adhesion properties of *A. castellanii*. We prepared polydimethylsiloxane (PDMS) substrates with Young's moduli of 4 kPa, 29 kPa, and 128 kPa. These Young's moduli were chosen in order to cover an elasticity range, for which a significant effect of substrate stiffness on the adhesion of mammalian cells has already been reported [1]. We systematically investigated the adhesion of *A. castellanii* on these materials by analyzing the number of adhering amoebae and their adhesion area as a function of substrate stiffness. We demonstrate that the adhesion area of *A. castellanii* is significantly larger on soft substrates compared to stiff substrates, showing the relevance of the cellular microenvironment and associated nanobiomechanical cues also for the adhesion of a eukaryotic human pathogen.

Experimental

Preparation of polydimethylsiloxane (PDMS) substrates

Silicone base and curing agent (Sylgard 184, DOW Corning) were mixed thoroughly in a ratio (*m*/*m*) of 80:1, 57:1, and 40:1 by following the curing procedure given in Trappmann et al. [11]. Afterwards, the mixtures were poured in sterile 6-well plates (Sarstedt, Nümbrecht, Germany) up to a thickness of approx. 2 mm and degased for 3.5 h. Thermal polymerization was carried out for 21 h at 70 °C followed by a slow cool down to room temperature.

Elasticity measurements

Mechanical properties of PDMS substrates were determined by microindentation using a micro-force measurements device (Basalt-BT01, Tetra GmbH, Ilmenau, Germany) [24]. The recorded force–distance curves were used to calculate the Young's modulus of the PDMS substrates and the work of adhesion with the Johnson–Kendall–Roberts (JKR) model [25]. This model is used to characterize the mechanical properties of soft materials in the presence of adhesion, since it takes into account the attractive forces between the microindenter tip and the sample. For all substrates, elastic moduli were determined from the unloading part of the curve to consider only the elastic behavior and not the plastic deformation of the sample. The measurements were performed under ambient conditions (25–26 °C temperature and 40–50% relative humidity). Analysis of the Young's moduli of the different PDMS substrates resulted in 4 ± 1 kPa (silicone base/curing agent = 80:1), 29 ± 3 kPa (57:1), and 128 ± 32 kPa (40:1).

Acanthamoeba culture

Trophozoites of *A. castellanii* (ATTC 30234) were cultured at room temperature in Peptone Yeast Glucose (PYG) 712 medium (20.0 g proteose peptone (BD, Sparks, USA), 1.00 g yeast extract (BD, Sparks, USA), 950 mL distilled water, 10.0 mL 0.4 M $MgSO_4 \cdot 7H_2O$ (AppliChem, Darmstadt, Germany), 8.00 mL 0.05 M $CaCl_2$ (AppliChem, Darmstadt,

Germany), 34.0 mL 0.1 M sodium citrate dihydrate (Merck, Darmstadt, Germany), 10.0 mL 0.005 M $(NH_4)_2Fe(SO_4)_2{\cdot}6H_2O$ (AppliChem, Darmstadt, Germany), 10.0 mL 0.25 M $Na_2HPO_4{\cdot}7H_2O$ (Roth, Karlsruhe, Germany), 10.0 mL 0.25 M KH_2PO_4 (Roth, Karlsruhe, Germany), 50.0 mL 2 M glucose (Sigma–Aldrich Chemie GmbH, Steinheim, Germany)). In this axenic culture, the PYG 712 medium was regularly exchanged in the cell culture flasks in order to avoid an encystment of *A. castellanii* trophozoites.

Adhesion experiments

The PDMS substrates were washed with PYG 712 medium before use. *A. castellanii* were detached from the cell culture substrate by cautiously hitting the culture flask. The acanthamoebae were counted by a Neubauer hemocytometer and 30.000 acanthamoebae were incubated in 1 mL PYG 712 for 1 h to ensure that the amoebae are fully spread at the time of the experiment. After this incubation period, 30 phase-contrast images were captured with a 10× objective (UPlanFL, Olympus, Japan) on an inverted microscope (IX-81, Olympus, Japan) for each PDMS substrate and for the control substrate (sterile 6-well plate, Sarstedt, Nümbrecht, Germany) by using a digital camera (C-9300, Hamamatsu, Japan). The experiments were carried out on three different days (on each day in triplicate). Cell numbers and areas were evaluated by manual image segmentation with ImageJ [26]. Statistical significance was analyzed by using a Kruskal–Wallis test and a multiple comparison test in Matlab (MathWorks, USA).

Results and Discussion

Polydimethylsiloxane (PDMS) has, in recent years, proven to be a versatile tool for cell adhesion studies, in particular for studying effects of microstructures on cell adhesion [27,28], and it is also well-known for its excellent biocompatibility [29,30]. Figure 1 shows typical phase-contrast images of *A. castellanii* trophozoites adhering to the PDMS substrates and to the control substrate used in this study. The phase contrast images reveal strong halos that surround the acanthamoebae. This means that the acanthamoebae do not flatten during spreading on neither of the substrates, but keep an ellipsoidal shape. Thus, they do not spread as extensively as many mammalian cell types [31,32]. Images of *A. castellanii* on substrates with different Young's moduli as well as on a tissue culture control sample (Figure 1) show that the adhesion of *A. castellanii* is, at first glance, not strongly influenced by the substrate stiffness. But a closer look reveals differences: On substrates with a low Young's modulus (4 kPa), *A. castellanii* occupy a larger area compared to acanthamoebae on substrates with a higher Young's modulus (128 kPa). The substrate with a Young's modulus of 29 kPa gave an intermediate value. On the control sample, the cell adhesion area was similar to the one on the 4 kPa substrate. The increase of adhesion area with decreasing Young`s modulus is opposite to the behavior of human mesenchymal stem cells [33] but is in good agreement with the trend observed in studies on neural stem cell cultures [34]. This result is reasonable, as during the infection process, *A. castellanii* adhere to comparably soft microenvironments in the brain and in the eye. Interestingly, there is no significant difference in the morphology of *A. castellanii* between PDMS substrates and the positive control substrate. This shows that *A. castellanii* trophozoites can adhere very well to PDMS without the need for further biofunctionalization, as the PDMS was used in its hydrophobic, non-functionalized state. This is very important to note, as recently, indications have been found that not only the elasticity of the substrate is a decisive parameter for cell adhesion, but instead also the linkage of adhesion molecules to the substrate [11]. Due to the usage of non-functionalized PDMS substrates, we can therefore exclude such an effect of adhesion-ligand anchorage in our experiments.

In order to characterize the dependence of the cell area on the substrate stiffness in further detail, we carried out an extensive analysis of the cell areas of *A. castellanii* by image segmentation of several thousands of acanthamoebae per substrate type.

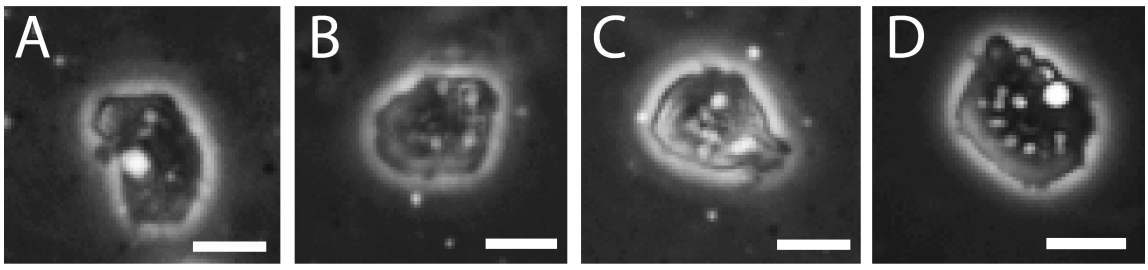

Figure 1: Phase contrast images of *A. castellanii* trophozoites on PDMS substrates with different Young's moduli and a control after 1 h in culture in PYG medium: (A) 4 kPa, (B) 29 kPa, (C) 128 kPa, and (D) control. The adhesion area of *A. castellanii* is influenced by substrate stiffness, i.e., the cell area on the stiff sample (C) is smaller than on the softer samples (A,B) and on the control sample (D). The comparison of acanthamoeba morphology on PDMS substrates and on the control sample shows that acanthamoebae adhere very well to the non-functionalized PDMS substrates. Scale bar: 15.2 µm.

The results of this analysis are summarized in Figure 2 and Figure 3. Figure 2 shows the mean values and standard deviations for the projected cell adhesion areas of *A. castellanii* as a function of the substrate stiffness. These values were determined from nine experiments in total, i.e., three independent experiments carried out on three independent measurement days. The data clearly show that the cell adhesion area decreases with increasing substrate stiffness of PDMS substrates. Statistical analysis revealed that all mean ranks are significantly different at a 0.001 level (***).

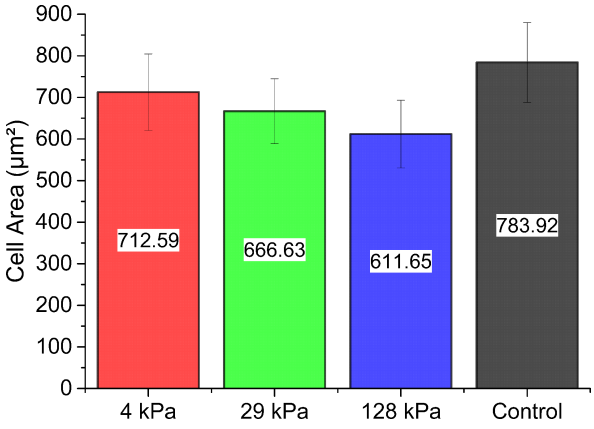

Figure 2: Cell adhesion area of *A. castellanii* as a function of the Young's modulus of the PDMS substrates and in comparison to the control substrate after 1 h of adhesion in PYG medium. These results were obtained from analyzing 3092 amoebae (4 kPa), 3044 amoebae (29 kPa), 3108 amoebae (128 kPa), and 2194 amoebae (control). The bar diagram gives the mean cell area (calculated from the mean of cell adhesion area on each substrate) and standard deviation. This standard deviation is a measure for the differences in cell adhesion area on different individual samples of the same type. The numeric mean values are additionally given inside the bars. The differences of the means are statistically significant (Kruskal–Wallis test; ***, $p < 0.001$, $n > 2194$ cells per substrate type).

In Figure 3, we present the distribution of projected cell areas as a function of substrate stiffness compared to the control sample. Interestingly, the distribution of projected cell areas does not follow a Gaussian distribution function, but shows a tail towards large cell areas. This tail of the distribution is a very typical feature of cell sizes, and has been reported for many cell types, such as mammalian cells [35,36], but also for *A. castellanii* [37]. Comparing the distribution of cell adhesion areas for substrates having different Young's moduli supports the results from Figure 1 and Figure 2, i.e., that substrate stiffness influences cell adhesion area. The difference between the control sample and the PDMS sample with Young's modulus 128 kPa is eye-catching here, but differences can also be observed between the different PDMS samples. In particular the pie charts demonstrate that the amount of large and small cells changes as a function of PDMS stiffness.

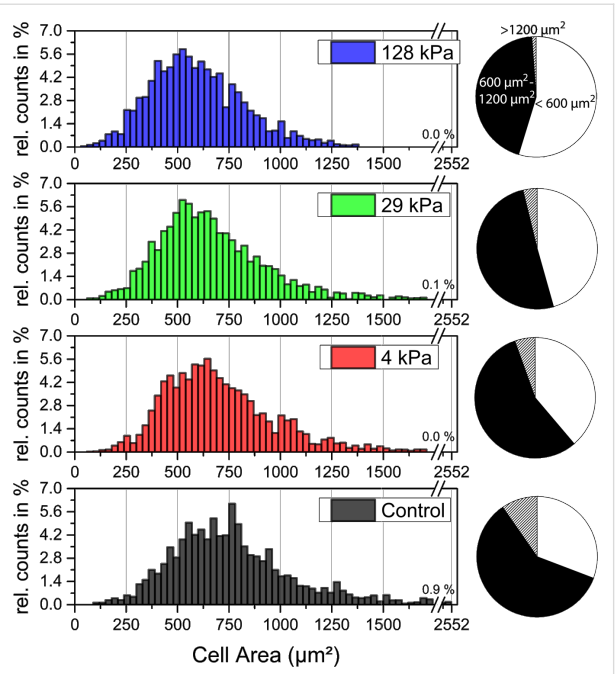

Figure 3: Average relative counts of projected cell areas of adhering *A. castellanii* on PDMS substrates and on the control substrates. The histograms show that the distribution is slightly asymmetric and can therefore not be fitted with a Gaussian. Average relative counts were calculated by determining the relative counts per sample and generating the average for each bin from all experiments, in order to equally rate all experiments. The value above the interception of the x-axis shows the relative counts of cell adhesion areas larger than 1750 µm². Differences in cell area distribution become particularly visible when comparing the pie charts (white: cell adhesion area < 600 µm²; black: 600 µm² ≤ cell adhesion area ≤ 1200 µm²; striped: cell adhesion area > 1200 µm²).

The dependence of the adhesion on the substrate stiffness is, however, not reflected in the number of acanthamoebae attached to the different surfaces (Figure 4). No systematic relation for the dependence of the number of attached acanthamoebae on the substrate stiffness could be found in our experiments after 1 h of adhesion. The incubation time of 1 h chosen here might be too short to generate severe impact on parameters such as cell proliferation, as the doubling time of acanthamoeba in axenic culture is on the timescale of days [38]. As acanthamoeba can also be grown in suspension [19], their proliferation might not be strongly influenced by the presence of any substrate.

In a recent study, we had investigated the adhesion of *A. castellanii* to hydrogel materials used in contact lenses [39]. We determined a very strong dependence of *A. castellanii* adhesion on the water content of contact lens materials, i.e., a strong increase in adhesion with increasing water content. In the study presented here, the PDMS material was hydrophobic and repelled water. Also according to literature, the water content of PDMS is negligible [40]. Therefore, a bias of our data by

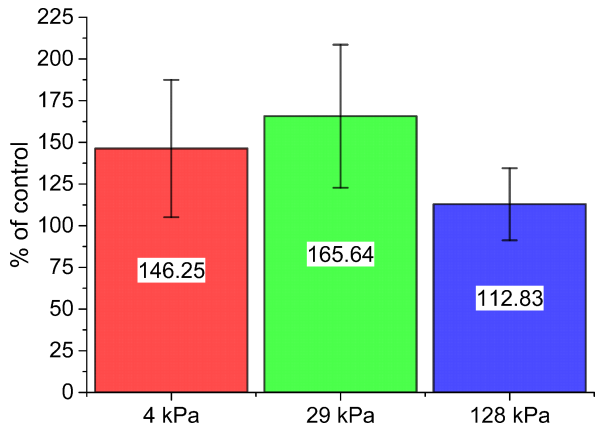

Figure 4: Numbers (in % of control) of *A. castellanii* adhering to PDMS substrates after 1 h of incubation. The values were normalized to the number of *A. castellanii* adhering to the control substrate. Here, no systematic effect of the substrate stiffness on the number of cells could be observed. Mean values are shown in a bar diagram, where each numeric value is given inside the bar. Error bars denote standard deviations.

changes in the water content of the substrates can be excluded for the experiments presented here. Furthermore, in our previous study, we did not find a significant dependence of the adhesion on the substrate stiffness for Young's moduli between 0.30 and 0.66 MPa [39]. In contrast to this previous study, we here discuss adhesion dependence on Young's moduli that are one order of magnitude smaller. However, it seems logical that *A. castellanii* spread larger on soft substrates, as their main human infection targets, eye and brain, are very soft, with the brain having Young's moduli of about 1–10 kPa and less [41]. However, the influence of the substrate stiffness on the adhesion of *A. castellanii* that we observe in our study is not as pronounced as for mammalian cells [2]. Such an extenuated effect is reasonable, as acanthamoebae have to be able to survive and migrate in very diverse natural environments, ranging from soil to water reservoirs.

Conclusion

We have presented an adhesion analysis of human pathogenic *A. castellanii* to soft elastic substrates. We find that the cell adhesion areas of *A. castellanii* change significantly as a function of the substrate stiffness, with the largest average cell adhesion areas present on the softest substrates with a Young's modulus of 4 kPa. In contrast, the number of adhering acanthamoebae is not significantly changed by the substrate stiffness after 1 h of adhesion. Our results indicate that adhesion of *A. castellanii* is influenced by substrate stiffness, presumably by mechanosensory mechanisms that allow them to sense and react on the stiffness of their surrounding environment. Our study provides first evidence for such a mechanosensory function in the adhesion of *A. castellanii*. Furthermore, mammalian cells are known to adhere preferably to substrates with mechanical properties similar to their natural environment. We show that *A. castellanii* adhere with larger contact areas on softer substrates. This is very interesting, as their natural targets in the human body are soft environments (brain, eye). Therefore, our study also shows very first indications for the relevance of mechanical aspects in the pathogenicity of parasites and can serve as a starting point for many future studies on the impact of mechanical parameters on the adhesion of pathogenic organisms.

Acknowledgements

We gratefully acknowledge Matthias Leippe (Zoological Institute, University of Kiel) for providing the acanthamoeba strain and for his advice. Furthermore, we thank Heidrun Ließegang and Julia F. Reverey for technical support in culturing *A. castellanii*. Manuela Lieb is acknowledged for her general support in laboratory work and Anneke Möhring for microindentation experiments. This study was supported by the Emmy Noether programme of the German Research Foundation (DFG), grant SE 1801/2-1.

References

1. Discher, D. E.; Janmey, P.; Wang, Y.-l. *Science* **2005,** *310,* 1139–1143. doi:10.1126/science.1116995
2. Engler, A.; Bacakova, L.; Newman, C.; Hategan, A.; Griffin, M.; Discher, D. *Biophys. J.* **2004,** *86,* 617–628. doi:10.1016/S0006-3495(04)74140-5
3. Pelham, R. J., Jr.; Wang, Y.-l. *Proc. Natl. Acad. Sci. U. S. A.* **1997,** *94,* 13661–13665. doi:10.1073/pnas.94.25.13661
4. Lo, C.-M.; Wang, H.-B.; Dembo, M.; Wang, Y.-l. *Biophys. J.* **2000,** *79,* 144–152. doi:10.1016/S0006-3495(00)76279-5
5. Wong, J. Y.; Velasco, A.; Rajagopalan, P.; Pham, Q. *Langmuir* **2003,** *19,* 1908–1913. doi:10.1021/la026403p
6. Bischofs, I. B.; Schwarz, U. S. *Proc. Natl. Acad. Sci. U. S. A.* **2003,** *100,* 9274–9279. doi:10.1073/pnas.1233544100
7. Solon, J.; Levental, I.; Sengupta, K.; Georges, P. C.; Janmey, P. A. *Biophys. J.* **2007,** *93,* 4453–4461. doi:10.1529/biophysj.106.101386
8. Engler, A. J.; Sen, S.; Sweeney, H. L.; Discher, D. E. *Cell* **2006,** *126,* 677–689. doi:10.1016/j.cell.2006.06.044
9. Zemel, A.; Rehfeldt, F.; Brown, A. E. X.; Discher, D. E.; Safran, S. A. *Nat. Phys.* **2010,** *6,* 468–473. doi:10.1038/Nphys1613
10. Tilghman, R. W.; Cowan, C. R.; Mih, J. D.; Koryakina, Y.; Gioeli, D.; Slack-Davis, J. K.; Blackman, B. R.; Tschumperlin, D. J.; Parsons, J. T. *PLoS One* **2010,** *5,* e12905. doi:10.1371/journal.pone.0012905
11. Trappmann, B.; Gautrot, J. E.; Connelly, J. T.; Strange, D. G. T.; Li, Y.; Oyen, M. L.; Cohen Stuart, M. A.; Boehm, H.; Li, B.; Vogel, V.; Spatz, J. P.; Watt, F. M.; Huck, W. T. S. *Nat. Mater.* **2012,** *11,* 742. doi:10.1038/NMAT3387
12. Gardel, M. L.; Sabass, B.; Ji, L.; Danuser, G.; Schwarz, U. S.; Waterman, C. M. *J. Cell Biol.* **2008,** *183,* 999–1005. doi:10.1083/jcb.200810060
13. Sabass, B.; Gardel, M. L.; Waterman, C. M.; Schwarz, U. S. *Biophys. J.* **2008,** *94,* 207–220. doi:10.1529/biophysj.107.113670
14. Riveline, D.; Zamir, E.; Balaban, N. Q.; Schwarz, U. S.; Ishizaki, T.; Narumiya, S.; Kam, Z.; Geiger, B.; Bershadsky, A. D. *J. Cell Biol.* **2001,** *153,* 1175–1186. doi:10.1083/Jcb.153.6.1175

15. le Duc, Q.; Shi, Q.; Blonk, I.; Sonnenberg, A.; Wang, N.; Leckband, D.; de Rooij, J. *J. Cell Biol.* **2010,** *189,* 1107–1115. doi:10.1083/jcb.201001149
16. Hoffman, B. D.; Grashoff, C.; Schwartz, M. A. *Nature* **2011,** *475,* 316–323. doi:10.1038/nature10316
17. Luo, T.; Mohan, K.; Iglesias, P. A.; Robinson, D. N. *Nat. Mater.* **2013,** *12,* 1064–1071. doi:10.1038/nmat3772
18. Seal, D.; Stapleton, F.; Dart, J. *Br. J. Ophthalmol.* **1992,** *76,* 424–427. doi:10.1136/bjo.76.7.424
19. Marciano-Cabral, F.; Cabral, G. *Clin. Microbiol. Rev.* **2003,** *16,* 273–307. doi:10.1128/cmr.16.2.273-307.2003
20. Hurt, M.; Neelam, S.; Niederkorn, J.; Alizadeh, H. *Infect. Immun.* **2003,** *71,* 6243–6255. doi:10.1128/iai.71.11.6243-6255.2003
21. Harrison, J. L.; Ferreira, G. A.; Raborn, E. S.; Lafrenaye, A. D.; Marciano-Cabral, F.; Cabral, G. A. *Infect. Immun.* **2010,** *78,* 4001–4011. doi:10.1128/iai.00047-10
22. Lorenzo-Morales, J.; Martin-Navarro, C. M.; López-Arencibia, A.; Arnalich-Montiel, F.; Piñero, J. E.; Valladares, B. *Trends Parasitol.* **2013,** *29,* 181–187. doi:10.1016/J.Pt.2013.01.006
23. Martín-Navarro, C. M.; Lorenzo-Morales, J.; Cabrera-Serra, M. G.; Rancel, F.; Coronado-Álvarez, N. M.; Piñero, J. E.; Valladares, B. *J. Med. Microbiol.* **2008,** *57,* 1399–1404. doi:10.1099/jmm.0.2008/003459-0
24. Piluso, S.; Hiebl, B.; Gorb, S. N.; Kovalev, A.; Lendlein, A.; Neffe, A. T. *Int. J. Artif. Organs* **2011,** *34,* 192–197. doi:10.5301/IJAO.2011.6394
25. Johnson, K. L.; Kendall, K.; Roberts, A. D. *Proc. R. Soc. London, Ser. A* **1971,** *324,* 301–313. doi:10.1098/rspa.1971.0141
26. Rasband, W. S. ImageJ. U.S. National Institutes of Health: Bethesda, MD, 2005; http://rsb.info.nih.gov/ij/ (accessed Feb 27, 2014).
27. Mussig, E.; Steinberg, T.; Schulz, S.; Spatz, J. P.; Ulmer, J.; Grabe, N.; Kohl, A.; Komposch, G.; Tomakidi, P. *Adv. Funct. Mater.* **2008,** *18,* 2919–2929. doi:10.1002/adfm.200800381
28. Tan, J. L.; Tien, J.; Pirone, D. M.; Gray, D. S.; Bhadriraju, K.; Chen, C. S. *Proc. Natl. Acad. Sci. U. S. A.* **2003,** *100,* 1484–1489. doi:10.1073/pnas.0235407100
29. Defrère, S.; Mestagdt, M.; Riva, R.; Krier, F.; Van Langendonckt, A.; Drion, P.; Jérôme, C.; Evrard, B.; Dehoux, J.-P.; Foidart, J.-M.; Donnez, J. *Macromol. Biosci.* **2011,** *11,* 1336–1345. doi:10.1002/mabi.201100077
30. Alauzun, J. G.; Young, S.; D'Souza, R.; Liu, L.; Brook, M. A.; Sheardown, H. D. *Biomaterials* **2010,** *31,* 3471–3478. doi:10.1016/j.biomaterials.2010.01.069
31. Cavalcanti-Adam, E. A.; Volberg, T.; Micoulet, A.; Kessler, H.; Geiger, B.; Spatz, J. P. *Biophys. J.* **2007,** *92,* 2964–2974. doi:10.1529/biophysj.106.089730
32. Rossen, N. S.; Hansen, A. J.; Selhuber-Unkel, C.; Oddershede, L. B. *PLoS One* **2011,** *6,* e25196. doi:10.1371/journal.pone.0025196
33. Rehfeldt, F.; Brown, A. E. X.; Raab, M.; Cai, S.; Zajac, A. L.; Zemel, A.; Discher, D. E. *Integr. Biol.* **2012,** *4,* 422–430. doi:10.1039/c2ib00150k
34. Saha, K.; Keung, A. J.; Irwin, E. F.; Li, Y.; Little, L.; Schaffer, D. V.; Healy, K. E. *Biophys. J.* **2008,** *95,* 4426–4438. doi:10.1529/biophysj.108.132217
35. Hidaka, C.; Cheng, C.; Alexandre, D.; Bhargava, M.; Torzilli, P. *Cell Tissue Res.* **2006,** *323,* 127–135. doi:10.1007/s00441-005-0050-y
36. Puliafito, A.; Hufnagel, L.; Neveu, P.; Streichan, S.; Sigal, A.; Fygenson, D. K.; Shraiman, B. I. *Proc. Natl. Acad. Sci. U. S. A.* **2012,** *109,* 739–744. doi:10.1073/pnas.1007809109
37. Stöhr, M.; Bommert, K.; Schulze, I.; Jantzen, H. *J. Cell Sci.* **1987,** *88,* 579–590.
38. Pumidonming, W.; Koehsler, M.; Walochnik, J. *Parasitol. Res.* **2010,** *106,* 553–559. doi:10.1007/s00436-009-1694-4
39. Reverey, J. F.; Fromme, R.; Leippe, M.; Selhuber-Unkel, C. *Contact Lens Anterior Eye* **2014,** *37,* 262–266. doi:10.1016/j.clae.2013.11.010
40. Lee, J. N.; Park, C.; Whitesides, G. M. *Anal. Chem.* **2003,** *75,* 6544–6554. doi:10.1021/ac0346712
41. Rehfeldt, F.; Engler, A. J.; Eckhardt, A.; Ahmed, F.; Discher, D. E. *Adv. Drug Delivery Rev.* **2007,** *59,* 1329–1339. doi:10.1016/j.addr.2007.08.007

License and Terms

BEILSTEIN JOURNAL OF NANOTECHNOLOGY

Hydrophobic interaction governs unspecific adhesion of staphylococci: a single cell force spectroscopy study

Nicolas Thewes[1], Peter Loskill[1,2], Philipp Jung[3], Henrik Peisker[3], Markus Bischoff[3], Mathias Herrmann[3] and Karin Jacobs[*1]

Full Research Paper

Open Access

Address:
[1]Experimental Physics, Campus E2 9, Saarland University, D-66123 Saarbrücken, Germany, [2]Present address: Dept. of Bioengineering and California Institute for Quantitative Biosciences (QB3), University of California at Berkeley, Berkeley, California 94720, USA and [3]Institute of Medical Microbiology and Hygiene, Saarland University, D-66421 Homburg/Saar, Germany

Email:
Karin Jacobs[*] - k.jacobs@physik.uni-saarland.de

* Corresponding author

Keywords:
atomic force microscopy (AFM); force spectroscopy; hydrophobic interaction; single cell; *Staphylococcus carnosus*

Beilstein J. Nanotechnol. **2014,** *5,* 1501–1512.
doi:10.3762/bjnano.5.163

Received: 21 March 2014
Accepted: 12 August 2014
Published: 10 September 2014

This article is part of the Thematic Series "Biological and bioinspired adhesion and friction".

Guest Editor: S. N. Gorb

Abstract

Unspecific adhesion of bacteria is usually the first step in the formation of biofilms on abiotic surfaces, yet it is unclear up to now which forces are governing this process. Alongside long-ranged van der Waals and electrostatic forces, short-ranged hydrophobic interaction plays an important role. To characterize the forces involved during approach and retraction of an individual bacterium to and from a surface, single cell force spectroscopy is applied: A single cell of the apathogenic species *Staphylococcus carnosus* isolate TM300 is used as bacterial probe. With the exact same bacterium, hydrophobic and hydrophilic surfaces can be probed and compared. We find that as far as 50 nm from the surface, attractive forces can already be recorded, an indication of the involvement of long-ranged forces. Yet, comparing the surfaces of different surface energy, our results corroborate the model that large, bacterial cell wall proteins are responsible for adhesion, and that their interplay with the short-ranged hydrophobic interaction of the involved surfaces is mainly responsible for adhesion. The ostensibly long range of the attraction is a result of the large size of the cell wall proteins, searching for contact via hydrophobic interaction. The model also explains the strong (weak) adhesion of *S. carnosus* to hydrophobic (hydrophilic) surfaces.

Introduction

Members of the genus *Staphylococcus* are known to form extremely resistant biofilms, some of which can cause severe infectious diseases [1]. *Staphylococcus carnosus* is an apathogenic member of that genus and has been described first in the early 1980s [2]. The name *Staphylococcus carnosus* reflects its important role in meat production as it reduces nitrate to nitrite and prevents food rancidity by producing the anti-oxidant enzymes catalase and superoxide dismutase [3].

Only recently, the genome of *S. carnosus* strain TM300 has been decoded [4,5]. In contrast to pathogenic staphylococcal species, such as *S. aureus* and *S. epidermidis*, the genome of *S. carnosus* lacks significant amounts of mobile genetic elements, and is poor in repetitive DNA sequences that are thought to facilitate the plasticity of genomes by allowing for enhanced genomic diversification due to recombinational events [5]. Although the *S. carnosus* genome encodes some homologues of adhesion factors found in *S. aureus*, it lacks the majority of adhesive molecules of its pathogenic relative that are thought to be important for the ability of the pathogen to colonize and invade its mammal hosts (reviewed in [1]). Due to its apathogenic properties, and its ability to be transformed with and to express virulence factors of pathogenic staphylococcal species ([6,7]), the strain TM300 is an ideal tool to study the properties of a single virulence factor and its impact on infectivity in this otherwise apathogenic species. Besides this, it has been shown that the survival of bacteria in a food industry environment is strongly related to their efficiency to adhere on abiotic surfaces [8-10]. Therefore, and because adhesion is the first step of the formation of biofilms, the characterization of bacterial adhesion forces has gained increasing importance in recent years [11].

In general, the adhesion of bacteria to a surface is determined by the nature of the bacterium, the surrounding medium, the surface chemistry, and the material composition reflecting the influence of the main interacting forces [12,13]: van der Waals forces, hydrophobic interaction and electrostatic forces. In addition, specific interactions amplify bacterial adhesion whenever corresponding binding partners are available. The adhesion process of microorganisms, such as *S. carnosus*, is usually characterized by using flow chambers [14]. Although flow chamber studies reproduce the natural adsorption process of microorganisms out of fluid flow, it is hard to determine quantitative adhesion force values. The outcome usually results from multiple parallel processes, such as adsorption, desorption, and adhesion. Moreover, results obtained from flow chamber experiments depend on the exact flow conditions of the used chamber [15]. In the last decade, a more quantitative method for measuring bacterial adhesion forces has been introduced: single-cell force spectroscopy is a special mode of an atomic force microscope (AFM) [16] and is optimized to investigate adhesion forces [17,18] of single bacterial cells in a very controlled manner: By using AFM-cantilevers functionalized with single bacteria, "bacterial probes", force/distance measurements are conducted. To date, single cell force spectroscopy is mostly used for exploring specific adhesion [19]. It is the aim of this study to characterize the unspecific adhesion mechanisms of *Staphylococci*, by using *S. carnosus* as an example, and to clarify the range of the attractive interaction of the cells to surfaces. We use abiotic surfaces in order to rule out effects due to specific interactions and to concentrate on the unspecific interactions of *S. carnosus* to surfaces of variable surface energy. As a unique feature of our study, we are able to probe different surfaces with the exact same bacterial cell. Thereby, we are able to demonstrate the importance of the hydrophobic interaction on the bacterial adhesion process. Moreover, we can measure the adhesion forces that are mediated by bacterial cell wall proteins (and further cell wall components) and test their dependency on the 'adhesion history' the cell has experienced before.

Experimental

Preparation of the substrates

The hydrophilic substrates used in this study are silicon wafers with a native silicon oxide layer (d = 1.7(2) nm) (the number in parentheses denotes the error of the last digit) purchased from Siltronic AG (Burghausen, Germany). In order to remove dirt, the silicon wafers were first immersed for 30 min in fresh 1:1 H_2SO_4 (conc.)/H_2O_2 (30%) solution, then in boiling deionized water for 90 min, during which the water was changed at least four times. Following a standard protocol, these hydrophilic surfaces can be rendered hydrophobic by the self-assembly of a monolayer of silane molecules (octadecyltrichlorosilane, OTS, Sigma-Aldrich), featuring a CH_3-tailgroup [20,21]. As has been shown in [21] by perfoming AFM, X-ray reflectometry, ellipsometry, and contact angle measurements, this protocol enables the preparation of a self-assembled monolayer (SAM) with a thickness of about 2.6 nm and an *rms* roughness below 0.2 nm. In [21] it was shown that the SAM is hydrophobic, homogeneous, dense, upright and in all-trans configuration. The contact angles, surface roughnesses and surface energies for hydrophilic and hydrophobic wafers are given in Table 1 and streaming potential measurements reveal that both surfaces are negatively

Table 1: Parameters of the model substrates: Root mean square (*rms*) roughness, advancing (adv) and receding (rec) contact angles Θ of water, surface energy γ (values taken from [21]) and surface charge as revealed by streaming potential measurements at pH 7.3 [22].

surface	*rms* (nm)	Θ_{adv}	Θ_{rec}	γ (mJ/m^2)	streaming potential (mV)
hydrophilic	0.09(2)	7(2)°	compl. wetting	64(1)	−104.4(1)
hydrophobic	0.12(2)	111(1)°	107(2)°	24(1)	−80.0(1)

charged at the used pH of 7.3 (Table 1). For this study, OTS surfaces of the same batch as in [21] have been used. Prior to the AFM force spectroscopy experiments with bacterial cells, both types of surfaces were immersed in PBS buffer.

Bacteria

For the experiments, freshly prepared exponential phase *S. carnosus* strain TM300 cells were used [4]. The bacteria were cultured on blood agar plates and transferred into 5 mL of TSB medium for 24 h at 37 °C. Before the experiments, 100 µL were transferred into 4 mL fresh TSB medium and cultured for 2.5 h at 37 °C and 150 rpm. To remove extracellular material, the bacteria were washed four times with phosphate-buffered saline (PBS, pH 7.3, ionic strength 0.1728 mol/L at 20 °C), each with 1 mL. Then, the bacteria were either used immediately or stored less than two hours at 4 °C. For the preparation of the bacterial AFM probes, bacterial solution was again diluted 1:6.

Preparation of the bacterial probes

Bacterial probes are based on tipless cantilevers (MLCT-O, Bruker, Billerica, MA, USA) with a nominal spring constant of 0.03 N/m. After the cantilevers were cleaned in an air plasma, they were vertically immersed into a solution of 4 mg/mL dopamine hydrochloride (99%, Sigma-Aldrich) in 10 mM TRIS-buffer (pH 7.9 at 22 °C) and kept at 4 °C in the fridge for 50 min. The cantilevers were then carefully rinsed in deionized water to remove unbound dopamine and dried under a laminar flow bench for at least one hour. The poly(dopamine)-covered cantilever was then inserted into the Bioscope Catalyst cantilever holder for measurements in liquids (Bruker, Billerica, MA, USA), mounted onto the AFM. Subsequently, it was calibrated in liquid by using the thermal tune technique [23], which allows for the calculation of the individual spring constant of the cantilever.

Afterwards, holder and cantilever were placed into a micromanipulation system (Narishige Group, Japan). The cantilever thereby is in the horizontal position with the functionalized side facing down. By using the micromanipulator, holder and cantilever were lowered and the cantilever dipped into a droplet of diluted bacterial solution (see above), which was previously placed on a polystyrene petri dish. Under the inspection of an inverted optical microscope, the cantilever was placed on top of an isolated bacterium, briefly and carefully tapped onto the cell, and immediately pulled back again. In order to keep the applied force low, the deflection of the cantilever was monitored by the light reflection off the cantilever and kept constant during motion. Care was taken to position the bacterium as close as possible to the end of the cantilever (not further away than two bacterial diameters) to safely exclude cantilever/substrate interactions.

The successful fixation of a single bacterium at the front end of the cantilever was confirmed with the inverted microscope, c.f. Figure 1. Subsequently, cantilever (and holder) were withdrawn from the bacterial solution, whereby a droplet clings to the cantilever, preventing the bacterium from drying. Cantilever and holder were then carefully transferred to the AFM and immediately immersed into the PBS filled petri dish containing the hydrophilic and hydrophobic substrates.

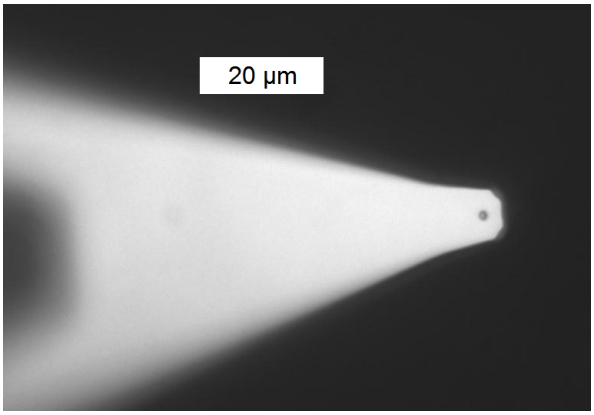

Figure 1: Optical image of a single *S. carnosus* bacterium immobilized by (poly)dopamine on a tipless cantilever.

Single cell force spectroscopy measurements

Single cell force spectroscopy measurements were performed by using a Bioscope Catalyst (Bruker, Billerica, MA, USA). The deflection of the cantilever is recorded during the approach and retraction of the bacterial probe to and from the surface. The deflection data was converted into force values by means of the spring constant of the cantilever, determined as described above. The approach is performed until a certain repulsive force is reached ("force trigger"), typically 150 pN in this study, if not indicated otherwise. Experiments were performed in 6 mL PBS at 20 °C and with tip velocities between 400 nm/s and 2400 nm/s over a total distance of typically 800 nm. (It is important to note here that the tip velocity describes the velocity of the piezo drive that controls the *z*-movement of the cantilever, which, however, is not necessarily identical with the velocity of the bacterium, especially at retraction.)

For each parameter set, at least 30 force/distance curves were recorded, each on a different surface spot to avoid systematic errors due to local irregularities of the surface or contamination due to preceding adhesion events. If two surfaces were to be compared, the first set of 30 force/distance curves was taken on one surface followed by a series of 30 curves on the second surface, then again 30 on the first surface. By doing this, we took control of the reproducibility of the measurements and can

rule out systematic errors like the degradation of the bacterial probe.

A typical force curve is shown in Figure 2. Upon approach, a jump-to-contact ("snap-in") event can be observed, followed by a steep rise of the force, indicating bacterium/surface contact. Since the exact contact formation and mechanics between the bacterial surface and the solid substrate is unclear, it is hard to make predictions on the shape of the force/distance curve. Upon retraction, the force/distance curve exhibits first the same steep slope as upon approach, yet, due to adhesive forces, a deep global minimum is recorded. Further retraction provokes a loss of contact ("jump-off contact"). In the repulsive regime (F > 0), a force of 150 pN is not enough to deform the bacterium: With a force trigger of 150 nN, only an indentation of ca. 10 nm is reached (cf. Figure 2). Therefore, very likely, only components of the cell wall are elastically deformed.

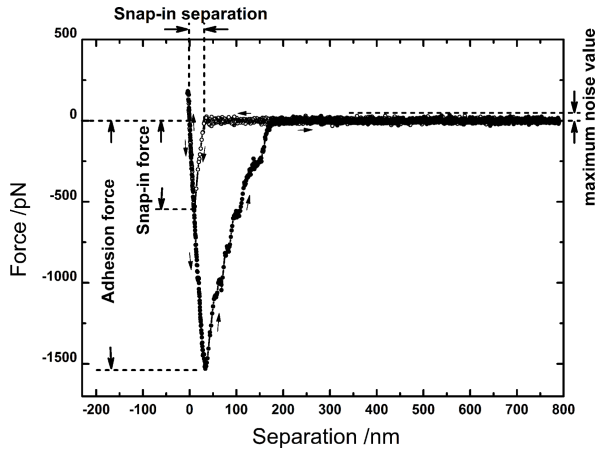

Figure 2: Typical force/distance curve, taken with a single *S. carnosus* probe on an OTS-covered (hydrophobic) Si wafer. By analyzing the curve, the adhesion force, the "snap-in force" and the "snap-in separation" can be obtained, the description of the latter is given in the text. The arrows indicate the direction of motion of the piezo drive.

Three general measures allow for a comparison of the adhesion process: Inspecting the approach curve, the "snap-in" event is characterized by the depth of the global minimum, called "snap-in force" and by the "snap-in separation", defined as the separation at which the deflection reaches 150% of the maximum baseline noise value (typically between 30 and 50 pN), c.f. Figure 2. The snap-in separation serves as a hands-on measure for the determination of the width of the snap-in event. Distances are measured relative to the point of zero force [24]. From the retraction curve, the adhesion force is taken as the depth of the global minimum [24]. Since in some cases, the overall adhesion force decreased after more than about 150 force/distance curves (possibly due to stress applied by the large number of adhesion events), the number of force/distance curves per bacterium was always kept below 150. The bacterium was never "lost" during the experiments, it was safely secured to the cantilever.

As a control for the specificity of force/distance curves for bacterial adhesion and to demonstrate that the cantilever does not influence bacterial adhesion, several experiments have been performed with a bare, (poly)dopamin-coated cantilever: Figure 3 displays the difference between the cantilever adhesion signal of the bare (poly)dopamin-coated cantilever (Figure 3A), and the very same cantilever with the bacterial cell attached (Figure 3B). Reversely, after a force/distance curve with an attached bacterium (Figure 3C), the bacterium was removed (by pressing it very hard to a solid substrate followed by shearing it off with a micromanipulator) and another force/distance curve of only the cantilever was recorded (Figure 3D). Clearly, the force/distance curves without bacterium exhibit (nearly) no snap-in event, and during retraction, only a small adhesion peak occurs and the further retraction curve is smooth without the characteristic jumps in the case of an attached bacterium.

Results and Discussion

First, we will concentrate on the robustness of single cell force microscopy. Each individual *S. carnosus* probe achieves a characteristic force/distance curve that can be reproduced numerous times (Figure 4). Differences from curve to curve occur occasionally (about 4 out of 30), yet span mostly only over one section of the retraction curve, otherwise reproducing the rest of the curve. This holds true even if a set of 60 force/distance curves on a hydrophobic wafer is interrupted by the recording of a set of 30 curves on a hydrophilic wafer: The first 30 curves on the hydrophobic wafer are shown in (Figure 4A), the second set of 30 curves is displayed in (Figure 4B), the curves on the hydrophilic wafer are not shown, since they do not differ from those shown in (Figure 7B). The characteristic features of the first set of curves on the hydrophobic wafer is perfectly reproduced by the second set, though in between, the surface energy of the adhesion partner (the hydrophilic surface) was reduced by a factor of three (c.f. Table 1). Hence, as the shape of the force/distance curves is that robust (surviving 150 contact events and surviving even a change of the type of substrate), these results already demonstrate that force/distance measurements are characteristic for the individual bacterial probe and are therefore most suitable to characterize bacterial adhesion.

Next, we explore the influence of the AFM force spectroscopy parameters on the force/distance curves. The tip (or rather the piezo drive) velocity was varied between 400 nm/s and 2400 nm/s, yet no significant influence on the adhesion force

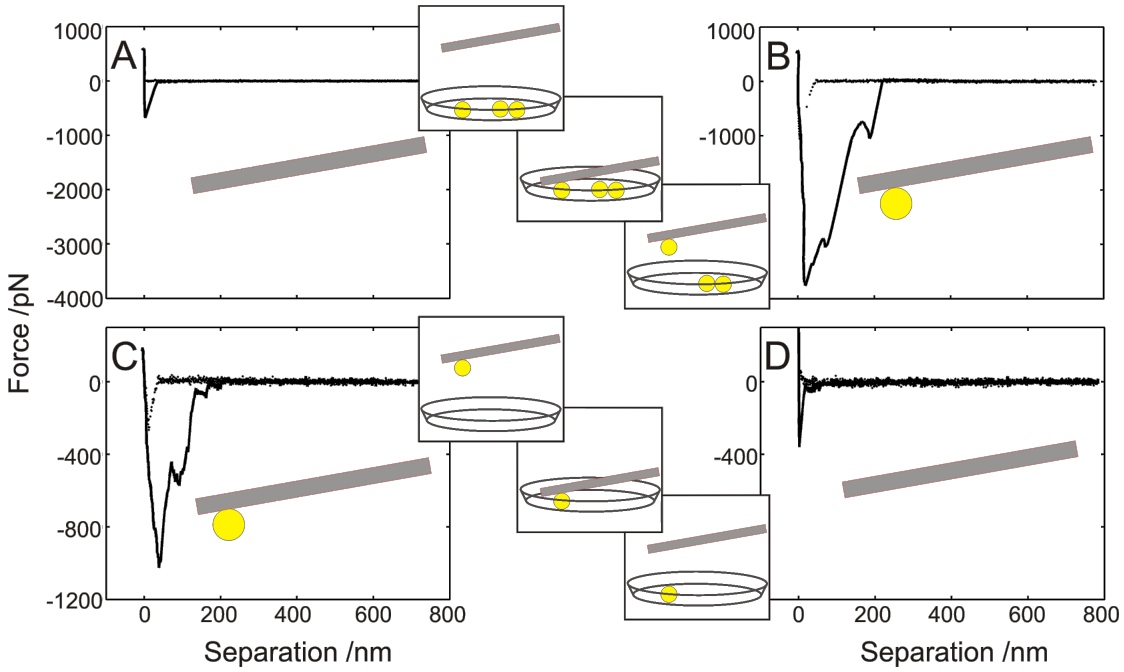

Figure 3: Test of artifacts of AFM force/distance curve with and without bacterium, each taken under the same conditions: (A) Bare (poly)dopamin-coated cantilever force/distance curve. (B) The same cantilever as in (A), yet after attachment of a bacterium. (C) A second cantilever with bacterium and its characteristic force/distance curve. (D) Force/distance curve after detaching the bacterium of the experiment shown in (C).

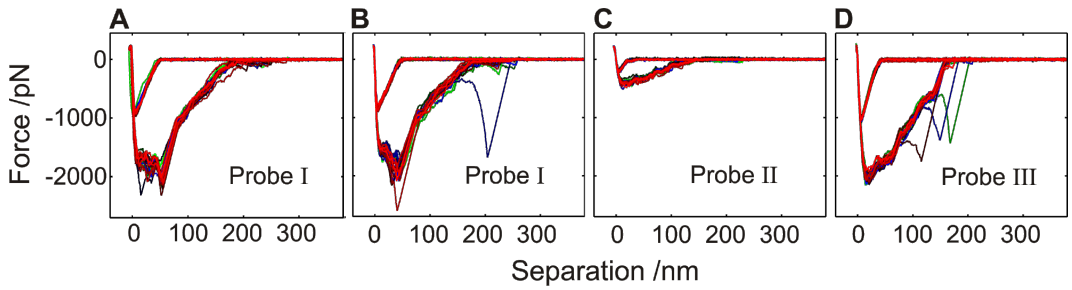

Figure 4: A–D: Overlay of 30 force/distance curves of three individual *S. carnosus* probes I, II and III on hydrophobic Si wafers, each with a force trigger of 150 pN. Between the experimental series shown in A and B, a set of 30 force/distance curves was taken with the identical bacterial probe on a hydrophilic Si wafer (not shown), yet the characteristic form of the second set of force/distance curves did not change significantly.

was recorded (Figure 5A). By varying the tip velocity, we implicitly varied the time the bacterium is enabled to gain contact to the surface. Within the range probed, the contact time (estimated to be of the order of a fraction of a second) does not influence the adhesion force. The snap-in separation, however, decreases with increasing tip velocity (Figure 5B), as does the snap-in force (Figure 5C), which is a first indication to a time-dependent contact-process, which will be detailed in the following. For further measurements, a tip velocity of 800 nm/s is used, since for that speed, one force/distance curve of 800 nm ramp size takes 0.5 Hz, which is a convenient frequency and corresponds to frequencies used in other studies [25].

Increasing the force trigger results in a slight increase of the adhesion force (Figure 6A), whereas the snap-in separation as well as the snap-in force remained constant (Figure 6B and Figure 6C). In the following, the lowest force trigger of 150 pN was used in order to mimic the natural adhesion process of the bacterium in planktonic state.

With the parameters for single cell force spectroscopy as detailed above, we can now specify the large differences in the adhesion of *S. carnosus* to hydrophobic and to hydrophilic surfaces, c.f. Figure 7A and Figure 7B: On the hydrophobic surface, a clear snap-in event is detectable, followed by a large

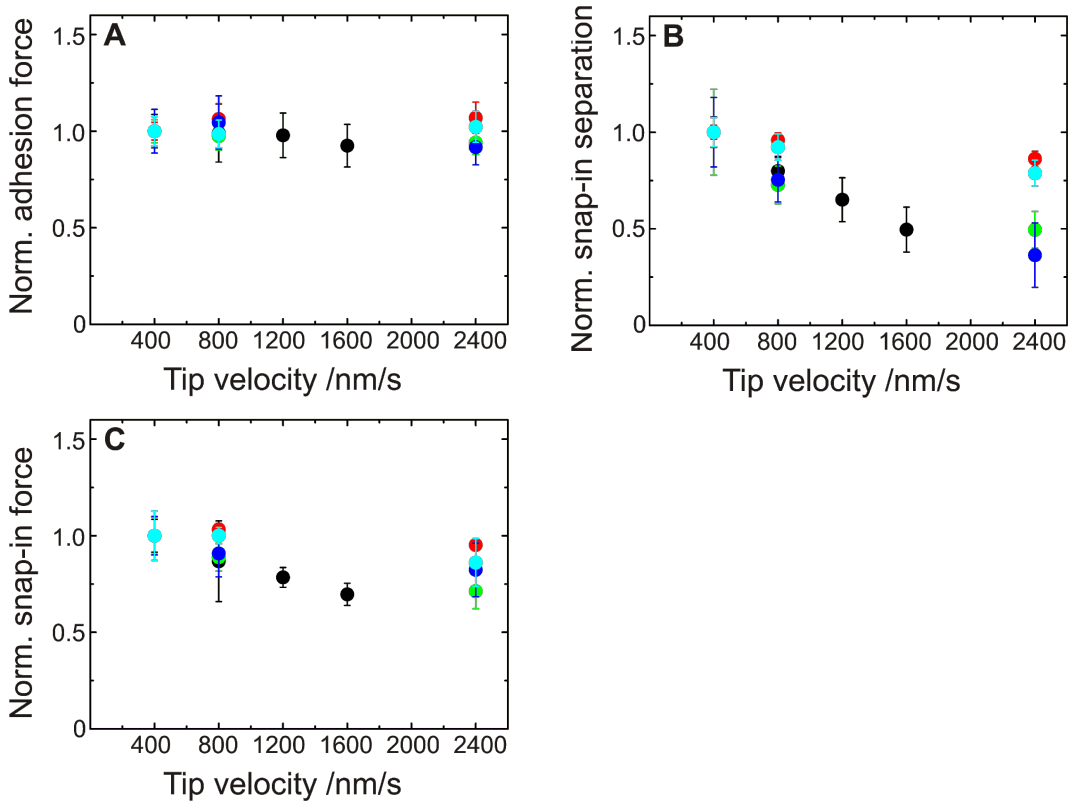

Figure 5: Influence of the tip velocity on the adhesion of *S. carnosus* shown for five different cells. For each bacterium, values for adhesion force (A), snap-in separation (B) and snap-in force (C) are shown. The values are normalized to the value of the measurement with the lowest tip velocity (400 nm/s). Different colors represent different bacterial probes.

adhesive peak upon retraction. On the hydrophilic surface, however, neither of the two can be recorded. It is important to note that the two curves depicted in Figure 7A and Figure 7B were taken under identical external conditions (temperature, buffer), the same AFM force spectroscopy parameters (force trigger, tip velocity) and, most significantly, were recorded with the same bacterium. Figure 7C demonstrates the individual adhesive properties of different bacteria. Gray bars comprise data of the exact same bacterial probe on the two different surfaces. The data of Figure 7A and Figure 7B are taken from the set of curves summarized in bar I.

Obviously, the adhesive mechanism of *S. carnosus* on hydrophobic OTS surface differs strongly from that on a hydrophilic Si wafer, as the adhesion of *S. carnosus* to hydrophilic Si wafers is barely resolvable. From force spectroscopy measurements with multiple bacteria as AFM probes (30–50 bacteria), we learned that on hydrophilic silicon oxide surfaces, the adhesion force is roughly an order of magnitude lower than on OTS-Si wafers [13]. Hence, the adhesion force of a single bacterium on a hydrophilic surface is expected to be below the experimental resolution (about 50 pN), which explains the present results.

What is the difference of bacterial adhesion to hydrophilic or hydrophobic surfaces? Adhesion is the sum of all forces between the interacting partners. In our case, van der Waals and electrostatic forces as well as forces due to the hydrophobic interaction are involved [26]. Since hydrophilic and hydrophobic Si wafers differ in composition only by a 2.6 nm thin OTS-monolayer on the surface, the van der Waals forces are nearly identical [13,27]. Forces due to electrostatic interactions between the negatively charged bacterium and the two types of wafer surfaces, which are both negatively charged (Table 1), are repulsive. Since the streaming potential is 20% more negative on the hydrophilic Si wafer, different electrostatic interactions give rise to a difference of adhesion forces of only a factor of 1.2, yet we record differences in the range of factors 10 to 40 (Figure 7C). Therefore, we hypothesize that the adhesion of *S. carnosus* is governed by hydrophobic interaction.

Inspecting the snap-off event in more detail, not only the large extent is striking but also the reproducible, stepwise reduction of the recorded force (see Figure 4). This is a strong indication of a reversible fold-and-stretch mechanism of the involved macromolecules. It is known that the bacterial surface is covered by a variety of proteinaceous and non-proteinaceous

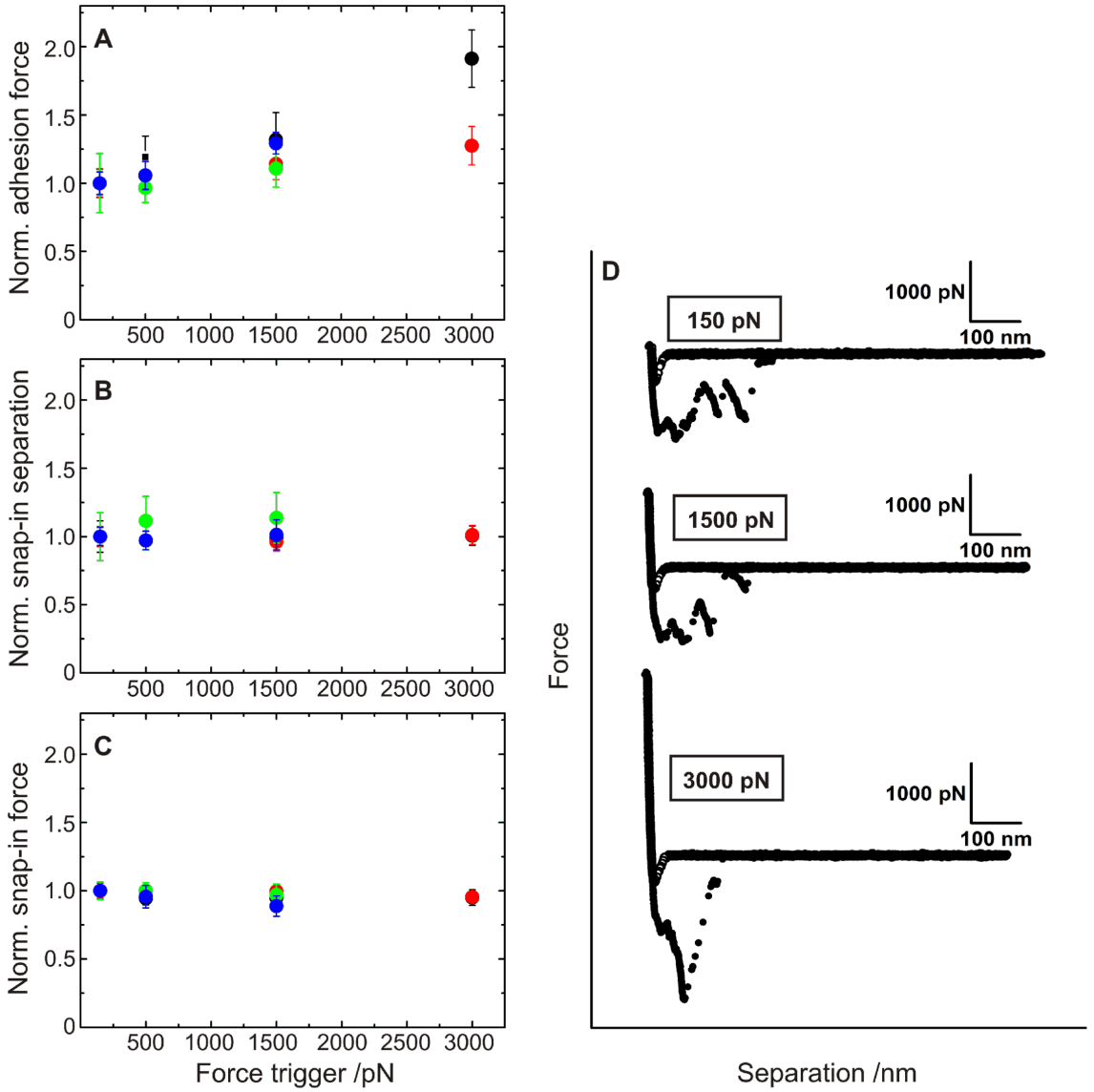

Figure 6: Influence of the force trigger on the adhesion of *S. carnosus*. A–C: For four bacterial probes, values for adhesion force, snap-in force, and snap-in separation are normalized to the value of the measurement with the lowest force trigger (150 pN). D: Exemplary force/distance curves for the exact same bacterial probe for three different force triggers. Different colors represent different bacterial probes.

polymers that can mediate adhesion (adhesins) [28,29]. The form of the retraction part can therefore be explained by a parallel and simultaneous stretching of cell wall proteins tethered to the surface as the piezo retracts [25,30].

Proteins are known to adsorb differently to hydrophilic and hydrophobic surfaces since the hydrophobic interaction can induce intramolecular conformational transitions and change the orientation of hydrophobic side groups of proteins [31-35]. This has also been shown by surface forces apparatus (SFA) experiments [36-38]. The range of the hydrophobic interaction depends on the correlation length of water molecules, which is below 1 nm [39]. Therefore, bacterial surface proteins have to come that close to the OTS surface in order to interact attractively. The SFA studies showed that the more hydrophobic the interacting partners (protein/surface) are, the stronger is the adhesion force.

An influence of further nonproteinaceous cell wall components (like teichoic acids) cannot be excluded and it will depend on the hydrophobicity of these components. However, proteins will play the key role in adhesion to hydrophobic surfaces due to their strong hydrophobic parts. Therefore, we will only talk about cell wall proteins in the following, but are aware of the fact that also other hydrophobic macromolecules may contribute to adhesion. For *S. aureus* for example, teichoic acids

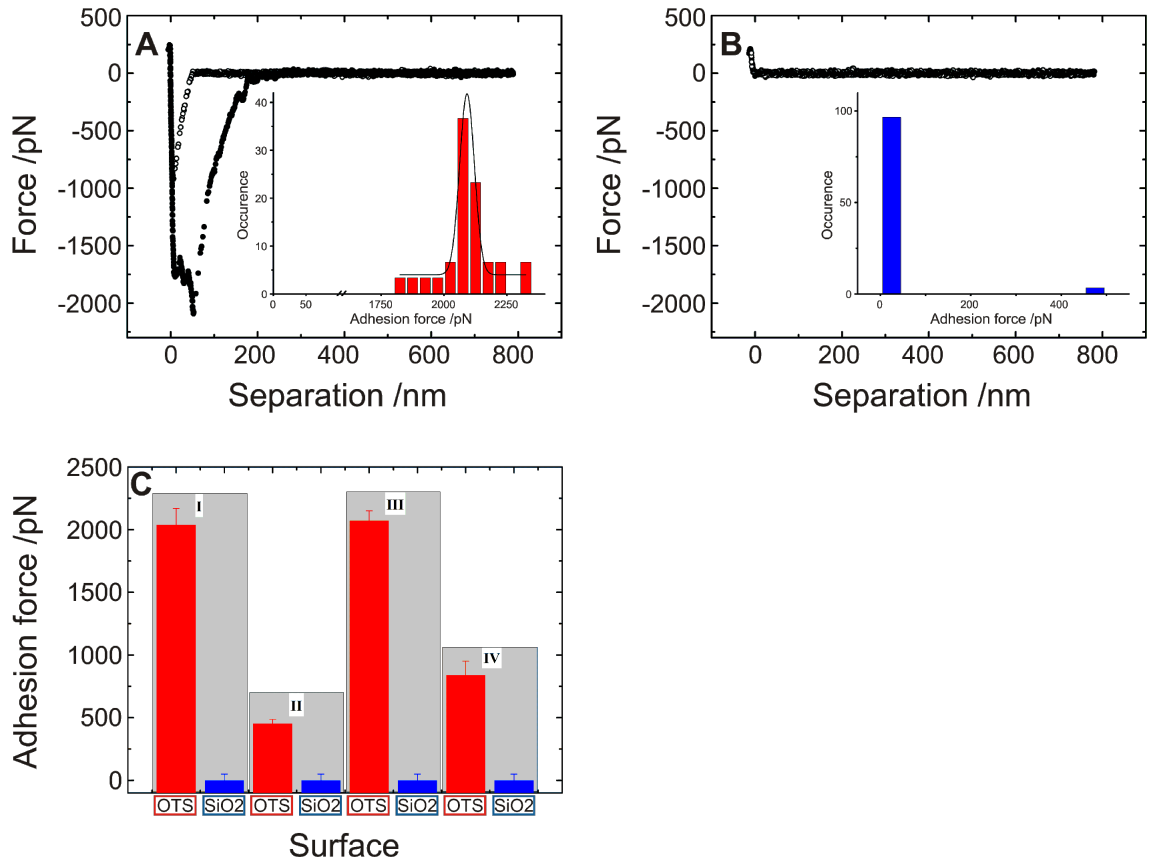

Figure 7: Exemplary force/distance curve taken with a single *S. carnosus* probe on (A) a hydrophobic OTS-covered Si wafer and on (B) a hydrophilic Si wafer. The insets summarize the results of the adhesion force of 30 force/distance curves. (C): Mean adhesion force and standard deviation showing the result of at least 60 force/distance curves of four *S. carnosus* (I–IV) measured on hydrophobic OTS-covered and on hydrophilic Si wafers, covered by a natural SiO_2. Each of the four bars represents measurements of the exact same bacterial probe.

are reported to be strongly hydrophilic [40]. Our model of bacterial adhesion, which will be proposed in the following, however, is not depending on the exact type of adhesive mediator.

Figure 8A summarizes the results of the measured adhesion forces for 30 different bacterial probes. It contains the OTS-wafer data shown in Figure 7C. For an individual *S. carnosus* bacterial probe on an OTS-wafer, the distribution of adhesion forces is rather narrow, the width of the distribution is typically less than 10% of the average adhesion force, as depicted in the inset of Figure 7A. Comparing different *S. carnosus* probes as shown in Figure 8A, the adhesion forces vary between 400 pN and 3000 pN, with the average at 1500(800) pN (solid line).

Inspecting the approach curve, it is noticeable that also the "snap-in" is an extended event rather than a sudden jump-to-contact (a jump-in or -out can be recorded whenever the gradient of the force exceeds the gradient of the restoring force of the cantilever (i.e., the spring constant) [24]). A closer look at the snap-in events reveals that the snap-in force is proportional to the snap-in separation (Figure 8B) and that the form of the curves greatly resemble each other. Moreover, since the adhesion force is also proportional to both, the snap-in force and -separation, see Figure 8C and Figure 8D, we deduce that the involved mechanisms are identical. Hence also upon approach, cell-wall polymers are involved in establishing the contact to the hydrophobic Si wafer. The snap-in separation reaches values up to 50 nm on hydrophobic surfaces, and can hence serve as an estimate for the hydrodynamic radius of the bacterial cell-wall proteins.

Based on the recently published genome sequence of *S. carnosus* strain TM300 (deposited in the EMBL nucleotide database under accession number AM295250), 19 putative cell-wall anchored proteins harboring LPXTG motifs are predicted, including homologues of well-studied *S. aureus* adhesins such as clumping factor A and B, fibronectin binding protein, and

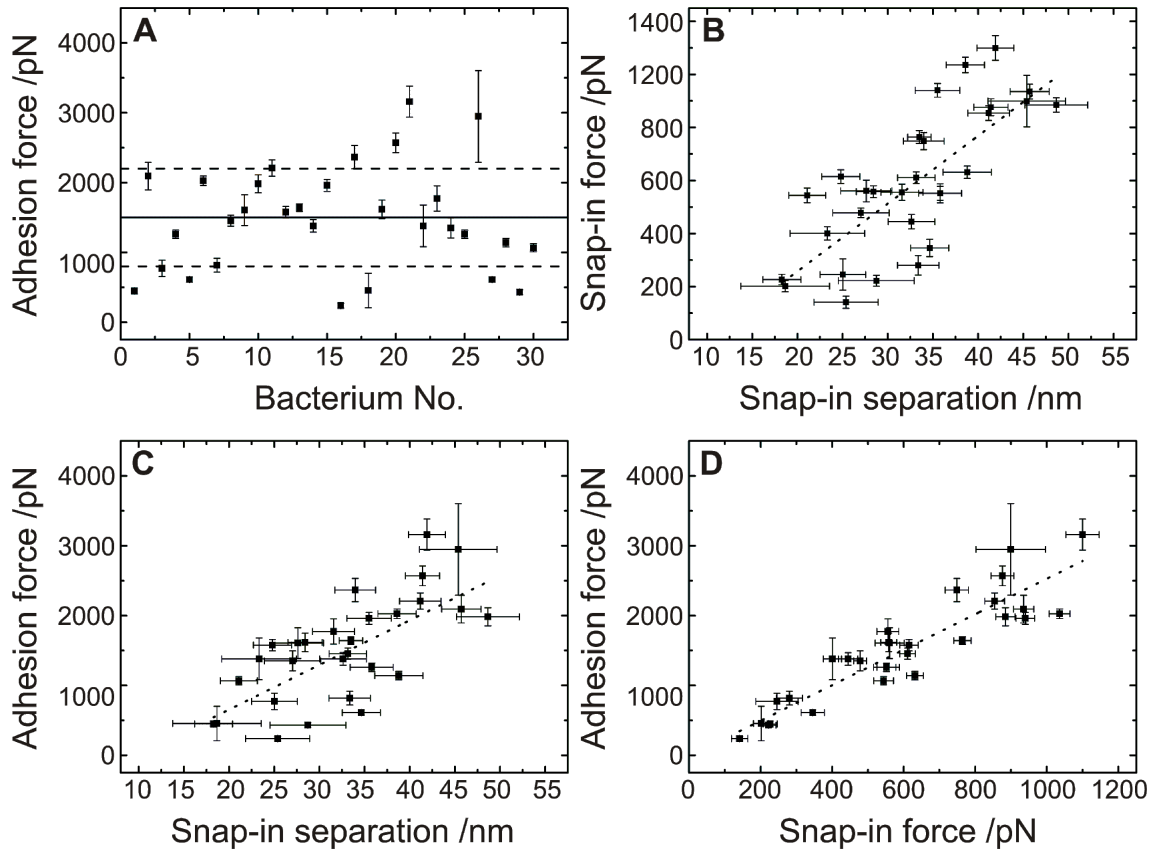

Figure 8: Results of 30 different single cell force spectroscopy experiments on OTS with *S. carnosus* bacterial probes, each data point consists of 30 force/distance curves with a force trigger of 150 pN and a tip velocity of 800 nm/s. A: Solid line: average adhesion force, dashed lines: range of the standard deviation. B–D: Dotted lines: linear fit to the data.

elastin binding protein (cf. [5]). However, nothing is known about the structures and the lengths (e.g., hydrodynamic radius under in vivo conditions) of these putitative cell-wall proteins, making it difficult to correlate the measured adhesion phenomena to specific proteins.

We can now revisit the presented results on the influence of the tip velocity (Figure 5) and the force trigger (Figure 6) to the adhesion process: The long cell-wall polymers need time to come into contact with the surface. The search for contact is a stochastic process; a higher tip velocity thereby results theoretically in a smaller snap-in separation because the residence time in each separation, and therefore the probability that a protein comes into contact in a certain distance, is smaller. Moreover, the polymer needs also time to perform conformational changes in the vicinity of the surface. Both time windows are reduced at higher tip speeds and, hence, the distance at which the cantilever starts to deflect, the snap-in separation, is reduced. The snap-in force is reduced, since the deflection of the cantilever is smaller at the lowest point of the approach curve.

Upon retraction, a variation of the tip velocity probes the rheological properties of the involved group of (stretched) macromolecules, which may also interact collaboratively [41]. Since for the group of cell-wall proteins, no rheological data is available, a prediction for the tip-velocity-dependent behavior is not possible. We find that the adhesion force is constant within the applied variation of tip velocities; moreover, snap-in and snap-off events are highly reproducible. Both together strongly indicate that at these speeds, the macromolecules act elastically. These findings are also in accordance with the study of Alsteens et al. [25], in which “protein nanosprings” are one model description of microbial adhesins.

According to our model of *S. carnosus* adhesion, a higher force trigger should provoke a larger contact area, a closer contact and involve additional cell- wall polymers to tether. All of which should result in a higher adhesion force and a different form of the retraction curve. The snap-in event, however, should not be affected. The experiments reveal that indeed snap-in separation and force are independent of force trigger, c.f. Figure 6B and Figure 6C and the adhesion force is

increasing as expected Figure 6A. Also, for each force trigger (as well as for each *S. carnosus* bacterial probe), a characteristic set of force/distance curve can be recorded (Figure 6D).

Merging all experimental results, we propose the model sketched in Figure 9: Upon approach, Figure 9A, the cell-wall proteins interact with the surrounding medium (1) and, if at reach, with the surface (2). If an attractive surface is in the vicinity, parts of the proteins can tether (unspecifically in our case) to the surface. Tethering can start at distances below 50 nm, c.f. Figure 8B and Figure 8C. The experiments show that this is the case for hydrophobic wafers. The distance of 50 nm can, hence, serve us as an upper estimate for the coil size of the protein in solution. A further approach gives more proteins the opportunity to tether (3) until a point is reached, at which the maximum attractive force is reached (4). From now on, the proteins start to act as elastic springs that are compressed by the force exerted by the cantilever through the piezo drive. Nevertheless, also in this phase, additional proteins may tether. Approach is stopped shortly after zero force has been reached (5).

Upon retraction, Figure 9B, first, the elastic springs are released (6), achieving the same slope in the curve as during approach. It indicates a reversible fold-and-stretch mechanism of multiple chains. Then, some of the springs start to be stretched against the steric repulsion of the coil (7) [36], followed by a loss of contact of single macromolecules, each of which gives rise to a sudden jump in the force/distance curve (8) and (9) until the entire bacterium has lost contact (10). Depending on type and number of the involved proteins, the retraction curve looks different for every bacterial probe, a fact that has been found earlier in non-bacterial systems involving macromolecules [30,36-38]. For the exact same bacterial probe and the identical contact area (realized by an identical force trigger) and even if 30 approach/retraction cycles have been performed on a different surface, the form of the force/distance curve is characteristic and can be taken as a "fingerprint" for the individual cell.

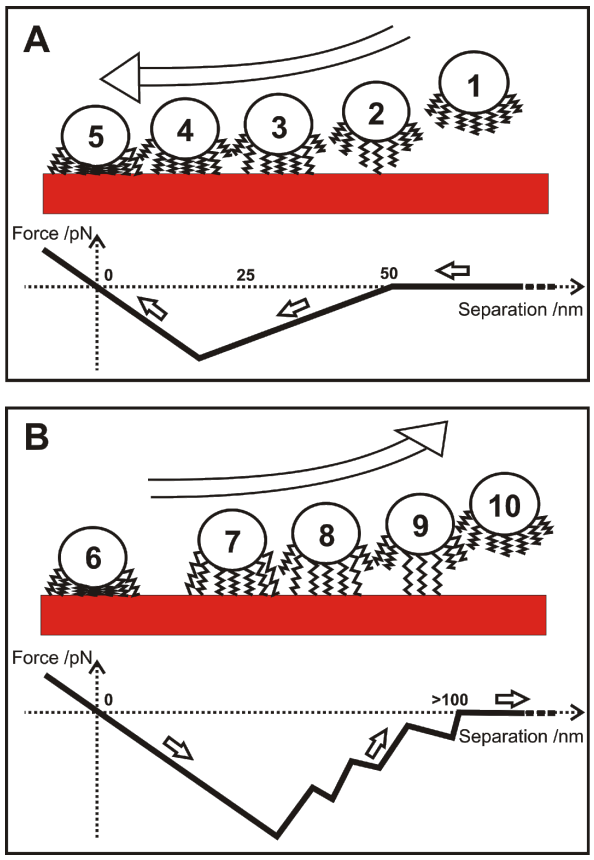

Figure 9: Sketch of approach (A) and retraction (B) of a single bacterial probe and respective force/distance curves. For clarity, neither the AFM cantilever nor the macromolecules that are not involved in adhesion are drawn.

Conclusion

To conclude, our experiments strongly corroborate the model that the unspecific adhesion of *S. carnosus* is mainly governed by number, properties and arrangement of the bacterial cell-wall proteins. Through this, the proteins are subject to van der Waals and electrostatic forces as well as forces due to hydrophobic interaction. Comparing hydrophilic and hydrophobic Si wafers (in our case differing only in a monomolecular OTS layer), we find for the exact same bacterial probe strong adhesion of *S. carnosus* to the hydrophobic wafers (up to about 3000 pN) and low adhesion (close to the experimental resolution, about 30–50 pN) to the hydrophilic ones. From that we infer that the hydrophobic interaction is responsible for the strong adhesion on the hydrophobic wafers, exceeding the forces exerted by electrostatic and van der Waals forces by at least an order of magnitude.

The main observations are (i) the form of the force/distance curves is characteristic for each bacterium, (ii) this form is independent of the "adhesive history" and (iii) the retraction curves (including the adhesion forces) are unaffected by the tip velocities probed. These observations lead us to the conclusion that cell-wall proteins act as elastic springs. Since the separation at which the cantilever starts to deflect, the snap-in separation, reaches values up to 50 nm on hydrophobic surfaces, we can estimate the extension of the cell-wall proteins.

Aiming at understanding the detailed form of the force/distance curves, it is inevitable to shed more light onto the "real" molecular composition of the bacterial surface, possibly with the help of atomistic simulations. For future studies, single-cell force

spectroscopy can additionally be combined with genetic tools that enable us to specifically modify the composition of the cell-wall proteins. That way, the responsible adhesins can be identified for each of the bacterial species.

Acknowledgements

This work was supported by the Deutsche Forschungsgemeinschaft (DFG) within the collaborative research center SFB 1027 and the research training group GRK 1276 (N.T.). P.J. and M.B. were supported by grants of the German Ministry for Education and Research 01Kl1014B and 01Kl1301B.

References

1. Rosenstein, R.; Götz, F. *Curr. Top. Microbiol. Immunol.* **2013,** *358,* 33–89. doi:10.1007/82_2012_286
2. Schleifer, K. H.; Fischer, U. *Int. J. Syst. Bacteriol.* **1982,** *32,* 153–156. doi:10.1099/00207713-32-2-153
3. Barrière, C.; Leroy-Sétrin, S.; Talon, R. *J. Appl. Microbiol.* **2001,** *91,* 514–519. doi:10.1046/j.1365-2672.2001.01411.x
4. Rosenstein, R.; Nerz, C.; Biswas, L.; Resch, A.; Raddatz, G.; Schuster, S. C.; Götz, F. *Appl. Environ. Microbiol.* **2009,** *75,* 811–822. doi:10.1128/AEM.01982-08
5. Rosenstein, R.; Götz, F. *Int. J. Med. Microbiol.* **2010,** *300,* 104–108. doi:10.1016/j.ijmm.2009.08.014
6. Fey, P. D.; Ulphani, J. S.; Götz, F.; Heilmann, C.; Mack, D.; Rupp, M. E. *J. Infect. Dis.* **1999,** *179,* 1561–1564. doi:10.1086/314762
7. Giese, B.; Dittmann, S.; Paprotka, K.; Levin, K.; Weltrowski, A.; Biehler, D.; Lâm, T.-T.; Sinha, B.; Fraunholz, M. J. *Infect. Immun.* **2009,** *77,* 3611–3625. doi:10.1128/IAI.01478-08
8. Gerke, C.; Kraft, A.; Süßmuth, R.; Schweitzer, O.; Götz, F. *J. Biol. Chem.* **1998,** *273,* 18586–18593. doi:10.1074/jbc.273.29.18586
9. Cramton, S. E.; Gerke, C.; Schnell, N. F.; Nichols, W. W.; Götz, F. *Infect. Immun.* **1999,** *67,* 5427–5433.
10. Møretrø, T.; Hermansen, L.; Holck, A. L.; Sidhu, M. S.; Rudi, K.; Langsrud, S. *Appl. Environ. Microbiol.* **2003,** *69,* 5648–5655. doi:10.1128/AEM.69.9.5648-5655.2003
11. Camesano, T. A.; Liu, Y.; Datta, M. *Adv. Water Resour.* **2007,** *30,* 1470–1491. doi:10.1016/j.advwatres.2006.05.023
12. Busscher, H. J.; Weerkamp, A. H. *FEMS Microbiol. Lett.* **1987,** *46,* 165–173. doi:10.1111/j.1574-6968.1987.tb02457.x
13. Loskill, P.; Hähl, H.; Thewes, N.; Kreis, C. T.; Bischoff, M.; Herrmann, M.; Jacobs, K. *Langmuir* **2012,** *28,* 7242–7248. doi:10.1021/la3004323
14. Planchon, S.; Gaillard-Martinie, B.; Leroy, S.; Bellon-Fontaine, M. N.; Fadda, S.; Talon, R. *Food Microbiol.* **2007,** *24,* 44–51. doi:10.1016/j.fm.2006.03.010
15. Harraghy, N.; Seiler, S.; Jacobs, K.; Hannig, M.; Menger, M. D.; Herrmann, M. *Int. J. Artif. Organs* **2006,** *29,* 368–378.
16. Binnig, G.; Quate, C. F.; Gerber, C. *Phys. Rev. Lett.* **1986,** *56,* 930–933. doi:10.1103/PhysRevLett.56.930
17. Helenius, J.; Heisenberg, C.-P.; Gaub, H. E.; Müller, D. J. *J. Cell Sci.* **2008,** *121,* 1785–1791. doi:10.1242/jcs.030999
18. Müller, D. J.; Dufrêne, Y. F. *Nat. Nanotechnol.* **2008,** *3,* 261–269. doi:10.1038/nnano.2008.100
19. Beaussart, A.; El-Kirat-Chatel, S.; Herman, P.; Alsteens, D.; Mahillon, J.; Hols, P.; Dufrêne, Y. F. *Biophys. J.* **2013,** *104,* 1886–1892. doi:10.1016/j.bpj.2013.03.046
20. Brzoska, J. B.; Azouz, I. B.; Rondelez, F. *Langmuir* **1994,** *10,* 4367–4373. doi:10.1021/la00023a072
21. Lessel, M.; Bäumchen, O.; Klos, M.; Hähl, H.; Fetzer, R.; Seemann, R.; Jacobs, K. *arXiv:1212.0998 [cond-mat.mtrl-sci]* **2012**.
22. Bellion, M.; Santen, L.; Mantz, H.; Hähl, H.; Quinn, A.; Nagel, A.; Gilow, C.; Weitenberg, C.; Schmitt, Y.; Jacobs, K. *J. Phys.: Condens. Matter* **2008,** *20,* 404226. doi:10.1088/0953-8984/20/40/404226
23. Hutter, J. L.; Bechhoefer, J. *Rev. Sci. Instrum.* **1993,** *64,* 1868–1873. doi:10.1063/1.1143970
24. Bushan, B., Ed. *Handbook of Nanotechnology;* Springer: Berlin Heidelberg New York, 2007.
25. Alsteens, D.; Beaussart, A.; El-Kirat-Chatel, S.; Sullan, R.-M. A.; Dufrêne, Y. F. *PLoS Pathog.* **2013,** *9,* e1003516. doi:10.1371/journal.ppat.1003516
26. Israelachvili, J. N. *Intermolecular and surface forces;* Elsevier Inc., 2011.
27. Loskill, P.; Puthoff, J.; Wilkinson, M.; Mecke, K.; Jacobs, K.; Autumn, K. *J. R. Soc., Interface* **2013,** *10,* 20120587. doi:10.1098/rsif.2012.0587
28. Linke, D.; Goldman, A., Eds. *Bacterial Adhesion;* Springer: Dordrecht Heidelberg London New York, 2011.
29. Koebnik, R.; Locher, K. P.; Van Gelder, P. *Mol. Microbiol.* **2000,** *37,* 239–253. doi:10.1046/j.1365-2958.2000.01983.x
30. Florin, E.-L.; Moy, V. T.; Gaub, H. E. *Science* **1994,** *264,* 415–417. doi:10.1126/science.8153628
31. Hähl, H.; Evers, F.; Grandthyll, S.; Paulus, M.; Sternemann, C.; Loskill, P.; Lessel, M.; Hüsecken, A. K.; Brenner, T.; Tolan, M.; Jacobs, K. *Langmuir* **2012,** *28,* 7747–7756. doi:10.1021/la300850g
32. Norde, W. *Colloids Surf., B* **2008,** *61,* 1–9. doi:10.1016/j.colsurfb.2007.09.029
33. Czeslik, C. *Z. Phys. Chem.* **2004,** *218,* 771–801. doi:10.1524/zpch.218.7.771.35722
34. Wahlgren, M.; Arnebrant, T. *Trends Biotechnol.* **1991,** *9,* 201–208. doi:10.1016/0167-7799(91)90064-O
35. Malmsten, M., Ed. *Biopolymers at interfaces;* Marcel Dekker: New York, 2003.
36. Wong, J. Y.; Kuhl, T. L.; Israelachvili, J. N.; Mullah, N.; Zalipsky, S. *Science* **1997,** *275,* 820–822. doi:10.1126/science.275.5301.820
37. Leckband, D.; Israelachvili, J. *Q. Rev. Biophys.* **2001,** *34,* 105–267. doi:10.1017/S0033583501003687
38. Helm, C. A.; Israelachvili, J. N.; McGuiggan, P. M. *Biochemistry* **1992,** *31,* 1794–1805. doi:10.1021/bi00121a030
39. van Oss, C. J. *Interfacial forces in aqueous media;* CRC Press, Taylor and Francis Group, 2006.
40. Xia, G.; Kohler, T.; Peschel, A. *Int. J. Med. Microbiol.* **2010,** *300,* 148–154. doi:10.1016/j.ijmm.2009.10.001
41. Bos, M. A.; van Vliet, T. *Adv. Colloid Interface Sci.* **2001,** *91,* 437–471. doi:10.1016/S0001-8686(00)00077-4

BEILSTEIN JOURNAL OF NANOTECHNOLOGY

Equilibrium states and stability of pre-tensioned adhesive tapes

Carmine Putignano[1,2], Luciano Afferrante[1], Luigi Mangialardi[1] and Giuseppe Carbone[*1]

Full Research Paper

Open Access

Address:
[1]Dipartimento di Meccanica, Matematica e Management (DMMM), Politecnico di Bari, V.le Japigia, 185, 70125, Bari, Italy, http://tribolab.poliba.it and [2]Department of Mechanical Engineering, Imperial College London, London SW7 2AY, United Kingdom

Email:
Giuseppe Carbone[*] - giuseppe.carbone@poliba.it

* Corresponding author

Keywords:
adhesion; double-peeling; energy release rate; peeling of pre-tensioned tape

Beilstein J. Nanotechnol. **2014,** *5,* 1725–1731.
doi:10.3762/bjnano.5.182

Received: 28 March 2014
Accepted: 17 September 2014
Published: 07 October 2014

This article is part of the Thematic Series "Biological and bioinspired adhesion and friction".

Guest Editor: S. N. Gorb

Abstract

In the present paper we propose a generalization of the model developed in Afferrante, L.; Carbone, G.; Demelio, G.; Pugno, N. *Tribol. Lett.* **2013,** *52,* 439–447 to take into account the effect of the pre-tension in the tape. A detailed analysis of the peeling process shows the existence of two possible detachment regimes: one being stable and the other being unstable, depending on the initial configuration of the tape. In the stability region, as the peeling process advances, the peeling angle reaches a limiting value, which only depends on the geometry, on the elastic modulus of the tape and on the surface energy of adhesion. Vice versa, in the unstable region, depending on the initial conditions of the system, the tape can evolve towards a state of complete detachment or fail before reaching a state of equilibrium with complete adhesion. We find that the presence of pre-tension in the tape does not modify the stability behavior of the system, but significantly affects the pull-off force which can be sustained by the tape before complete detachment. Moreover, above a critical value of the pre-tension, which depends on the surface energy of adhesion, the tape will tend to spontaneously detach from the substrate. In this case, an external force is necessary to avoid spontaneous detachment and make the tape adhering to the substrate.

Introduction

The understanding of adhesion of thin films is of prominent importance in a huge number of biological and biomechanical applications. As an example, the extraordinary adhesive abilities characterizing the hairy attachment systems of insects, reptiles and spiders have drawn significant research efforts aimed at reproducing such properties in artificial bio-mimetic adhesives [1-3]. In nature, many adhesive systems consist of arrays of hierarchical hairs or setae, enabling large contact areas and hence high adhesion owing to the van der Waals interaction forces [4]. This morphology enables many insects, spiders and some vertebrates to climb on almost any surface, from smooth ones to cinder block-like surfaces [5]. In this

respect, it has been shown in [6,7] that the highly flexible terminal spatula elements, which behave as compliant contacting surfaces, play a crucial role in the adhesion. Many efforts have been taken trying to reproduce these structures to enhance adhesion and realize bio-inspired systems that could be employed, for example, in industrial material processing or as innovative smart solutions in structural design [8].

For these reasons, the mechanism of adhesion and detachment of systems such as thin films have been investigated by many experimental [9-13] and theoretical [3,14-24] approaches. However, many issues are not yet clear and our knowledge on this topic is still far from being complete. For example, in spite of several theoretical investigations about rough contact mechanics [25-29], the role of roughness in this kind of systems is not yet well understood. Furthermore, viscoelasticity, which entails prominent effects in terms of friction and contact anisotropy [30,31], has not yet been included in analytical and numerical models. In nature, on the other side, geckos exhibit extremely high adhesive performance also on rough substrates. The secret of this amazing behavior is mainly related to the fibrillar hierarchical geometry of the adhesion pads that makes these structures very compliant, despite the fact that they are usually constituted mainly of a relatively stiff material, namely β-keratin. The study of the mechanism of detachment of thin films can also help to elucidate some aspect of insects and, in particular, gecko adhesion. To avoid toe detachment, the gecko often employs the use of opposing feet and toes leading to a V-shaped geometry [9,10,32-35], which can be modelled by multiple-peeling schemes, as shown in [15,17,36], in which, based on the ground-breaking analysis proposed by Kendall [37], the crucial role of the spatula-shaped terminal elements in the biological hairy adhesive systems is pointed out.

In this paper, we focus our attention on some yet unclear aspects of the peeling process and, in particular, on the stability of this mechanism in presence of a pre-tension.

The peeling process of a thin elastic tape

In this section, we extend the formulation given in [36], focusing our attention on the stability analysis of the peeling process and on the effect of pre-tension on the mechanism of detachment. The formulation of the problem is developed considering two different initial configurations of an elastic tape with cross section $A = bt$, as shown in Figure 1. In the first configuration (Figure 1a) a portion of the tape length h is not attached to the substrate and it is rotated before applying the external force P. In the latter (Figure 1b) the tape has to be stretched by a quantity h before loading. In both cases, the tape can be pre-tensioned before being attached to the substrate. Incidentally, this loading procedure, with the force acting along the vertical axis and the edge of the tape being constrained to move along the same direction, is interesting because the double-peeling mechanism, due to symmetry, can be reduced to a scheme of this type [36].

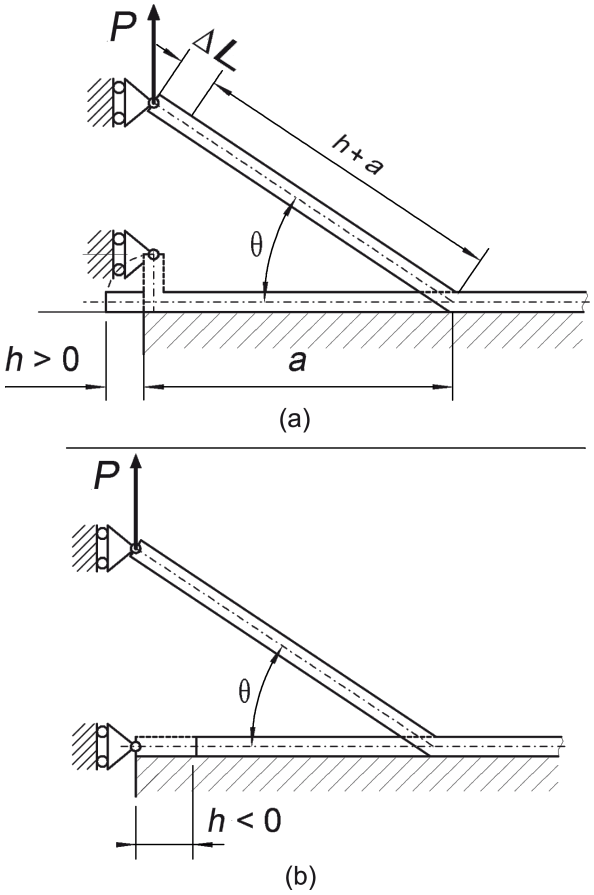

Figure 1: Double peeling of a tape. Initial configuration (a): a length h of the tape is not attached to the substrate and it is rotated before applying the external force P; initial configuration (b): the tape is stretched of a quantity h before loading.

During the peeling process the non-contact area is modeled as an interfacial crack, which determines the peeling advance as it propagates. The tape is assumed to be linearly elastic and incompressible.

A vertical force P is applied to the edge of the tape, as shown in Figure 1, and increases the length of the tape by a quantity

$$\Delta L = \frac{(a+h)}{Ebt} N = \frac{(a+h)}{Ebt}\left(\frac{P}{\sin\theta} - P_0\right), \qquad (1)$$

where $N = P/\sin\theta - P_0$ is the normal force acting along the tape axis, P_0 is the pre-tension and E is the Young modulus.

The change of the elastic energy stored in the system is

$$U_{\mathrm{el}} = \frac{1}{2}\left(\frac{P}{\sin\theta} + P_0\right)\Delta L = \frac{1}{2}\frac{(a+h)}{Ebt}\left(\frac{P^2}{\sin^2\theta} - P_0^2\right), \quad (2)$$

and the potential energy, which is the opposite of the work done by the external force P, is

$$\begin{aligned} U_P &= -P(a+h+\Delta L)\sin\theta \\ &= -P(a+h)\sin\theta\left[1+\frac{1}{Ebt}\left(\frac{P}{\sin\theta} - P_0\right)\right]. \end{aligned} \quad (3)$$

Equilibrium requires the stationarity of the total energy U_{tot}, i.e., according to the Griffith criterion

$$G = \Delta\gamma\,, \quad (4)$$

where $\Delta\gamma$ is the Dupré energy of adhesion [38], and G is the energy release rate at the crack tip, defined as

$$G = -\left(\frac{\partial U_{\mathrm{el}}}{\partial S} + \frac{\partial U_P}{\partial S}\right)_P, \quad (5)$$

when the external load P is given. In Equation 5 S is the detached area.

Before solving the problem it is convenient to introduce the following dimensionless quantities

$$\begin{aligned} \hat{\delta} &= \delta/h, \\ \hat{a} &= a/h, \\ \hat{P} &= P/(Ebt), \\ \hat{G} &= G/(Et), \end{aligned} \quad (6)$$

where we have defined δ through the relation $\delta + h = (a + h + \Delta L)\sin\theta$. From Equation 5 we obtain the following expression for the dimensionless energy release rate

$$\hat{G} = \frac{\hat{P}}{\sin\theta}(1-\cos\theta) - \frac{\hat{P}\hat{P}_0}{\sin\theta} + \frac{\hat{P}^2}{2\sin^2\theta} + \frac{\hat{P}_0^2}{2}, \quad (7)$$

where we have used the geometric condition $a = (a + h + \Delta L)\cos\theta$ (see Figure 1), leading to

$$\hat{a} = \frac{\cos\theta\left[1+\left(\frac{\hat{P}}{\sin\theta} - \hat{P}_0\right)\right]}{1-\cos\theta\left[1+\left(\frac{\hat{P}}{\sin\theta} - \hat{P}_0\right)\right]}. \quad (8)$$

Note that Equation 7 is coherent with what was found in [39] for the single peeling of a pre-tensioned tape. Finally, from Equation 4 and Equation 7 the load $\hat{P}$ can be related to the peeling angle θ_{eq} at equilibrium and the corresponding dimensionless vertical displacement $\hat{\delta}$ takes the form

$$\begin{aligned} \hat{\delta} + 1 &= -\left(\frac{\partial \hat{U}_{\mathrm{el}}}{\partial \hat{P}} + \frac{\partial \hat{U}_P}{\partial \hat{P}}\right)_{\hat{a}} \\ &= \frac{\hat{P} + \sin\theta - \hat{P}_0\sin\theta}{1-\cos\theta - \left(\hat{P}\cot\theta - \hat{P}_0\cos\theta\right)}. \end{aligned} \quad (9)$$

Results and Discussion

In this section we discuss the influence of the pre-tension on the peeling process while paying particular attention to the detection of the critical transition thresholds between different regimes of detachment.

Stability analysis of the peeling process

Figure 2 shows the dimensionless peeling force $\hat{P}$ (Figure 2a) as a function of the peeling angle θ_{eq} at equilibrium, and the relative dimensionless total energy $\hat{U}$ (Figure 2b) at a given load $\hat{P} = \overline{P}$ as a function of the peeling angle (even out of equilibrium). We observe that, for the considered case, given the applied load, two equilibrium states exist: one in the region $h/a > 0$ (corresponding to the tape configuration shown in Figure 1a), and the other in the region $h/a < 0$ (corresponding to the configuration in Figure 1b). In the latter case ($h/a < 0$), the equilibrium (dashed line in Figure 2a) is unstable since it corresponds to a maximum of the total energy $\hat{U}$ (see Figure 2b). Vice versa, in the region $h/a > 0$, the total energy $\hat{U}$ takes a local minimum at the peeling angles solving Equation 4 and, therefore, the corresponding configurations (solid line in Figure 2a) are stable.

In order to investigate what happens at a fixed pull-off force $\hat{P} = \overline{P}$, when the system is initially in non-equilibrium conditions, let us consider the starting configurations A, B, C and D shown in Figure 2a. Starting from point A, the tape evolves towards smaller and smaller peeling angles in order to minimize the total energy. At the end of this process, the peeling angle vanishes. Really, such a configuration cannot be reached because for the vertical load P to be balanced an infinite stress

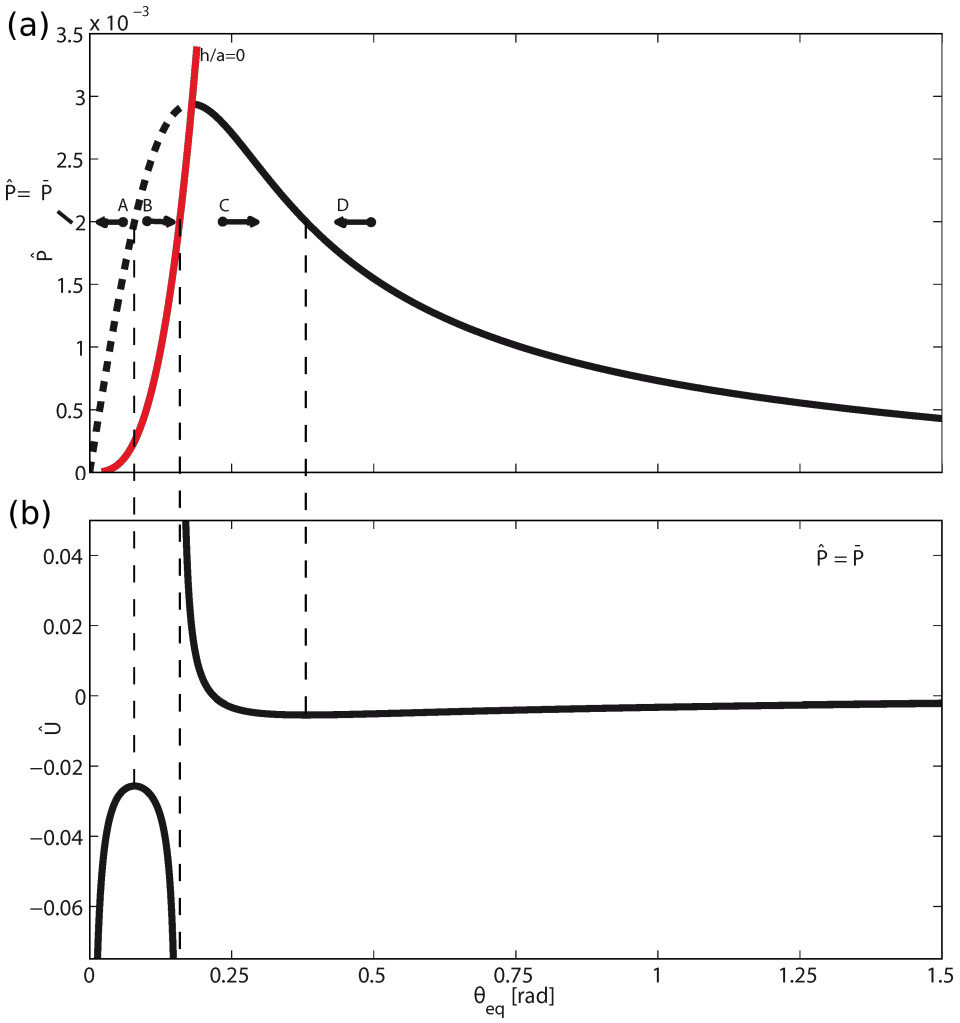

Figure 2: The dimensionless peeling force $\hat{P}$ as a function of the peeling angle θ_{eq} at equilibrium (a); the total energy $\hat{U}$ as a function of the peeling angle θ even out of equilibrium (b). For a fixed peeling force, depending on the initial configuration of the tape, the system can evolve towards states of partial adhesion (points *C* and *D*), complete detachment (point *B*) or can fail before reattaching to the substrate (point *A*).

in the tape would be necessary. Therefore, the tape will fail before adhering to the substrate. On the contrary, when the system starts from point *B*, the tape peeling angle increases until the red curve is touched and, as a result, the complete detachment of the tape occurs.

When the system initially moves from a non-equilibrium configuration in the region on the right side (points *C* and *D*), it will be always able to reach a stable equilibrium with a finite detached area, corresponding to the local minimum of the total energy.

The above results lead to the conclusion that solutions corresponding to the dashed curve of Figure 2a are physically admissible only when the tape is initially stretched (see Figure 1b). However, they are unstable. In fact, depending on the starting conditions, a small perturbation can bring the tape to failure (point *A* of Figure 2a) or to complete detachment from the substrate (point *B* of Figure 2a). In particular, the condition $h/a = 0$ defines a boundary that separates stable and unstable regions. Notice these results are coherent with what was found in [36].

Effect of pre-tension

First of all, we observe that the presence of a pre-tension P_0 does not modify the conclusions of the stability analysis in the above section. The pre-tension P_0 only affects the boundary $h/a = 0$ between stable and unstable regions. Figure 3 shows the dimensionless pull-off force $\hat{P}$ as a function of the peeling angle θ_{eq} at equilibrium, for different dimensionless values of $\hat{P}_0$. Again, unstable solutions are plotted with dashed lines, and the stable ones with solid lines. Note that the maximum pull-off force $\hat{P}$ that can be sustained by the tape increases with the pre-

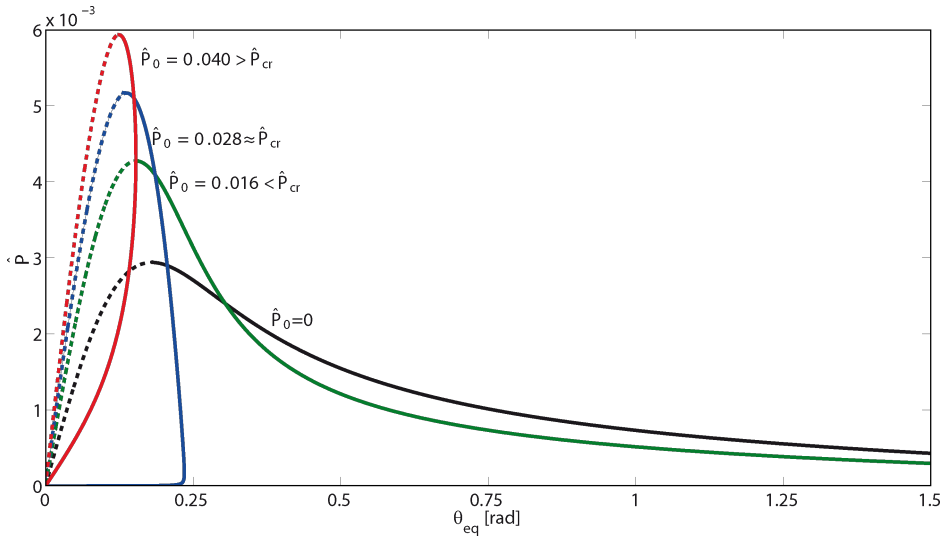

Figure 3: The dimensionless peeling force $\hat{P}$ as a function of the peeling angle θ_{eq} at equilibrium, for different values of the dimensionless pre-tension $\hat{P}_0$. The pre-tension generally increases the pull-off force at low peeling angles.

tension $\hat{P}_0$, and correspondingly the lower bound θ_{lim} of the peeling angle, at which the pull-off force takes its maximum value, reduces. However, a critical value $\hat{P}_{0,cr} = \sqrt{2\Delta\hat{\gamma}}$ of the pre-tension can be identified, above which the tape spontaneously detaches without applying any external vertical force. Indeed, when the pre-tension $\hat{P}_0$ exceeds the threshold $\hat{P}_{0,cr}$, the tape spontaneously detaches. Interestingly, in this case, finite values of the pull-off force $\hat{P}$ are necessary to make the system adhering to the surface. Furthermore, above $\hat{P}_{0,cr}$ the peeling angle cannot exceed a critical value θ_{cr}.

Figure 4 shows the variation of the dimensionless displacement $\hat{\delta}$ with the peeling angle θ_{eq} at equilibrium. Stable solutions are plotted with solid lines, the unstable ones with dashed lines. The displacement diverges as the peeling angle approaches θ_{lim}, so at the maximum pull-off force the corresponding displacement is infinite, and this explains why with a finite force we can detach a tape of infinite length. Observe that at $\theta_{eq} = 0$ the term $\delta + h$ necessarily vanishes and, thus, $\hat{\delta} = -1$. Moreover, Figure 4 shows that on the unstable branches (dashed lines) the dimensionless displacement $\hat{\delta} < -1$. This means that on the

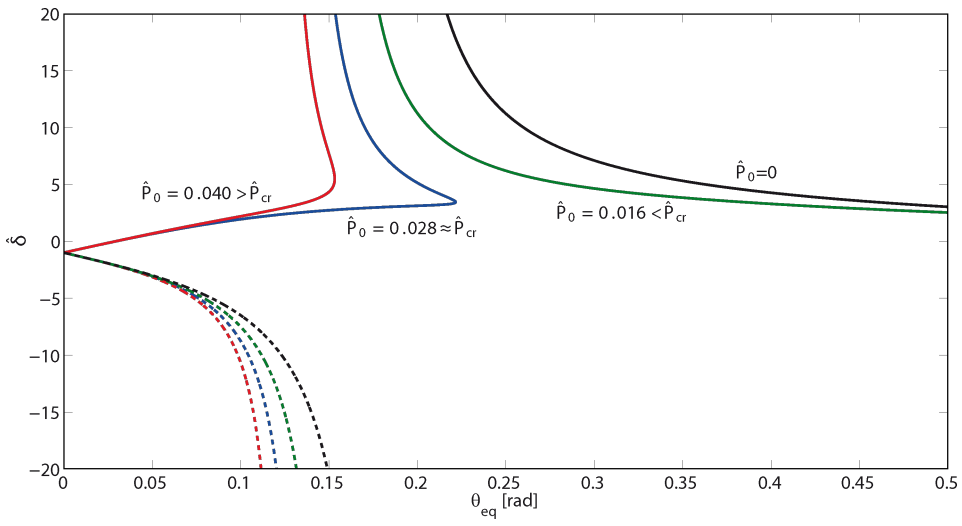

Figure 4: The dimensionless displacement $\hat{\delta}$ as a function of the peeling angle θ_{eq} at equilibrium, for different values of the dimensionless pre-tension $\hat{P}_0$.

unstable branches the quantity h is negative, and the configuration of the tape is the one represented in Figure 1b.

Conclusion

The mechanism of detachment of an elastic thin tape adhering to a rigid substrate has been investigated, generalizing the model proposed in [36] with the incorporation of pre-tension in the tape and by performing an equilibrium stability analysis. Two equilibrium states are found: one being stable, the other being unstable. The two regimes strictly depend on the initial conditions of the system. In particular, solutions on the unstable branch are possible only when the tape is locally stretched before applying the pull-off force. In this case, if the starting point is at the left side of the unstable curve, in order to minimize the total energy, the peeling angle decreases until it vanishes. At the same time, in order to balance the applied vertical load, the stress in the tape increases and at zero peeling angle it should diverge. However, the tape, not being able to support infinite loads, necessarily fails before the new full adhesive equilibrium state can be reached. If the starting condition is at the right side of the unstable curve, the tape evolves towards a new state involving complete detachment.

Pre-tension does not change the above conclusions on the equilibrium stability. However, a pre-tensioned tape can sustain higher values of the pull-off force, before complete detachment. Interestingly, we find that above a critical value of the pre-tension, the tape cannot spontaneously adhere to the substrate, and an external load is therefore necessary to prevent spontaneous detachment.

Acknowledgements

The authors are thankful to the Italian Ministry of Education, University and Research for supporting the research activity within the projects PON01_ 02238 and PON02_ 00576_ 3333604. CP also gratefully acknowledges the support of Marie Curie IEF project SOFT-MECH (grant number 622632).

References

1. Geim, A. K.; Dubonos, S. V.; Grigorieva, I. V.; Novoselov, K. S.; Zhukov, A. A.; Shapoval, S. Yu. *Nat. Mater.* **2003,** *2,* 461–463. doi:10.1038/nmat917
2. Pugno, N. M. *J. Phys.: Condens. Matter* **2007,** *19,* 395001. doi:10.1088/0953-8984/19/39/395001
3. Pugno, N. M. *Nano Today* **2008,** *3,* 35–41. doi:10.1016/S1748-0132(08)70063-X
4. Autumn, K.; Sitti, M.; Liang, Y. A.; Peattie, A. M.; Hansen, W. R.; Sponberg, S.; Kenny, T. W.; Fearing, R.; Israelachvili, J. N.; Full, R. J. *Proc. Natl. Acad. Sci. U. S. A.* **2002,** *99,* 12252–12256. doi:10.1073/pnas.192252799
5. Scherge, M.; Gorb, S. *Biological micro- and nanotribology;* Springer, 2001.
6. Glassmaker, N. J.; Jagota, A.; Hui, C.-Y.; Noderer, W. L.; Chaudhury, M. K. *Proc. Natl. Acad. Sci. U. S. A.* **2007,** *104,* 10786–10791. doi:10.1073/pnas.0703762104
7. Carbone, G.; Mangialardi, L.; Persson, B. N. J. *Phys. Rev. B* **2004,** *70,* 125407. doi:10.1103/PhysRevB.70.125407
8. Fearing, J. *Gecko adhesion bibliography;* Department of EECS, University of California, Berkeley, 2008.
9. Autumn, K.; Dittmore, A.; Santos, D.; Spenko, M.; Cutkosky, M. *J. Exp. Biol.* **2006,** *209,* 3569–3579. doi:10.1242/jeb.02486
10. Gravish, N.; Wilkinson, M.; Autumn, K. *J. R. Soc., Interface* **2008,** *5,* 339–348. doi:10.1098/rsif.2007.1077
11. Autumn, K.; Liang, Y. A.; Hsieh, S. T.; Zesch, W.; Chan, W. P.; Kenny, T. W.; Fearing, R.; Full, R. J. *Nature* **2000,** *405,* 681–685. doi:10.1038/35015073
12. Lepore, E.; Pugno, F.; Pugno, N. M. *J. Adhes.* **2012,** *88,* 820–830. doi:10.1080/00218464.2012.705639
13. Ke, C.; Zheng, M.; Zhou, G.; Cui, W.; Pugno, N.; Miles, R. N. *Small* **2010,** *6,* 438–445. doi:10.1002/smll.200901807
14. Autumn, K.; Majidi, C.; Groff, R. E.; Dittmore, A.; Fearing, R. *J. Exp. Biol.* **2006,** *209,* 3558–3568. doi:10.1242/jeb.02469
15. Pugno, N. M. *Int. J. Fract.* **2011,** *171,* 185–193. doi:10.1007/s10704-011-9638-2
16. Pugno, N. M.; Cranford, S. W.; Buehler, M. J. *Small* **2013,** *9,* 2747–2756. doi:10.1002/smll.201201343
17. Varenberg, M.; Pugno, N. M.; Gorb, S. N. *Soft Matter* **2010,** *6,* 3269–3272. doi:10.1039/c003207g
18. Carbone, G.; Pierro, E.; Gorb, S. N. *Soft Matter* **2011,** *7,* 5545–5552. doi:10.1039/c0sm01482f
19. Carbone, G.; Pierro, E. *Small* **2012,** *8,* 1449–1454. doi:10.1002/smll.201102021
20. Afferrante, L.; Carbone, G. *J. R. Soc., Interface* **2012,** *9,* 3359–3365. doi:10.1098/rsif.2012.0452
21. Afferrante, L.; Carbone, G. *J. Phys.: Condens. Matter* **2010,** *22,* 325107. doi:10.1088/0953-8984/22/32/325107
22. Afferrante, L.; Carbone, G. *Macromol. React. Eng.* **2013,** *7,* 609–615. doi:10.1002/mren.201300125
23. Carbone, G.; Pierro, E. *Soft Matter* **2012,** *8,* 7904–7908. doi:10.1039/c2sm25715g
24. Carbone, G.; Pierro, E. *Meccanica* **2013,** *48,* 1819–1833. doi:10.1007/s11012-013-9724-9
25. Carbone, G.; Bottiglione, F. *J. Mech. Phys. Solids* **2008,** *56,* 2555–2572. doi:10.1016/j.jmps.2008.03.011
26. Putignano, C.; Afferrante, L.; Carbone, G.; Demelio, G. *Int. J. Solids Struct.* **2012,** *49,* 338–343. doi:10.1016/j.ijsolstr.2011.10.009
27. Putignano, C.; Afferrante, L.; Carbone, G.; Demelio, G. *J. Mech. Phys. Solids* **2012,** *60,* 973–982. doi:10.1016/j.jmps.2012.01.006
28. Putignano, C.; Afferrante, L.; Carbone, G.; Demelio, G. P. *Tribol. Int.* **2013,** *64,* 148–154. doi:10.1016/j.triboint.2013.03.010
29. Afferrante, L.; Carbone, G.; Demelio, G. *Wear* **2012,** *278-279,* 28–33. doi:10.1016/j.wear.2011.12.013
30. Carbone, G.; Putignano, C. *J. Mech. Phys. Solids* **2013,** *61,* 1822–1834. doi:10.1016/j.jmps.2013.03.005
31. Carbone, G.; Putignano, C. *Phys. Rev. E* **2014,** *89,* 032408. doi:10.1103/PhysRevE.89.032408
32. Autumn, K.; Hsieh, S. T.; Dudek, D. M.; Chen, J.; Chitaphan, C.; Full, R. J. *J. Exp. Biol.* **2006,** *209,* 260–272. doi:10.1242/jeb.01980
33. Autumn, K.; Peattie, A. *Integr. Comp. Biol.* **2002,** *42,* 1081–1090. doi:10.1093/icb/42.6.1081

34. Tian, Y.; Pesika, N.; Zeng, H.; Rosenberg, K.; Zhao, B.; McGuiggan, P.; Autumn, K.; Israelachvili, J. *Proc. Natl. Acad. Sci. U. S. A.* **2006,** *103,* 19320–19325. doi:10.1073/pnas.0608841103
35. Pesika, N. S.; Tian, Y.; Zhao, B.; Rosenberg, K.; Zeng, H.; McGuiggan, P.; Autumn, K.; Israelachvili, J. N. *J. Adhes.* **2007,** *83,* 383–401. doi:10.1080/00218460701282539
36. Afferrante, L.; Carbone, G.; Demelio, G.; Pugno, N. *Tribol. Lett.* **2013,** *52,* 439–447. doi:10.1007/s11249-013-0227-6
37. Kendall, K. *J. Phys. D: Appl. Phys.* **1975,** *8,* 1449–1452. doi:10.1088/0022-3727/8/13/005
38. Maugis, D. *Contact, Adhesion, Rupture of Elastic Solids;* Springer Series in Solid-State Sciences, Vol. 130; Springer: Berlin, Heidelberg, New York, 1999.
39. Chen, B.; Wu, P.; Gao, H. *J. R. Soc., Interface* **2009,** *6,* 529–537. doi:10.1098/rsif.2008.0322

License and Terms

BEILSTEIN JOURNAL OF NANOTECHNOLOGY

Aquatic versus terrestrial attachment: Water makes a difference

Petra Ditsche* and Adam P. Summers

Review

Open Access

Address:
Friday Harbor Laboratories, University of Washington, 620 University Road, Friday Harbor, WA, 98250, USA

Email:
Petra Ditsche* - pditsche@UW.edu

* Corresponding author

Keywords:
adhesion; biofilm; friction; hooks; suction

Beilstein J. Nanotechnol. **2014,** *5,* 2424–2439.
doi:10.3762/bjnano.5.252

Received: 07 March 2014
Accepted: 21 November 2014
Published: 17 December 2014

This article is part of the Thematic Series "Biological and bioinspired adhesion and friction".

Guest Editor: S. N. Gorb

Abstract

Animal attachment to a substrate is very different in terrestrial and aquatic environments. We discuss variations in both the forces acting to detach animals and forces of attachment. While in a terrestrial environment gravity is commonly understood as the most important detachment force, under submerged conditions gravity is nearly balanced out by buoyancy and therefore matters little. In contrast, flow forces such as drag and lift are of higher importance in an aquatic environment. Depending on the flow conditions, flow forces can reach much higher values than gravity and vary in magnitude and direction. For many of the attachment mechanisms (adhesion including glue, friction, suction and mechanical principles such as hook, lock, clamp and spacer) significant differences have to be considered under water. For example, the main principles of dry adhesion, van der Waals forces and chemical bonding, which make a gecko stick to the ceiling, are weak under submerged conditions. Capillary forces are very important for wet adhesion, e.g., in terrestrial beetles or flies, but usually do not occur under water. Viscous forces are likely an important contributor to adhesion under water in some mobile animals such as torrent frogs and mayflies, but there are still many open questions to be answered. Glue is the dominant attachment mechanism of sessile aquatic animals and the aquatic realm presents many challenges to this mode of attachment. Viscous forces and the lack of surface tension under submerged conditions also affect frictional interactions in the aquatic environment. Moreover, the limitation of suction to the pressure difference at vacuum conditions can be ameliorated under water, due to the increasing pressure with water depth.

Introduction

Attachment in animals, plants and microorganisms serves a variety of functions: the interconnection of body parts, fixation of the whole animal, a locomotor structure, or eggs to the substrate, and forming a stable platform for copulation, feeding, phoresy, parasitism or predation [1,2]. Here we focus on attachment of animals to stiff, solid substrates under two biologically

relevant conditions – in a dry or humid environment (terrestrial) in comparison to completely submerged in water (aquatic). Our aim is to provide a framework for considering these two conditions of attachment. We will contrast the forces that act to dislodge an attached organism in submerged and emerged environments and distinguish between the attachment forces in these disparate arenas. The difference between a submerged attachment event and one that is dry is neither clear-cut nor simple. Consider the classic example of a toe of a gecko adhered to a leaf. On its face, this is a case of terrestrial adhesion, but depending on humidity there could be a monolayer of water on the surface of the leaf, or there might be a patch of standing water on the leaf after rainfall. Even in this terrestrial example, there is the possibility of submerged mechanics applying at some size scale. Similarly, there are cases in the fully submerged environment where terrestrial mechanics might apply. For example, when spiders bring with them a ball of air as they dive beneath the surface, or when two superhydrophobic surfaces interact underwater. Therefore, the first task that we face is to make clear what we mean as we try to distinguish between these two environments, while also keeping in mind that there is a continuum and counterintuitive exceptions to the framework we are proposing.

For our purposes, a terrestrial environment has air as surrounding fluid. However, the air can be completely dry or rather humid. Therefore, effects of water can play some role in a terrestrial environment, especially in form of capillary forces. The aquatic or immersed environment is one in which water surrounds the organism completely, or at least the entire attachment organ and the attachment surface. Here, water plays a central role and must be considered to be surrounding and separating the two surfaces brought into contact. Some unusual immersed attachment examples might be an insect stepping into a droplet of water sitting on a branch. The size scale of the droplet is such that the entire attachment process is occurring underwater. However, in this very example we can see a gray area in that the foot has recently been dry, so the tendency of air to surround the attachment organ as it penetrates the droplet may be important. Our generalizations about aquatic environments apply when the foot of the insect brings none of the terrestrial environment with it into the aquatic environment.

The natural world is replete with examples of aquatic attachment and terrestrial attachment in the sense that we propose. In the terrestrial realm, virtually every case of arthropod attachment, from flies on ceilings to a spider dancing on a web is an example. There are examples in diverse taxa, including suctorial bats, several variations of lizards, and countless beetles, spiders and ants. In every stream, there are mobile larvae that spend their lives attaching to the substrate. These insects are ruled by the water forces imposed by local flow conditions. There are vertebrate examples in waterfall climbing gobies and frogs, and echinoderms that adhere in the intertidal zone. In short, though there is certainly a continuum between aquatic and terrestrial conditions, the vast majority of biological adhesion takes place in a system dominated by one extreme or the other.

Review

Forces that act to dislodge

Attachment to the substrate is aimed at either locomotion or staying in place [3]. For either purpose, the animal has to overcome forces acting to dislodge it, and it is in the nature of these forces that terrestrial and aquatic systems vary widely. The forces are not the same in terrestrial systems compared with aquatic ones in either scale or type (Table 1). While in terrestrial systems gravitation is the most relevant, in aquatic systems gravity is mostly cancelled by buoyancy. In contrast, in aquatic systems flow forces such as drag and lift are very important while they are seldom substantial in terrestrial systems. The magnitude of these forces varies by environment and so does the direction: while gravity always acts only in the direction of the earth, drag pushes the animal across the surface, and lift can pull it off regardless of orientation (Figure 1). Moreover, aquatic flows are often variable in magnitude and direction on very short time scales. In running waters and some directed marine currents there is a general main flow direction, while the waves

Table 1: Forces of detachment in terrestrial and aquatic environments. Relative importance: ✔ – usually important, ✖ – usually not important.

	terrestrial	aquatic	direction	magnitude	determining parameters
gravity	✔	✖	predictable	predictable	mass, acceleration of gravity
buoyancy	✖	✔	predictable	predictable	volume, density
inertial forces	✔	✔	unpredictable	unpredictable	mass, acceleration
lift and drag forces, acceleration reaction force	✖	✔	unpredictable	unpredictable	shape and size, orientation, velocity, fluid density and viscosity

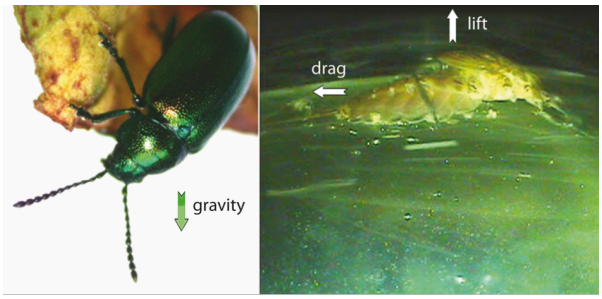

Figure 1: A) Green dock beetle *Gastrophysa viridula* as an example for terrestrial attachment (image: Stanislav Gorb, reproduced with permission by the author), B) Mayfly larvae *Epeorus* attaching to a substrate in running water (image: Petra Ditsche). Arrows show the direction of the most important forces acting on the animals.

in the marine intertidal move the water in different directions with high frequency. In many cases, water flow is not laminar (laminar means particles do not cross streamlines) but rather turbulent, with sudden, stochastically determined changes in direction [4]. There are also important issues of scaling to consider that some detachment forces will scale with the cube of animal length while others scale with the square.

In both the terrestrial and the aquatic environment the attachment event is surrounded by fluid, in one case air and in the other water. Air and water have different properties that have several consequences for the organisms living in these fluids [5]. Three principle factors have a significant effect on the types of forces acting to dislodge attached organisms. The first is density; water is around 1000 times denser than air, which means that both inertia and buoyancy are very different in these two fluids (Table 2). Second, air has just around 1.8% of the (dynamic) viscosity of water, which affects the scale of forces between the fluid and the organism. Thirdly, water is a polar liquid while air is a largely inert gas. This difference has profound effects on physicochemical interactions in the dry and in the wet environment.

Gravity

Gravity is usually the most important force acting on the attachment of terrestrial animals. The gravitational force on an organism is simply

$$F_g = m \cdot g \tag{1}$$

and always acts in the direction of the centre of the Earth (g: gravitational acceleration). The magnitude of the gravitational force (F_g) scales with the mass of the organism (m) and therefore with the cube of any length parameter. The magnitude of the gravitational force is the same in terrestrial and aquatic environments and, for biological purposes, it is constant regardless of time or place. Gravity is the archetype for a predictable force, though the frame of reference of the organism does not always point in the ventral direction. In Figure 1, the beetle is attached to a substrate above it and the gravitational vector points almost exactly opposite to the attachment force.

Buoyancy

The density of water (ρ_w) is much higher than the density of air and is closer to the typical density of living organisms (ρ_a), so buoyancy can substantially offset the gravitational force in the aquatic environment whereas in the terrestrial environment it is usually negligible. The buoyant force (F_b) always acts in the opposite direction to the gravitational force and is defined as

$$F_b = \left(\rho_a - \rho_w\right) \cdot V \cdot g \tag{2}$$

Buoyancy, like gravitational force scales with the cube of a length parameter because it scales with the displaced volume (V). It varies little with time and in space as neither density nor volume typically vary rapidly. There are interesting exceptions to this rule of thumb that have implications for attachment. Organisms with an air compartment in an aquatic environment must deal with changes in volume imposed by the ideal gas law. The volume of the compartment will vary locally with pressure and temperature. For organisms able to transit the first 10 m of depth in an aquatic environment, this is a 50% decrease in volume when descending or a doubling when ascending. This implies a similar change in the buoyant force while the offsetting gravitational force would remain the same. Under some conditions, it is possible to have the buoyant force exceed gravity. This positive buoyancy can require an organism to

Table 2: Density and viscosities of air and water at 20 °C.

parameter	unit	air	freshwater	saltwater
density	[kg/m^3]	1.205	0.998×10^3	1.024×10^3
dynamic viscosity	[Pa·s]	18.08×10^{-6}	1.002×10^{-3}	1.072×10^{-3}
kinematic viscosity	[m^2/s]	15.00×10^{-6}	1.004×10^{-6}	1.047×10^{-6}

attach to an underwater substrate just to keep from floating to the surface.

Inertial forces

For an animal sitting on a leaf moving in the wind, an insect landing on a substrate, a clingfish attaching to kelp moving in the current, or simply during walking on a substrate, inertial forces contribute to detachment. Whether the surface or the organism is in motion, there are forces associated with changes in velocity

$$F_{\mathrm{i}} = m \cdot a \tag{3}$$

The direction of inertial forces (F_{i}) is determined by direction of the acceleration vector, and the magnitude is dependent on both mass (m) and acceleration (a). The dependence on the mass implies a scaling coefficient of the cube of a length parameter, but the picture is complicated by the nature of the scaling of acceleration. Although the rules for the scaling of acceleration are not well-described, in many systems there is an inverse scaling such that very high accelerations are found in very small systems. There is no equation for the scaling of inertial forces that takes into account both acceleration and mass (although see [6] for some special cases that are well-described). Neither the direction nor the magnitude of inertial forces is affected by water, so they are the same in both in aquatic and terrestrial environment. The predictability of inertial forces is linked to the predictability of acceleration and it is difficult to make a case that this will vary with environment.

Flow forces

In aquatic systems drag and lift forces are the most important forces acting on an attached organism [4,7,8]. Drag and lift have several causes and depend on a variety of parameters. They are both highly variable in magnitude and direction and, thus, hard to predict. Drag is a force due to fluid movement that acts in the direction of the free stream flow. It has two components, friction drag (or skin friction) and pressure drag (or form drag), which both depend on shape and fluid parameters but in quite different ways [4]. Friction drag is caused by friction of the water flowing over the surface of the animal body. It varies directly with the viscosity of the fluid [4] and the wetted surface area of the organism. Pressure drag is caused by the wake formed downstream of an animal. This turbulent wake creates a low pressure zone downstream of the animal [9]. Friction drag is proportional to the product of surface area and velocity, while pressure drag is proportional to the product of the area in frontal projection and velocity squared. Pressure drag (F_{d}) can be calculated by the drag coefficient (C_{d}), the density of the fluid (ρ), the area in frontal protection (S_{f}) and the flow velocity (U):

$$F_{\mathrm{d}} = \frac{1}{2} \cdot C_{\mathrm{d}} \cdot \rho \cdot S_{\mathrm{f}} \times U^2 \tag{4}$$

In the same medium the importance of these two types of drag varies with flow speed and the size of the animal. Friction drag dominates for small animals and slow flow speeds, and pressure drag dominates for large animals and/or fast flow speeds. In either regime, the resistance of an animal to the water flow is determined by its body shape. Of course, animals of the same body shape and size will experience much higher drag forces at the same flow velocity in water compared to air (see below in Table 3), because of the higher density and viscosity in water.

Lift, acting at right angles to the free stream of flow, is dependent on the shape and is proportional to the projected planform area (S_{p}) of the organism, the fluid density and the square of the fluid velocity:

$$F_{\mathrm{l}} = \frac{1}{2} \cdot C_{\mathrm{l}} \cdot \rho \cdot S_{\mathrm{p}} \cdot U^2 \tag{5}$$

The dependency on U^2 means that the lift force as well as drag force are very important components of the total detachment force. The lift coefficient (C_{l}) and the drag coefficient describe the effect of shape.

In unsteady flow another force matters, namely the acceleration reaction force [4]. Consider an animal accelerating during swimming, some water must move as well, so the animal not only accelerates its own mass but also this “added mass of the fluid” [10]. The same force occurs when water accelerates over a stationary object. The acceleration reaction force acting on an attached animal in a wave is proportional to its volume (V_{a}) and the water acceleration [11]. It can be calculated from the added mass coefficient (C_{a}), the density of the fluid, the volume of the animal and the acceleration.

$$F_{\mathrm{a}} = C_{\mathrm{a}} \cdot \rho \cdot V \cdot a \tag{6}$$

While drag is highest at the maximum velocity, the acceleration reaction force has its maximum when the acceleration is highest. For larger organisms the acceleration reaction force can be several times higher than drag force, while for small organisms drag matters most [11].

For example, let us consider a hemispherical attached organism, closely adhered to the substrate, in a terrestrial and an aquatic context. We will assume a mass of 2.2 g, a radius of 1 cm, an ambient temperature of 20 °C and flow velocities between 1 and 30 m/s, and for the purposes of a comparison of inertia we

assign an acceleration of three times of Earth's gravity [12,13]. From the literature we find that a hemisphere has a drag coefficient of 0.32 and a lift coefficient of about 0.75 [4,14]. Table 3 shows that in the terrestrial case the gravitational force is dominant, while in the aquatic system lift and drag matter. We can calculate that the density of the organism is 2.2 g/(4π/3·1 cm^3)/2 = 1.05 g/cm^3. The projected frontal area is S_f = (π·1 cm^2)/2 =1.57 cm^2, the planform area S_p = π·1 cm^2 = 3.14 cm^2 and the surface area is (4π·1 cm^2)/2 = 12.57 cm^2. With these parameters, we consider the relative magnitude of the detachment forces, bearing in mind that they may not act normal to the substrate. The force due to gravity is exactly the same in aquatic and terrestrial environments, but the net force when buoyancy is subtracted leads to a 20-fold higher force in terrestrial environments. This could release a constraint on size in the aquatic environment. Drag and lift, whether in relatively calm or extremely swift flows, are three orders of magnitude higher in the aquatic environment than on land. This suggests that shape might be far more variable in the terrestrial environment because there is less selective pressure to streamline. Moreover, drag and lift forces in aquatic environment can reach much higher values compared with gravity on land. Lastly, consider the inertial forces that are predicted on the basis of an plausible natural acceleration. They are the same in both environments, but they are three times higher than the static gravitational forces and 60 times higher than the net gravitational/buoyancy force for an aquatic organism. This brings home the importance of considering the movement of the attached organism. Accelerations due to locomotion or due to movement of the substrate may be a dominant force driving detachment. Furthermore, when considering safety factors expressed as a multiple of body mass, bear in mind that the inertial forces could easily exceed this safety factor three- or four-fold.

Forces of attachment

Attachment mechanisms are diverse and we can categorize them into three types by the time course of operation: permanent, temporary and transitory [15,16]. Animals attaching themselves permanently to the ground for their whole (adult) lifetime are called sessile. Blue mussels or barnacles are very prominent examples of this sessile type. Other animals such as molluscs, claw-bearing aquatic arthropods or sea stars, use alternating attachment for locomotion or for short-time fixation (temporary attachment) and are called motile or mobile. An intermediate form between temporary and permanent attachment can be found, for example, in many marine larvae, allowing them to explore possible substrates prior to permanent attachment. Transitory adhesion allows simultaneous adhesion and locomotion on a viscous film as practiced by molluscs or some flatworms [16]. The boundary between temporary and transitory adhesion is not always clear [16].

Taking into account (1) the fundamental physical mechanisms, (2) the biological function and (3) the duration of attachment time, the attachment mechanisms have been divided into eight main functional principles: wet and dry adhesion, friction, suction and the mechanical principles hooks, clamps, locks and spacers [2]. We will discuss the differences between these fundamental principles when applied under water. In nature some animals combine these fixation principles, for example limpets use suction and glue, black fly larvae support their hooks by secretion and some squids combine suckers with hooks.

Attachment is a two-body problem so there is interplay with the substrate, and the properties of the substrate also must be taken into account [17]. Common solid substrates in aquatic systems

Table 3: Calculation of the detachment forces of a theoretical hemispherical organism (mass: 2.2 g and radius: 1 cm).

	forces in terrestrial environment [mN]	forces in aquatic environment [mN]
weight (gravitational force)	21.582	21.582
buoyancy	0.025	20.594
weight − buoyancy	**21.557**	**0.988**
drag (*U* = 0.5 m/s)	0.008	6.299
drag (*U* = 1 m/s)	0.030	25.195
drag (*U* = 2 m/s)	0.121	100.781
drag (*U* = 5 m/s)	0.757 (wind)	629.875
drag (*U* = 30 m/s)	27.270 (whole gale)	22.675 × 10^3 (base of a waterfall)
lift (*U* = 0.5 m/s)	0.035	29.525
lift (*U* = 1 m/s)	0.141	118.103
lift (*U* = 2 m/s)	0.567	472.413
lift (*U* = 5 m/s)	3.547	2.952 × 10^3
lift (*U* = 30 m/s)	127.700 (whole gale)	106.29 × 10^3 (base of waterfall)
inertial force (*a* = 3*g*)	64.746	64.746

are stones, plants, wood pieces, artificial substrates and even other animals. Stones (Figure 2), artificial substrates and plants have large variation in surface texture, from smooth to very rough and smooth to hairy or covered with waxes [18,19]. Also the surface energy and with it the wettability of surfaces as well as the elasticity of the substrates are important properties, which can influence attachment [17].

Another important point needs to be considered for aquatic systems. While most terrestrial animals make contact directly with the substrate, in aquatic environments the substrates are usually covered with a biofilm and fouling organisms (Figure 3). Biofilms play not only an important role in stimulating or inhibiting the settlement of fouling invertebrates [20-25], but they also change the surface properties of the primary substrate considerably and by this can affect the attachment forces significantly [26,27]. While biofilms can vary greatly in composition and thickness, they are usually softer than the primary substrate, and change the surface topography [26]. Moreover, microorganisms can change the wettability of the substrates surface, which is probably the reason for a different response of some larvae to these surfaces [28].

Some examples of attachment forces for different animals and attachment devices are given in Table 4 and Table 5. Very large attachment forces are generated by glue adhesion and suction. However, as the given values have been determined under very different conditions (substrates of different material, surface energy, roughness and elasticity; different measurement methods) the values are hard to compare and principally serve to demonstrate that wide-scale comparative studies are sorely needed in this field. Scale issues are also important; some studies are on a particular body part, e.g., the attachment of a single seta, while others are on whole organisms. This is certain

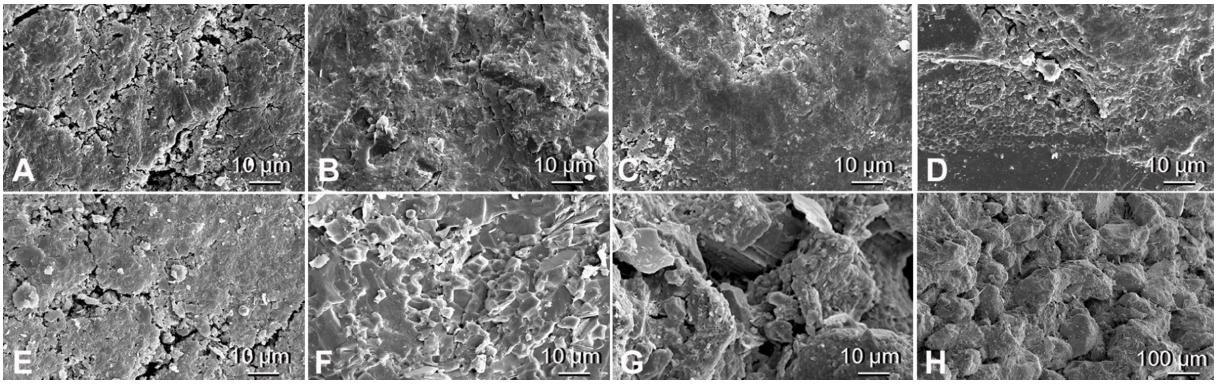

Figure 2: SEM pictures of the surface of selected rocks found in running waters: (A) andesite, (B) slate, (C) basalt, (D) quartz gravel (E) greywacke, (F) quartzite and (G, H) sand stone. (Reproduced from [18]).

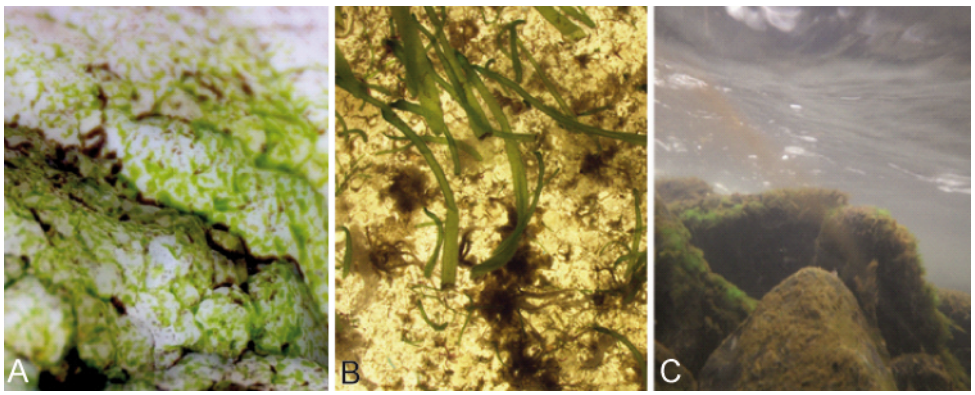

Figure 3: Examples of substrates which have been exposed to an aquatic environment and are covered with biofilm and periphyton; A) stone of the marine intertidal covered with biofilm and algae (image: Petra Ditsche); B) artificial substrates after 6 week exposure in the sea, with biofilm and growth of first macroalgae (image: Adam Summers); C) biofilm and macroalgae cover the stones of this stream in a thick layer (image: Sarah Kaehlert).

Table 4: Examples for attachment parameters measured parallel to the substrate according to different authors (whole animal, on smooth substrates at water level and terrestrial environment, respectively).

taxon	attachment device	substrate	attachment force [N]	tenacity [kPa]	force/body mass	ref.
Gekko gecko (Gekkonidae, Reptilia)	adhesive pad (dry)	glass	17		≈17	[29]
		PMMA	27		≈27	
Gekko gecko (Gekkonidae, Reptilia)	adhesive pad (submerged)	glass	5		≈5	[29]
		PMMA	24		≈24	
Staurois guttatus (Ranidae, Amphibia)	adhesive pads (dry)	polyethylene	1165 (whole animal)	3.0 (pads)	43	[30]
Staurois guttatus (Ranida, Amphibia)	adhesive pads (submerged)	polyethylene	42 (whole animal)	0.1 (pads)	1.5	[30]
Chthamalus fragilis (Cirripedia, Crustcea) (ca. 8 mg)	glue	polystyrene	0.11	105		[31]
Patella vulgata (Patellidae, Gastropoda)	glue, sucker	glass	50	50		[32]
Simulium vittatum (Simuliidae, Insecta) (ca. 6 mm long)	circlet of hooks, secretion	wire	0.012			[33]

Table 5: Examples for attachment parameters measured perpendicular to the substrate according to different authors (whole animal, on smooth substrates at water level and terrestrial environment, respectively).

taxon	attachment device	substrate	attachment force [N]	tenacity [kPa]	force/body mass	ref.
Staurois guttatus (Ranidae, Amphibia)	adhesive pads (dry)	polyethylene	0.373 (whole animal)	2.4 (pads)	13.8	[30]
Staurois guttatus (Ranidae, Amphibia)	adhesive pads (submerged)	polyethylene	0.089 (whole animal)	0.1 (pads)	3.3	[30]
Bivalvia (species non def.)	glue	glass		320–750		[34]
Patella vulgata (Patellidae, Gastropoda)	glue, sucker	glass	up to 240	up to 230		[32]
Lottia gigantea (Patellidae, Gastropoda)	glue, sucker	Lucite		50		[35]
Hapalothrix lugubris (Blephariceridae, Insecta)	sucker	rock	0.084 (one sucker)			[36]
Gobiesox maeandricus, *Gobiesocidae*, *Actinpterygii/Pisces*	sucker	epoxy resin	up to 50	20–50	80–250	[37]

to add substantial variability and we cannot calculate a reasonable attachment force for the whole animal from measurements of a single seta, tube foot or sucker.

Adhesion

A variety of different mechanisms contributes to adhesion: (i) mechanical interlocking on a very small scale, (ii) electrostatic forces, (iii) diffusion, (iv) chemical bonding as ionic, covalent or hydrogen bonds, and (v) dispersive or van der Waals forces. While the first three mechanisms of adhesion presumably contribute just a minor part to general adhesion, the latter two are generally accepted as the primary mechanisms in many systems [19]. The mechanisms involved in wet and dry adhesion are different (Table 6). Dry adhesion occurs in a dry environment and no fluid film is involved. When adhesion takes place in a humid environment, there is a substantial increase in adhesive forces [38]. Moreover, some animals secrete a liquid themselves [19,39]. If a fluid film is present, we have the conditions of wet adhesion. In wet adhesion two other forces contribute considerably to adhesion: (vi) capillary forces, and (vii) viscous forces. The latter is often called Stefan adhesion. A special case of wet adhesion is the secretion of adhesives (glue), which we will discuss below.

Adhesion that occurs under immersed conditions is greatly complicated by the difficulty in displacing water from the

Table 6: The mechanisms of adhesion under dry, wet and immersed conditions. Relative importance: ✔ – usually important, ✖ – usually not important.

	dry conditions	wet conditions (liquid film)	immersed conditions
mechanical interlocking	✔	✔	✔
electrostatic forces	✔	✖	✖
chemical bonding	✔	✖	✖
van der Waals forces	✔	✖	✖
capillary forces	✖	✔	✖
viscous forces	✖	✔	✔

contacting interfaces and the ability of water to weaken many forms of bonds [40]. The relevant ones are described in the following.

van der Waals forces and chemical bonding

van der Waals forces are the sum of attractive forces between molecules that have regions of slightly negative and slightly positive charges. These forces are only effective over a very small distance, less than one nanometer [41]. Therefore, these forces are considerably weakened in the presence of water, which tends to form a separating film between the surfaces. For example on polyvinylsiloxane (PVS) surfaces, van der Waals forces are decreased to 12% of the value in air when submerged under water [42].

Capillary forces

Capillary adhesion occurs when a water film separates two hydrophilic surfaces in air. Pulling the surfaces apart will create a larger air–water boundary surface area. The surface tension of the liquid will resist to this increase and this is manifest as an adhesive force. According to [3] Laplace's law ought to be applied:

$$\Delta p = \gamma \cdot \left(\frac{1}{r_o} - \frac{1}{r_e} \right) \quad (7)$$

The pressure difference (Δp) can be calculated from surface tension (γ), the overall radius of the liquid (r_o) and the radius of the curved edge (r_e) (Figure 4).

In contrast, under fully immersed conditions the surface tension should be zero, so that generally no capillary forces will occur under these conditions. This is an important difference between adhesion in terrestrial and aquatic systems. Nevertheless, there are exceptions. Some terrestrial animals can step in droplets, e.g., on plant surfaces or even be completely submerged under water for a short time due to heavy rainfall. For example, the beetle *Gastrophysa viridula* can walk under water [43]. This beetle develops higher adhesive forces on hydrophobic surfaces compared to hydrophilic ones. The hydrophobic setose pads of the beetle hold air under water, so if it encounters hydrophobic surfaces the contact interface gets de-wetted, but not on hydrophilic surfaces. Additional capillary bridges between foot and substrate are formed due to the fluid secreted by the beetle and shear adhesion forces are in the same range as in air [43]. Similar results were described for geckos attaching to hydrophilic surfaces underwater and in air while no significant decrease in attachment forces were measured on hydrophobic surfaces under dry and wet conditions [29].

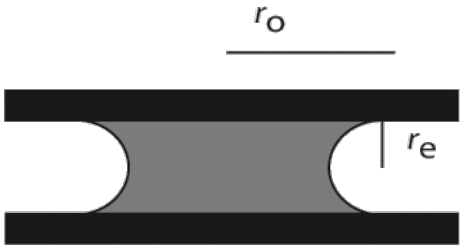

Figure 4: Two hydrophilic surfaces separated by water. Graph shows the location of the overall radius (r_o) of the wetted surface and the radius of the curved edge (r_e). The latter is half the thickness of the liquid.

Viscous forces and Stefan adhesion

In the late 1800's Stefan proposed a closed form solution to the problem of separating two rigid plates in a fluid [44]. If the plates are pulled away from each other in vertical direction, the fluid has to move inwards. Stefan's solution was expressed in terms of the time it would take to separate the plates to a particular distance given an applied force. Recasting this equation into the force domain shows that force is proportional to the fourth power of the radius of the plates, the viscosity of the fluid, the speed of separation and the inverse of the separation

distance. The equation for Stefan adhesion predicts very high forces for materials with the viscosity of mucus, but assumes rigid plates, and attempts to quantify the effect in limpets and tree frogs have yielded equivocal results [45,46]. It is clear that viscous forces play a role in the wet adhesion of tree frogs [46,47], and may also be important for some slugs or snails [3] or torrent frogs [30]. The application of Stefan's equation is not unproblematic for biological cases though, because it ignores the material properties of the surfaces and is limited to unrealistic shapes. Smooth, and rigid plates are not what we usually find in nature, and elastic and structured surfaces of different shape will show a different behaviour. Moreover, other effects can cause failure sooner than predicted by Stefan's equation. Under increasing stress, air bubbles in the viscous fluid can cause cavitation, which means that growing bubbles provide extra volume required for the plate separation [48]. Another process that causes instabilities is called air fingering, air moves in from the edge of the sample to the centre and by this brings the atmospheric pressure well into the sample [48]. These effects will be most important if the surrounding fluid is air. If the surrounding fluid is water instead, these effects are assumed to be different due to the incompressibility of water. Peeling is another component that can considerably reduce detachment force if the plates are not separated at right angle.

The low viscosity of air means that in terrestrial environments, it is hard to imagine an important contribution of viscosity. However, it is potentially very important where there is a secreted layer of fluid between the attachment organ and the surface in terrestrial systems. In aquatic systems viscous forces are obviously important due to the much higher viscosity of water compared to air. Moreover, the viscosity of the interstitial fluid might not be that of water because it is possible that some secreted mucus dictates the sliding force. The topic is further complicated by the fact that animals can secrete more than one material. Moreover, as the viscosity of the material increases there is a transition to glues. In particular, adhesive gels of gastropods can contain specific glue proteins with gel stiffening properties [49].

Determining the effects of compliant materials, irregular and divided surfaces, and non-convex surfaces should be a high priority for understanding aquatic adhesion. There has been considerable effort in the engineering world with regard to this area. In particular, the problems faced by tires on roads of varying roughness and wetness has driven the development of theories that may be applicable to biological systems [50,51]. These theories are difficult to assess in a biological context, but an examination of the parameters, surface roughness, substrate compliance, friction, and fluid properties, implies they will be useful. A further complication in water bears mention: The biofilm of fouled surfaces has a high effective viscosity and is also viscoelastic [26]. It is likely that an empirical understanding of viscous adhesion of animals to biofilms will have to be developed.

Glue

Many organisms use adhesive polymers to glue themselves to a substrate. Biological adhesives can vary widely in structure and capability, be remarkably complex and involve a large range of interactions and components with different functions [40]. The strength of the adhesive bond is determined by the biochemical nature of the adhesive secretion [52]. Many adhesives are non-specific and can adhere to many different types of substrates. Many of these glues form strong attachments under water, a process that is complicated by the difficulty in replacing water from the adhesive interface [40].

It is clear that the physico-chemical conditions are different under water than in air and therefore different kinds of glues are required. However, due to the complexity of the topic it is not possible to discuss these complex chemical issues in this review. Nevertheless, glue is probably the most common attachment mechanism in benthic marine animals, where the organisms are often exposed to strong currents in varying directions. Adhesives are used for long term fixation to the substrate, e.g., by mussels and barnacles [40], and glue is also used for temporary adhesion, e.g., in snails, flatworms and seastars [52,53]. For example, echinoderms and flatworms use a duo-gland system for attachment and detachment [16,54].

Many freshwater animals, such as molluscs and insect larvae, also use glue to attach to the substrate, often in running waters. For example black fly larvae place hooks in their secretion [22]. They are also able to secrete a sticky thread that helps them to reattach themselves again if swept away [55]. Some cased caddis larvae anchor their cases more or less permanently to the substrate with silk [56]. The invasive zebra mussel has become abundant on rocks and man-made structures in rivers and lakes in part because of its strong attachment by byssal threads [56-58] (Figure 5A).

Friction

Friction, the resistance developed when one surface is moved across another, is complex and we will touch only on the main principles here. Friction does not depend on the sliding speed, but in general, kinetic friction (friction during movement) is lower than static friction (friction until movement starts) [19]. Moreover, friction is independent of the nominal (apparent) contact area defined by the geometry of the body. Instead, the real contact area between the two surfaces matters. The real contact area is defined by topography, material properties and

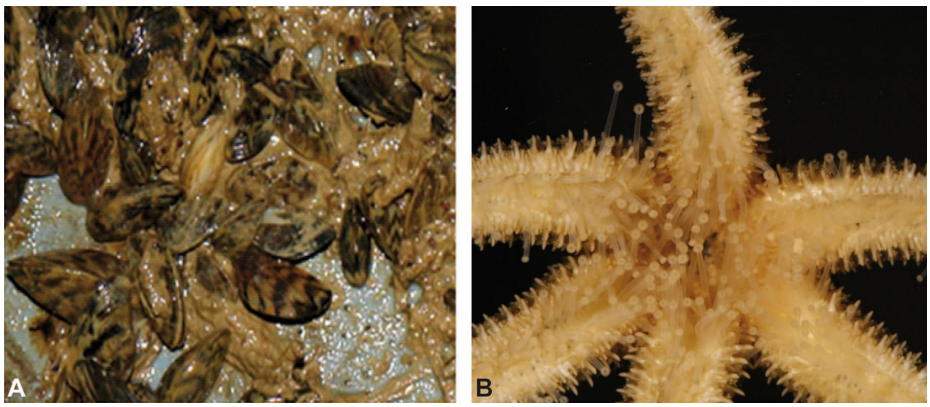

Figure 5: A) Zebra mussles attaching by byssal threads to a substrate, B) echinoderm foot (images: Petra Ditsche).

normal load. Normal load is the sum of external load and adhesion [59]. There is a close relationship between friction and adhesion, and solids with a high frictional coefficient usually have stronger adhesive properties [38].

In terrestrial systems, we can distinguish between two cases in which friction plays different roles in adhesion, namely dry and wet. Dry friction occurs between dry, clean surfaces in a very dry atmosphere. In this case, the friction force is usually proportional to the real contact area, as it is actually the force needed to shear the junctions formed between the surfaces in contact.

In contrast, in wet friction a film of water or another liquid is involved. This liquid can originate from humidity in the air or from secretion by the animal. Under such boundary lubrication conditions there is a constant contact between the surfaces and friction is defined by physico-chemical properties of the bonds formed between the molecules of the fluid and the solid surface. This includes capillary forces, which can contribute considerably if the liquid has a high surface tension like water.

If the surfaces are fully immersed in water, we have a case of full-film lubrication. The surfaces are completely separated by the fluid and friction is defined by the nominal surface area and the viscosity of the fluid that has to be sheared. Moreover, in this case the surface tension is zero and no capillary forces contribute to friction. Thus, friction under submerged conditions will usually be reduced compared to wet friction. Complicating matters, the animal may secrete a fluid or material that modifies the properties of water to either increase or decrease friction in this full-film regime. The specific impact on friction will depend on properties of the secretion, such as surface energy and viscosity. Some monolayer films separating two surfaces can also decrease friction dramatically when the surfaces are immersed under water [60]. Under certain conditions such as an insect stepping into a water drop or a water spider walking under water, mixed lubrication might occur. In this case, friction is a mixture of cases of full-film lubrication and boundary lubrication.

The growth of biofilms and fouling organisms on aquatic substrates can have a significant impact on friction. The decreased tenacity of Northern clingfish on fouled surfaces is explained by the lubricating effects of the slimy parts of the biofilm decreasing friction at the margins of the suction disc [27]. Friction is often combined with other attachment mechanisms, such as the just mentioned suction. Friction also contributes to mechanical attachment mechanisms such as hooks, clamps and spacers. Thorns and other protuberances found on the underside of many torrential insects can also increase friction with the substrate as well as an increased surface area of the animal contacting the substrate [56]. Specialized friction pads, which increase friction on smooth and most rough surfaces, can be found on the underside of the gill lamellae of some mayfly larvae [61] (Figure 6) and in torrent dwelling fishes.

Suction

The term sucker has been used for many attachment devices, so we want to clarify that we are just covering structures for which attachment is due to a difference between the pressure under the suction cup and the ambient pressure. In some cases this pressure difference is not the only factor in total attachment, as in cephalopods with hook-lined sucker disks.

Suckers are common in aquatic animals. In freshwater we can find true suckers, for example in some fish, leeches and Blephariceridae larvae. The latter live in torrential mountain streams and can resist very high currents (*Hapalothrix lugubris* withstand flow velocities of 4.5 m/s) and generate attachment forces up to 8.4 g per sucker, which equals about 84 mN [36].

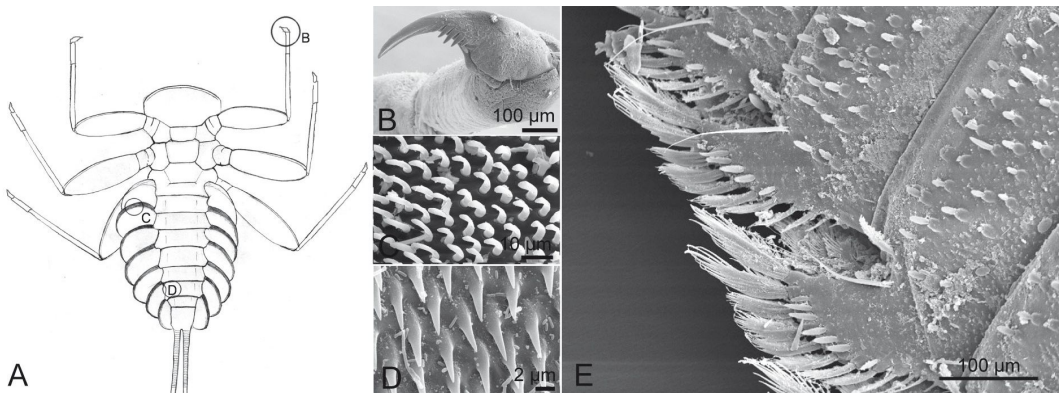

Figure 6: (A–D) Attachment devices of *E. assimilis* larvae: (A) ventral view, (B) claw of the foreleg, (C) setae of the pads on the ventral side of the gill lamellae, (D) areas with spiky acanthae on the lateral parts of the abdominal sternits. Reproduced with permission from [26]; (E) Structure on the distal edge of the ventral side of the beetle larva *Elmis* sp. Reproduced from [18].

Gobiies, balitorid loaches and loricariid catfishes also have specialized suction discs, which help them to stay in place in the high-speed currents in stream environments [62-64]. Some gobies are even able to climb waterfalls by using a pelvic fin derived suction disc [63,65]. Moreover, lampreys are able to climb waterfalls with an oral sucker [66]. In marine systems, for example octopus, limpets and several lineages of fish have suction cups [67-69]. Clingfish (Figure 7), shark suckers, snailfish and lumpsuckers are marine taxa with a dedicated suctorial disc [37,70,71].

In comparison to suction cups working in air, one of the most important differences is the incompressibility of water. Therefore, the volume of the water filled cavity will not change measurably (Figure 8). While pressures lower than a vacuum are not possible in air, this is possible if the suction cup is filled with water. For a vacuum (0 MPa) the tenacity developed at a maximal pressure difference would be 0.1 MPa at sea level.

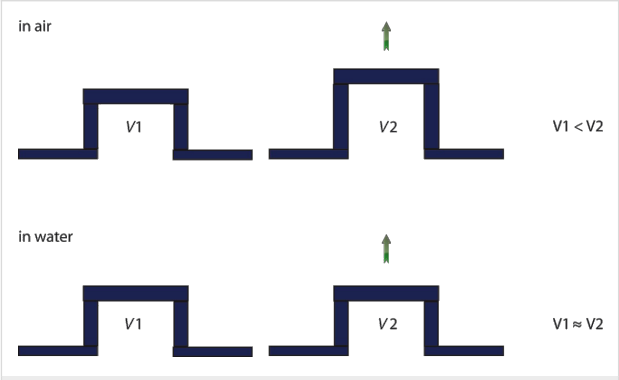

Figure 8: In air the volume of the cavity of suction cups increases. Due to the incompressibility of water the volume of suction cups stays the same while working under water.

However, the pressure measured under an octopus sucker went negative in 35% of the cases and the lowest pressure measured was 0.168 MPa [72]. The same study shows that seawater can

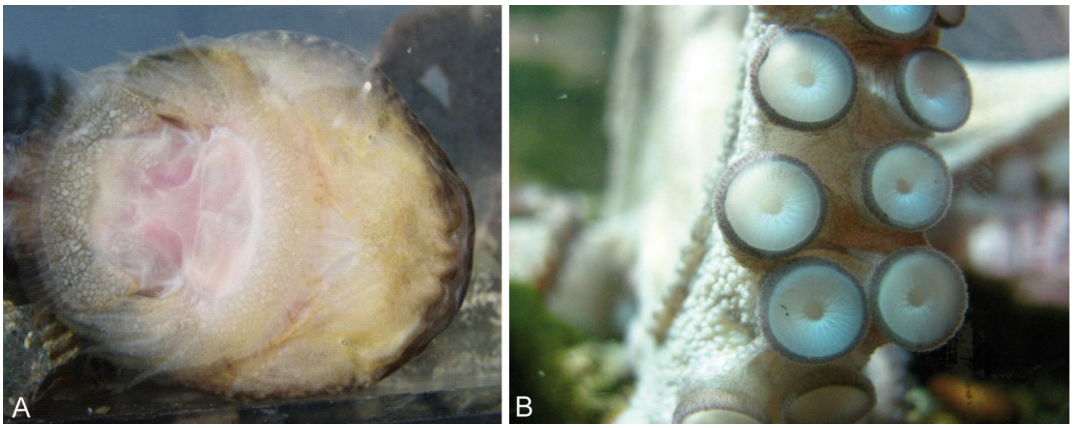

Figure 7: (A) Suction disc on the ventral side of Northern clingfish. Reproduced with permission from [27]. (B) Multiple suction discs on an octopus arm (image: Francesca Tramacere).

sustain negative pressure, but the values are not as low as for pure water. Particles and microbubbles in the seawater provide nucleating sites that stabilize the growth of larger gas bubbles [72]. Suction also depends on the surface energy of the substrate, as no negative pressures were found on non-wettable surfaces [68,72]. Many superhydrophobic surfaces are known for their ability to hold an air film under water for a varying time span [73-75]. Therefore, these surfaces could hold micro bubbles that serve as cavitation nucleating sites as in seawater. Whether this effect would occur after a long-time exposure of the substrates or at higher pressure has not been resolved. Ambient pressure also has an impact on cavitation [76]. It is possible that extremely high pressures can reduce the cavitation threshold, but this is just likely to matter at great depth.

The attachment force of the sucker (F_s) is determined by the pressure difference (ΔP) and the area (A) of the suction cup:

$$F_s = \Delta P \cdot A \tag{8}$$

For animals living far below the water surface the increasing pressure will also cause a different situation. As the hydrostatic pressure increases 0.100 MPa per 10 m depth, the possible pressure difference between the lower side of the suction cup and its environment increases. Thus, the theoretically possible attachment force increases as well simply by living in deeper aquatic regions (Figure 9). However, other factors such as limits of the muscles creating the pressure difference under the suction cup, and the ability to seal the edges of the suction disc will also influence the pressure difference. This explains why limpets show some effect of pressure on attachment but far less than theory would predict [35]. In contrast, the very strong suckers of some decapods are able to take advantage of the high pressure difference in deeper aquatic regions and pressure differences up to 0.83 MPa were measured. Such suckers are limited by cavitation of seawater at sea level, tenacity will increase with depth until a limit determined through morphology is reached [76]. The disc margin is often adorned with hairy structures, extremely soft tissue or secretions that serve to fix the edges of the disc as a dislodging force is applied [2,36,69].

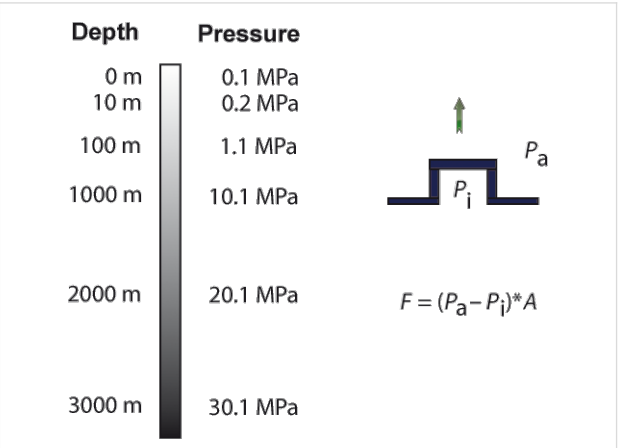

Figure 9: The pressure difference of the cavity under the suction cup and its environment determines the maximal possible suction force. As the pressure increases with water depth the theoretically maximal possible suction force increases with water depth as well.

Suckers typically work well on smooth substrates [19,56,77] because a seal between the disc margin and the substrate is more difficult to achieve on a rough surface. However, in some aquatic systems suckers develop higher tenacities on rough surfaces than on smooth ones [35,37]. The size of the suction disc has also a significant impact on the maximum roughness of the substrate to which it can attach [27].

Mechanical principles of fixation: hook, lock, clamp and spacer

Though in broad strokes there should be little difference in the performance of these mechanical means of attachment in the two environments discussed here, there are some subtle but potentially powerful effects that should be considered. Since friction between the contacting surfaces contributes to the attachment forces, there could be quite different forces when the entire system is submerged simply because of the effect of a water film on friction. And, related to attachment force, it might take substantially more force to form an attachment in the aquatic environment because the viscosity and density of water make it harder to bring surfaces into close apposition.

Most arthropods living in flowing water have well-developed tarsal claws, with which they hold onto rough surfaces [56]. These claws show a variety of different shapes and sizes (Figure 10) and are the most common attachment devices of aquatic macroinvertebrates in both running and still water [78]. The larvae of some taxa, such as mayflies and caddis larvae usually bear one claw at their tarsi, while many others like stoneflies or several aquatic beetles have two tarsal claws (Figure 10). Double claws might act in the same direction or in accordance to the clamp principle (or something intermediate). Free-living caddis larvae like *Rhyacophila* have additional claws like grapples on their posterior prolegs. Circlets of outwardly directed hooks imply the spacer principle. They occur on the prolegs in larvae of several Diptera taxa such as Chironomidae, Diamesinae, Simuliidae and Deuterophlebiidae [79]. While the hook circlets of the Simuliidae are only engaged in secreted silk mats, those of the Deuterophlebiidae are used directly on the stones. In contrast to the clamp mechanism, in the spacer principle the hooks press outwardly directed. The lock principle is not very suitable for attachment to substrates as it needs two specialized surfaces, but very common for the

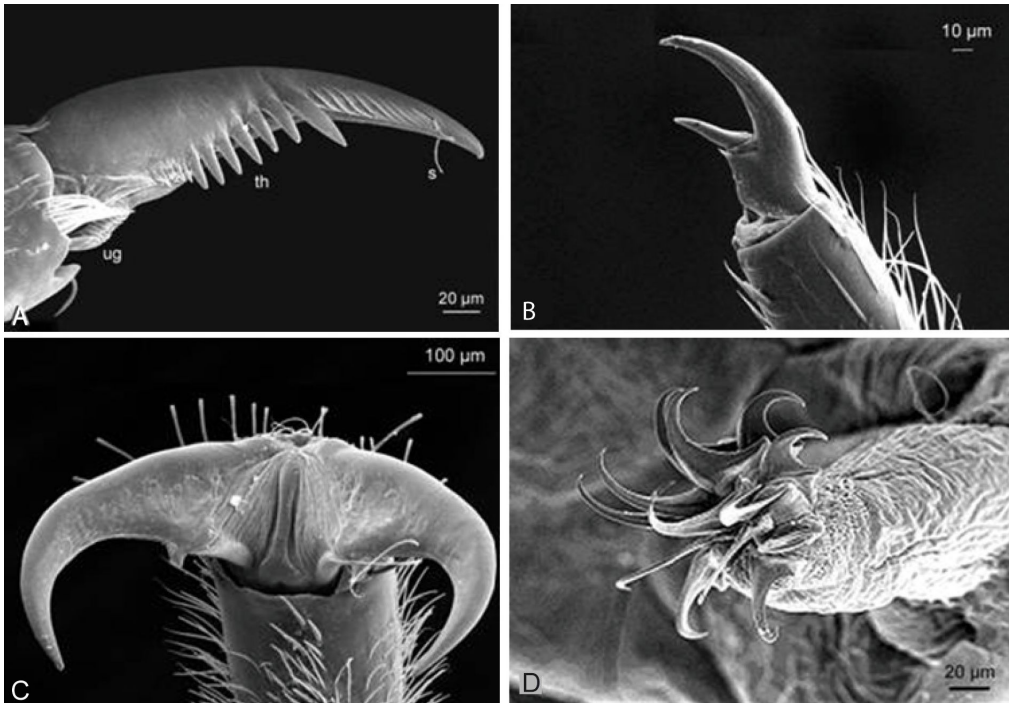

Figure 10: A) Tarsal claw of the mayfly larva *Baetis vardarensis.* Abreviations: ug unguitractor, th theeth, s sensilla. B) Tarsal claw of the second leg of caddies larva from *Rhyacophila sp.* dorsalis group, C) Double claws of the stream stonefly larva *Perla marginata*, D) Circlet of hooks on the proleg of a Chironomidae larva. Reproduced from [18].

connection of body parts or during copulation [2]. In marine environment claws are found in many arthropods.

While the immersion itself does not show considerable effect on mechanical interlocking principles, the secondary effect of the fouling of aquatic surfaces can cause a significant impact on attachment. On smooth substrates a biofilm cover can even increase friction forces of claws [26]. The claws can pierce the gel like part of the biofilm and interlock inside with attached organisms of the biofilm. Moreover, the higher viscosity of the biofilm gives additional resistance. In contrast, on rough substrates the opposite effect takes place [26]. Here the lubricating effect of the gel like part of the biofilm that separates the substrate and the claw dominates.

Conclusion

Attachment in the aquatic realm is not just quantitatively different from that on land, but it is qualitatively different. Completely different phenomena are responsible for the most significant dislodgement and attachment forces under each of the two conditions. The constraints on attachment, and the opportunities offered by secure attachment, are different in the two realms and will require very different approaches to systematizing and characterizing biological diversity with respect to this parameter. Many open questions remain with regard to aquatic attachment, and some can be approached by comparing the more thoroughly studied terrestrial environment.

A major impediment to systematizing attachment performance across environments is the lack of standardization of methods and the difficulty of scaling up small experimental units to the performance of the whole animal. We suggest that as research in this area progresses it would be very useful to make raw data accessible in open source outlets so that derived performance parameters can be computed ex post facto as theoretical models and technology improve. It is particularly important to broaden the knowledge base about the performance of animals as a whole, because this is what is evolutionarily selected over time and what will lead to the most immediate ecological insights.

Size effects on attachment, especially in the submerged case, might provide key insights into selective pressures and may yield clarity regarding the ecology of the organism. Paying attention to the scaling of detachment forces, for example, leads to some questions worth pursuing. Gravity and inertia dominate the dry world while lift and drag rule the water currents. Forces due to gravity scale with mass and, therefore, also with the cube of length, while those from lift and drag are scaling with the square of length. Do aquatic organisms have no size constraints because the effects of gravity are ruled out by lift and drag? Are

the biggest attached organisms aquatic? Indeed, some benthic animals such as the giant sea star *Pisaster giganteus* can become very large. However, the topic is complicated by other factors influencing the magnitude of the detachment forces. First, in wave-swept environments, the acceleration reaction force can be high and as it depends on the volume, it scales with the cube of length as well. This is assumed to be one reason why organisms inhabiting the marine intertidal region are often small compared to the ones living in the subtidal region, where waves are less pronounced [80]. Second, if benthic animals are small enough to reside in the boundary layer, which develops over the surface of substrates, they might take advantage of the reduced flow velocity close to the substrate. Thus, being very small might be of advantage under certain circumstances, for instance in high-flow-rate streams [81-83]. Actually, most macrozoobenthos organisms in streams are very small, even considerably smaller than the macrozobenthos of the marine intertidal. Third, flow forces acting on an animal depend on the flow velocity, which can show huge variations between different habitats and even inside the same habitat. Fourth, the shape and other properties (such as elasticity) of the animal also strongly influences drag and lift forces. Even more complicated, their effect on the different flow forces can vary. For example, a shape that reduces drag does not necessarily reduce lift and vice versa. Moreover, the behavior and way of living of an animal strongly influence the detachment forces acting on it. Beside mechanical factors also biological factors can limit the size of organisms [84].

Another interesting point regarding size is the relation of the animal size to the maximal possible attachment forces. Our calculation showed that for the same hypothetical animal much higher detachment forces could occur in aquatic systems at high flow velocities (Table 3). Therefore, the question arises, whether the highest attachment forces in relation to the body size occur in aquatic systems. To test this idea we need a more complete picture of size parameters than is often reported.

A most intriguing aspect of this review is the demonstration that we need better understanding of viscosity-mediated attachment. Viscous adhesion is clearly important to the real, biologically messy, and sometimes mucus-laden real world, but the underlying processes are not fully understood for submerged cases. The community needs useful theoretical models that account for the compliance of the substrate and the attachment organ, the surface energies and the shapes of real world examples of attachment.

Submerged organisms must cope with water and also with ubiquitous biofilms. The complexities of a pure liquid pale in comparison to the presumably non-Newtonian behaviour of this viscoelastic polymer, adherent to virtually every submerged surface. The effect must depend on the type of the attachment device, and also with the thickness and composition of biofilms. This complicates real world performance measures, but the issue must be faced sooner rather than later if we are to put attachment in an ecological context in the aquatic world. Early investigations in this area demonstrate the complexity of the interaction between attachment organ and substrate, with examples of increases and decreases in tenacity with biofilm growths.

We are working in an age of unmatched technology for imaging and experimentation, with a rapidly diminishing core of natural historians [85]. The investigation of aquatic adhesion is going to be successful as disparate fields examine the same problems, and first hand observation of nature becomes more valuable not less. This review should serve as a call not only for better theory or experimentation, but for a more complete, thorough and detailed observation of the attachment phenomenon in a natural setting.

References

1. Nachtigall, W. *Biological Mechanisms of Attachment;* Springer-Verlag: New York, Heidelberg, 1974. doi:10.1007/978-3-642-85775-1
2. Gorb, S. N. *Philos. Trans. R. Soc., A* **2008,** *366,* 1557–1574. doi:10.1098/rsta.2007.2172
3. Vogel, S. *Comparative Biomechanics - Life's physical word;* Princeton University Press, 2003.
4. Vogel, S. *Life in Moving Fluids,* 2nd ed.; Princeton University Press, 1994.
5. Denny, M. W. *Air and water: The biology and physics of life's media;* Pinceton University Press, 1995.
6. Vogel, S. J. *J. Biosci.* **2005,** *30,* 303–312. doi:10.1007/BF02703667
7. Bell, E. C.; Gosline, J. M. *Mar. Ecol.: Prog. Ser.* **1997,** *159,* 197–208. doi:10.3354/meps159197
8. Statzner, B. *Int. Rev. Hydrobiol.* **2008,** *93,* 593–605. doi:10.1002/iroh.200711018
9. Koehl, M. *Sci. Am.* **1982,** *247,* 124–134. doi:10.1038/scientificamerican1282-124
10. Daniel, T. L. *Am. Zool.* **1984,** *24,* 121–134. doi:10.1093/icb/24.1.121
11. Koehl, M. A. R. *Am. Zool.* **1984,** *24,* 57–70. doi:10.1093/icb/24.1.57
12. Gaylord, B. *Limnol. Oceanogr.* **2000,** *45,* 174–188. doi:10.4319/lo.2000.45.1.0174
13. Denny, M. *J. Exp. Biol.* **1994,** *194,* 97–115.
14. Legendre, D.; Colin, C.; Coquard, T. *Philos. Trans. R. Soc., A* **2008,** *366,* 2233–2248. doi:10.1098/rsta.2008.0009
15. Del Campo, A.; Schwotzer, W.; Gorb, S. N.; Aldred, N.; Santos, R.; Flammang, P. Preface. In *Biological and Biomimetic Adhesives, Challenges and Opportunities;* Santos, R.; Aldred, N.; Gorb, S.; Flammang, P., Eds.; The Royal Society of Chemistry: Cambridge, UK, 2013; vii–xvi. doi:10.1039/9781849737135-FP007
16. Flammang, P. Adhesive Secretion in Echinoderms: An Overview. In *Biological Adhesives;* Smith, A. M.; Callow, J. A., Eds.; Springer-Verlag: Heidelberg, Germany, 2006; pp 183–206. doi:10.1007/978-3-540-31049-5_10

17. Scherge, M.; Gorb, S. N. *Biological Micro- and Nanotribology;* Springer-Verlag: Heidelberg, Germany, 2001. doi:10.1007/978-3-662-04431-5
18. Ditsche-Kuru, P. Influence of the surface roughness of hard substrates on the attachment of selected running water macrozoobenthos. Ph.D. Thesis, Rheinische Friedrich-Wilhelms-Universität, Bonn, Bonn, Germany, 2009.
19. Gorb, S. N. *Attachment Devices of Insect Cuticle;* Kluwer Academic: Dordrecht, Netherlands, 2001.
20. Bao, W.-Y.; Satuito, C. G.; Yang, J.-L.; Kitamura, H. *Mar. Biol.* **2007,** *150,* 565–574. doi:10.1007/s00227-006-0383-4
21. Hadfield, M. G. *Annu. Rev. Mar. Sci.* **2011,** *3,* 453–470. doi:10.1146/annurev-marine-120709-142753
22. Kiel, E. *Limnologica* **2001,** *31,* 179–183. doi:10.1016/S0075-9511(01)80018-9
23. Kitamura, H.; Hirayama, K. *Nippon Suisan Gakkaishi* **1987,** *53,* 1377–1381. doi:10.2331/suisan.53.1377
24. Kitamura, H.; Kitahara, S.; Koh, H. B. *Mar. Biol.* **1993,** *115,* 387–392. doi:10.1007/BF00349836
25. Maki, J. S.; Ding, L.; Stokes, J.; Kavouras, J. H.; Rittschof, D. *Biofouling* **2000,** *16,* 159–170. doi:10.1080/08927010009378441
26. Ditsche, P.; Michels, J.; Kovalev, A.; Koop, J.; Gorb, S. *J. R. Soc., Interface* **2014,** *11,* 20130989. doi:10.1098/rsif.2013.0989
27. Ditsche, P.; Wainwright, D. K.; Summers, A. P. *J. Exp. Biol.* **2014,** *217,* 2548–2554. doi:10.1242/jeb.100149
28. Maki, J. S.; Rittschof, D.; Schmidt, A. R.; Snyder, A. G.; Island, P.; Carolina, N. *Biol. Bull.* **1989,** *177,* 295–302. doi:10.2307/1541944
29. Stark, A. Y.; Badge, I.; Wucinich, N. A.; Sullivan, T. W.; Niewiarowski, P. H.; Dhinojwala, A. *Proc. Natl. Acad. Sci. U. S. A.* **2013,** *110,* 6340–6345. doi:10.1073/pnas.1219317110
30. Endlein, T.; Barnes, W. J. P.; Samuel, D. S.; Crawford, N. A.; Biaw, A. B.; Grafe, U. *PLoS One* **2013,** *8,* e73810. doi:10.1371/journal.pone.0073810
31. Dougherty, W. J. *J. Crustacean Biol.* **1990,** *10,* 469–478. doi:10.2307/1548336
32. Grenon, J.-F.; Walker, G. *J. Exp. Mar. Biol. Ecol.* **1981,** *54,* 277–308. doi:10.1016/0022-0981(81)90162-3
33. Eymann, M. *J. North Am. Benthological Soc.* **1988,** *7,* 109–116. doi:10.2307/1467916
34. Waite, J. H. *Integr. Comp. Biol.* **2002,** *42,* 1172–1180. doi:10.1093/icb/42.6.1172
35. Smith, A. M.; Kier, W. M.; Johnsen, S. *Biol. Bull.* **1993,** *184,* 338–341. doi:10.2307/1542452
36. Frutiger, A. *Freshwater Biol.* **2002,** *47,* 293–302. doi:10.1046/j.1365-2427.2002.00814.x
37. Wainwright, D. K.; Kleinteich, T.; Kleinteich, A.; Gorb, S. N.; Summers, A. P. *Biol. Lett.* **2013,** *9,* 20130234. doi:10.1098/rsbl.2013.0234
38. Bowden, F. P.; Tabor, D. *The Friction and Lubrication of Solids;* Clarendon Press: Oxford, UK, 1986; Vol. 1.
39. Federle, W.; Baumgartner, W.; Hölldobler, B. *J. Exp. Biol.* **2004,** *207,* 67–74. doi:10.1242/jeb.00716
40. Smith, A. M.; Callow, J. A. *Biological Adhesives;* Springer-Verlag: Heidelberg, Germany, 2006. doi:10.1007/978-3-540-31049-5
41. Kendall, K. *Science* **1994,** *263,* 1720–1725. doi:10.1126/science.263.5154.1720
42. Varenberg, M.; Gorb, S. *J. R. Soc., Interface* **2008,** *5,* 383–385. doi:10.1098/rsif.2007.1171
43. Hosoda, N.; Gorb, S. N. *Proc. R. Soc. London, Ser. B* **2012,** *279,* 4236–4242. doi:10.1098/rspb.2012.1297
44. Stefan, J. Versuche zur scheinbaren Adhesion. In *Annalen der Physik und Chemie;* Poggenorf, J. J., Ed.; Verlag von Johan Ambrosius Barth: Leipzig, Germany, 1875; Vol. 154, pp 316–318.
45. Smith, A. M. *Integr. Comp. Biol.* **2002,** *42,* 1164–1171. doi:10.1093/icb/42.6.1164
46. Barnes, W. J. P.; Oines, C.; Smith, J. M. *J. Comp. Physiol., A* **2006,** *192,* 1179–1191. doi:10.1007/s00359-006-0146-1
47. Hanna, G.; Barnes, W. J. *J. Exp. Biol.* **1991,** *155,* 103–125.
48. Gay, C. *Integr. Comp. Biol.* **2002,** *42,* 1123–1126. doi:10.1093/icb/42.6.1123
49. Smith, A. M. The biochemistry and mechanics of Gastropod adhesive gels. In *Biological Adhesives;* Smith, A. M.; Callow, J. A., Eds.; Springer-Verlag: Heidelberg, Germany, 2006; pp 167–182. doi:10.1007/978-3-540-31049-5_9
50. Persson, B. N. J. *Eur. Phys. J. E* **2002,** *8,* 385–401. doi:10.1140/epje/i2002-10025-1
51. Persson, B. N. J.; Albohr, O.; Tartaglino, U.; Volokitin, A. I.; Tosatti, E. *J. Phys.: Condens. Matter* **2005,** *17,* 1–82. doi:10.1088/0953-8984/17/1/R01
52. Dodou, D.; Breedveld, P.; de Winter, J. C. F.; Dankelman, J.; van Leeuwen, J. L. *Biol. Rev. Cambridge Philos. Soc.* **2011,** *86,* 15–32. doi:10.1111/j.1469-185X.2010.00132.x
53. Hermans, C. O. *Oceanogr. Mar. Biol.* **1983,** *21,* 283–339.
54. Egger, B.; Ladurner, P.; Nimeth, K.; Gschwentner, R.; Rieger, R. *Dev. Genes Evol.* **2006,** *216,* 565–577. doi:10.1007/s00427-006-0069-4
55. Wotton, R. S. *Aquat. Insects* **1986,** *8,* 255–261. doi:10.1080/01650428609361259
56. Hynes, H. B. N. *The ecology of running waters;* Liverpool University Press: Liverpool, United Kingdom, 1970.
57. Crisp, D. J.; Walker, G.; Young, G. A.; Yule, A. B. *J. Colloid Interface Sci.* **1985,** *104,* 40–50. doi:10.1016/0021-9797(85)90007-4
58. Anderson, K. E.; Waite, J. H. *J. Exp. Biol.* **2000,** *203,* 3065–3076.
59. Czichos, H. *Tribology: a systems approach to the science and technology of friction, lubrication and wear;* Elsevier: Amsterdam, Netherlands, 1978.
60. Briscoe, W. H.; Titmuss, S.; Tiberg, F.; Thomas, R. K.; McGillivray, D. J.; Klein, J. *Nature* **2006,** *444,* 191–194. doi:10.1038/nature05196
61. Ditsche-Kuru, P.; Koop, J. H. E.; Gorb, S. N. *J. Exp. Biol.* **2010,** *213,* 1950–1959. doi:10.1242/jeb.037218
62. Gerstner, C. L. *Can. J. Zool.* **2007,** *85,* 133–140. doi:10.1139/z06-199
63. Maie, T.; Schoenfuss, H. L.; Blob, R. W. *J. Exp. Biol.* **2012,** *215,* 3925–3936. doi:10.1242/jeb.072967
64. Roberts, T. R. *Raffles Bull. Zool.* **1998,** *46,* 271–288.
65. Schoenfuss, H. L.; Blob, R. W. *J. Zool.* **2006,** *261,* 191–205. doi:10.1017/S0952836903004102
66. Reinhardt, U. G.; Eidietis, L.; Friedl, S. E.; Moser, M. L. *Can. J. Zool.* **2008,** *86,* 1264–1272. doi:10.1139/Z08-112
67. Kier, W. M.; Smith, A. M. *Integr. Comp. Biol.* **2002,** *42,* 1146–1153. doi:10.1093/icb/42.6.1146
68. Smith, A. M. *J. Exp. Biol.* **1991,** *161,* 151–169.
69. Tramacere, F.; Beccai, L.; Kuba, M.; Gozzi, A.; Bifone, A.; Mazzolai, B. *PLoS One* **2013,** *8,* e65074. doi:10.1371/journal.pone.0065074
70. Arita, G. S. A comparative study of the structure and function of the adhesive apparatus of the Cyclopteridae and Gobiesocidae. Masterthesis, University of British Columbia, Canada, 1962.
71. Budney, L. A.; Hall, B. K. *J. Appl. Ichthyol.* **2010,** *26,* 167–175. doi:10.1111/j.1439-0426.2010.01398.x

72. Smith, A. M. *J. Exp. Biol.* **1991,** *157,* 257–271.
73. Balasubramanian, A. K.; Miller, A. C.; Rediniotis, O. K. *AIAA J.* **2004,** *42,* 411–414. doi:10.2514/1.9104
74. Barthlott, W.; Schimmel, T.; Wiersch, S.; Koch, K.; Brede, M.; Barczewski, M.; Wahlheim, S.; Weis, A.; Kaltenmeier, A.; Leder, A.; Bohn, H. F. *Adv. Mater.* **2010,** *22,* 2325–2328. doi:10.1002/adma.200904411
75. Balmert, A.; Bohn, H. F.; Ditsche-Kuru, P.; Barthlott, W. *J. Morphol.* **2011,** *272,* 442–451. doi:10.1002/jmor.10921
76. Smith, A. M. *J. Exp. Biol.* **1996,** *199,* 949–958.
77. Nachtigall, W. *Biological Mechanisms of Attachment;* Springer-Verlag: New York, Heidelberg, 1974. doi:10.1007/978-3-642-85775-1
78. Ditsche-Kuru, P.; Barthlott, W.; Koop, J. H. E. *Zoology* **2012,** *115,* 379–388.
79. Allan, J. D. *Stream Ecology-Structure and function of running waters;* Chapman & Hall: New York, NY, USA, 1995. doi:10.1007/978-94-011-0729-7
80. Denny, M. W.; Daniel, T. L.; Koehl, M. A. R. *Ecol. Monogr.* **1985,** *55,* 69–102. doi:10.2307/1942526
81. Steinmann, P. Die Tierwelt der Gebirgsbäche: eine faunistisch-biologische Studie. Ph.D. Thesis, University of Basel, Basel, Switzerland, 1907.
82. Ambühl, H. *Schweiz. Z. Hydrol.* **1959,** *21,* 133–264. doi:10.1007/BF02505455
83. Nachtigall, W. *Biol. Unserer Zeit* **2000,** *30,* 148–157. doi:10.1002/(SICI)1521-415X(200003)30:3<148::AID-BIUZ148>3.0.CO;2-F
84. Denny, M. *J. Exp. Biol.* **1999,** *202,* 3463–3467.
85. Tewksbury, J. J.; Anderson, J. G. T.; Bakker, J. D.; Billo, T. J.; Dunwiddie, P. W.; Groom, M. J.; Hampton, S. E.; Herman, S. G.; Levey, D. J.; Machnicki, N. J.; del Rio, C. M.; Power, M. E.; Rowell, K.; Salomon, A. K.; Stacey, L.; Trombulak, S. C.; Wheeler, T. A. *BioScience* **2014,** *64,* 300–310. doi:10.1093/biosci/biu032

License and Terms

BEILSTEIN JOURNAL OF NANOTECHNOLOGY

The capillary adhesion technique: a versatile method for determining the liquid adhesion force and sample stiffness

Daniel Gandyra[1], Stefan Walheim[*1], Stanislav Gorb[2], Wilhelm Barthlott[3] and Thomas Schimmel[*1,4]

Full Research Paper

Open Access

Address:
[1]Institute of Applied Physics and Center for Functional Nanostructures (CFN), Karlsruhe Institute of Technology (KIT), 76128 Karlsruhe, Germany, [2]Zoological Institute, University of Kiel, 24118 Kiel, Germany, [3]Nees Institute for Biodiversity of Plants, University of Bonn, 53115 Bonn, Germany, and [4]Institute of Nanotechnology (INT), Karlsruhe Institute of Technology (KIT), 76021 Karlsruhe, Germany

Email:
Stefan Walheim[*] - stefan.walheim@kit.edu; Thomas Schimmel[*] - thomas.schimmel@kit.edu

* Corresponding author

Keywords:
adhesion; AFM cantilever; air layer; capillary forces; hairs; measurement; micromechanical systems; microstructures; Salvinia effect; *Salvinia molesta*; sensors; stiffness; superhydrophobic surfaces

Beilstein J. Nanotechnol. **2015,** *6,* 11–18.
doi:10.3762/bjnano.6.2

Received: 12 September 2014
Accepted: 21 November 2014
Published: 02 January 2015

This article is part of the Thematic Series "Biological and bioinspired adhesion and friction".

Associate Editor: K. Koch

Abstract

We report a novel, practical technique for the concerted, simultaneous determination of both the adhesion force of a small structure or structural unit (e.g., an individual filament, hair, micromechanical component or microsensor) to a liquid and its elastic properties. The method involves the creation and development of a liquid meniscus upon touching a liquid surface with the structure, and the subsequent disruption of this liquid meniscus upon removal. The evaluation of the meniscus shape immediately before snap-off of the meniscus allows the quantitative determination of the liquid adhesion force. Concurrently, by measuring and evaluating the deformation of the structure under investigation, its elastic properties can be determined. The sensitivity of the method is remarkably high, practically limited by the resolution of the camera capturing the process. Adhesion forces down to 10 μN and spring constants up to 2 N/m were measured. Three exemplary applications of this method are demonstrated: (1) determination of the water adhesion force and the elasticity of individual hairs (trichomes) of the floating fern *Salvinia molesta*. (2) The investigation of human head hairs both with and without functional surface coatings (a topic of high relevance in the field of hair cosmetics) was performed. The method also resulted in the measurement of an elastic modulus (Young's modulus) for individual hairs of 3.0×10^5 N/cm^2, which is within the typical range known for human hair. (3) Finally, the accuracy and validity of the capillary adhesion technique was proven by examining calibrated atomic force microscopy cantilevers, reproducing the spring constants calibrated using other methods.

Introduction

Surface outgrowths such as hairs or trichomes, which widely occur on biological surfaces, sometimes have unique adhesive and elastic properties optimally adapted to specific functional requirements. As these are often mimicked in technical applications, their characterization is of great interest in a biomimetic approach. Prominent examples are the trichomes of the floating fern *Salvinia molesta*, which are responsible for the high air layer persistence of its leaves under water [1-3]. Artificial surfaces capable of retaining air under water have great potential in fluid transportation or as ship hull coatings [4,5] because of the significant drag reduction [6-12]. However, an essential requirement for the functionality of these surfaces is the persistence of the air layer [13-15]. As all of the highly engineered surfaces developed to date have failed in this respect [9-12], it is interesting to study the properties of the hairs of *Salvinia molesta* as a model for future developments. The key factors are the high water adhesion of the trichome tips (the "Salvinia effect", [1]) and the high elasticity of the trichomes [2,3], which allows the pinning of the air–water interface by the trichome tips which hold it under perturbations without the loss of air by bubble formation.

Although the adhesive force of small elastic structures play a key role in understanding biological and biomimetic structures (as well as sensors, micromechanical or microfluidic systems), the precise, simultaneous measurement of both the elastic and the adhesive properties of small mechanical systems is not trivial. Here, we present a novel technique, the capillary adhesion technique (CAT), for the combined determination of the adhesion force of a single small structural entity to a liquid and its elastic properties. Capillary bridges were thoroughly studied with respect to kinetics and geometry dependence, in addition to the investigation and discussion of the contact angle and the related capillary length. The nucleation radius and growth of the liquid meniscus pulled from a flat surface were studied by Debregeas et al. [16]. The contact angle and contact angle hysteresis measurements on a curved surface (lens) pulling away from a meniscus were used to determine the advancing and receding contact angle of different solid materials [17] and the dynamics of this formation process [18]. Furthermore, the normal force of capillary bridges between solid objects was investigated [19].

Here, we create a meniscus from a flat, water surface until rupture occurs in order to determine the adhesion force using a simple energetic approach: the first derivative of the added surface energy of the meniscus with respect to the pulling direction. Using this method, we have investigated the hairs (trichomes) of *Salvinia molesta* and obtained precise values for the water adhesion force of the trichome tip and for the trichome elasticity. These data can now be used as a guideline for the design of biomimetic surfaces. To demonstrate the wide range of applications of this method, we also investigated human head hairs as a second example. Finally, calibrated atomic force microscopy (AFM) cantilevers were tested as a representative for an artificial micromechanical system, which at the same time allowed us to prove the validity and accuracy of the method.

Results and Discussion

The capillary adhesion technique (CAT)

The capillary adhesion technique differs substantially from common methods using various force sensors [20-23]. The principle is shown in Figure 1. A single small structure, here a trichome of the floating fern *Salvinia molesta*, is fixed at its base with reverse action tweezers. The tweezers are fixed on a stepper motor with the trichome tip facing downwards. Then, the tip is brought into contact with the surface of a liquid, here, water. When the trichome is pulled upwards, a meniscus is developed, which is eventually released when its tensile force exceeds the water adhesion force of the trichome tip. A constant pulling velocity of 120 µm/s was used. The pulling process is captured with a CCD camera, allowing the monitoring of both the meniscus shape and the deformation of the structure (here, the trichome) under investigation.

Based on the image shortly before the meniscus snap-off, the profile of the meniscus can be fitted with an elliptic function:

$$y(x) = -\frac{b}{a}\sqrt{a^2 - \left(x - a - \frac{c}{2}\right)^2} + b, \qquad (1)$$

with parameters a, b and c as shown in Figure 2. The nature of the visual assessment of these parameters leads to a certain systematic error in the resulting adhesion force and elasticity values, which is essentially determined by the resolution of the CCD camera. The CCD camera resolution was 768 × 576 pixels. When the function $y(x)$ is rotated around the y-axis, the rotationally symmetric shape of the meniscus in three dimensions can be modelled, which leads to the calculation of the resulting surface area [24] of the water meniscus as:

$$A = 2\pi\int_0^b x(y)\sqrt{1 + \left(x'(y)\right)^2}\,dy. \qquad (2)$$

Wolfram Mathematica software was used for the calculations. To form the meniscus, beginning with the originally flat surface before capillary contact, a minimum energy of

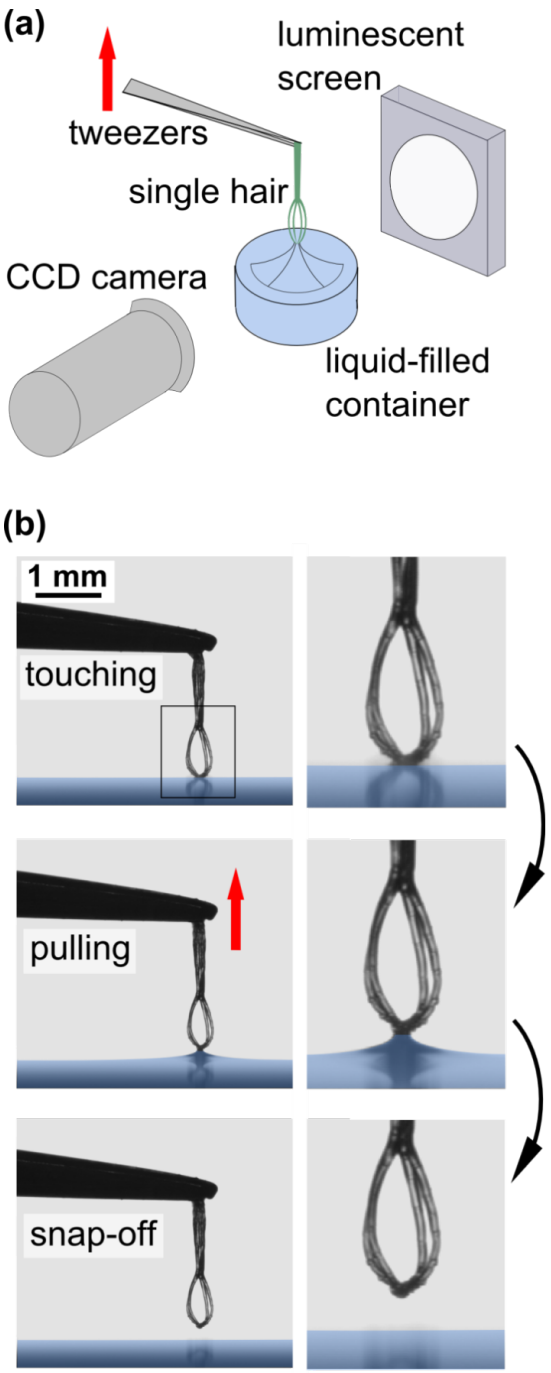

Figure 1: Description of the experimental method. (a) The experimental setup: A small elastic entity, in this case a hair (trichome) of *Salvinia molesta*, is placed between a luminescent screen and a CCD camera above a container filled with liquid. Using reverse action tweezers fixed on a stepper motor, the trichome is vertically descended onto the surface of the liquid (water). (b) After touching the liquid, the subsequent removal of the hair results in the formation of a meniscus. As the tip is pulled upwards, the meniscus eventually snaps off. The geometry of the mensicus immediately before snap-off (i.e., rupture of the meniscus) and the deformation of the trichome are recorded and evaluated.

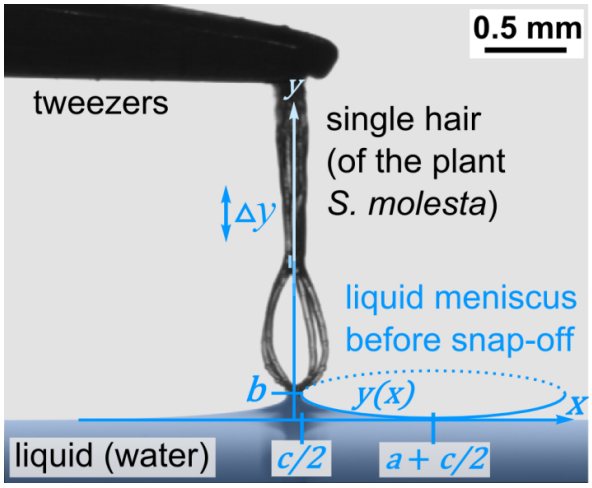

Figure 2: Meniscus immediately before snap-off. The profile can be fit by an elliptical function (Equation 1, $y(x)$) with fitting parameters a, b, c as shown above. From Equation 2, the surface area of the meniscus is derived, enabling calculation of the energy required to build the meniscus (Equation 3) and the maximum pulling force on the trichome (Equation 4) equivalent to the water adhesion force of the trichome tip. By evaluating the elongation of the trichome, Δy, the elastic properties are determined.

$$W = A\cdot\sigma+\pi\left(\frac{c}{2}\right)^2\cdot\sigma^*-\pi\left(a+\frac{c}{2}\right)^2\cdot\sigma \qquad (3)$$

is required, which consists of the surface energy of the meniscus plus the interface energy of the tip–water contact area minus the surface energy of the original flat air–water interface before formation of the capillary contact. Here, $\sigma = 0.07275$ N/m [25] is the surface tension of the liquid (here, water), and σ^* is the interface tension of the contact area. Although the value of σ^* is unknown, it is not required for further calculations (see below). The force pulling at the trichome tip is equal to its water adhesion force and is given by:

$$F = \frac{\partial W}{\partial b} = \frac{\partial A}{\partial b}\cdot\sigma. \qquad (4)$$

Based on the images before and after the meniscus snap-off, the elongation, Δy, of the trichome in the direction of the force was observed. Assuming Hooke's law, its spring constant is

$$D = \frac{F}{\Delta y}. \qquad (5)$$

Likewise, other elastic constants such as Young's modulus can be determined, as shown later in the section where human head hairs are examined. The contribution of the weight force of the water within the meniscus to the force pulling at the tip in

contact with the water, is typically negligible. For the applications and examples shown in this work, the meniscus weight force was two orders of magnitude less than the contribution of the increasing liquid surface. This can be calculated using

$$V = 2\pi\left[\int_{0}^{c/2} x \cdot b\, dx + \int_{c/2}^{a+c/2} x \cdot y(x)\, dx\right] \quad (6)$$

for the liquid volume within the meniscus, as given in [24], and thus

$$F_G = \rho \cdot V \cdot g \quad (7)$$

is the weight force, where ρ is the density of the liquid and g is the gravitational acceleration.

Determining the adhesion force and elasticity of *Salvinia molesta* trichomes

The floating fern *Salvinia molesta* attracts considerable attention due to its ability to maintain a persistent layer of air on its leaves under water. This feature could be of high technological relevance, opening perspectives for completely new concepts for drag reduction of ships, for example, lubricating a ship hull with a permanent layer of air under water. As demonstrated, *Salvinia molesta* maintains this persistent air layer with a unique combination of hydrophobic hairs (trichomes) exhibiting hydrophilic, water-attracting tips (the Salvinia effect) [1]. The hydrophobic properties of the trichome surface prevent water from penetrating into the space between the multicellular trichomes, thus retaining a layer of air. The hydrophilic tips of the hairs, however, attract the water meniscus and adhere to the air–water interface, thus preventing the loss of air by formation of air bubbles.

In line with the method described above, 75 eggbeater-shaped trichomes of the floating fern *Salvinia molesta* were examined as taken from the central region of 15 adult leaves, 3 mm away from the edge, five from each of the leaves. This approach is explained by the fact that the trichomes at the edges exhibit different dimensions and shape. Our investigation resulted in an average value of the trichome tip adhesion force of F = (19.5 ± 0.3 ± 0.4) μN, where the statistical and systematic errors are noted, respectively. This high water adhesion force present at the tips of the eggbeater-shaped hairs is one key factor for the persistence of the air layer on the surface of submerged *Salvinia molesta* leaves due to the pinning of the air–water interface [1].

The elasticity of the trichomes was also studied, as there are indications that it may also play a key role in the air layer persistence. This elasticity may allow a moving air–water interface to be maintained by means of the hydrophilic pins, even under perturbations, without breaking water contact to the pins (which would lead to a loss of air by bubble formation) [1-3].

By applying CAT and investigating the 75 *Salvinia molesta* trichomes from the 15 different leaves mentioned above, we determined the average spring constant of the trichomes of *Salvinia molesta* to be D_{pulling} = (2.1 ± 0.2 ± 0.2) N/m, where the data denotes the average value, followed by the statistical and systematic errors, respectively. The data also support the assumption that the trichomes serve as soft springs (see above). The eggbeater shape of the trichomes is deemed to be ideal for this purpose. In fact, the experimental data show that the branched eggbeater-shaped part of the trichomes is responsible for the largest part of the length change of the trichomes as a response to an external force.

Determination of a spring constant according to Hooke´s law requires a linear elongation with increasing force, which is also proved by our method. In general, CAT allows the determination of the force–elongation curves of single structural entities. For this purpose, not only the image of the meniscus immediately before snap-off, but also other data taken between regarding the liquid surface–tip interaction and the snap-off are necessary to determine force and elongation. Figure 3 shows the results for a single *Salvinia molesta* trichome. As can be clearly seen, a linear function provides a very good approximation for the pulling force with respect to the trichome elongation, thus following Hooke's law. This is valid over the whole range from a smaller force to the maximum force immediately before snap-off.

Determining the water adhesion force, elasticity and Young's modulus of human head hairs

As a second application example of CAT, the water adhesion force of human head hairs as well as their spring constant and Young's modulus was studied by describing the elastic properties.

For this purpose, hairs from the same person both in the natural state and with two different thin film surface coatings were used. The effect of the surface coating of human head hair on its adhesive properties is highly relevant, for example, in the field of hair cosmetics. We investigated natural hair, hair with silicone-coated ends (poly(dimethylsiloxane) (PDMS), Sylgard 184, Dow Corning, water contact angle approx. 110°) and hair with Teflon-coated ends (poly(1,1,2,2-tetrafluoroethylene) (PTFE), Teflon AF, Dupont, water contact angle approx. 120°).

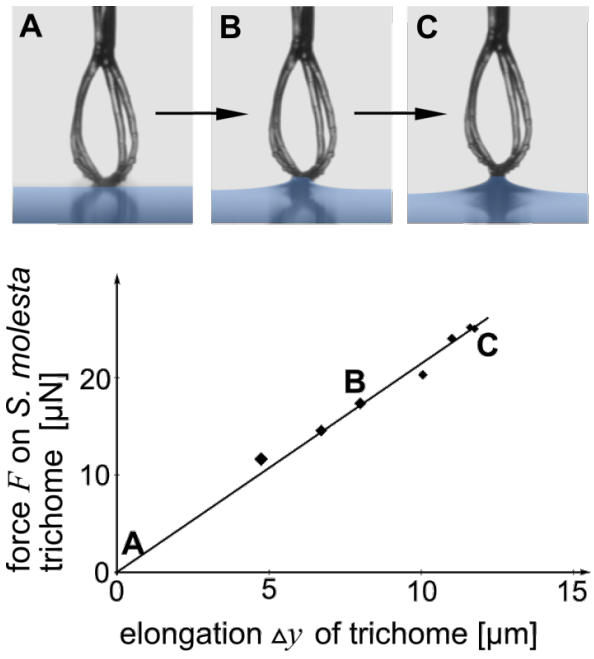

Figure 3: Force–elongation curve of a *Salvinia molesta* trichome. CAT allows force–elongation curves of small elastic structures to be measured based on the evaluation of the meniscus at different stages of the experiment. The linear fit to the data illustrates that the deformation follows Hooke's law quite well: before snap-off, the elongation of the trichome shows a linear force dependence. The systematic error of the force *F* corresponds to half of the height of each measuring point, whereas the systematic error of Δ*y* was 3 µm in each case.

15 hairs of each type were examined. They were fixed horizontally with the tweezers on a stepper motor, which served as a bending spring in contrast to the tension spring setup described in the previous section. The bending spring length was 1 cm. Figure 4 shows the experimental setup and images immediately before and after a typical meniscus snap-off event.

The results are summarized in Table 1. The water adhesion force of the ends of the hairs measured in their natural state was $F = (44.7 \pm 1.2 \pm 0.6)$ µN where the data is followed by the statistical and systematic errors, respectively. This value is significantly higher than for the cases of the PDMS- or Teflon-coated hairs, that is, the adhesion force decreases when the hair ends are hydrophobically coated. In contrast, the bending spring constant remained the same (within the limits of accuracy of the measurement). Averaged over all 45 hairs, the bending spring constant was $D_{\text{bending}} = (19.9 \pm 0.9 \pm 0.4)$ mN/m.

This version of CAT also allowed the measurement of Young's modulus for the structures under investigation. In the case of an elastic bar acting as a bending spring (fixed at one end and pulled at the other end downwards), Young's modulus is given by [26]

$$E = \frac{6 \cdot F \cdot l^2}{d^4 \cdot \tan\alpha}, \tag{8}$$

where the pulling force, F, is equivalent to the adhesion force, the hair length $l = 1$ cm, the hair diameter, d (individually and precisely determined using optical microscopy), and the angle α between the hair and water surface at the touching point immediately before snap-off, as extracted from the images shown in Figure 4. For the evaluation, the assumption of homogeneous and isotropic elastic properties was made. The resulting data are also shown in Table 1. For each type of hair coating (natural, PDMS- or Teflon-coated ends), the Young's modulus was the same within the accuracy of the measurement. Its average value was $E = (3.04 \pm 0.11 \pm 0.22) \times 10^5$ N/cm^2, with the statistical and systematic errors follow the data, respectively. The relative humidity during the measurements was roughly RH = 50% and the temperature was 22 °C.

Literature values citing Young's modulus of human head hair are scarce. For example, in [27] a value of 3.89×10^5 N/cm^2 (RH = 60%) was indicated. In [28], a range between 1.5 and 4.6×10^5 N/cm^2 (RH = 65%) was indicated for 2–92 year-old humans, and in [29] a range of $1.23–4.10 \times 10^5$ N/cm^2 (RH = 30%) was given for 15–35 year-old humans. Thus, our results (3.04×10^5 N/cm^2, RH = 50%, hairs from a 29 year-old human) are in good agreement with these literature values, indicating that CAT yields reliable results.

Validating the capillary adhesion technique using calibrated AFM cantilevers

A proof of the validity of the CAT method is given by examining a calibrated atomic force microscopy (AFM) cantilever. The cantilever was studied under the same conditions as the human head hairs (i.e., the chip on which the cantilever was attached was approximately horizontally fixed (11°) in the tweezers, see Figure 5). 15 independent measurements of the same calibrated cantilever were performed using the CAT, resulting in an average value for the water adhesion force of the cantilever tip of $(11.8 \pm 0.4 \pm 0.3)$ µN and a spring constant of $(0.195 \pm 0.002 \pm 0.011)$ N/m. This is in agreement with the spring constant of 0.18 N/m given by the manufacturer, which confirms the reliability of our method.

Conclusion

To conclude, a versatile, novel technique was presented, which determines both the adhesion force of individual small mechanical entities to a liquid in addition to their elastic properties, both with remarkable sensitivity mostly limited by optical resolution limits. Using this method, the water adhesion force and the elastic spring constant of the tips of *Salvinia molesta*

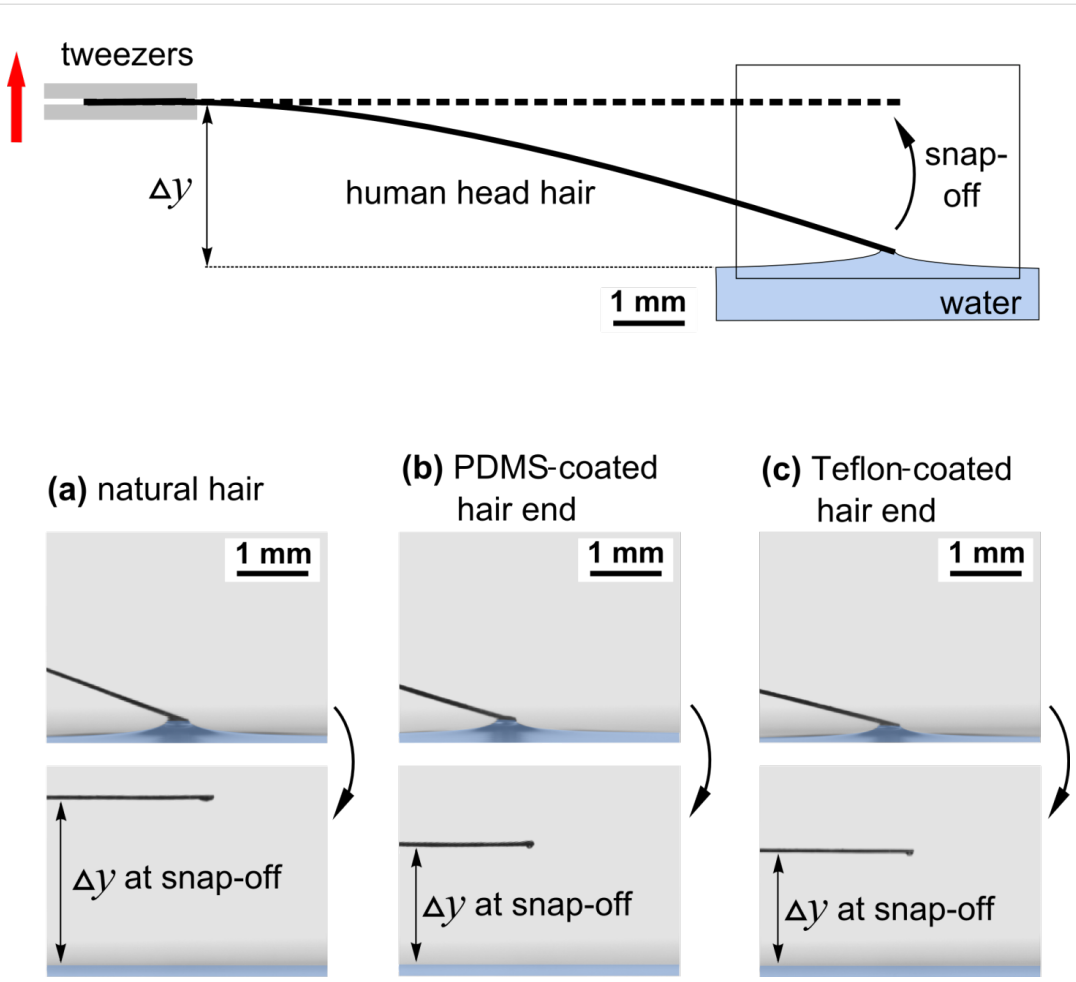

Figure 4: Examination of a human head hair. In this variation of the CAT, the hair is used as a bending spring. It is horizontally placed above the surface of the liquid in the tweezers and the bending before snap-off is measured with hair surfaces of different conditions (a) no coating (natural hair surface), (b) hair coated with teflon and (c) hair coated with silicone. Whereas the adhesion force depends on the coating, the elastic properties, such as the spring constant or Young's modulus of the hair, remain unchanged by the coating.

Table 1: The elastic and adhesive behavior of human head hairs with different coatings.[a]

	Natural hair	PDMS-coated hair end	Teflon-coated hair end
adhesion force (μN)	44.7 ± 1.2 ± 0.6	36.6 ± 1.0 ± 0.6	35.1 ± 1.3 ± 0.6
spring constant (mN/m)	19.1 ± 0.8 ± 0.3	20.6 ± 0.8 ± 0.4	20.1 ± 1.0 ± 0.4
Young's modulus (× 10^5 N/cm^2)	2.96 ± 0.10 ± 0.20	3.10 ± 0.12 ± 0.23	3.07 ± 0.12 ± 0.22

[a]The data for each measurement is followed by the associated statistical and systematic error, respectively.

trichomes were determined as $F_{adhesion}$ = (19.5 ± 0.3 ± 0.4) μN and D = (2.1 ± 0.2 ± 0.2) N/m, respectively, where the data is followed by the associated statistical and systematic error. As water adhesion and elasticity are key factors in order for *Salvinia molesta* leaves to maintain a persistent air layer under water, the resulting values can now be used as a basis for developing artificial air-retaining surfaces for technical applications based on a biomimetic approach. An example which further demonstrates the potential of this method was the investigation of the water adhesion force of natural and coated human head hairs, which is of high relevance for hair cosmetics, and the measurement of Young's modulus of the hairs. The latter was determined to be 3.0 × 10^5 N/cm^2, which is in good agreement with values from literature. Finally, further proof of the validity

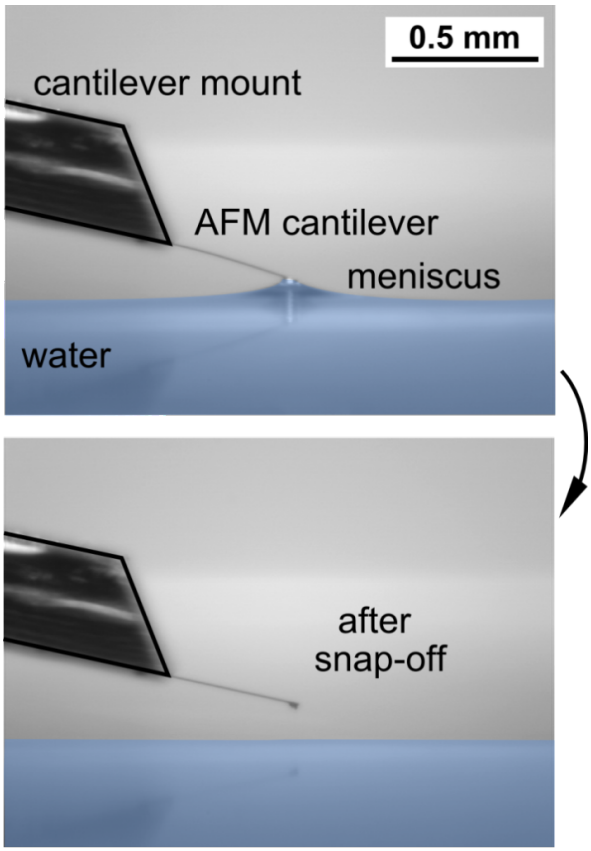

Figure 5: Proof of concept and accuracy of CAT, using specially calibrated AFM cantilevers. Determining the spring constant of the calibrated cantilever using the same settings as used for the individual hairs (see above, Figure 4) yields a spring constant in agreement with that given by the manufacturer.

of the capillary adhesion technique (CAT) was given by the measurement of the elastic force constant of 0.195 N/m for a calibrated atomic force microscopy cantilever.

Acknowledgements

We thank the German Ministry of Education and Research, BMBF, for funding within the project "Air Retaining Surfaces". Daniel Gandyra acknowledges support by the State of Baden-Wuerttemberg within a Baden-Wuerttemberg Scholarship.

References

1. Barthlott, W.; Schimmel, T.; Wiersch, S.; Koch, K.; Brede, M.; Barczewski, M.; Walheim, S.; Weis, A.; Kaltenmaier, A.; Leder, A.; Bohn, H. F. *Adv. Mater.* **2010,** *22,* 2325–2328. doi:10.1002/adma.200904411
2. Solga, A.; Cerman, Z.; Striffler, B. F.; Spaeth, M.; Barthlott, W. *Bioinspiration Biomimetics* **2007,** *2,* 126. doi:10.1088/1748-3182/2/4/S02
3. Koch, K.; Barthlott, W. *Philos. Trans. R. Soc. London, Ser. A* **2009,** *367,* 1487–1509. doi:10.1098/rsta.2009.0022
4. Koch, K.; Bhushan, B.; Barthlott, W. *Prog. Mater. Sci.* **2009,** *54,* 137–178. doi:10.1016/j.pmatsci.2008.07.003
5. Bhushan, B.; Jung, Y. C. *Prog. Mater. Sci.* **2011,** *56,* 1–108. doi:10.1016/j.pmatsci.2010.04.003
6. Kim, J.; Kim, C. J. Nanostructured surfaces for dramatic reduction of flow resistance in droplet-based microfluidics. In *The Fifteenth IEEE International Conference on Micro Electro Mechanical Systems,* IEEE International Conference on Micro Electro Mechanical Systems, Las Vegas, NV, USA, Jan 20–24, 2002; pp 479–482. doi:10.1109/MEMSYS.2002.984306
7. Ou, J.; Perot, B.; Rothstein, J. P. *Phys. Fluids* **2004,** *16,* 4635. doi:10.1063/1.1812011
8. McHale, G.; Shirtcliffe, N. J.; Evans, C. R.; Newton, M. I. *Appl. Phys. Lett.* **2009,** *94,* 064104. doi:10.1063/1.3081420
9. Balasubramanian, A. K.; Miller, A. C.; Rediniotis, O. K. *AIAA J.* **2004,** *42,* 411–414. doi:10.2514/1.9104
10. Shirtcliffe, N. J.; McHale, G.; Newton, M. I.; Zhang, Y. *ACS Appl. Mater. Interfaces* **2009,** *1,* 1316–1323. doi:10.1021/am9001937
11. McHale, G.; Newton, M. I.; Shirtcliffe, N. J. *Soft Matter* **2010,** *6,* 714–719. doi:10.1039/b917861a
12. Dong, H. Y.; Cheng, M. J.; Zhang, Y. J.; Wei, H.; Shi, F. *J. Mater. Chem. A* **2013,** *1,* 5886–5891. doi:10.1039/c3ta10225d
13. Cerman, Z.; Striffler, B. F.; Barthlott, W. Dry in the Water: The Superhydrophobic Water Fern *Salvinia* – a Model for Biomimetic Surfaces. In *Functional Surfaces in Biology;* Gorb, S. N., Ed.; Springer-Verlag: Berlin, 2009; Vol. 1, pp 97–111. doi:10.1007/978-1-4020-6697-9_7
14. Sheng, X. L.; Zhang, J. H. *Colloids Surf., A* **2011,** *377,* 374–378. doi:10.1016/j.colsurfa.2011.01.033
15. Samaha, M. A.; Tafreshi, H. V.; Gad-el-Hak, M. *C. R. Mec.* **2012,** *340,* 18–34. doi:10.1016/j.crme.2011.11.002
16. Debregeas, G.; Brochard-Wyart, F. *J. Colloid Interface Sci.* **1997,** *190,* 134–141. doi:10.1006/jcis.1997.4855
17. Restagno, F.; Poulard, C.; Cohen, C.; Vagharchakian, L.; Léger, L. *Langmuir* **2009,** *25,* 11188–11196. doi:10.1021/la901616x
18. Cohen, C.; Restagno, F.; Poulard, C.; Léger, L. *Langmuir* **2010,** *26,* 15345–15349. doi:10.1021/la102545z
19. Butt, H.-J.; Kappl, M. *Adv. Colloid Interface Sci.* **2009,** *146,* 48–60. doi:10.1016/j.cis.2008.10.002
20. Gorb, S. N.; Beutel, R. G.; Gorb, E. V.; Jlao, Y.; Kastner, V.; Niederegger, S.; Popov, V. L.; Scherge, M.; Schwarz, U.; Vötsch, W. *Integr. Comp. Biol.* **2002,** *42,* 1127–1139. doi:10.1093/icb/42.6.1127
21. Jiao, Y.; Gorb, S.; Scherge, M. *J. Exp. Biol.* **2000,** *203,* 1887–1895.
22. Huber, G.; Mantz, H.; Spolenak, R.; Mecke, K.; Jacobs, K.; Gorb, S. N.; Arzt, E. *Proc. Natl. Acad. Sci. U. S. A.* **2005,** *102,* 16293–16296. doi:10.1073/pnas.0506328102
23. Gorb, S. N.; Filippov, A. E. *Beilstein J. Nanotechnol.* **2014,** *5,* 837–845. doi:10.3762/bjnano.5.95
24. Bronstein, I. N.; Semendjajew, K. A.; Musiol, G.; Mühlig, H. *Handbook of Mathematics;* Springer: Berlin, Heidelberg, New York, Tokyo, 2007.
25. Adamson, A. W.; Gast, A. P. *Physical Chemistry of Surfaces;* John Wiley & Sons: New York, 1997.
26. Meschede, D., Ed. *Gerthsen Physik;* Springer: Berlin, 2010. doi:10.1007/978-3-642-12894-3
27. Robbins, C. R. *Chemical and Physical Behavior of Human Hair;* Springer Verlag: New York, 2002.
28. Naruse, N.; Fujita, T. J. A. *Geriatr. Soc.* **1971,** *19,* 308–314.
29. Johri, M. C.; Jatar, D. P. *Med., Sci. Law.* **1982,** *22,* 63–67.